VICERRECTORÍA DE INVESTIGACIÓN Y POSTGRADO
DIRECCIÓN DE POSTGRADOS Y POSTÍTULOS

FACULTAD DE CIENCIAS
DEPARTAMENTO DE ASTRONOMÍA

THE IONIZED GAS KINEMATICS OF LYMAN CONTINUUM EMITTERS
CINEMÁTICA DEL GAS EN GALAXIAS CON EMISIÓN DE FOTONES IONIZANTES

Tesis presentada para optar al Grado Académico de Magíster en Astronomía.

AUTOR: MATÍAS IGNACIO RODRÍGUEZ HENRÍQUEZ

LA SERENA, CHILE, OCTOBER 2022

CONSTANCIA

Don .....

HACE CONSTAR:

Que el trabajo correspondiente a la presente Tesis de Magíster, titulada "Cinemática del gas en galaxias con emisión de fotones ionizantes", ha sido realizada por Don Matías Ignacio Rodríguez Henríquez, bajo mi dirección.

Para que conste y en cumplimiento de las normativas vigentes de la Universidad de la Serena, Chile, firmo el presente documento en La Serena, Chile, el 25 de Octubre de 2022.

TESIS PARA OPTAR AL GRADO DE MAGÍSTER EN ASTRONOMÍA

TÍTULO: THE IONIZED GAS KINEMATICS OF LYMAN CONTINUUM EMITTERS
CINEMÁTICA DEL GAS EN GALAXIAS CON EMISIÓN DE FOTONES IONIZANTES

PRESENTADA POR: MATÍAS IGNACIO RODRÍGUEZ HENRÍQUEZ
DIRECTOR DE TESIS : RICARDO O. AMORÍN

TRIBUNAL CALIFICADOR

El tribunal de tesis, conformado por:

PRESIDENTE :
MIEMBROS DEL TRIBUNAL: *
*
*

ACUERDAN OTORGARLE LA CALIFICACIÓN DE:

La Serena, Chile, **25 de Octubre de 2022**

“ Living is easy with eyes closed, misunderstanding all you see.” - John Lennon

ACKNOWLEDGMENTS

To my family, friends, and colleagues. I chase my dreams by grabbing your hands.

I'm grateful to have the opportunity of learning from such a tremendous mentor, Ricardo Amorín. He believes in my capacities more than myself and helps me to reach desires that once were thought too distant. Thanks to Vital Ferndez, Verónica Firpo, Mario Llerena and Dania Muñoz for every idea and advice given at the *Gaussian Reunions*. All of you motivate me to do my best.

I acknowledge the financial support from DIDULS/ULS through the project PTE2053851, and the support of ANID FONDECYT Regular Grant 1202007.

Summary

Green peas (GPs) are low-mass starburst galaxies in the nearby universe that can provide key insight into cosmic reionization. Here we study the ionized gas kinematics of a sample of GPs at redshift z$\sim$ 0.3. Most of these objects are confirmed Lyman continuum emitters (LCEs) with absolute escape fractions between 1-63 percent. The galaxies show strongly asymmetric emission-line profiles that can be modeled with multiple Gaussian components. A broad component with an intrinsic velocity dispersion of $\gtrsim$100-270 km/s is present in all galaxies in the sample, indicating the presence of an unresolved outflow. Narrower components trace the prominent HII regions within the galaxies and show an intrinsic velocity dispersion of $\lesssim$70 km/s, which accounts for a large percentage of the total line flux. Classical diagnostic diagrams indicate very strong radiation fields consistent with stellar photoionization. Remarkably, we find significant correlations between LyC escape fractions and outflow velocity, with strong LCEs exhibiting broader emission line profiles (FWZI) and greater intrinsic velocity dispersion of the broader component. Our results suggest that outflows and strong gas turbulence driven by the collective action of massive stars winds and SNe in the galaxies' massive clusters can be responsible for creating channels in a likely clumpy interstellar medium from which LyC photons escape into the intergalactic medium. Therefore, we propose that the presence of broad components may be a good indirect diagnostic for the escape of ionizing photons and a useful tool to identify potential LyC leakers in the reionization era with the *James Webb Telescope*.

Table of contents

Chapter 1

Introduction

1.1. The epoch of Reionization

1.1.1. Cosmological context

The Standard Model (ΛCDM) allows us to distinguish between the different phases of the universe and its constituents (Figure 1.1) and explain how everything evolved from a very hot and dense plasma to the large structures that astronomers observe today. In this picture, the early universe filled with hot ionized gas expanded and cooled, so that electrons could recombine with protons to form neutral hydrogen (Planck Collaboration et al., 2020, $z \sim 1090$). This transition is imprinted in the cosmic microwave background (CMB), as the last scattering from the thermal radiation of the early universe produced by free electrons. Gravity shaped the neutral

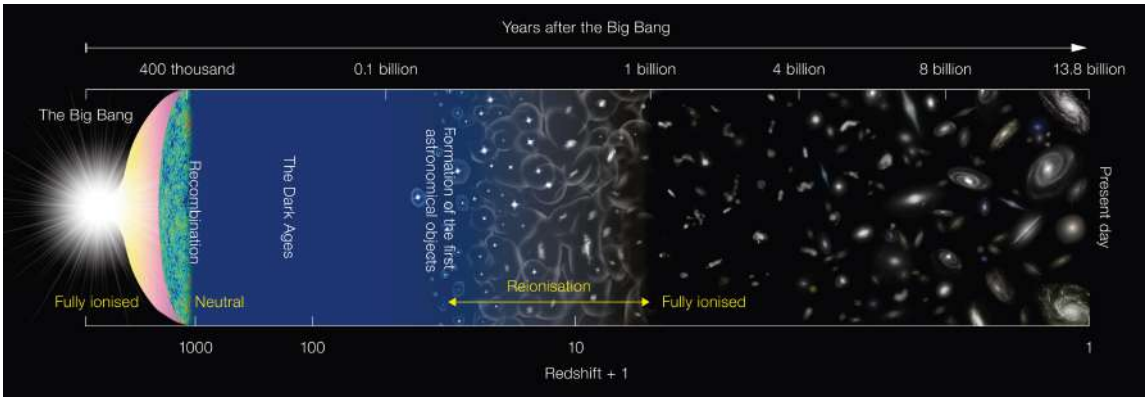

Figure 1.1: This diagram illustrates the major events in the evolution of the Universe since the Big Bang. The Universe was in a neutral state 400 years after the Big Bang and then gradually ionized during the first thousand years of cosmic evolution, as it has reminded to this day. Credit: *NAOJ.*

gas during these dark ages when there were no light sources other than the redshifted CMB. Then, the gas began to collapse at the intersections of the filaments, and the first galaxies formed. In them, the first massive stars extremely metal-poor stars produced intense Lyman continuum photons (LyC; E> 13.2 e.V, $\lambda < 912$Å) capable of ionizing neutral hydrogen. As galaxies grew and more massive stars formed, ionizing radiation began to escape into the surrounding intergalactic medium (IGM), creating ionized bubbles that grew and merged over time. These interactions marked the beginning of cosmic reionization (Robertson et al., 2015, $6 \lesssim z \lesssim 10$), one of the largest transformations of the universe, in which almost all neutral hydrogen (HI) was completely ionized as we see it today. The cosmic feedback generated by the first astrophysical objects had a major impact on the formation and evolution of galaxies (Ocvirk et al., 2016), which preceded to the most active cosmic era in the formation of galaxies (Madau & Dickinson, 2014, $1 \lesssim z \lesssim 3$).

Numerous observations give attest to the large amounts of neutral hydrogen present in the high-redshift universe, two of which we mentioned here. Quasars (QSOs) are extremely luminous galaxies that emit radiation throughout the electromagnetic spectrum and can be seen at high redshifts in our universe. Using these objects as background light allows us to estimate the amount of HI in the IGM due to the Gunn-Peterson effect (Gunn & Peterson, 1965; Becker et al., 2021). As UV light of the QSOs moves and expands through the universe, clouds of neutral hydrogen in the line of sight produce absorptions in the QSO spectra because they are extremely efficient at absorbing photons with wavelengths shorter than Lyα ($\lambda = 1216$Å). Using this method we can demonstrate that cosmic reionization is complete at $z \sim 6$ (Yang et al., 2020; Fan et al., 2006), as absorption by neutral hydrogen increases with distance (see Figure 1.2). The CMB can also be used as a background light to determine when this process occurred. Because the free electrons of the IGM interact with the light and polarize it via Thompson scattering, we can detect signatures of scattering in the CMB photons after the epoch of recombination. These imprints enable us to estimate the amount of free electrons (amount of ionized gas) in the IGM which is quantified with the Thomson optical depth. The latest results of the Planck mission report a Thomson optical depth of $\tau_e = 0.054 \pm 007$. Using the latter, and assuming instantaneous cosmic reionization is possible to estimate the redshift when process occurred $z = 7.7 \pm 0.7$ (Planck Collaboration et al., 2020).

Understanding how the reionization of the universe occurred, i.e., what objects and physical processes favoured this transition, and understanding how these first

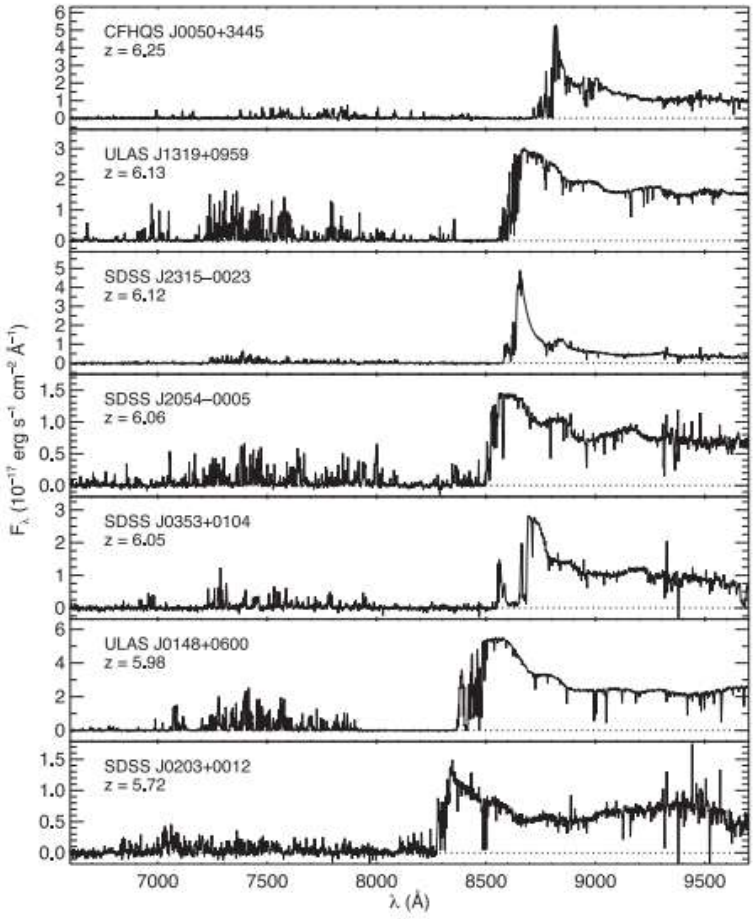

Figure 1.2: Spectra of $z \sim 6$ quasars, with decreasing redshift to the lower rows. As the distance to the background light (QSO spectra) increases, the neutral hydrogen absorptions also increase which is due larger amounts of neutral gas. The figure is from Becker et al. (2015)

galaxies evolved are two of the most important open questions in modern astrophysics, motivating not only a numerous investigations, but also a major goal of new observatories such as the *James Webb Space Telescope* (JWST).

1.1.2. First galaxies and the cosmic reionization

While the period of cosmic reionization is getting constrained (e.g Planck Collaboration et al., 2020; Fan et al., 2006), the question of which objects regulated and dominated this process is still open. The debate revolves around two main cosmic sources that can provide ionizing photons: Accreting black holes (Madau & Haardt, 2015, AGN) and massive stars inside galaxies (Robertson et al., 2015). While both should contribute to cosmic reionization (Dayal et al., 2020; Finkelstein et al., 2019),

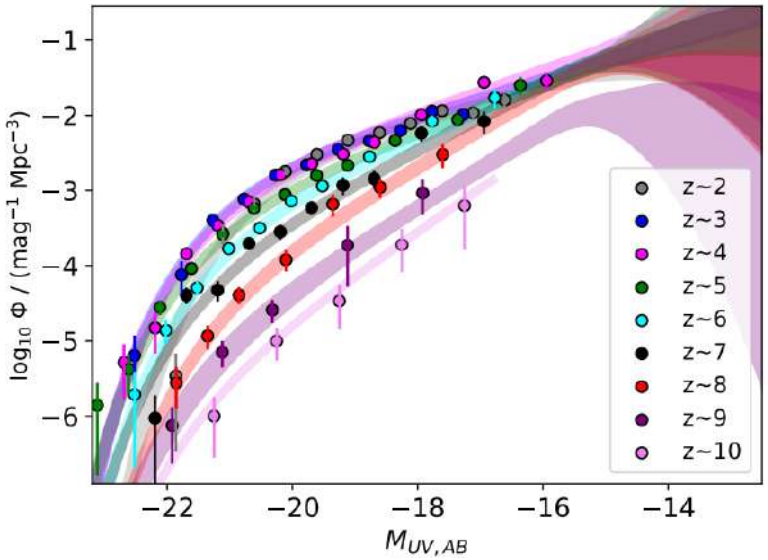

Figure 1.3: The rest-frame UV luminosity functions (i.e, the number density of galaxies per UV luminosity/absolute magnitude; LFs) at $z \sim 2-10$ obtained from observations of the *Hubble Frontier Fields*, including lensed galaxies. The colors differs for each redshift and the shaded areas represent the 68 % confidence contours. The figure is from Bouwens et al. (2022).

the question regards in the relative contribution of each candidate populations. To determine the contribution of both candidates in terms of the emission rate of LyC photons ($\dot{n}_{ion}$),i.e., the density of LyC photons produced per unit time available for hydrogen ionization in the IGM, we need to test the theory by measuring three critical parameters,

$$\dot{n}_{ion} = f_{esc}^{LyC}\ \varepsilon_{ion}\ \rho_{UV} \tag{1.1}$$

where f_{esc}^{LyC} is the fraction of ionizing radiation (measured at $\lambda_{rest} \approx 900$Å) that escapes to the IGM, ε_{ion} is the ionizing photon production efficiency of either stellar populations in galaxies or by the AGN, and the value ρ_{UV} is the UV luminosity density of such AGN or galaxies at $z > 6$. While f_{esc}^{LyC} is unlikely to be observed due to the high IGM opacity (e.g Inoue et al., 2014), the other two parameters have been constrained by observations. To quantify the UV luminosity density ρ_{UV} at a given time, astronomers use the volume density of galaxies derived from galaxy searches as a function of luminosity (i.e. UV luminosity function; see Figure 1.3), multiply this volume density by the UV luminosity, and then integrate this product over the entire range of observed (and expected) UV galaxy luminosities (Bouwens et al., 2022).

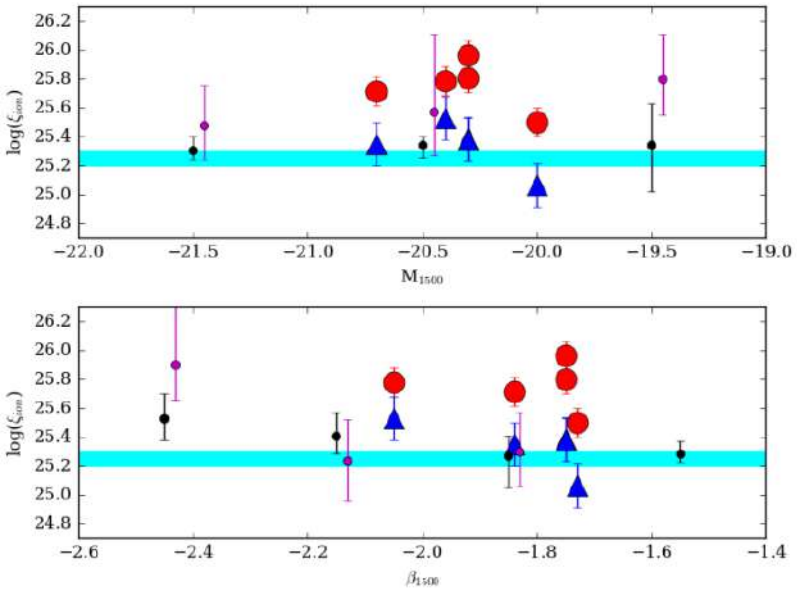

Figure 1.4: The efficiency of ionizing photon production (ε_{ion}) as function of the absolute UV magnitude (top panel) and the UV slope (spectral shape; bottom panel) of five GPs Lyman continuum leakers. Large red symbols show ε_{ion}, while blue large symbols show the intrinsic efficiency ε^0_{ion} , the efficiency after correction for dust attenuation. The small black and magenta symbols represent LBGs at high redshift (see Schaerer et al. (2016)), and the cyan band illustrates canonical values for ε^0_{ion} determined by synthesis models. The figure is from Schaerer et al. (2016).

However, this is not so straightforward, as we need to extrapolate the observed luminosity function to luminosities that are fainter than what we can readily probe with the available data sets (i.e, the faint-end slope of the luminosity function). On the other hand, the efficiency of ionizing photon production (ε_{ion}) can be estimated using stellar synthesis models to reproduce the galaxy spectral energy distribution (SED). For high redshift studies, Robertson et al. (2013) determined the canonical values of $\log(\varepsilon_{ion}) \approx 25.2 - 25.3$ erg^{-1} Hz, corresponding to constant star-formation rate and slightly sub-solar metallicity. However, for a given SED shape (which is related to the UV slope β) the ε_{ion} can vary greatly as it depends on the metallicity, initial mass function, and star-formation history, which are key parameters for ionizing photon production. Therefore, another approach to determine ε_{ion} is to use the hydrogen recombination lines (e.g Schaerer et al., 2016; Bouwens et al., 2016). Since recombination lines are produced in star-forming regions by photoionization, one can estimate the intrinsic ionizing photon production rates with Balmer luminosities through analytical relations (see Figure 1.4). With this background, we resume the discussion of the main sources of reionization as follows.

Bright AGNs can inject large amounts of ionizing photons ($f^{LyC}_{esc} \sim 1$) into the

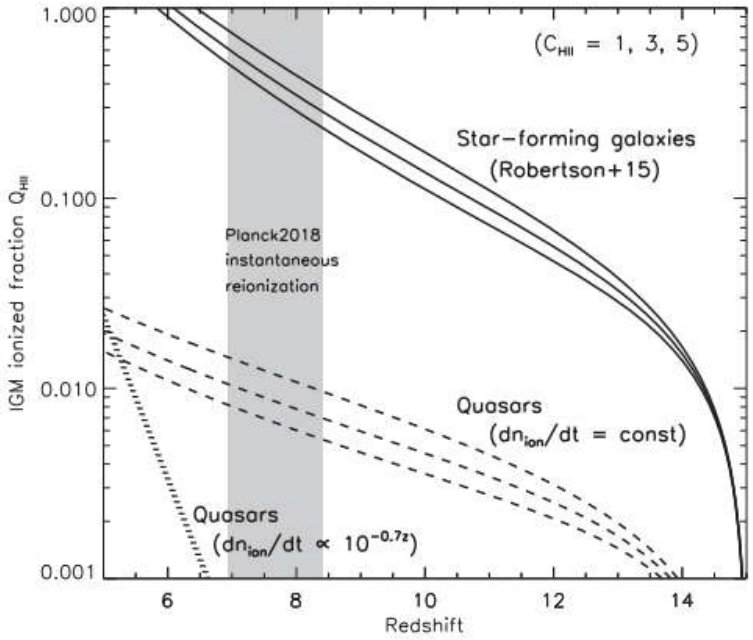

Figure 1.5: The evolution of the ionized fraction of the intergalactic medium. The three solid curves represent the contribution of star-forming galaxies with different clumping factors ($C_{HII} = 1, 3, 5$; see Matsuoka et al. (2018)), while the dashed and dotted curves represent the quasar contributions for the same clumping factors, for models with different ionizing photon density (Equation 1.1.2). The shaded area represent the 1σ confidence of the instantaneous reionization redshift, taken from *Planck Collaboration 2018*. The QSOs are not the major contributors for cosmic reionization. The figure is from Matsuoka et al. (2018).

IGM (Lusso et al., 2015). However, they seem to be unusual (low ρ_{UV}) at high redshifts (e.g Shen et al., 2020; Matsuoka et al., 2018), and with lower emissivities than in the nearby Universe (Dayal et al., 2020). Therefore, bright AGNs are unlikely to be a major contributor to cosmic reionization. On the other hand, fainter AGNs may be numerous and make a larger contribution (Giallongo et al., 2015) to the reionization process, but their role is still unclear. Star-forming galaxies (SFGs) seem to be the best candidates as the main contributors to cosmic reionization (see Figure 1.5). However, there is no consensus on which galaxies, the relatively more massive/larger ones or the lower-mass/smaller ones, provide the larger budget of ionizing radiation. The massive galaxies have a stronger gravitational potential that facilitates efficient star formation, which implies larger amounts of LyC photons. Nevertheless, they are rare at high redshifts (e.g Naidu et al., 2020; Wyithe & Loeb, 2013) and have more material (gas and dust) that can obstruct the ionizing radiation to escape. In contrast, compact SFGs are very common at high redshifts (e.g Finkelstein et al., 2019; Bouwens et al., 2015; Robertson et al., 2015) and have

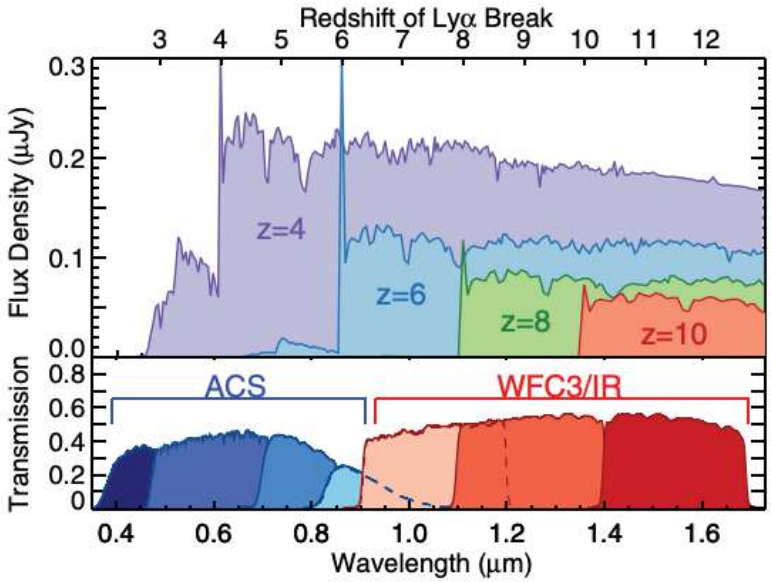

Figure 1.6: Model galaxy spectra at four different redshifts ($z = 4, 6, 8, 10$), compared to the *Hubble Space Telescope* optical (ACS) and near-infrared (WFC3) filter sets. The Lyman break shifts to redder wavelengths for increasing redshift, thus, galaxies do not appear at shorter wavelengths producing what is known as a Lyman Break Galaxy (LBG). The figure is from Finkelstein (2016).

a weaker gravitational potential, making them more susceptible to stellar feedback that can contribute to the erosion of the IGM and increase the escape fraction of LyC photons (e.g Izotov et al., 2021; Trebitsch et al., 2017). In order for reionization to occur at $z > 6$, we require these objects to have $f_{esc}^{LyC} \sim 0.1 - 0.2$ (Naidu et al., 2020; Finkelstein et al., 2019; Robertson et al., 2015).

Confirm that low-mass compact SFGs are the main contributors of the cosmic reionizaition requires the determination of the three parameters of the Equation 1.1. While ε_{ion} and ρ_{UV} are measurable quantities in the population of galaxies at high redshift, especially feasible with new observatories like the *JWST* and the next generation of giant telescopes that will operate in Chile (*GMT* and *ELT*) during the next decade (See review Robertson, 2021), it is impossible to directly measure the f_{esc}^{LyC} from objects at the epoch of reionization ($z > 6$) due to the high amounts of neutral gas in the IGM which easily absorb ionizing radiation (e.g Inoue et al., 2014; Fan et al., 2006). Therefore, we must study Lyman continuum emitters (*LCE*) at lower redshifts to develop indirect diagnostics that help us estimate the escape fraction of galaxies at higher redshifts. These diagnostics may also provide constrain to the physics that controls the escape fraction (environments, mechanisms, etc), which is crucial to investigate the impact of SFG on cosmic reionization and draw

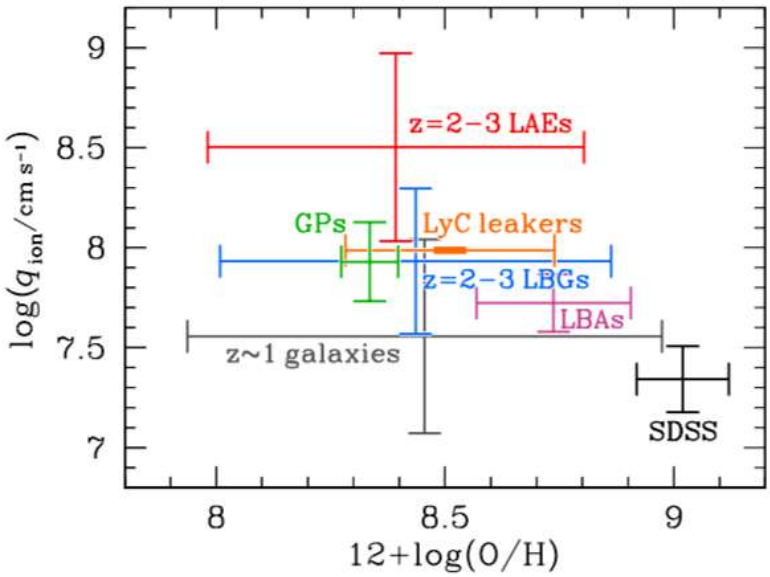

Figure 1.7: Average ionization parameter (q_{ion}) and metallicity for different types of galaxies. The black bars labeled as SDSS represent 136,000 nearby star-forming galaxies from SDSS Data Release 7 MPA/JHU. The green bars labeled as GPs represent 66 green pea galaxies at $z < 0.36$. The pink bars labeled as LBAs represent 37 Lyman break analogs at $z < 0.30$ whose properties are similar to those of high-z LBGs. The orange bars labeled as LyC leakers represent the two confirmed local Lyman continuum emitters Haro 11 and Tol 1247. An intermediate-redshift sample of 69 galaxies ($z \sim 1$) is shown as gray bars. High redshift galaxies ($z = 2 - 3$) are divided into Lyman break galaxies (LBGs; EW(Lyα)$<$ 20Å) shown as blue bars, and Lyman alpha emitter (LAEs; EW(Lyα)$>$ 20Å), which are shown as red bars. The GPs show similar properties two high redshift galaxies and LyC leakers. The figure is from Nakajima & Ouchi (2014).

solid conclusions.

The most successful strategy in the search for indirect indicators is based on the detection and study of LyC emitting objects with properties similar to those of the first galaxies but observed at lower redshifts, where LyC photons manage to reach our telescopes after overcoming the opacity of the IGM in the line-of-sight. Lyα emitting galaxies (LAEs, EW$>$ 20Å) are thought to be the most promising analogs of galaxies in the epoch of reionization because their common characteristics such as low metallicity, low-intermediate mass, low dust-attenuation, high star formation rate, and their highly ionized ISM (e.g Ouchi et al., 2020; Finkelstein et al., 2011). Recently, Naidu et al. (2022) using stacks and indirect methods of LyC escape fraction estimate that half of LAE at $z \approx 2$ have $f_{esc}^{LyC} \approx 50\,\%$. The author extrapolate the result to $z > 6$ based in the invariance of some properties of the LAEs. Furthermore, the majority of galaxies at $z > 6$ are expected to be LAEs (e.g Matthee et al., 2018; Stark et al., 2011).

Although at intermediate redshifts $z \sim 2-3$ is expected the existence of a greater number of galaxies analogous to those of reionization as the ones mentioned above, only a handful of *LCE* have been confirmed after enormous observational efforts (e.g de Barros et al., 2016; Vanzella et al., 2016; Steidel et al., 2018; Ji et al., 2020). This is due to its weak intrinsic emission, unknown galactic properties that favor detection, and other observational limitations (e.g. confusion with near line-of-sight objects Vanzella et al., 2016). In order to avoid the aforementioned observational limitations, one of the alternatives to study the escape of ionizing photons is to find local analogs of the systems that we expect to emit such photons in the early universe. The last years, numerous *LCE* have been found at $z \sim 0.3$ (e.g Flury et al., 2022a; Izotov et al., 2018a,b, 2016b,a). These objects belong to the extreme populations of Green Pea galaxies (GPs Cardamone et al., 2009), which are local counterparts of high redshift galaxies (LBG) and LAEs (e.g Yang et al., 2017; Schaerer et al., 2016; Nakajima & Ouchi, 2014) according to their physical properties (e.g metallicity, compactness, etc). In the next section we review the insights of the LyC escape to latter discuss about the achievements made by studying the Green Pea galaxies.

1.2. Escape of ionizing radiation

The escape fraction of ionizing radiation (f_{esc}^{LyC}) is determined as the ratio between the LyC photons (E> 13.2 e.V, $\lambda < 912$Å) that manage to escape from the galaxy to ionize the IGM, and the total amount produced within the object. The absolute escape fraction of LyC is defined as,

$$f_{esc}^{LyC} = \frac{F_{\lambda LyC}^{obs}}{F_{\lambda LyC}^{mod}} \tag{1.2}$$

where $F_{\lambda LyC}^{obs}$ is the Lyman continuum flux measured in a window close to $\lambda \approx$ 900Å corrected by Galactic extinction, and $F_{\lambda LyC}^{mod}$ is the intrinsic (modeled) flux of Lyman continuum photons produced by the galaxy. The $F_{\lambda LyC}^{mod}$ can be calculate by fitting the UV SED of the galaxy or from recombination lines of hydrogen, which are proportional to the number of ionizing photos emitted per unit time (e.g Izotov et al., 2016b) (More details in Section 2.2.1).

As mentioned in previous section, this quantity is crucial to determine how the reionization process take place. However, direct detection of this radiation is extremely challenging as farther we see in the universe because the increasingly amounts

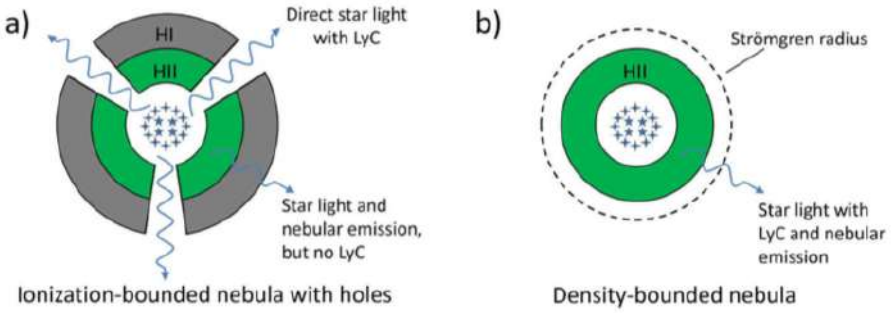

Figure 1.8: Schematic illustrations of the escape of ionizing radiation mechanisms. A galaxy is here represented by a centrally concentrated cluster of stars, surrounded by ionized gas (green region), and possibly an outer region of neutral gas (gray). A) A ionization-bounded nebula, in which LyC photons escape through low filling-factor channels (picket fence model). B) A density-bounded nebula, where all the neutral gas is photoionized by the starburst, thus, LyC photons are not absorbed by the ISM. The figure is from Zackrisson et al. (2013).

of HI, and the fact that ionizing radiation stretch to longer wavelength as it travels toward us, reaching Lyman-series wavelengths which are easily absorbed by low HI column density (Inoue et al., 2014). In consequence, we need to establish indirect probes of the escape of ionizing radiation in order to study distant *LCE*.

The young massive star complexes inside star-forming galaxies impregnate the ISM with UV photons and line-of-sight effects may determine the escape of them into the IGM. In this sense, the spatial distribution of the stars, gas, and dust in the ISM of the galaxy are fundamental to determine how the Lyman photons can escape. To better understand this problem we present simple geometric perspectives (see Figure 1.8) which describe how the LyC photons may escape (e.g Zackrisson et al., 2013),

- Ionization-bounded nebula: In the idealize scenario of a star-forming region, young massive stars produce UV photons that ionize the surrounding neutral gas. The detailed balance (ionization equilibrium) produced by the ionizing photon production and the recombination rate of the gas delimit a region called the Strömgren-Sphere, whose inside posses only ionized gas. In this picture, the ISM is *optically thick* to the ionizing radiation which cannot escape from the nebulae, being absorbed by the neutral gas which then cools down by emitting recombination lines. However, privilege paths (holes or channels) with low covering factor of neutral gas can be produced by stellar feedback (Heckman et al., 2011) through which LyC radiation can manage to escape (see Figure 1.8) without getting absorbed. The latter model is also known as the *picket-fence*.

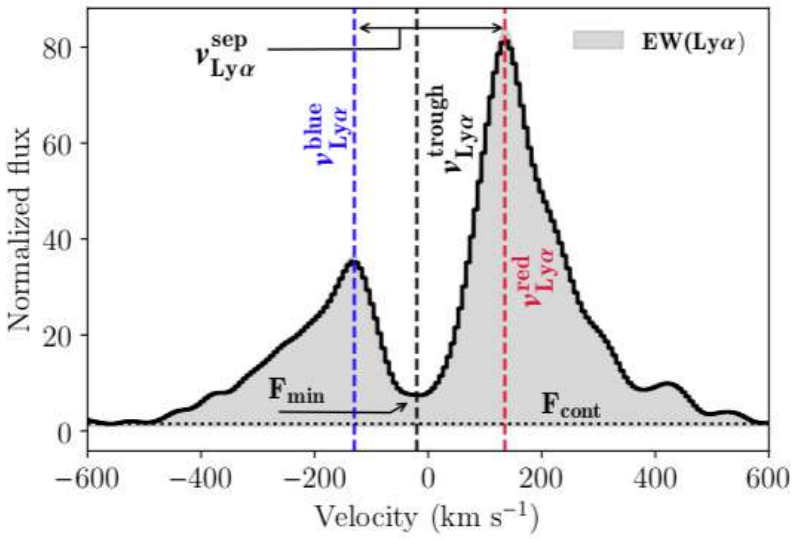

Figure 1.9: The double peak Lyα emission-line profile of the galaxy J1011+1947. The blue dashed-line show the velocity of the blue peak, while the red dashed-line show the velocity of the red peak. The separation velocity (v_{sep}) is calculated as the velocity difference between the peaks. The dotted-line is the continuum flux, and the shaded area represent the emission flux used to calculate the equivalent width. The figure is from Gazagnes et al. (2020).

- Density-bounded nebula: In this scenario the starburst ionize all the surrounding neutral gas, and the region is delimited by the ionized gas content (see Figure 1.8). As the young massive stars continue to produce ionizing radiation, which is not absorbed by the ISM, these LyC photons can escape to the IGM (Nakajima & Ouchi, 2014; Jaskot & Oey, 2013). Thus, high escape fraction is expected from starburst with this condition.

Despite the simplicity of these models and the fact that galaxies have more complex geometry and material distribution (Ramambason et al., 2020), we should expect from these scenarios that *LCE* share some physical properties such as compactness, a high-ionization state of the ISM, low column densities of neutral gas, and low dust content (Rosdahl et al., 2022). All these signatures can be traced by different observables along the electromagnetic spectrum of these objects, and conform the most used indirect diagnostics to find *LCE*.

The emission-line ratio $[OIII]\lambda5007$Å$/[OII]\lambda3727$Å(Izotov et al., 2018b, O_{32}) is a good tracer of the ionization structure of the ISM within the galaxy. In the *ionization-bounded* model, lower ionization species (e.g [O II],[S II]) are spatially distributed in the outermost part of the nebula (Osterbrock & Ferland, 2006), while higher ionization species are closer to the center (e.g [O III]). As we approximate to the

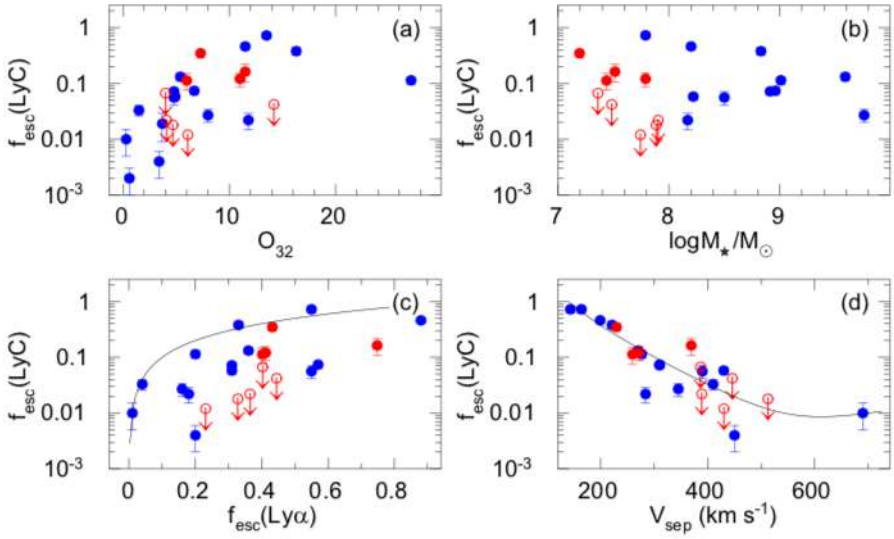

Figure 1.10: Relations between the escape fraction of LyC in low-redshift LCE and (A) The O_{32} emission-line flux ratio, (B) the stellar mass (M_*), (C) the escape fraction of Lyα ($f_{esc}^{Ly\alpha}$), and (D) the velocity separation between the Lyα peaks. The blue and red circles are confirmed LCEs (see Izotov et al. (2021)), while open circles are galaxies with upper-limits measurements. All the relations show considerable scatter, however, the peak separation seems to be the tightest correlation. The figure is from Izotov et al. (2021).

density-bounded regime, there is a notorious decrement of [O II], which produce large values of O_{32}. Then, high values of O_{32} may be related to a high probability of ionization radiation to escape (Nakajima & Ouchi, 2014; Jaskot & Oey, 2013).

The UV absorption lines trace the cold ISM gas of galaxies. In optically thick regimes these absorptions are saturated (flux $\sim$ 0). Thus, a significant residual intensity in the core of these interstellar absorption-lines is evidence of a low covering factor of the LyC sources, indicating porosity which can be related to the *picket-fence* or the *density-bound* models (e.g Saldana-Lopez et al., 2022; Gazagnes et al., 2020; Heckman et al., 2011).

Notably, the Lyα emission is a great indirect diagnostic of *LCE*. This emission is produced by recombination of hydrogen atoms that were ionized by LyC photons, therefore both are closely related. Moreover, Lyα radiation is resonant and easily scattered by neutral hydrogen, which gives special features in the emission-line profile and provides great insights about the neutral gas. Double-peak Lyα emissions in star forming galaxies reflects the radiative transfer complexity of the resonant radiation, and a small separation (both peaks close to the systemic redshift, Figure 1.9) indicate low column densities of HI which benefit the escape of ionizing radiation (e.g Izotov et al., 2021; Gazagnes et al., 2020; Jaskot et al., 2019; Verhamme et al., 2015).

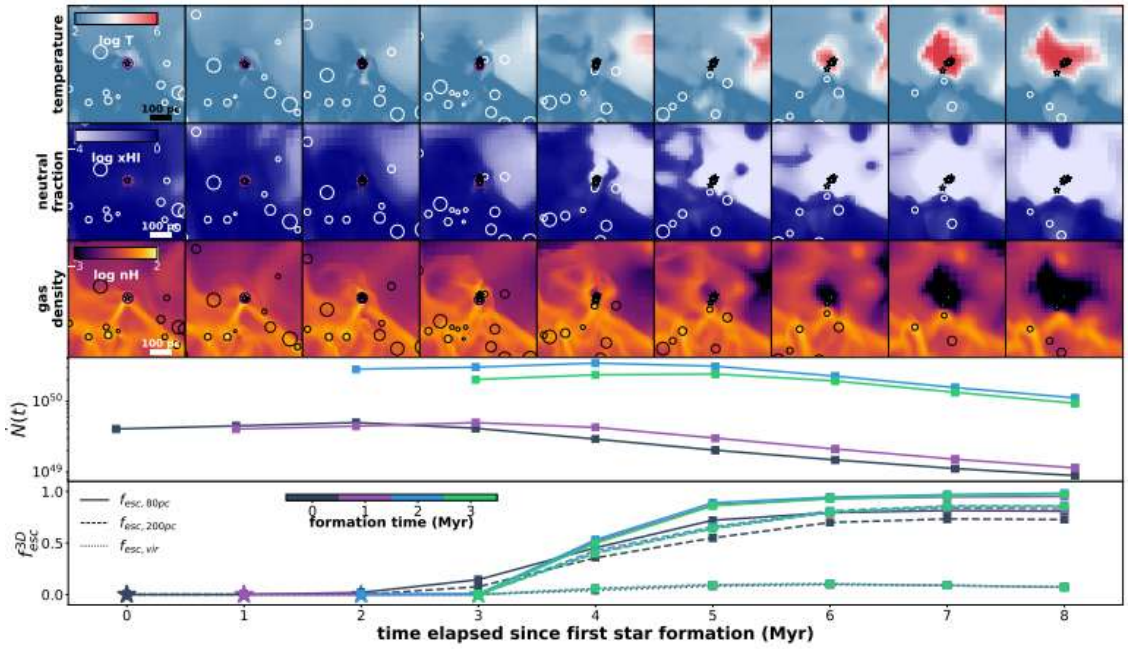

Figure 1.11: Evolution of young stellar complexes. The three upper rows show zoomed-in distributions of temperature, neutral hydrogen fraction, and gas density respectively. The main clump is shown as the purple circle, and the newborn stars are indicated as cyan stars. The luminosity weighted escape fraction, and the ionizing emissivity (bottom rows) of these stars are coloured based on their formation time. Different escape fractions as function of distance are represented as solid-line (80 pc), dashed-line (200 pc), and dotted-line (virial radius). The escape fractions increase with time as stellar feedback erode the ISM. The figure is from Yoo et al. (2020).

Furthermore, Jaskot et al. (2019) demonstrate that this property correlates with the ionizing state, suggesting a density-bounded geometry in some *LCE*.

All the mentioned features are used as indirect diagnostic to find *LCE* but they show large scatter in correlation with the f_{esc}^{LyC} (see Figure 1.10), being insufficient as good diagnostics alone and making difficult to use them to confidently find *LCE* at high redshifts. However, they transform this field of study by helping with the detection of numerous *LCE* at low redshift (e.g Flury et al., 2022a; Izotov et al., 2018a,b, 2016a,b) and at high redshift (e.g Saxena et al., 2022; Vanzella et al., 2022; Steidel et al., 2018).

On the other hand, astrophysical simulations give crucial information about the mechanisms that allow the escape of ionizing radiation by studying the process in detail (e.g, Figure 1.11). Rosdahl et al. (2022) found that star formation feedback and supernovae (SNe) regulate the periods of escape of LyC in fractions of a few Myr. The authors found that f_{esc}^{LyC} peaks in intermediate-mass, intermediate-brightness, and low-metallicity galaxies ($M_* \approx 10^7\ M_\odot$, $M_{1500} \approx -17$, $Z \leq 5 \times 10^{-3}\ Z_\odot$), dropping

for higher metallicity and other ranges of masses, similar results to those of Ma et al. (2020). Hydrodynamical simulations of galaxy formation demonstrate an important role of SNe and stellar feedback as the primary drivers of mechanical energy and turbulence in the ISM, allowing paths of low column density from which ionizing radiation can escape (e.g Trebitsch et al., 2017). Other works, such as Kakiichi & Gronke (2021) show that LyC leakage succeeds even at early times before SNe onset, where radiative mechanisms are the main contributor to turbulence. Nevertheless, is hard to compare these results with observations given the difficulties of studying *LCE* in detail (e.g lack of spatial resolution). Hence, *LCE* in the nearby universe open a great possibility to analyze the mechanisms involved in the LyC leakage and can be compared with predictions of astrophysical simulations.

1.3. Local analogs: Green Pea Galaxies

The *green peas* (GP) are a population of starburst galaxies that have been extensively investigated during the last decade (Cardamone et al., 2009; Amorín et al., 2010; Fernández et al., 2022). Their physical properties are very rare in the nearby universe but are similar to those found in high-redshift galaxies (Schaerer et al., 2016; Kim et al., 2021). They were discovered in the Galaxy Zoo project (Lintott et al., 2008) calling the attention of volunteers due to their round point form and notorious green color in the *gri* filters composite images from the Sloan Digital Sky Survey (*SDSS*). The green color emerge from the strong emission of [OIII]λ5007Å (EW$_{[\mathrm{OIII}]} \sim 200-2000$Å) which at redshift $0.1 < z < 0.3$ falls into the r (green) color band. GP galaxies have extreme emission-line properties and are characterized by their low mass $M_* \sim 10^8 - 10^{10}$ (Izotov et al., 2011), compactness (Yang et al., 2017) high specific star-forming rates sSFR $\sim\sim 10^{-9} - 10^{-7}\ yr^{-1}$ (Cardamone et al., 2009), sub-solar metallicity 12+log(O/H) ~ 8.1 or about 20 % the solar in average, and low dust content (Amorín et al., 2010, 2012a; Fernández et al., 2022). Many of these characteristics, including large rest-frame EW of optical nebular emissions (i.e Hα, [O III]) make GP similar to high-redshift $z > 6$ galaxies (see Figure 1.13; Schaerer et al., 2016), and are in excellent agreement with the *LCE* characteristics found in astrophysical simulations (Rosdahl et al., 2022). Further, the nebular conditions of the GP show a high degree of ionization inferred by unusually high O_{32} ratios and low [O II] and [S II] emission, which as mentioned before, could imply density-bounded regimes. Given this, astronomers suspect that Lyα and LyC photons may escape

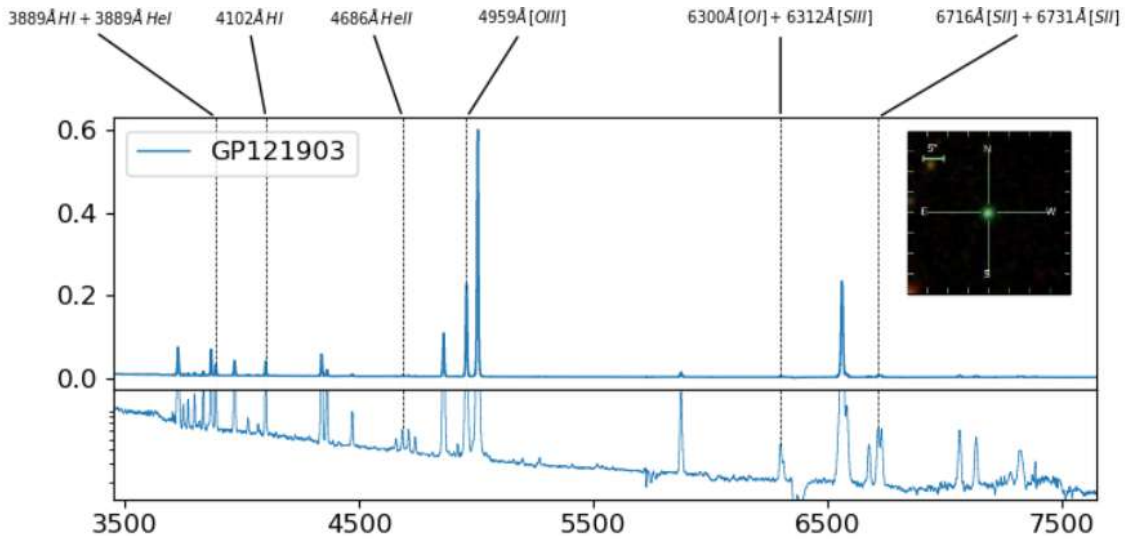

Figure 1.12: Optical spectrum of the GP J121903. The lower panel is displayed in logarithmic scale to highlight continuum features and the broadening of the emission-lines. The image on the upper left corner belong to the SDSS sky server (*gri* composition). The bright emission-line profiles, and green appearance in the SDSS images is typical for a GP galaxy. The figure is from Fernández et al. (2022).

from some GP galaxies (Jaskot & Oey, 2013). Then, observations with *COS* instrument aboard the Hubble Space Telescope (HST) show that most of the observed GPs are strong Lyα emitters, with a variety of values for the Lyα escape fractions, thus reinforcing that GPs share properties closely resembling those of high-redshift LAEs (e.g Henry et al., 2015; Verhamme et al., 2015; Yang et al., 2017). Double peaks in the Lyα profiles and small velocity separations between them are commonly seen in GPs, which indicate low HI column densities facilitating the escape of ionizing radiation (e.g Verhamme et al., 2017; Orlitová et al., 2018). All this background and the combination of indirect diagnostic such as compactness of the starburst (Σ_{SFR}), high EW Hβ, high O_{32} ratios and Lyα emission led to a series of deep observations with *COS* that confirmed the significant detection of ionizing LyC radiation in GP galaxies with escape fractions ranging between $f_{esc}^{LyC} \sim 2\,\% - 70\,\%$ (e.g Izotov et al., 2021; Wang et al., 2019; Izotov et al., 2018a,b, 2016a,b).

Recently, a Large Program with HST, the *Low-z Lyman Continuum Survey* (LzLCS, PI: A. Jaskot; Flury et al., 2022a), was conducted with the COS instrument onboard the HST during its cycle 26. The LzLCS observed 66 star-forming galaxies, many but not all of them classified as GPs, to detect LyC radiation and complete a reference sample with a wide parameter space in their physical properties to find which of them correlate best with their escape (or non-escape) of ionizing

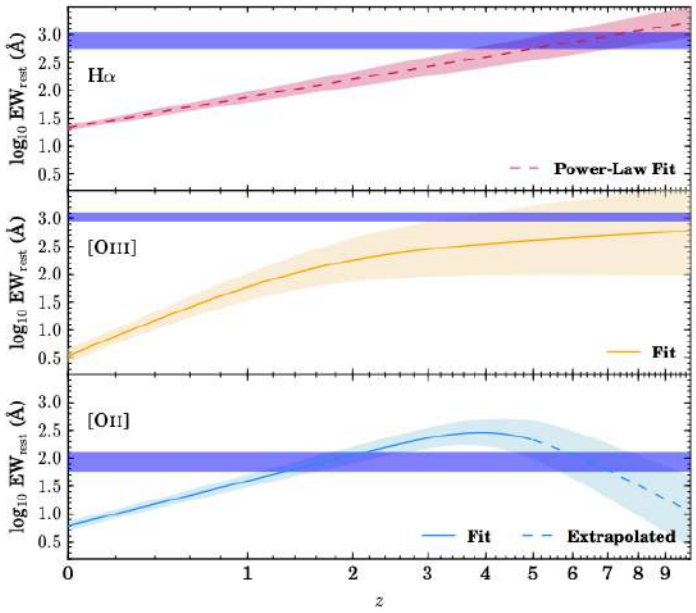

Figure 1.13: The redshift evolution of the average (rest-frame) equivalent widths (EW) of Hα, [OIII]λ5007Å, and [OII]$\lambda\lambda$3726, 3729Å, respectively, for galaxies with stellar masses $9.5 < log(M_*/M_\odot) < 10$ as fitted by Khostovan et al. (2016), The blue horizontal band represent the range of EWs observed for five GPs at $z \sim 0.3$ that leaks ionizing radiation. The nearby LCEs show line EWs typical of star-forming galaxies at $z \gtrsim 6$. The figure is from Schaerer et al. (2016).

photons. The first results of LzLCS reported significant LyC detections on 53 % galaxies of the sample, with a wide range of escape fractions $f_{esc}^{LyC} \sim 2\,\% - 50\,\%$, and revealed that galaxies with high escape fractions have highly ionized gas (high O_{32}) and/or compact star formation (high Σ_{SFR}).

1.4. Motivation for this thesis

Despite such successful results, we still lack a comprehensive understanding of how and why LyC photons escape from most GP galaxies. The search for empirical correlations between the escape fraction with various integrated properties may help in proposing a plausible scenario to be contrasted with the models and simulations and could be used to find *LCE* at higher redshifts with state-of-the-art instrumentation (e.g JWST). However, all the known correlations between f_{esc}^{LyC} and global physical properties show significant scatter and none uniquely predict LyC emission (see Figures 1.10 and 1.14), making it difficult to confidently use them to identify high-redshift LyC emitters. Thus, understanding where the scatter in these relations comes from and exploring other indirect diagnostics is crucial to find an interpreta-

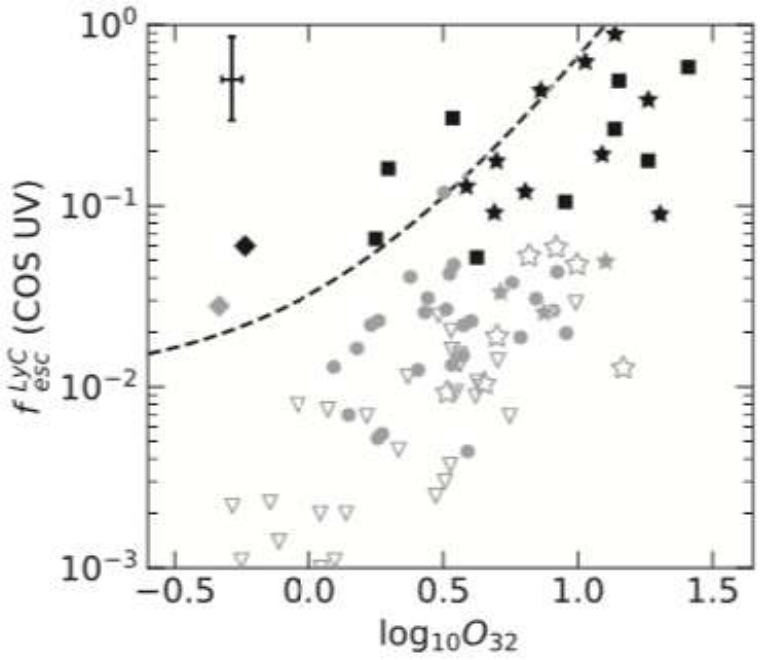

Figure 1.14: The relation between the escape fraction of LyC photons measured by UV-continuum fitting, and the extinction-corrected O_{32} flux ratio from the *Low-z Lyman continuum survey*. The filled black figures are strong LCEs, the gray filled figures are weak LCEs, and the open gray figures are the upper-limits for non-LCEs (see Section 2.2.1 for details). Objects of the LzLCS sample are shown as squares (strong LCEs), circle (weak LCEs) and triangles (non-LCEs), while the stars represent the *Izotov* objects, and the diamonds the *Wang* objects. Finally, the dashed line illustrate the relation of Izotov et al. (2018a). This correlation show large scatter, where a value of $O_{32} \sim 10$ do not differentiate between non-LCEs or LCEs. The figure is from Flury et al. (2022b).

tion of how the LyC leakage works.

Based on the physical properties of the *LCE* and the results of astrophysical simulations it seems that the escape of LyC photons is tightly connected to stellar feedback and supernovae explosions. The GP starbursts are extremely young ($\sim 3-5$ Myr) and massive (Jaskot & Oey, 2013). These are made up of massive star cluster complexes, containing young massive stars which during their short lives (a few Myr) emit UV radiation and expel large amounts of enriched gas into the ISM through intense stellar winds, before exploding as SNe. The aforementioned interactions inject a huge amount of energy and enriched material into the ISM in a mechanism that we call feedback. This process (feedback) favors the chemical enrichment of the galaxy by transporting metals over great distances due to galactic-scale superwinds (or outflows; Tenorio-Tagle et al., 2010). Hence, the outflows can generate favorable conditions for the escape of ionizing photons due to perturbations in the ISM of the

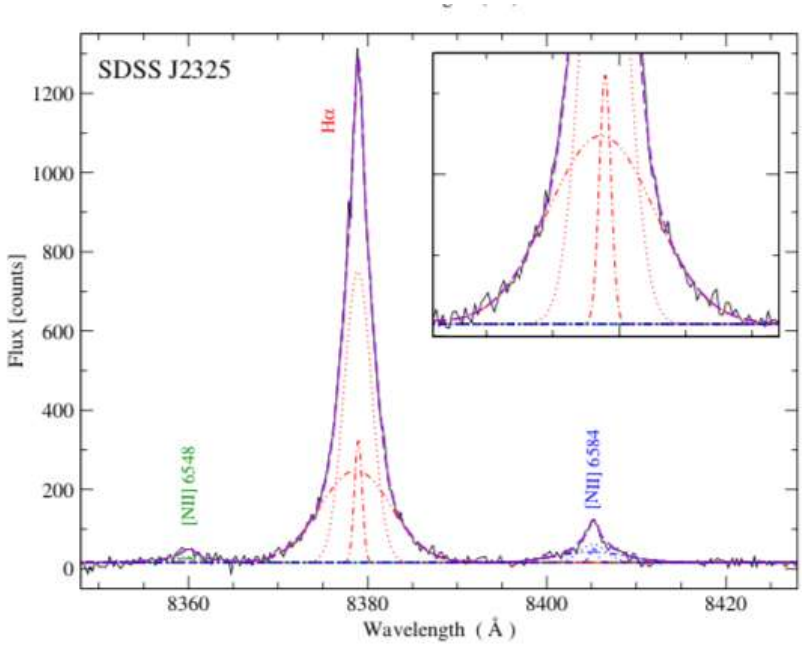

Figure 1.15: Multiple Gaussian fitting of the Hα and the [NII]$\lambda\lambda$6548, 6584Å emission-line profiles of the GP galaxy SDSS J2325. Two low velocity dispersion ($\sigma_{n1} \sim 70\ km\ s^{-1}$ and $\sigma_{n2} \sim 10\ km\ s^{-1}$) and a high velocity dispersion ($\sigma_{broad} \sim 180\ km\ s^{-1}$) component are necessary to well reproduce the emission-line profiles, reflecting the complex ionized gas kinematics of these objects. The figure is from Amorín et al. (2012b).

galaxies, modifying line-of-sight paths or holes through which photons can emerge. Observationally, evidence of feedback by winds from massive stars and supernovae in GP galaxies is based on results from high dispersion optical and UV spectroscopy, which show evidence of outflows and an extremely turbulent medium (e.g Amorín et al., 2012b; Bosch et al., 2019; Hogarth et al., 2020). These results are based on the complex emission-line profiles, which can be modeled by multiple kinematic components of low and high dispersion of velocities ($\sim 30 - 250\ km\ s^{-1}$; see Figure 1.15) in both permitted and forbidden emission-lines, and also the presence of low-brightness gas somewhat denser and with less temperature, at higher speeds (FWZI $> 1500\ km\ s^{-1}$).

Therefore, GP galaxies provide the best opportunity in the local universe to study in detail the physical conditions and the escape of LyC photons in high-redshift galaxies, due to the similarity to LAEs and LBGs (Schaerer et al., 2016; Nakajima et al., 2020) which are constrained by their low fluxes and small angular sizes. This is essential for understanding the formation and evolution of galaxies across cosmic history.

1.5. Aim and objectives of this work

The motivation for this work is based on previous findings by our group (Amorín et al., 2012b; Bosch et al., 2019; Hogarth et al., 2020) in which GPs observed at sufficient spectral resolution show clear evidence of increased turbulence and very energetic outflows likely driven by stellar feedback and SNe. These results are consistent with hydrodynamical simulations that strongly suggest that feedback mechanisms may play a key role in favoring the escape of ionizing photons.

Therefore, we define the following key questions this thesis will help answer:

1. What is the kinematics of the ionized gas of LyC emitters observed at $z \sim 0.3$? Are there substantial differences with galaxies of the same type that are not LyC emitters?

2. Is the presence of outflows a feature common to all LyC leakers? If so, what are their relative velocities and relative contribution?

3. Is it possible to find solid evidence on the ionization state of the kinematic components of the ISM that help to understand the escape of LyC ionizing photons?

4. Is there a correlation between f_{esc} and some kinematic properties, such as the intrinsic velocity dispersion of the ionized gas or the outflow velocity? If so, are these correlations causally connected to the proposed models for LyC escape?

5. Is turbulence, measured through the intrinsic velocity dispersion of the kinematic components, a reliable indicator of photon escape as some numerical simulations predict?

Using high-quality data and a technique successfully tested in previous work (Amorín et al., 2012b; Bosch et al., 2019; Hogarth et al., 2020), this project investigates for the first time the integrated kinematics of ionized gas traced by the optical emission of strong collisionally excited and recombination lines from a sample of LyC-emitting and non-emitting galaxies at $z \sim 0.3$ from the LzLCS and from previous work.

This will allow us to address the following general objectives:

- Determine the kinematic state of the LyC emitters and their influence on the escape of ionizing photons.

- Search for indirect markers of LyC escape based on their ionized ISM kinematic properties that could be applied to higher redshift galaxies observed with new and future instrumentation (e.g. JWST, ELT)

In Section 2 we describe our sample selection and data reduction and calibration. In Section 3 we present our analysis of bright optical emission lines of galaxies from a sample LyC emitting and non-emitting objects. In Section 4 we present the main results and their interpretation based on scaling relations between physical parameters derived from nebular analysis (chemical abundances, ionization state, Lya emission, etc.), resolved morphology and kinematic parameters (velocity dispersion, outflow velocity, evidence of merging, etc). Finally, in Section 5 we discuss the resulting relations for the LyC photon escape fraction in terms of predictions and theoretical scenarios, while in Section 6 we summarize our conclusions and propose future directions for this research line.

Chapter 2

Sample and data

2.1. The Low-z Lyman Continuum Survey

The *Low-z Lyman Continuum Survey* is the largest spectroscopic campaign to detect LyC radiation of galaxies in the nearby Universe. This *HST* program began in the cycle 26 (LzLCS, PI: A. Jaskot, PID: 15626; Flury et al., 2022a) and consist of 134 orbits of observations using the *Cosmic Origin Spectrograph* (COS) instrument with the G140L grating to obtain UV spectra ($850 \lesssim \lambda_{rest} \lesssim 1900$Å, R $\sim 1000 - 1500$) of 66 GP-like Lyman continuum emitters (*LCE*) candidates at $z \sim 0.3$. The sample was selected from star-forming galaxies which have at least one of the following criteria: I high star formation density ($\Sigma_{SFR} > 0.1 M_{\odot}\ yr^{-1}\ kpc^{-2}$), II high O_{32} ratio ($O_{32} > 3$), and III steep UV continuum slopes ($\beta < -2$). Over these 66 galaxies, 35 have detection of Lyman continuum leakage with $\sigma > 2$ confidence (significance), nearly tripling the number of known *LCEs* in the local Universe. The escape fractions measured span a wide range from $2-51\,\%$, while the 31 non-leakers galaxies provide 1σ upper limits of $\approx 1\,\%$. In addition to these 66 LzLCS galaxies, the sample also includes 23 *LCEs* candidates previously observed with *HST/COS* and published in Izotov et al. (2016a,b, 2018a,b, 2021); Wang et al. (2019), including some of the strongest known *LCEs* in the nearby Universe. For consistency, the team re-process the G140L observations with the same methodology as in Flury et al. (2022a) to obtain LyC fluxes and escape fractions, yielding a total of 15 *LCEs* with 2σ confidence in the detection.

The broad range of physical properties of the galaxies in the sample ($\log(M_*/M_{\odot}) = 7.2-10.8$, SFR $= 3-80\ M_{\odot}\ yr{-}1$, $12+\log(O/H) = 7.5-8.6$) allow the exploration of the reliability of indirect diagnostics on cosmologically relevant escape fractions

and to determine which properties correlate with the escape fraction. As results, Flury et al. (2022b) find strong trends between the escape fraction of LyC and Lyα emission-line properties such as the $f_{esc}^{Ly\alpha}$, EW Lyα and v_{sep}, suggesting that line-of-sight effects play a key role in identify *LCE*. Further, *LCEs* are compact, with high values of O_{32}, EW(Hβ), and Σ_{SFR}, thus indicating that stellar feedback also plays a crucial role in ionizing radiation to escape.

2.2. Our Sample

In order to investigate the relation between ionized gas kinematics and LyC leakage, we use a subsample of the *Low-z Lyman Continuum Survey* galaxies at $z \sim 0.2$-0.4, for which high-resolution optical spectra have been obtained. This sample consists of fourteen galaxies (*LzLCS* sample) from Flury et al. (2022a,b); Saldana-Lopez et al. (2022) and six galaxies (*Izotov* sample) from Izotov et al. (2016a,b, 2018a). For each galaxy, we use the homogenized set of physical properties and redshifts presented in (Flury et al., 2022a), where physical properties of previous studied objects (*Izotov* sample) were reprocessed.

In Tables 2.1 and 2.2 we present the identification, coordinates, redshift, and escape fractions metrics (explained in the following section) of the 20 galaxies in this thesis.

Table 2.1: Principal characteristics of the *Izotov* sample objects, including the galaxy ID, the J2000 coordinates (R.A. and Dec.), the redshift (z), the grade of confidence of Lyman continuum detection (significance), and the three metrics of the escape of LyC photons ($F_{\lambda LyC}/F_{\lambda 1100}$, $f_{esc}^{LyC}(H\beta)$, and $f_{esc}^{LyC}(UV)$; See Section 2.2.1 for details). The upper part of the table (separated by the horizontal line) show the galaxies observed with the instrument *X-Shooter*, and the lower part show the galaxy observed with the instrument *ISIS*.

Galaxy ID	R.A. [a]	Dec. [b]	z [c]	sign.	$F_{\lambda LyC}/F_{\lambda 1100}$	$f_{esc}^{LyC}(H\beta)$	$f_{esc}^{LyC}(UV)$
J0901+2119	135.44	21.324	0.299	2.123	$0.062^{+0.035}_{-0.030}$	$0.011^{+0.006}_{-0.005}$	$0.026^{+0.063}_{-0.017}$
J0925+1403	141.385	14.054	0.301	8.210	$0.124^{+0.016}_{-0.014}$	$0.054^{+0.011}_{-0.009}$	$0.092^{+0.019}_{-0.034}$
J1011+1947	152.91	19.789	0.332	8.210	$0.201^{+0.036}_{-0.033}$	$0.041^{+0.005}_{-0.005}$	$0.090^{+0.232}_{-0.030}$
J1154+2443	178.704	24.726	0.369	8.210	$0.535^{+0.053}_{-0.049}$	$0.286^{+0.027}_{-0.024}$	$0.625^{+0.375}_{-0.241}$
J1442-0209	220.631	−2.164	0.294	5.871	$0.094^{+0.027}_{-0.024}$	$0.067^{+0.014}_{-0.012}$	$0.120^{+0.064}_{-0.050}$
J1152+3400	178.02	34.014	0.342	8.210	$0.134^{+0.019}_{-0.017}$	$0.109^{+0.014}_{-0.013}$	$0.177^{+0.195}_{-0.063}$

[a] Right Ascension in degrees (J2000).

[b] Declination in degrees (J2000).

[c] Redshift obtained from SDSS spectra.

Table 2.2: Same as the Table 2.1 but for the *LzLCS* sample. Here, the escape fractions of the non-LCE are shown as upper limits. The upper part of the table show the galaxies observed with the instrument *X-Shooter*, and the lower part show the galaxies observed with the instrument *ISIS*.

Galaxy ID	R.A. [a]	Dec. [b]	z [c]	sign.	$F_{\lambda LyC}/F_{\lambda 1100}$	$f_{esc}^{LyC}(H\beta)$	$f_{esc}^{LyC}(UV)$
J003601+003307	9.003	0.552	0.348	1.506	< 0.017	< 0.005	< 0.029
J004743+015440	11.928	1.911	0.353	5.150	$0.040^{+0.012}_{-0.010}$	$0.049^{+0.014}_{-0.012}$	$0.013^{+0.021}_{-0.003}$
J011309+000223	18.287	0.040	0.306	4.584	$0.040^{+0.013}_{-0.012}$	$0.123^{+0.042}_{-0.035}$	$0.022^{+0.016}_{-0.012}$
J012217+052044	20.569	5.346	0.366	4.988	$0.048^{+0.013}_{-0.012}$	$0.084^{+0.022}_{-0.019}$	$0.038^{+0.046}_{-0.016}$
J081409+211459	123.536	21.250	0.227	1.204	< 0.031	< 0.040	< 0.007
J091113+183108	137.806	18.519	0.262	8.210	$0.121^{+0.021}_{-0.019}$	$0.083^{+0.014}_{-0.013}$	$0.023^{+0.018}_{-0.007}$
J095838+202508	149.660	20.419	0.302	2.177	$0.031^{+0.017}_{-0.015}$	$0.012^{+0.007}_{-0.006}$	$0.019^{+0.028}_{-0.011}$
J131037+214817	197.653	21.805	0.283	5.724	$0.058^{+0.016}_{-0.014}$	$0.053^{+0.014}_{-0.013}$	$0.016^{+0.020}_{-0.006}$
J091703+315221	139.261	31.872	0.300	8.210	$0.149^{+0.015}_{-0.014}$	$0.131^{+0.014}_{-0.012}$	$0.161^{+0.073}_{-0.055}$
J105331+523753	163.378	52.631	0.253	4.019	$0.019^{+0.007}_{-0.006}$	$0.027^{+0.009}_{-0.009}$	$0.012^{+0.006}_{-0.004}$
J113304+651341	173.266	65.228	0.241	2.525	$0.046^{+0.025}_{-0.021}$	$0.083^{+0.041}_{-0.038}$	$0.022^{+0.022}_{-0.009}$
J124835+123403	192.144	12.567	0.263	2.177	$0.028^{+0.017}_{-0.015}$	$0.028^{+0.017}_{-0.014}$	$0.047^{+0.043}_{-0.026}$
J144010+461937	220.041	46.327	0.301	4.682	$0.014^{+0.004}_{-0.004}$	$0.013^{+0.004}_{-0.004}$	$0.005^{+0.002}_{-0.002}$
J154050+572442	235.209	57.412	0.294	0.000	< 0.003	< 0.004	< 0.001

[a] Right Ascension in degrees (J2000).

[b] Declination in degrees (J2000).

[c] Redshift obtained from SDSS spectra.

2.2.1. Escape fraction and classification of the galaxies

One of our principal aims is to determine possible differences between the ionized gas kinematics of LCEs and Non-LCE. To classify the galaxies in these categories according to the escape fraction of LyC photons we adopt the values determined in Flury et al. (2022b), which relies on I) the grade of confidence that the LyC flux detection does not arise from background fluctuations (significance) and II) the value of the LyC escape fraction ($f_{\rm esc}^{LyC}$) that can be estimated by the following three metrics:

- $F_{\lambda LyC}/F_{\lambda 1100}$: This is an empirical proxy for the escape fraction of ionizing radiation. It consist of the flux density ratio between the Lyman continuum flux measured in a rest-frame 20Å window as close as possible to $\lambda_{rest} = 900$Å ($F_{\lambda LyC}$), and the UV starlight continuum average flux in a rest-frame 20Å window close to $\lambda_{rest} = 1100$Å, both corrected by MW extinction. Despite this ratio is not a direct measurement of the escape fraction, is free of any assumption. More details about this metric can be found in Wang et al. (2019).

- $f_{\rm esc}^{LyC}(H\beta)$: Following the equation 1.1, is necessary to derive the intrinsic LyC flux to determine the absolute escape fraction of ionizing radiation. This method uses the relation between the total number of ionizing photons emitted by the nebulae ($N(LyC)$), which relates to extinction corrected Hβ flux density ($F_{H\beta}^{corr}$, recombination line), and the LyC flux density ($F_{\lambda LyC}^{mod}$). Here, the transformation between $N(LyC)$ and $F_{\lambda LyC}^{mod}$ depends on the stellar population age, which can be determined by the rest-frame EW(Hβ) after assuming a continuous star formation. Then, an appropriate model yields $F_{H\beta}^{corr}/F_{\lambda LyC}^{mod}$ which combined with the observed LyC flux density gives the $f_{\rm esc}^{LyC}$. Please, see Figures 12-13 in Izotov et al. (2016a), and Figure 17 in Flury et al. (2022a) for more details.

- $f_{\rm esc}^{LyC}(UV)$: In this method, the intrinsic LyC flux density is obtained by fitting the rest-frame UV continuum from the *COS UV* spectra. The best-fit SED is obtained from low-resolution STARBURST99 templates (Leitherer et al., 2010) of a weighted linear combination of single-burst spectra, after applying a uniform Reddy et al. (2016) attenuation law, and adding the nebular continuum. Then, the intrinsic SED (before UV attenuation) gives the $f_{\rm esc}^{LyC}$ by the equation 1.1. More details about the UV fitting can be found in Saldana-Lopez et al. (2022).

Hence, considering what was mentioned above, we summarized the procedure of classification:

- *Strong-LCE (SLCE)*: The galaxy is classified as a *SLCE* if it has $f_{\rm esc}^{LyC} > 0.05$ and a significance $\sigma > 5$ in the LyC detection.

- *Weak-LCE (WLCE)*: The galaxy is classified as a *WLCE* if it has a significance $\sigma > 2$, but $f_{\rm esc}^{LyC} < 0.05$.

- *Non-LCE (NLCE)*: The galaxy is classified as a *NLCE* if it has a significance $\sigma < 2$. In this case, the $f_{\rm esc}^{LyC}$ is computed with the upper limit obtained from the 68 % confidence interval of the LyC flux density.

Because the classification depends on the $f_{\rm esc}^{LyC}$, then, the category of a galaxy could change in agreement with the metric used. While this occurs for three objects in our sample that change between *SLCE* to *WLCE*, we use the $f_{\rm esc}^{LyC}(UV)$ metric as the principal flag to resolve the category in most of our analysis. According to Flury

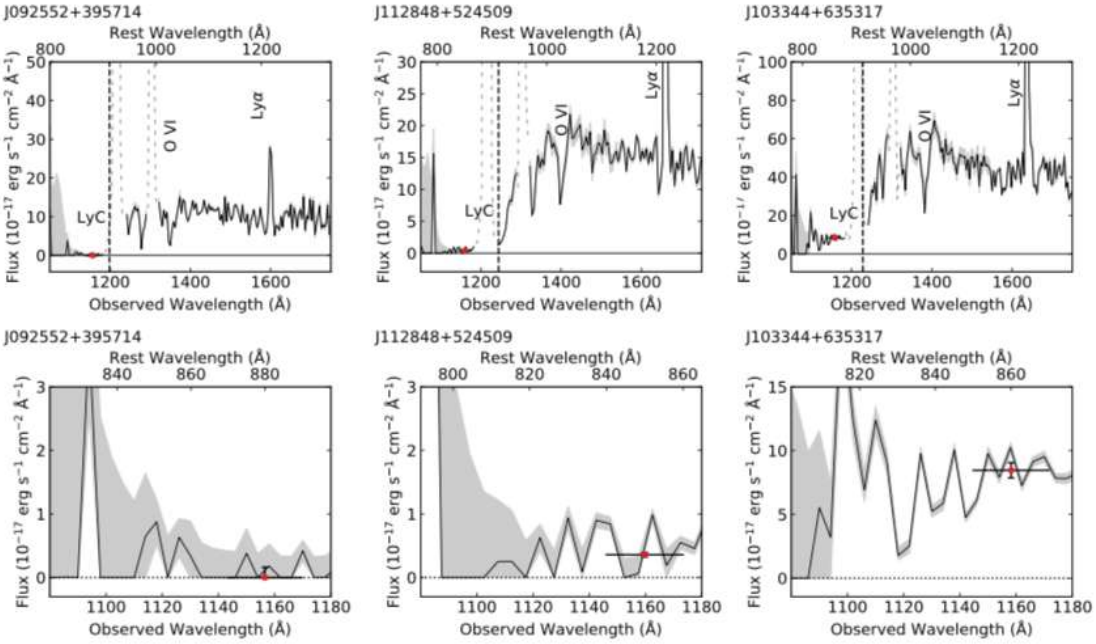

Figure 2.1: The UV spectra of a non-emitter (NLCE; left panel), a marginally detected LCE (WLCE; middle panel), and a well-detected LCE (SLCE; right panel) from the *Low-z Lyman continuum survey* sample. The spectra is shown as a black line, the gray shaded region illustrate the 1σ uncertainty in flux density, the red circle is the observed LyC flux with vertical black line showing the 68 % confidence interval of the LyC flux measured inside the 20Å horizontal line. The dashed vertical line in the upper panel indicates the Lyman limit. The figure is from Flury et al. (2022a).

et al. (2022a), this is the most reliable of the three metrics because is less affected by systematics. Therefore, we consider 3 of the galaxies as *NLCE*, 11 of the galaxies as *WLCE*, and 6 of the galaxies as *SLCE*.

2.2.2. Physical properties of the galaxies

The physical properties of the galaxies were measured for every source in the LzLCS, including the literature sources. The following properties are relevant in this work and were calculated by the LzLCS team using Sloan Digital Sky Survey Data Release 15 (SDSS DR15) optical spectra, the Galaxy Evolution Explorer (GALEX) photometry, or the LzLCS COS spectra [1],

[1]Along this work we assume a flat cosmological model (Flat Lambda CDM) with a Hubble constant of $H_0 = 70\ km\ s^{-1}\ Mpc^{-1}$, a non-relativistic matter density of $\Omega_m = 0.3$, and vacuum energy density parameter $\Omega_\Lambda = 0.7$.

Lyα properties

The Lyα properties were determined using the HST/COS spectra. The data were corrected by Galactic extinction by using Green et al. (2018) dust maps and Fitzpatrick (1999) extinction law.

- Lyα equivalent width: To determine the rest-frame equivalent width of Lyα (EW(Lyα) in units of Å), a linear fitting of the continuum was performed within 100Å of Lyα. After subtracting the linear fit, the flux of the emission-line was integrated within 1206Å and 1240Å to avoid contamination. Finally, the flux is divided by the continuum flux and corrected by redshift.

- Lyα escape fraction: Similar to the escape fraction of ionizing photons, The Lyα escape fraction ($f_{\rm esc}^{Ly\alpha}$) is determined by comparing the observed Lyα flux and the intrinsic (total) Lyα flux. The latter is determined by using the Hβ flux corrected by Galactic and internal extinction and calculating the ratio of Lyα/Hβ emissivities. See Flury et al. (2022a) for details.

- Lyα peak velocity separation: The separation between the double peaks of Lyα emission (v_{sep} in units of $km\ s^{-1}$) can't be measured from the data obtained with the G140L grating, due to lack of resolution. Thus, previous observations made with the G160M grating were used to resolve the double peaks. However, only a small percentage of the objects in the sample have this data.

Half-light radius

The half-light radius (r_{50} in units of kpc) is the radius containing the 50 % of the counts in the MIRROR-A NUV COS images, calculated after subtracting a median background and correcting for vignetting effects. The light contained inside this radius comes from the young stellar populations of the galaxies.

O_{32} Oxygen ratio

The emission-line ratio $[OIII]\lambda$5007Å/$[OII]\lambda$3727Å (O_{32}) was calculated from SDSS DR15 spectra fluxes, after correcting by Galactic and internal extinction. The Galactic reddening was corrected by using Green et al. (2018) dust maps and Fitzpatrick (1999) extinction law, while the internal extinction was corrected by determining the Balmer decrement and applying the Cardelli et al. (1989) extinction law.

Table 2.3: The Lyα emission-line properties for the *Izotov* sample objects, including the galaxy ID, the escape fraction of Lyα, the equivalent width (EW(Lyα)), and the velocity separation between the peaks of the emission-line (v_{sep}). The upper part of the table show the galaxies observed with the instrument *X-Shooter*, and the lower part show the galaxy observed with the instrument *ISIS*.

Galaxy ID	$f_{esc}^{Ly\alpha}$	EW(Lyα) [a]	v_{sep} [b]
J0901+2119	0.147 ± 0.013	179.000 ± 3.900	345.0 ± 12.5
J0925+1403	0.537 ± 0.033	83.000 ± 2.100	310.0 ± 10.0
J1011+1947	0.090 ± 0.006	121.000 ± 3.100	276.0 ± 5.4
J1154+2443	0.482 ± 0.044	133.000 ± 3.300	199.0 ± 10.0
J1442-0209	0.291 ± 0.024	129.000 ± 3.200	310.0 ± 10.0
J1152+3400	0.213 ± 0.022	79.000 ± 2.000	270.0 ± 10.0

[a] Equivalent width of the Lyα emission-line profile (Å).

[b] Velocity separation between peaks of the Lyα emission ($km\ s^{-1}$).

Table 2.4: Same as Table 2.3, but for the *LzLCS* sample.

Galaxy ID	$f_{esc}^{Ly\alpha}$	EW(Lyα) [a]	v_{sep} [b]
J003601+003307	0.116 ± 0.011	93.900 ± 9.330	-
J004743+015440	0.194 ± 0.019	41.526 ± 4.427	-
J011309+000223	0.398 ± 0.075	31.291 ± 3.560	-
J012217+052044	0.594 ± 0.069	70.616 ± 6.793	-
J081409+211459	0.008 ± 0.005	0.420 ± 0.828	-
J091113+183108	0.157 ± 0.011	53.475 ± 4.864	370.0 ± 64.0
J095838+202508	0.107 ± 0.012	67.565 ± 6.496	-
J131037+214817	0.126 ± 0.011	37.709 ± 3.603	-
J091703+315221	0.127 ± 0.001	29.696 ± 3.48	313.0 ± 32.6
J105331+523753	0.039 ± 0.006	7.389 ± 1.398	420.0 ± 107.7
J113304+651341	0.288 ± 0.025	37.216 ± 3.212	320.0 ± 72.1
J124835+123403	0.422 ± 0.030	97.340 ± 8.418	455.0 ± 50.1
J144010+461937	0.110 ± 0.009	28.665 ± 2.948	527.0 ± 58.1
J154050+572442	0.046 ± 0.006	8.113 ± 1.368	-

[a] Equivalent width of the Lyα emission-line profile (Å).

[b] Velocity separation between peaks of the Lyα emission ($km\ s^{-1}$).

Star formation rate and star formation surface density (Hβ)

The Hβ flux from the SDSS DR15 spectra was used to calculate the star formation rate ($\mathrm{SFR}_{H\beta}$ in units of $M_\odot\ yr^{-1}$) using the calibrations from Kennicutt & Evans (2012), after being corrected by Galactic and internal extinction with the same procedure as above. Then, the star formation rate is divided by $2\pi r_{50}^2$ to obtain the star formation surface density ($\Sigma_{\mathrm{SFR},H\beta}$ in units of $M_\odot\ yr^{-1}\ kpc^{-2}$).

Table 2.5: Other physical properties we use of the *Izotov* sample objects, including the galaxy ID, the O_{32} oxygen ratio ($\log_{10}O_{32}$), the stellar mass ($\log_{10}M_*$), the COS/NUV half-light radius (r_{50}), the star formation rate measured from Hβ luminosity ($\log_{10}\mathrm{SFR}_{H\beta}$), and the star formation rate surface density ($\log_{10}\ \Sigma_{\mathrm{SFR},H\beta}$). The upper part of the table show the galaxies observed with the instrument *X-Shooter*, and the lower part show the galaxy observed with the instrument *ISIS*.

Galaxy ID	$\log_{10}O_{32}$	$\log_{10}M_*$ [a]	r_{50} [b]	$\log_{10}\mathrm{SFR}_{H\beta}$ [c]	$\log_{10}\ \Sigma_{\mathrm{SFR},H\beta}$ [d]
J0901+2119	1.100 ± 0.033	9.800 ± 0.152	0.585 ± 0.127	1.126 ± 0.027	0.794 ± 0.098
J0925+1403	0.816 ± 0.029	8.380 ± 0.130	0.403 ± 0.125	1.366 ± 0.023	1.358 ± 0.137
J1011+1947	1.432 ± 0.073	9.000 ± 0.140	0.279 ± 0.133	1.438 ± 0.020	1.749 ± 0.208
J1154+2443	1.151 ± 0.036	8.200 ± 0.127	0.635 ± 0.149	0.987 ± 0.027	0.584 ± 0.105
J1442-0209	0.930 ± 0.029	8.960 ± 0.139	0.417 ± 0.124	1.356 ± 0.023	1.317 ± 0.131
J1152+3400	0.823 ± 0.027	9.590 ± 0.149	0.376 ± 0.137	1.400 ± 0.021	1.450 ± 0.159

[a] Stellar mass of the galaxy ($M_\odot$).

[b] Half-light radius (kpc).

[c] Star formation rate from Hβ ($M_\odot\ yr^{-1}$).

[d] Star formation rate surface density ($M_\odot\ yr^{-1}\ kpc^{-2}$).

Table 2.6: Same as Table 2.5, but for the *LzLCS* sample.

Galaxy ID	$\log_{10}O_{32}$	$\log_{10}M_*$ [a]	r_{50} [b]	$\log_{10}\mathrm{SFR}_{H\beta}$ [c]	$\log_{10}\ \Sigma_{\mathrm{SFR},H\beta}$ [d]
J003601+003307	1.113 ± 0.039	8.754 ± 0.425	0.445 ± 0.148	1.181 ± 0.024	1.086 ± 0.146
J004743+015440	0.655 ± 0.026	9.203 ± 0.430	0.618 ± 0.145	1.314 ± 0.024	0.934 ± 0.105
J011309+000223	0.357 ± 0.086	9.111 ± 0.430	0.627 ± 0.133	0.642 ± 0.076	0.250 ± 0.119
J012217+052044	0.881 ± 0.047	8.762 ± 0.423	0.713 ± 0.151	0.933 ± 0.041	0.429 ± 0.100
J081409+211459	0.200 ± 0.021	9.551 ± 0.432	1.439 ± 0.125	1.200 ± 0.020	0.086 ± 0.042
J091113+183108	0.384 ± 0.026	10.410 ± 0.370	0.442 ± 0.117	1.403 ± 0.022	1.313 ± 0.117
J095838+202508	0.912 ± 0.031	8.696 ± 0.421	0.488 ± 0.130	1.188 ± 0.021	1.013 ± 0.117
J131037+214817	0.306 ± 0.027	9.600 ± 0.418	0.418 ± 0.123	1.092 ± 0.024	1.051 ± 0.130
J091703+315221	0.422 ± 0.023	9.313 ± 0.431	0.407 ± 0.129	1.293 ± 0.020	1.276 ± 0.139
J105331+523753	0.531 ± 0.023	9.285 ± 0.431	0.618 ± 0.117	1.438 ± 0.020	1.058 ± 0.085
J113304+651341	0.699 ± 0.027	9.647 ± 0.383	0.700 ± 0.118	0.872 ± 0.024	0.383 ± 0.077
J124835+123403	0.664 ± 0.026	8.750 ± 0.428	0.333 ± 0.149	1.241 ± 0.023	1.397 ± 0.196
J144010+461937	0.382 ± 0.023	9.546 ± 0.431	0.641 ± 0.131	1.552 ± 0.020	1.141 ± 0.091
J154050+572442	0.223 ± 0.029	9.621 ± 0.431	0.946 ± 0.135	1.397 ± 0.025	0.647 ± 0.067

[a] Stellar mass of the galaxy ($M_\odot$).

[b] Half-light radius (kpc).

[c] Star formation rate from Hβ ($M_\odot\ yr^{-1}$).

[d] Star formation rate surface density ($M_\odot\ yr^{-1}\ kpc^{-2}$).

Stellar-mass

The stellar masses of the galaxies (M_* in units of $M_\odot$) were determined by fitting stellar population to aperture-matched photometry from SDSS and GALEX assuming a non-parametric star formation history, a Kroupa (2001) initial mass function, CLOUDY photoionization models, and a Calzetti (2001) dust attenuation curve.

For each galaxy in our sample, all the mentioned physical properties are shown in the Tables 2.1, 2.2, 2.3,2.4, 2.5, and 2.6. Further information about the determination of parameters can be found in Flury et al. (2022a).

2.3. Spectroscopic data

As mentioned in Section 1.4, the use of spectroscopy is essential to obtain physical information about celestial objects. High resolution spectra allows us to characterize the ionized gas kinematics of the objects, by finding multiple kinematic components with different velocity dispersion. Therefore, we use high-resolution spectra from two different instruments: I) The *X-Shooter* onboard of the Very Large Telescope (VLT), and II) The *ISIS* onboard of the William Herschel Telescope (WHT). Both sets of data are comparable in terms of resolution and depth.

2.3.1. VLT/X-Shooter spectra

We made use of high-resolution spectra obtained for 13 galaxies in our sample with the *X-Shooter* instrument at the Very Large Telescope (VLT: CODES; PI: D. Schaerer). With a total integration time of 50-100 minutes per object, eight object's spectra were reduced by our collaborators (Marques-Chaves et al., 2022) using the ESO Reflex reduction pipeline (version 2.11.5; Freudling et al., 2013), and five object's spectra were reduced using IRAF (Guseva et al., 2020) to produce flux-calibrated spectra. The data is presented and described with detail in the mentioned articles. For these datasets, we only used the VIS arm, which has a spectral resolution of $R \sim 8935$ (13.0 $km\ s^{-1}$), comparable to that of our *ISIS* spectra (see Figure 2.2).

2.3.2. WHT/ISIS spectra

In this study, we present new observations for a subsample of 7 galaxies which were obtained with the Intermediate Dispersion Spectrograph and Imaging System (ISIS)[2] on the 4.2 m William Herschel Telescope (WHT) at the Roque de los Muchachos Observatory in the nights of 8-12 of January 2018 (Program P27, PI: R. Amorín). The instrumental configuration follows the same strategy presented by Hogarth et al. (2020).

[2]http://www.ing.iac.es/astronomy/instruments/isis/

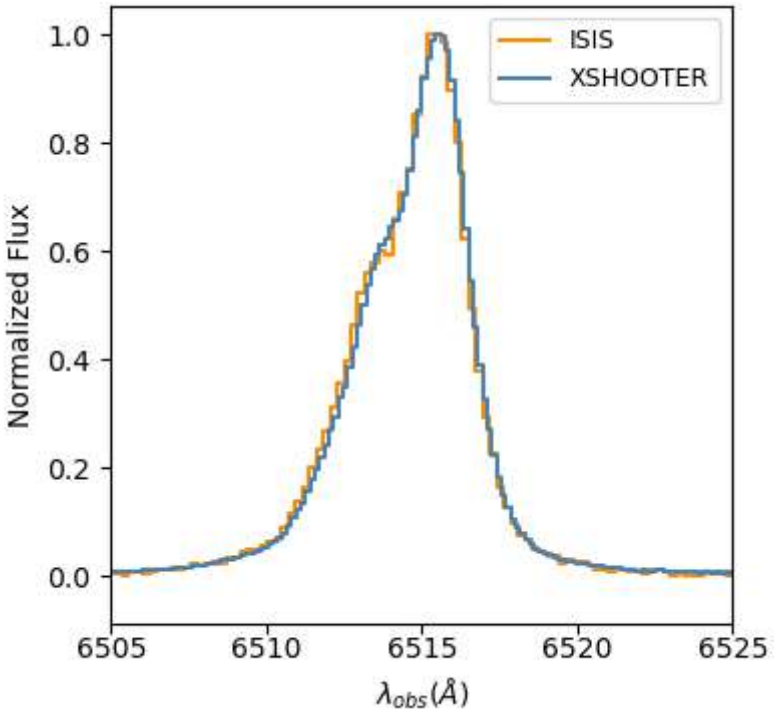

Figure 2.2: J 0925 + 1403 Double ionized Oxygen [OIII]λ5007Å transition obtained with three different astronomical instruments. This demonstrates the similar performance in terms of resolution ($R \sim 8900$) with the selected configurations for the *ISIS* spectro-imager and the *X-Shooter* spectrograph. Global emission-line profiles are in total agreement between both instruments and multi-component fitting of both emissions converge to a similar solution.

In short, we used the R1200B and R1200R gratings for the light split by the D6100 dichroic into the blue and red arms of the spectrograph, respectively. The blue arm was centred around the observed wavelength of Hβ and [O III]$\lambda\lambda$4959, 5007Å, whereas the red arm was centred at the observed wavelength of Hα and includes the emission from [O I]λ6300Å, [N II]$\lambda\lambda$6548,6583Å and [S II]$\lambda\lambda$6716,6731Å. We used a long slit 0.9" wide, oriented at the parallactic angle to reduce the effects of atmospheric dispersion. Observing nights were non-photometric and with an average seeing of $\sim$1". With a spatial scale of 0.20 and 0.22 arcsec per pixel for the blue and red detectors, respectively, the average spectral dispersion and Full Width Half Maximuum (FWHM), as measured on bright sky lines and lamp lines, were 0.24 Å pixel^{-1} and 0.73Å, respectively, which correspond to a Hα FWHM velocity resolution of about 14.3 km s^{-1}, R$\sim$ 8900 at 6500Å. The combined spectra have total exposure times of 60-120 minutes per object, depending on the target.

Our group reduced and calibrated the data using standard IRAF subroutines

following Hägele et al. (2007) and Hogarth et al. (2020). Spectral wavelength calibration was performed using CuNe+CuAr lamp arcs obtained immediately after science exposures and have uncertainties $\lesssim$0.1Å (~ 5 km s^{-1}). The spectra has been corrected for atmospheric and Galactic extinction and flux calibrated using spectrophotometric standard stars. Finally, one-dimensional spectra was extracted using an optimal spatial aperture matching the spatial extent of the emission lines in the 2D spectra.

We emphasize that in first instance only the 13 objects observed with the *X-Shooter* instrument were considered to be analyzed, and the resting 7 objects observed with *ISIS* instrument were added in a latter stage of the development of this thesis, because the dataset was not reduced and processed. Thus, in the first chapters we only show results of the 13 *X-Shooter* objects, and we add the 7 *ISIS* objects latter in Chapter 5, after apply the same following methodology to the brighter emission-lines (i.e Hα, [OIII]λ5007Å). This improve greatly the statistics of the found correlations and their implications.

Chapter 3

Methodology

3.1. Fitting of emission lines profiles

The optical spectrum of all galaxies in the sample shows prominent emission-line profiles. Some of the observed lines are emitted after recombination or high probable de-excitation of electrons in atomic nuclei, causing what is known as "permitted line", while other emissions came from low probable de-excitation of electrons in species that were excited by collisions inside a low-density medium, causing a "forbidden line". These are imprints of the numerous star-forming regions inside the galaxies, where young massive stars evolve and impregnate the interstellar medium with energy. Radiation, cosmic rays, and mechanical feedback of massive stars can knock out electrons from surrounding gas and dust, and because these free electrons have a certain velocity they produce an increase in the kinetic energy of the interstellar medium that then tries to cool down by the transformation of kinetic energy into radiation like the two mechanisms mentioned above.

In the previous chapter, we already discussed the complex kinematics that some GPs display as asymmetric emission-line profiles made by multiple supersonic components. This is a common characteristic not only for GPs but also for giant HII regions. Detailed studies have shown that the principal mechanisms that can produce fast internal motions are well represented by Gaussian functions (e.g Melnick et al. (1999)). We tried to perform four multi-component models including one, two, three, and four Gaussian components for each galaxy, with the Gaussian components described by the function,

$$f(x; A, \mu, \sigma) = \frac{A}{\sigma\sqrt{2\pi}} e^{[-(x-\mu)^2/2\sigma^2]} \tag{3.1}$$

where the parameter A correspond to area under the curve, μ to center, and σ to deviation, that in our work represent the flux (10^{-17} erg s^{-1} cm^{-2}), the central velocity (km s^{-1}), and the velocity dispersion (km s^{-1}) respectively.

Therefore, we used two Python tools *fitELP* (Firpo et al. in prep), and *LiMe* (Fernandez-Vital et al. in prep) to perform the fits of emission-lines profiles with multiple Gaussian components. The codes are specially designed to do the mentioned task (see the section below), allowing us to analyze the internal kinematics of the galaxies in our sample, and characterize them. Also, these libraries provide relevant statistical information about the fitted models to evaluate the goodness of a fit and compare the results. Some of the statistical parameters used are the Chi-square (χ^2), reduced Chi-square (χ^2_ν), Akaike Information Criterion statistic (AIC), and the Bayesian Information Criterion statistic (BIC) defined as,

$$\chi^2 = \sum_i^N \frac{[y_i^{meas} - y_i^{model}(v)]^2}{\epsilon_i^2} \tag{3.2}$$

$$\chi^2_\nu = \frac{\chi^2}{(N - N_{varys})} \tag{3.3}$$

$$AIC = N \ln\left(\frac{\chi^2}{N}\right) + 2N_{varys} \tag{3.4}$$

$$BIC = N \ln\left(\frac{\chi^2}{N}\right) + \ln(N)N_{varys} \tag{3.5}$$

Where N is the number of data points, y_i^{meas} is the set of measured data, y_i^{model} is the model calculation that depends on the set of variables v, ϵ_i is the uncertainty of the data, and N_{varys} is the number of variable parameters.

Assuming that our data uncertainties have Gaussian distribution, so we can set χ^2 as an *objective function* to be minimized, that is a function that takes the parameters values of a model function to calculate a residual array scaled by the data uncertainties, and then applied a least-squares algorithm to find a minimum. Usually, in a linear model, a value of $\chi^2_\nu \sim 1$ is used as a measure of the goodness of fit, taking into account the degrees of freedom ($N - N_{varys}$) of the model fitted and also considering that the data uncertainties ϵ_i are correctly scaled. In our case, we applied a non-linear model and the degrees of freedom can vary during the fit, so we cannot necessarily obtain such representative values of χ^2_ν (Andrae et al., 2010) to confirm if our model under or over-fit the data. However, we can use the AIC statistic (Akaike

(1974)) or *BIC* statistic to compare which model is better in terms of the quality of the fit and how many variable parameters are used, getting higher values if more parameters are added and they do not improve notoriously the goodness of fit. Hence, as in Wei et al. (2016), we use the likelihood of model M_α to be correct with respect to another model M_β defined with the next expression that considers the Akaike weights,

$$P(M_\alpha) = \frac{exp(-AIC_\alpha/2)}{exp(-AIC_\alpha/2) + exp(-AIC_\beta/2)} \tag{3.6}$$

With all that tools in mind, we adopted a similar parametric fitting procedure as described in Hogarth et al. (2020), which was already applied in other works as Amorín et al. (2012b), Hägele et al. (2012) and Firpo et al. (2010). This modeling of emission-line profiles assumes that all the gas moves similarly inside the galaxy, but are different regions delimited by the excitation potential. Despite the complex anatomy of each galaxy, we study them by taking the most simple scenario. High excited species are expected to be closer to the radiation source, while low excited atoms should be farther away (see Figure 3.1). To trace this structure we define two principal zones, each one represented by the brightest emission-line in the optical spectrum according to the energies involved.

Following that criteria, the kinematic of high excited species is represented by the forbidden line [OIII]λ5007Å. The advantage of this emission line resides in the absence of contamination of close emissions and the high SNR. First, the local continuum of the emission line is adjusted with a low-order polynomial. Next, we applied one, two, three, and four Gaussian components models to fit the emission-line profile, with all the parameters of each component free to vary (i.e flux, central velocity, and velocity dispersion). Finally, the kinematic solution that minimizes χ^2 for each model is copied to lower SNR emission lines such as [OIII]λ4959Å, with free fluxes only. To check the consistency of the models we examine the ratio of amplitudes between the doublet [OIII]λ4959Å and [OIII]λ5007Å to be approximately the theoretical value of 1/3, which is in good agreement in all the models.

For low excited species, the kinematic is represented by the recombination line of Hydrogen Hα. In this case is necessary to fit not just the Hα emission-line profile, but also the [NII] that are blended within the wings. Because these species are assumed to be in the same spacial zone, we can reduce the free parameters in the fitting procedure. First, we considered a fixed velocity distance between the peak of Hα

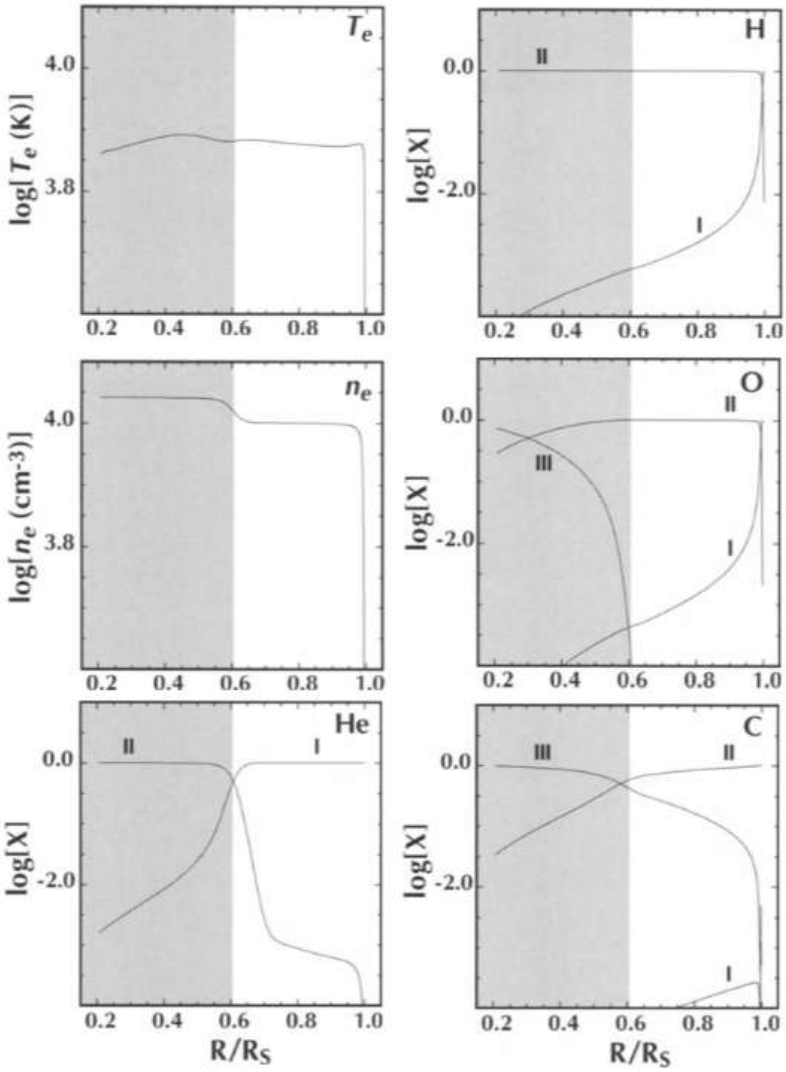

Figure 3.1: Properties and ionization structure of MAPPINGS III photoionization model for an isochoric region excited by a star with an effective temperature of 35.000K. Properties as electron temperature T_e and electron density n_e are shown, with different atoms species as Helium (He), Hydrogen (H), Oxygen (O) and Carbon (C), Roman numbers represent neutral atoms (I), one time ionized (II) and doubly ionized (III). The figure is from Dopita & Sutherland (2003)

and the peaks of the [NII] lines, so each Gaussian component will have the same distance between Hα and [NII]. In other words, the central velocities of Hα are free to vary, but the central velocities of [NII] are arranged to a specific distance. The dispersion velocity of [NII] components are also expected to follow the kinematics of Hα so they are fixed, whilst the fluxes of the [NII]λ6548Å are set by the theoretical ratio of 1/3 respect those of [NII]λ6584Å. Therefore, we significantly reduce the free parameters of the fitting from 18 (for two Gaussian components in each emission

line) to 8. Finally, the kinematic solution that minimizes χ^2 for each model is copied to lower SNR emission lines such as Hβ, [OI]λ6300Å, and [SII]$\lambda\lambda$6717, 6731Å, where the amplitudes of the components are the only free parameter to vary.

We find some cases where we added another (third) component which results in a broad, low flux component with an inconsistent central velocity between Hα and [OIII]λ5007Å. Hence, we fixed the central velocity of the components of Hα to those of [OIII]λ5007Å owing to its isolation compared to the recombination line that has contamination of the [NII] lines. After that, all the kinematic solutions agree in terms of the central velocity of the broad component, and also in velocity dispersion which continues as a free parameter. Moreover, we perform a non-parametric analysis of the [OIII]λ5007Å profiles, providing another description of the gas kinematics to compare with our multi-component models. For details see Section 4.4.

Libraries

As previously mentioned, we use two python libraries to do the multi-components model fitting for emission-line profiles. These codes are based on the Non-Linear Least-Square Minimization and Curve-Fitting (LMFIT Newville et al., 2014) package, used to solve curve fitting and non-linear optimization problems. Both libraries provide powerful tools to describe the ionized gas kinematics of galaxies using spectra and are specially designed to do this.

fitELP

Fit Emission-Line Profiles (*fitELP*, Firpo in prep) is a python code design for the analysis of the internal kinematics of star-forming regions using long-slit or echelle spectral data. The tool allows performing spectral emission-line fits by using multi-Gaussian components and getting a detailed kinematic study of each target, producing pdf and latex tables with the kinematics results such as radial velocities, intrinsic velocity dispersion, fluxes, emission-line measure, and global fluxes. Also, is possible to produce classic emission-line diagnostics diagrams, using the values calculated in the kinematic analysis.

While using this library, I contribute to its improvement by implementing visualization tools to highlight the fit of emission lines at low flux scales, the reading of different kinds of data, and the calibration of kinematics results.

LiMe

A Line measuring library (*LiMe*, Fernandez-Vital in prep) delivers powerful tools that work with single and large data sets of spectra (e.g integral field units) and can mask and detect emission-line profiles to be fitted with Gaussian and Non-Gaussian components, for studying the ionized gas kinematics and also the object's chemical composition. Also, is possible to calculate Non-parametric measurements (i.e w80, FWZI, etc) to compare with the parametric analysis. The results are stored in different kinds of formats, such as text files and pdf tables.

3.2. Non-parametric measurements

With the intention of having another description of the ionized gas kinematics to compare with our multi-component Gaussian models, we perform non-parametric interpercentile range measurements (See Figure 3.2; Whittle , 1985), that are widely used in astronomy, to the [OIII]λ5007Å emission-line profiles in our sample. Following the work of Liu et al. (2013), we measured velocities at some specific fraction of the accumulated flux of the lines. So, we define the quantities:

- ν_5, ν_{10}, ν_{50}, ν_{90}, and ν_{90}: These are the velocities measured at 5 %, 10 %, 50 %, 90 %, and 95 % of the cumulative flux, respectively. The ν_{50} is equivalent to the median velocity ν_{med} of the profile.

- $w80$ and $w90$: These are measures of the velocity line-width. $w80 = \nu_{90} - \nu_{10}$ encompass the 80 % of the global line flux, and $w80 = \nu_{95} - \nu_{15}$ encompass the 90 % of the global line flux. For a Gaussian profile we have that $w80 = 2.563\sigma = 1.088\times$ FWHM.

- *FWZI*: The velocity width of the profile where the model falls within 1σ of the continuum level.

- *FWHM*: The velocity width at half maximum of the emission-line profile.

To quantify the asymmetry and the shape of the [OIII]λ5007Å emission-line profile, we use the following parameters:

- A: The asymmetry parameter, defined as $A \equiv ((\nu_{90} - \nu_{med}) - (\nu_{med} - \nu_{10}))/w80$. This parameter is related to *Skewness*, which leads a value $A = 0$ for a symmetric profile.

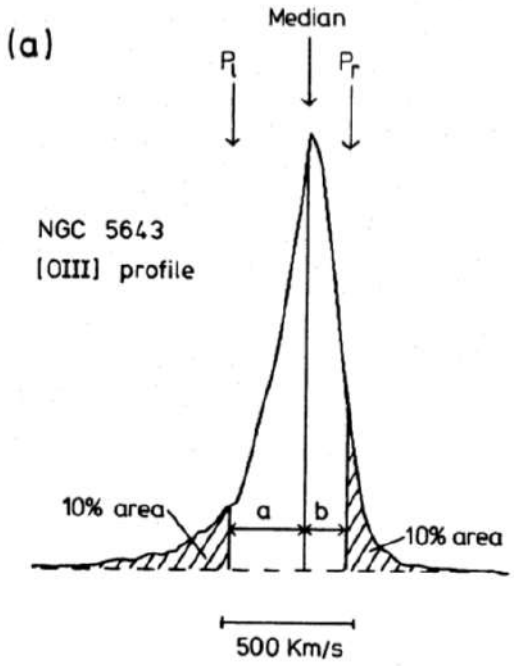

Figure 3.2: Definition of different quantities used to perform the interpercentile analysis. Here are shown the 10, 50, and 90 interpercentile with the markers P_l, Median, and P_r in the [OIII]λ5007Å emission of NGC 5643. The shaded areas represent 10 % of the total flux of the emission, so the rest of the area (inside P_l and P_r) is equivalent to the $w80$ described above. The figure is from Whittle (1985).

- K: The shape parameter, defined as $K \equiv w90/(1.397 \times \text{FWHM})$. This parameter is related to *Kurtosis*, which for a Gaussian profile $K = 1$. In contrast, for a profile with heavy wings $K > 1$, and without wings $K < 1$.

We applied this analysis using *LiMe*, and we include the seven galaxies observed with *ISIS*, so we can have a bigger panorama of the ionized gas kinematics, and the asymmetries that concur with the diversity of emission-line shapes for *LCE* and *NLCE*.

Chapter 4

Analysis and results

4.1. Ionized gas kinematics

The most relevant characteristic between the emission-line profiles of all the galaxies in the sample is their asymmetric form, which for LCE generally is evident in the blue part of the profile (see Figure 4.1). In all the cases, there was no solution to fit neither Hα nor [OIII]λ5007Å with only one kinematic component, so then we apply models with two Gaussian components (G2) and with three Gaussian components (G3) following our methodology. Models with four Gaussian components were not considered because adding another component does not significantly improve our fitting statistics of brighter lines (i.e AIC of Hα, [OIII]λ5007Å), and almost all cases converge to a solution where one of the Gaussian has zero amplitude, and/or an observed velocity dispersion less than instrumental resolution. Moreover, some of the low SNR emission lines are unable to be reproduced with more than two Gaussian causing uncertainties when trying to characterize the components by the use of different emission-line ratios.

Here we define the different kinematics parameters used to describe the ionized gas kinematics. The center of each Gaussian was measured in angstroms (Å) according to calibrated spectra, and transformed to velocity (Δv_r in $km\ s^{-1}$) using the non-relativistic Doppler effect between the center of the emission line (λ_0) and the center of the Gaussian component (λ), with c the speed of light,

$$\Delta v = \left(\frac{\lambda - \lambda_0}{\lambda_0} \right) \cdot c \tag{4.1}$$

Meanwhile, the dispersion of the components (σ_{obs}) measured in Å is transformed

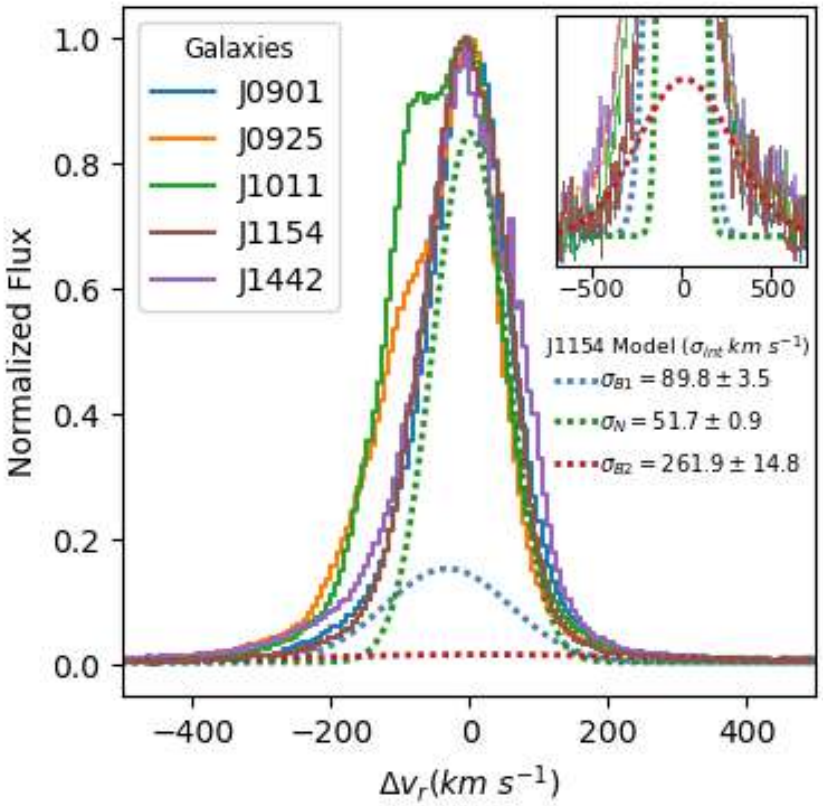

Figure 4.1: Complex structures of the [OIII]λ5007Å global emission-line profiles of the *Izotov* galaxies sample. Asymmetries are remarkable on the blue side of the global velocity profile. Also, it displays the three-component model of J1154, with each Gaussian component shown as a dotted line. The contribution of the broader component is small in terms of flux, but still necessary to reproduce the faint wings of the emission line (see inset of the figure). These galaxies have the bigger escape fractions in our study.

to $km\ s^{-1}$ in an analogous manner. Then, we correct the observed velocity dispersion of Hα and [OIII]λ5007Å assuming quadrature to calculate the intrinsic velocity dispersion,

$$\sigma_{int}^2 = \sigma_{obs}^2 - \sigma_{ins}^2 - \sigma_{ther}^2 \tag{4.2}$$

We subtract the dispersion contribution caused by the instrumental setup, σ_{ins}, which corresponds to a value of $\sigma_{ins} \sim 14.3\ km\ s^{-1}$ for the optical spectroscopic arm of the X-shooter, and we also subtract the thermal broadening caused by random thermal motions of the gas which depends on the mass of the specie m_{ion}, and the electron temperature of the galaxy which is assumed to be approximately $T_e \sim 1.2 \cdot 10^4\ K$ (Amorín et al., 2012a). The division factor at the left corresponds to the

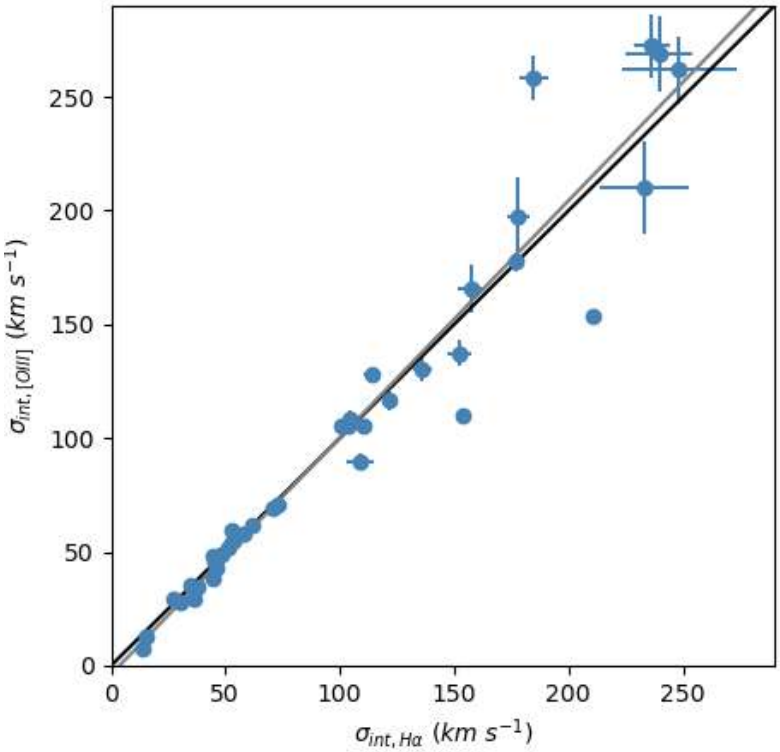

Figure 4.2: Comparison of the intrinsic velocity dispersion σ_{int} $(km\ s^{-1})$ of Gaussian components that are independently fitted to Hα and [OIII]λ5007Å of our sample. A good agreement is found between both ions kinematics, with larger scatter for broader components ($\sigma_{int} > 100(km\ s^{-1})$). The black solid line represents the identity, while the solid gray line is a Least Square Fitting ($m = 1.04, c = -3.83$).

transformation for Å to $km\ s^{-1}$.

$$\sigma_{ther} = \frac{c \cdot \lambda_0}{\lambda} \cdot \sqrt{\frac{k_B \cdot T_e}{m_{ion} \cdot c^2}} \tag{4.3}$$

It is remarkable that the ionized gas kinematics of the galaxies in our sample are similar to other GPs already studied in the literature (Amorín et al., 2012b; Bosch et al., 2019; Hogarth et al., 2020), where both, permitted and forbidden emission-lines have complex structures made out of multiple components with different kinematic characteristics. Results of the Hα and [OIII]λ5007Å multi-component fitting are summarized in Table 4.1, and Table 4.2, while details of the components' kinematics and fluxes of all the fitted emission-lines of each galaxy are presented in Appendix A. The Figure 4.2 illustrate the agreement between the intrinsic velocity dispersion

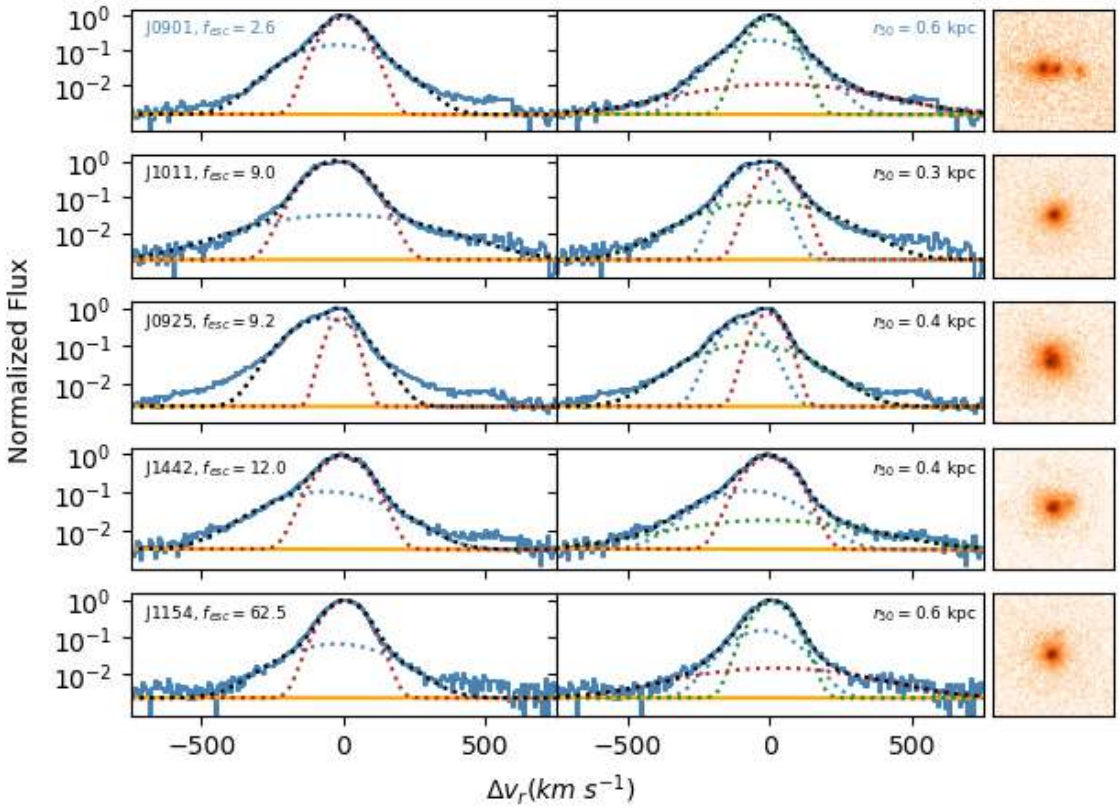

Figure 4.3: Comparison between two and three Gaussian component models of [OIII]λ5007Å for each galaxy in the *Izotov* sample. Blue and black labels show the LyC escape fraction ($f_{\rm esc}^{LyC}(UV)$) and the half-light radii ($r_{50}(UV)$) for *WLCE* and *SLCE*, respectively. The left panel shows the two-component models (G2), the central panel displays the three-component models (G3), and the right panel shows the NUV/COS image of the galaxy (boxes of 3 arcsec of width). In the left and central figures, the blue line represents the observed spectra, and the dotted black line indicates the multi-Gaussian model. The local continuum fitting is shown as a solid orange line. Each fitted Gaussian component is shown as a dotted color line (see Appendix A for more details). The y-axis is normalized to the emission peak flux and displayed on a logarithmic scale to highlight the emission line wings at low surface brightness. The faint bump observed at $\Delta v \sim 500\ km\ s^{-1}$ is identified as the faint HeI λ5015Å emission line.

results between all the components of three Gaussian model for the Hα and the [OIII]λ5007Å emission-lines profiles of the studied objects.

We can rapidly check the accuracy of the applied models by observing the residuals of the fitted emission line. We find that most bright lines (i.e Hα, [OIII]λ5007Å, Hβ) of the galaxies fitted using two-Gaussian components show large residuals near the peak of the global emission-line profile (See Figures in Appendix A), and/or at the low surface brightness wings. The impact of adding a third kinematic component is significant and can be seen in Figure 4.3 and Figure 4.4, where the [OIII]λ5007Å

profiles are plotted in a logarithmic scale for each model. An eye inspection let us distinguish how the extended wings are fitted with large accuracy after adding another component, which is at least 1 order of magnitude fainter that the peak flux of the line profile. Overall, we find that the addition of a third Gaussian component reduces the magnitude of the residuals in nearly all bright emission lines (see panels in Appendix A), what is also reflected in the statistical parameters values, like the Akaike Information Criteria which produces differences $\Delta AIC > 10$ between both models. For faint lines, such as [NII]λ6584Å, [SII]$\lambda\lambda$6717, 6731Å, and [OI]λ6300Å this is not always the case due to signal-to-noise limitations.

Also, by considering the premise that all the gas moves similarly, and because all the parameters are free for the fitting of Hα, and [OIII]λ5007Å, we can compare the consistency of both fitted models. At first sight, we can see that the kinematics of the two-component model corresponding to J0925 and J1011 (both *SLCE*) from *the Izotov sample* (Table 4.1) are completely inconsistent, where the velocity shift of the broad (B) and narrow (N) components have notoriously differences (bigger than instrumental resolution) between Hα and [OIII]λ5007Å. Moreover, for both ions, the intrinsic velocity dispersion of J0925 is significantly in disagreement, so we choose not to consider these models in our analysis. In contrast, by adding another kinematic component, we get kinematic results that are in good agreement. According to this, both galaxies show a similar kinematic structure composed of two narrow components ($N1$ and $N2$) separated by $\Delta v_{N1,N2} \sim 90 - 100\ km\ s^{-1}$, with intrinsic velocity dispersion of $\sigma_{int} \sim 40 - 60\ km\ s^{-1}$ that tend to follow the global shape of the emission-line profile, in addition to a broad blue-shifted component (B) having a velocity dispersion of $\sigma_{int} \sim 150 - 210\ km\ s^{-1}$ that reproduces the extended wings of the profile. We see a similar kinematic structure in the galaxy J012217 (*WLCE*), where two model component does not well reproduce the global emission-line profiles, in contrast to the three-component model composed of narrow components that contribute great flux to the global emission, and a broader component that reproduces the wings. Fainter emission-line profiles along with all the optical spectra are well reproduced after copying these kinematics solutions.

The ionized gas kinematics of J0901 (*WLCE*), J1154 (*SLCE*), J1442 (*SLCE*), J004743 (*WLCE*), and J091113 (*WLCE*) are quite similar. The emission-lines profiles can be decently described by a narrow component (N) almost at the global velocity profile, with intrinsic velocity dispersion of $\sigma_{int} \sim 30{-}60\ km\ s^{-1}$ which provides more than $\sim 50\,\%$ of the total flux of Hα and [OIII]λ5007Å, while the resting contribution

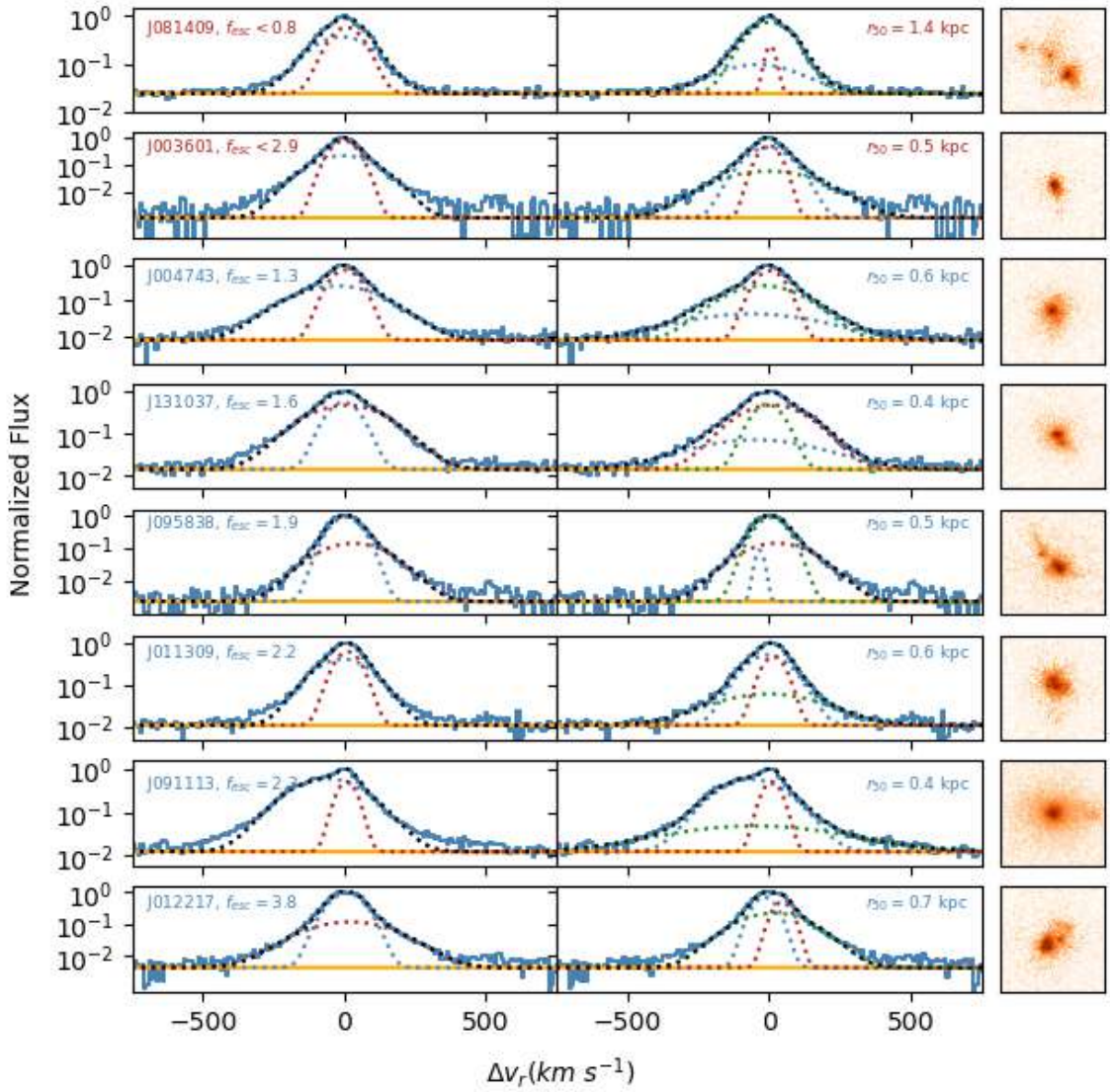

Figure 4.4: Same as Figure 4.3 for the *LzLCS* sample. Red label show the upper limit of the LyC escape fraction ($f_{\rm esc}^{LyC}(UV)$) and the half-light radii ($r_{50}(UV)$) for *NLCE*

corresponds to a broad component (B) blue-shifted by at least $\Delta v \sim -20\ km\ s^{-1}$, with intrinsic velocity dispersion of $\sigma_{int} \sim 130-170\ km\ s^{-1}$. This broader component tries to compensate for the asymmetries from the blue side of the emission-line profiles, and also fit the underlying extended wings. In the case of J091113 (*WLCE*), this broader component shows the same characteristics, but contributes a greater percentage of the emission-line flux, accounting for more than $\sim 80\,\%$ of the total flux. Subsequently, after adding another component to those objects, the narrow contribution (N) remains almost the same while the broader component (B) is split

Table 4.1: Kinematics components of Hα and [OIII]λ5007Å for galaxies in the *Izotov* sample. The left half shows the G2 model, while the right half shows the G3.

Ion	Comp.[a]	Δv_r[b]	σ_{int}[c]	EM_f[d]	Comp.[a]	Δv_r[b]	σ_{int}[c]	EM_f[d]
J0901+2119, f_{esc}(UV) = 2.57, Weak LCE								
Hα	B	-19.2 ± 1.2	131.4 ± 1.5	29.0	B1	-25.1 ± 1.6	100.5 ± 2.5	29.5
	N	-2.0 ± 0.4	51.2 ± 0.4	71.0	N	0.2 ± 0.4	48.3 ± 0.5	62.3
	-	-	-	-	B2	13.0 ± 5.9	184.8 ± 6.1	8.2
[OIII]	B	-21.0 ± 1.3	126.4 ± 1.5	28.5	B1	-22.1 ± 1.0	105.5 ± 1.5	32.3
	N	1.1 ± 0.4	51.7 ± 0.5	71.5	N	2.8 ± 0.3	49.2 ± 0.4	63.8
	-	-	-	-	B2	35.8 ± 8.4	258.1 ± 9.7	3.9
J1011+1947, f_{esc}(UV) = 8.98, Strong LCE								
Hα	B	-34.2 ± 3.2	202.1 ± 4.2	16.4	N1	-66.1 ± 8.9	53.3 ± 3.2	42.1
	N	-28.4 ± 0.4	67.7 ± 0.5	83.6	B	-29.4 ± 2.3	177.3 ± 2.9	21.2
	-	-	-	-	N2	13.3 ± 6.0	45.9 ± 2.0	36.7
[OIII]	B	-5.7 ± 6.7	243.1 ± 8.6	9.1	N1	-63.8 ± 8.2	54.7 ± 3.1	46.3
	N	-24.8 ± 0.5	72.2 ± 0.5	90.9	B	-18.5 ± 3.4	177.5 ± 4.4	15.9
	-	-	-	-	N2	22.2 ± 6.1	46.9 ± 2.2	37.8
J0925+1403, f_{esc}(UV) = 9.17, Strong LCE								
Hα	B	-93.2 ± 4.4	216.4 ± 4.9	22.3	N1	-107.0 ± 4.2	57.7 ± 2.0	31.4
	N	-46.3 ± 0.7	71.3 ± 0.7	77.7	B	-72.2 ± 1.6	211.0 ± 2.0	23.9
	-	-	-	-	N2	-9.8 ± 1.5	44.6 ± 0.7	44.7
[OIII]	B	-66.1 ± 1.4	92.5 ± 1.0	72.0	N1	-95.1 ± 5.2	58.1 ± 2.7	35.2
	N	-8.6 ± 1.3	32.8 ± 1.5	28.0	B	-69.8 ± 1.8	154.0 ± 2.5	23.5
	-	-	-	-	N2	-3.8 ± 1.5	38.5 ± 0.9	41.3
J1442-0209, f_{esc}(UV) = 11.97, Strong LCE								
Hα	B	-51.2 ± 2.0	167.8 ± 2.2	24.6	B1	-65.3 ± 6.0	113.9 ± 3.6	19.6
	N	-3.4 ± 0.4	63.5 ± 0.5	75.4	B2	-14.0 ± 6.1	236.4 ± 8.1	10.2
	-	-	-	-	N	0.9 ± 0.5	61.9 ± 0.6	70.2
[OIII]	B	-59.7 ± 2.4	160.3 ± 2.3	23.3	B1	-70.9 ± 4.9	127.7 ± 3.5	19.4
	N	-2.3 ± 0.5	62.2 ± 0.5	76.7	B2	-2.9 ± 11.9	272.3 ± 13.7	6.0
	-	-	-	-	N	0.2 ± 0.5	61.7 ± 0.5	74.6
J1154+2443, f_{esc}(UV) = 62.47, Strong LCE								
Hα	B	-16.8 ± 2.7	151.1 ± 3.7	16.1	B1	-17.1 ± 3.2	109.0 ± 6.2	18.4
	N	2.7 ± 0.4	53.5 ± 0.5	83.9	N	3.9 ± 0.5	51.2 ± 0.7	77.0
	-	-	-	-	B2	14.2 ± 15.7	248.4 ± 25.0	4.6
[OIII]	B	-21.7 ± 3.4	144.2 ± 4.3	15.1	B1	-22.9 ± 4.2	89.8 ± 3.5	22.0
	N	5.6 ± 0.5	54.9 ± 0.5	84.9	N	9.4 ± 0.7	51.7 ± 0.9	72.7
	-	-	-	-	B2	24.6 ± 11.8	261.9 ± 14.8	5.3

[a] Component of the model.

[b] Velocity shift ($km\ s^{-1}$) between the central peak of the emission-line and the center of the component (see text for details).

[c] Intrinsic velocity dispersion ($km\ s^{-1}$) (see text for details).

[d] Percentage of relative to the global flux of the emission-line.

Table 4.2: Same as Table 4.1, but for galaxies in the *LzLCS* sample.

Ion	Comp.[a]	Δv_r[b]	σ_{int}[c]	EM_f[d]	Comp.[a]	Δv_r[b]	σ_{int}[c]	EM_f[d]
J081409, $f_{esc}(UV) < 0.75$, Non-LCE								
Hα	B	-10.2 ± 1.2	96.0 ± 1.8	54.0	B	-31.4 ± 3.6	136.2 ± 4.0	17.1
	N	6.5 ± 0.8	56.8 ± 1.4	46.0	N1	2.0 ± 0.4	71.0 ± 0.8	79.0
	-	-	-	-	N2	3.2 ± 1.1	15.5 ± 2.4	3.9
[OIII]	B	-9.0 ± 1.8	94.8 ± 2.6	52.6	B	-40.5 ± 7.2	130.6 ± 5.6	15.1
	N	7.9 ± 0.9	52.3 ± 1.7	47.4	N1	4.0 ± 0.5	69.3 ± 0.9	79.1
	-	-	-	-	N2	5.7 ± 0.7	12.5 ± 1.2	5.9
J003601, $f_{esc}(UV) < 2.91$, Non-LCE								
Hα	B	0.1 ± 1.4	99.6 ± 2.4	42.6	N1	-2.6 ± 0.7	52.7 ± 2.2	54.3
	N	-1.9 ± 0.4	37.3 ± 0.7	57.4	B	6.6 ± 2.6	152.2 ± 5.1	24.9
	-	-	-	-	N2	-1.0 ± 0.8	27.3 ± 2.3	20.8
[OIII]	B	-3.6 ± 0.9	92.4 ± 1.5	39.8	N1	-3.1 ± 0.5	59.6 ± 1.8	52.4
	N	-1.1 ± 0.3	37.5 ± 0.5	60.2	B	-1.5 ± 2.4	137.3 ± 5.6	15.6
	-	-	-	-	N2	-0.2 ± 0.4	29.6 ± 0.9	32.0
J004743, $f_{esc}(UV) = 1.32$, Weak LCE								
Hα	B	-32.9 ± 0.8	140.5 ± 0.9	56.1	B1	-43.2 ± 8.1	233.4 ± 19.5	12.1
	N	1.3 ± 0.3	48.0 ± 0.4	43.9	B2	-28.9 ± 1.3	121.3 ± 2.8	48.7
	-	-	-	-	N	2.1 ± 0.4	45.7 ± 0.5	39.2
[OIII]	B	-25.6 ± 0.9	134.1 ± 1.1	50.5	B1	-60.1 ± 14.1	210.2 ± 20.5	10.9
	N	3.1 ± 0.3	44.8 ± 0.4	49.5	B2	-18.7 ± 1.8	116.5 ± 4.0	43.9
	-	-	-	-	N2	3.3 ± 0.3	43.2 ± 0.5	45.3
J131037, $f_{esc}(UV) = 1.63$, Weak LCE								
Hα	N	-7.9 ± 0.5	47.4 ± 0.9	28.7	B1	-50.3 ± 9.3	178.0 ± 5.1	18.3
	B	4.6 ± 0.7	124.0 ± 1.0	71.3	N	-13.1 ± 0.5	44.7 ± 0.8	23.9
	-	-	-	-	B2	15.2 ± 1.4	104.7 ± 1.8	57.8
[OIII]	N	-2.3 ± 0.7	50.3 ± 1.2	33.0	B1	-45.9 ± 20.2	197.3 ± 17.4	13.3
	B	6.8 ± 1.0	123.9 ± 1.6	67.0	N	-4.9 ± 0.9	47.9 ± 1.4	27.7
	-	-	-	-	B2	12.6 ± 1.9	108.4 ± 3.6	59.0
J095838, $f_{esc}(UV) = 1.88$, Weak LCE								
Hα	N	2.7 ± 0.2	43.5 ± 0.3	72.5	N1	-18.4 ± 1.5	14.1 ± 2.6	3.5
	B	22.2 ± 1.5	102.3 ± 2.0	27.5	N2	4.7 ± 0.3	45.6 ± 0.4	72.5
	-	-	-	-	B	22.3 ± 1.4	110.2 ± 2.1	23.9
[OIII]	N	5.8 ± 0.2	45.3 ± 0.3	74.4	N1	-32.5 ± 1.2	7.7 ± 2.4	2.1
	B	31.8 ± 1.4	104.7 ± 1.7	25.6	N2	7.5 ± 0.3	45.2 ± 0.3	72.0
	-	-	-	-	B	28.9 ± 1.2	105.5 ± 1.6	25.9
J011309, $f_{esc}(UV) = 2.20$, Weak LCE								
Hα	B	-6.4 ± 0.7	93.9 ± 1.0	62.3	N1	-5.8 ± 0.7	73.3 ± 1.2	60.1
	N	9.4 ± 0.4	41.0 ± 0.7	37.7	B	6.6 ± 3.3	157.4 ± 6.2	17.1
	-	-	-	-	N2	14.7 ± 0.6	34.6 ± 0.9	22.7
[OIII]	B	-5.5 ± 1.0	87.8 ± 1.3	58.7	N1	-3.5 ± 1.0	70.8 ± 1.6	58.5

Table 4.2: Same as Table 4.1, but for galaxies in the *LzLCS* sample.

Ion	Comp.[a]	Δv_r[b]	σ_{int}[c]	EM$_f$[d]	Comp.[a]	Δv_r[b]	σ_{int}[c]	EM$_f$[d]
	N	12.6 ± 0.5	39.8 ± 0.9	41.3	B	-2.0 ± 5.3	165.7 ± 10.3	13.6
	-	-	-	-	N2	16.5 ± 0.7	35.4 ± 1.0	27.8
J091113, f_{esc}(UV) = 2.32, Weak LCE								
Hα	B	-64.3 ± 1.2	121.2 ± 0.8	80.5	B1	-72.2 ± 2.0	104.0 ± 1.8	62.3
	N	6.3 ± 0.9	34.0 ± 1.2	19.5	B2	-42.3 ± 7.2	239.5 ± 14.4	16.5
	-	-	-	-	N	10.7 ± 0.8	36.5 ± 1.1	21.2
[OIII]	B	-61.2 ± 0.9	114.4 ± 0.7	80.9	B1	-61.9 ± 0.9	105.1 ± 1.0	70.0
	N	9.0 ± 0.7	29.7 ± 0.9	19.1	B2	-49.7 ± 9.2	269.1 ± 16.6	11.5
	-	-	-	-	N	10.6 ± 0.5	29.6 ± 0.6	18.5
J012217, f_{esc}(UV) = 3.76, Weak LCE								
Hα	N	6.6 ± 0.3	53.6 ± 0.4	67.0	N1	-16.5 ± 3.5	37.5 ± 1.9	39.9
	B	9.7 ± 1.9	163.0 ± 2.8	33.0	B	12.2 ± 1.6	153.8 ± 2.2	38.8
	-	-	-	-	N2	50.1 ± 3.5	30.2 ± 1.6	21.4
[OIII]	N	8.3 ± 0.3	50.9 ± 0.4	75.7	N1	-14.9 ± 2.1	34.4 ± 1.1	39.4
	B	20.5 ± 2.4	137.2 ± 3.7	24.3	B	16.8 ± 1.1	110.3 ± 1.5	37.7
	-	-	-	-	N2	46.6 ± 2.1	28.0 ± 1.0	22.9

[a] Component of the model.

[b] Velocity shift ($km\ s^{-1}$) between the central peak of the emission-line and the center of the component (see text for details).

[c] Intrinsic velocity dispersion ($km\ s^{-1}$) (see text for details).

[d] Percentage of relative to the global flux of the emission-line.

into two broad emissions (B1 and B2). The narrower of these broad emissions also seems to compensate for the blue side asymmetry (bump) and has a velocity shift similar to B but with smaller intrinsic velocity dispersion of $\sigma_{int} \sim 100-130\ km\ s^{-1}$. On the other side, the broader component fits the extended wings of the emission-line profiles, with only $\sim 4-15\,\%$ of the total flux, and a velocity dispersion $\sigma_{int} \sim 190-270\ km\ s^{-1}$. At last, the galaxy J131037 (*WLCE*) shares all the elements mentioned above but contrasts with the other galaxies because the global asymmetry lies to the red side of the spectrum and this is traduced in a broad component that has a positive radial velocity.

The *NLCE* objects J081409. and J003601, show narrower and more symmetric emission-line profiles. Two-component models show a narrow component (N) with velocity dispersion $\sigma_{int} \sim 40-50\ km\ s^{-1}$, and a broad component (B) with $\sigma_{int} \sim 90-100\ km\ s^{-1}$, both almost the half of the total flux, and placed very close to the global velocity of the emissions (peak). After adding another component the kinematic panorama changes. For both objects we found that the narrow component

gets fainter and narrower, with $\sigma_{int} \sim 10 - 30\ km\ s^{-1}$, and a flux contribution about $\sim 6 - 30\,\%$ that models the top of the emission-lines profile. A narrow (mid) component shows a key role in the fitting with a contribution of $\sim 50 - 80\,\%$ of the global flux, and with $\sigma_{int} \sim 50 - 70\ km\ s^{-1}$. Also, both galaxies show a broader component with $\sigma_{int} \sim 130 - 150\ km\ s^{-1}$ that supply flux for the wings, which in the case of J081409 is greatly blue-shifted. Similar to J003601, the galaxy J011309 (*WLCE)* shows an analog kinematic description, but with slighter different velocity shifts due to more asymmetrical lines shape and broader wings.

An exception is the galaxy J095838 (*WLCE*), with a red-shifted asymmetry at the bottom, that can be well described by a broad component with $\sigma_{int} \sim 105\ km\ s^{-1}$ that provides $\sim 25\,\%$ of the flux, and a narrow component with $\sigma_{int} \sim 45\ km\ s^{-1}$ providing the rest of the global flux. Both models (two and three components) converge almost to the same solution. A third narrower component appears in bright emission-lines with $\sigma_{int} \sim 10\ km\ s^{-1}$, but only contributes $\sim 4\,\%$.

In summary, there are three kinds of kinematics results in our sample. One group of LCE galaxies (J0925, J1011, and J012217), with the most complex emission-line profiles, where is necessary at least two well-separated narrow components correctly fit the large-scale variations of the emissions. Another group of LCE (J0901, J1154, J1442, J004743, J091113, and J131037) can be modeled with one narrow component, and one or two broader components that try to model the bumps asymmetries in the global profiles, and the underlying wings, respectively. On the other hand, the *NLCE* (J081409, and J003601) exhibit narrower and symmetrical emission-lines, with components close to the global velocity profile. The *WLCE* J011309 coincide with this category, while J095838 (*WLCE*) seem unrelated. We emphasize the existence of a faint broad component that tries to reproduce the wings in all the bright emission-lines of the objects that were analyzed, including *NLCE* and *LCE*. Also, we highlight that none of the *X-Shooter* 2D spectra show spatially resolved structures.

Finally, the use of different statistical parameters allows us to compare each model and the goodness of fit (see Section 3). In general, the fit statistics are improved after adding another component (i.e χ^2, χ^2_ν, AIC, BIC), but as said in the caveats of the Section 3, there are particular cases, where one or two Gaussian component(s) is enough to correctly fit the profiles, and the addition of new parameters have no improve. Cases of lower SNR, such as [NII]$\lambda\lambda 6548, 6584$Å, [SII]$\lambda\lambda 6717, 6731$Å, and [OI]$\lambda 6300$Å are crucial because of their relevance in astrophysical diagnostics that we use to describe the physical properties of the components. According to this, we

adopt some criteria described in the following sections to choose which model to use to describe each galaxy and avoid uncertainties in diagnostic diagrams, electron density calculation, and extinction correction for luminosity determination. Thus, we emphasize that the spectral and spatial resolution are key in the interpretation of the ionized gas kinematics.

4.2. Emission-line diagnostic of the components

Classic diagnostic diagrams

Taking advantage of every optical emission-line fitted, we employed classical line ratios diagrams to explore the excitation properties, and the sources of ionization radiation that can affect the kinematic components, including the global contribution of each galaxy. Commonly known as BPT diagnostic diagrams, we made use of [OIII]λ5007/Hβ vs. [NII]λ6584/Hα, [SII]λ6717, 6731/Hα (Baldwin et al., 1981) and [OI]λ6300/Hα (Veilleux & Osterbrock, 1987) line ratios to characterize Gaussian components.

One of the key objectives of this work is to examine the characteristics and functions of the kinematics components in our models. We previously mentioned there are cases where lack of spectral resolution, low SNR, or different astrophysical mechanisms provoke faint emission-lines such as [NII]λ6584Å, [SII]$\lambda\lambda$6717, 6731Å, and [OI]λ6300Å do not show all the components as the brighter (high SNR) emission-lines, causing uncertain values when trying to calculate ratios. This restricts us to determine physical properties for not all the kinematics components that we found. Moreover, the *SLCE* seems to be more affected, where the broad components that try to fit faint wings (three-component models) do not appear in [SII]$\lambda\lambda$6717, 6731Å and [OI]λ6300Å of some galaxies. Therefore, we consider three-component models only for those galaxies that can not be reproduced by two-component models (J0925, J1011 and J012217), or in galaxies that show all the components at emission-lines used in the diagnostic diagrams. Another way, the two-component model is preferred as a better representation to apply diagnostic diagrams accounting that in almost all objects produce a decent fit of the emission-lines profiles. Thus, the galaxies J0901, J1154, J1442, and J003601 were analyzed using only two Gaussian components, while the others were analyzed using three Gaussian components. Nevertheless, there are special cases such as J1154 (*SLCE*) that just need one narrow component to fit each

S II emission, causing segregation in the analysis of other components.

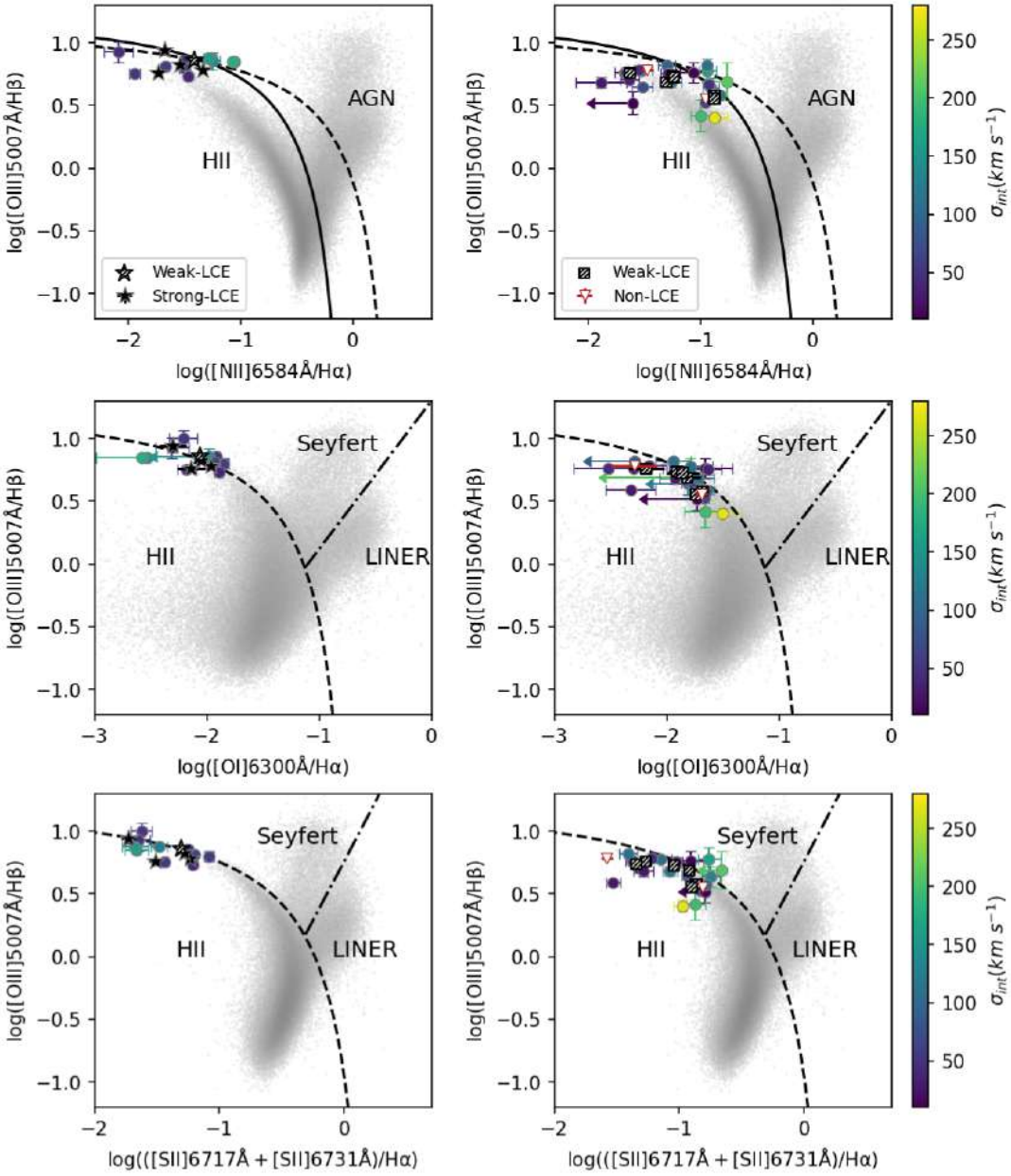

Figure 4.5: Classical emission-line diagnostics (BPT) for the multi-component fitting. The left column shows the ratios of the *Izotov* sample, while the right column shows the ratios of the *LzLCS* sample. Integrated flux ratios are represented as stars and squares. *SLCE* are filled, *WLCE* are hashed and *NLCE* are open triangles (red). Individual components are illustrated as circles with the color depending on $\sigma_{int,[OIII]}$, and components with large uncertainties ($> 15\,\%$) are considered as an upper limit. The scatter-density gray region is composed of galaxies of the SDSS-DR7 MPA-JHU. Regions of different excitation mechanisms are labeled and established by theoretical and empirical lines such as Kewley et al. (2001) (dashed line), Kauffmann et al. (2003) (solid line), and Kewley et al. (2006) (dotted-dashed line). Broader components of some *Izotov* galaxies (strongest leakers) cannot be analyzed because do not appear in the faints [O I] and/or in [S II].

The diagrams are shown in Figure 4.5. In the left column are shown the classic diagnostic diagrams of the *Izotov* sample, which includes the strongest LCE, while the right column shows the diagnostics of the *LzLCS* sample. The global fluxes contributions are illustrated as stars and squares. *SLCE* are represented as filled figures, *WLCE* as hashed figures, and *NLCE* as red open triangles. The individual kinematic components are represented by circles with color grading depending on the intrinsic velocity dispersion σ_{int} of [OIII]λ5007Å. Values are compared with a large catalog of SDSS-DR7 MPA-JHU galaxies plotted in gray, and distinctive areas of diverse excitation mechanisms are demarcated. The theoretical "maximum star-burst line", determined by the upper limit of pure stellar photoionization models (Kewley et al., 2001) is shown as a dashed line in all the diagrams. Galaxies above this line are likely to be excited by active nuclear activity (AGN). For the [N II]/Hα diagram, also is illustrated the empirical line Kauffmann et al. (2003) as a solid line, used to distinguish between star-forming galaxies and possible Composite galaxies that also could have contributed to nuclear activity. Types of AGNs can also be differentiated as a LINER or Seyfert according to the empirical line established by Kewley et al. (2006), which in [S II]/Hα, and [O I]/Hα is shown as a dotted-dashed line.

By seeing the diagrams we can check that almost all the integrated fluxes and individual components are located at the very top of the maximum star-burst line, being fully consistent with emission-line ratios produced by the photoionization of hot massive stars. The global ratios of our *Izotov* sample are in good agreement with that founded by Guseva et al. (2020), where five of the LCE in our sample are positioned near Lyman Break Analogs and high-z star-forming galaxies.

Presumably, we notice that *SLCE* and it components (left column) have greater [O III]/Hβ> 0.7 than the *WLCE* and *NLCE* (right column) [O III]/H$\beta\leq$ 0.7, thus indicating higher ionization parameters. This difference is notoriously evident in the [S II]/H$\alpha$and [O I]/Hα diagrams.

When we compare the location of the individual components, it's possible to observe that for the *WLCE* and *NLCE* (right column) the distribution is similar along the three diagrams. Apparently, the turbulent gas has a higher contribution in metals when compared to Hα, producing a displacement to the right of the diagrams. Also, in the [N II]/Hα and [S II]/Hα diagrams, some of the broads components exceed the limit of Kewley et al. (2001) indicating an additional contribution to the photoionization as an excitation mechanism. In contrast, the broader of these components

have the lowest [O III]/Hβ but still indicate high stellar photoionization.

On the other hand, the broad components of the *Izotov* galaxies do not show great differences in [O III]/Hβ compared to the narrower components and the integrated fluxes, but there are notorious differences when we see the axes that compromise Hα. In [N II]/Hα diagram, the broad components are at the right indicating additional shock contribution, but the [S II]/Hα, and [O I]/Hα diagrams illustrate quite the opposite, where broad emission gets fainter for the collisionally excited ions. It is well known that *SLCE* have [S II] deficiency. Recently Wang et al. (2021) confirmed this using the complete sample the *LzLCS*, and this could be used as an indirect method to find LCE. Also, Ramambason et al. (2020) founded that LCE with high escape fractions ($f_{\rm esc}^{LyC} > 0.2$) can also have [O I] deficiency. All this suggests that the turbulent gas (broad emission) that does not appear in these emissions could be related to the weakness of both ions. Furthermore, is expected that the *SLCE* be density-bounded, which means that the flux of ionizing radiation coming from the starburst is so large that the gas between these sources and the observer is fully ionized. In this regime, the outer part where [S II] is emitted should be absent or extremely weak.

All these characteristics indicate that high-ionization parameters and hard UV ionizing radiation produced by young massive stars play a key role in the escape of LyC photons. The use of spatially resolved spectroscopy would help us to study the astrophysical mechanism involved in the excitation of the gas with more detailed, such as the shocks contributions.

4.3. Electron density of the components

One of the most valuable physical properties in nebular diagnostic used to describe the conditions of emission nebulae is the electron density n_e. This parameter, combined with the electron temperature determines the population of excited states of ions and atoms available. At low densities, the excited states are populated as a result of collisions generally with electrons, and the timescales are often long enough that a radiative decay will be produced back to the ground state, emitting what is known as forbidden emission-line. Thus, the emission-line intensity is proportional to the collision rates, which is proportional to the number densities of the two colliding species. The three-level atoms (such as [S II] or [O II]), where two different excited states have a small energy separation (nearly equal excitation energy) and

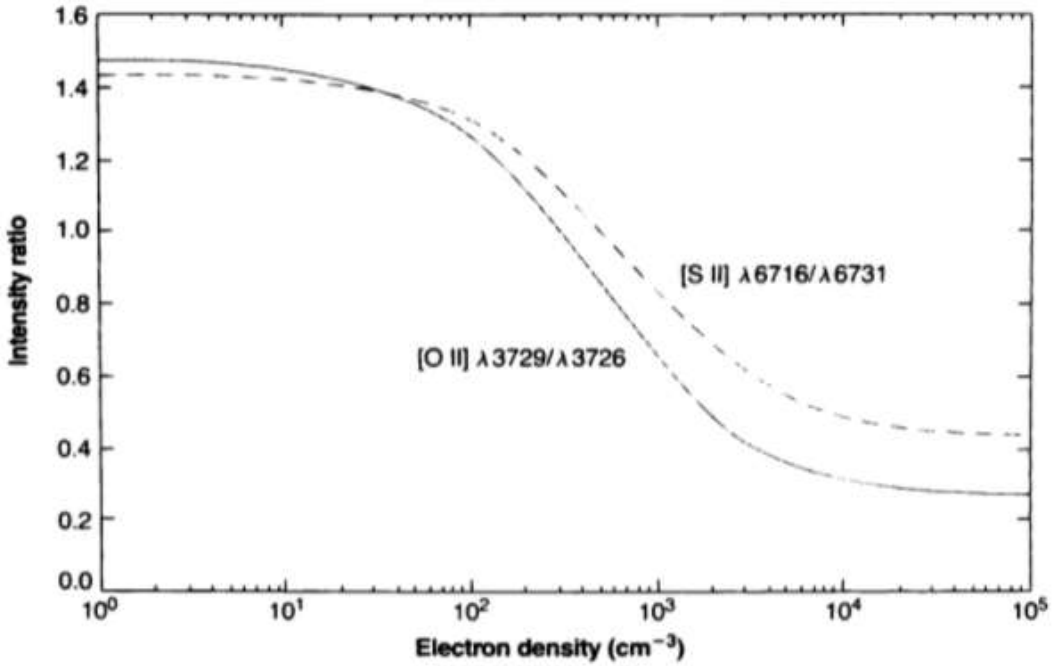

Figure 4.6: Dependence of intensity ratios for the ions [SII]$\lambda\lambda$6717, 6731Å, and [OII]$\lambda\lambda$3726, 3729Å, according to electron density n_e. Assuming a fixed value of electron temperature T_e ($\sim 10,000K$ for this figure), the intensity of the forbidden transitions is sensible to the electron density and converges to different values for low-density and high-density limits. The figure is from Osterbrock & Ferland (2006).

very different probability to do the radiative transition, make them suitable for use as density diagnostic by comparing the intensity of the forbidden emission-lines of both levels. This is possible because at the low-density limit the intensity of the transitions emitted is proportional to the collision rates (as said before), but at high density, the two levels are thermalized and are populated according to the Boltzmann ratios. This implies a different intensity ratio between both limits, which provides us with information about the density (Figure 4.6).

Because the calculation of level populations and intensity ratios of forbidden emission-lines depends on the collision strengths and the Einstein coefficients of spontaneous transition probabilities, we made use of *PyNeb* (Luridiana et al., 2015) library, which provided an excellent atomic database to compute the n_e for each kinematic component, and the global profile contribution of our fitted models, according to the [SII]$\lambda\lambda$6717, 6731Å fluxes ratios.

Owing to the temperature dependence ($T_e^{1/2}$) to derive the electron density, we adopt the electron temperatures reported in Flury et al. (2022a) from the SDSS Optical Spectra. From these values, we made an iteration of 5000 steps Monte Carlo

Table 4.3: The electron number density of the individual kinematic components, and the total flux integration for each galaxy of the *Izotov* sample. The left half of the table shows the two components model, while the right half shows the three components model. Both sides include the Hα intrinsic velocity dispersion.

Comp.[a]	ne([SII])[b]	$\sigma_{\text{int,H}\alpha}$[c]	Comp.[a]	ne([SII])[b]	$\sigma_{\text{int,H}\alpha}$[c]
J0901+2119, f_{esc}(UV) = 2.57, Weak LCE					
B	8345^{+3968}_{-3490}	131.4 ± 1.5	B1	2853^{+3925}_{-1645}	100.5 ± 2.5
N	180^{+105}_{-59}	51.2 ± 0.4	N	188^{+120}_{-66}	48.3 ± 0.5
-	-	-	B2	-	184.8 ± 6.1
Global	693^{+270}_{-214}	-	Global	682^{+558}_{-328}	-
J1011+1947, f_{esc}(UV) = 8.98, Strong LCE					
B	-	202.1 ± 4.2	N1	404^{+359}_{-211}	53.3 ± 3.2
N	925^{+400}_{-285}	67.7 ± 0.5	B	-	177.3 ± 2.9
-	-	-	N2	1888^{+1512}_{-759}	45.9 ± 2.0
Global	911^{+652}_{-374}	-	Global	1009^{+744}_{-413}	-
J0925+1403, f_{esc}(UV) = 9.17, Strong LCE					
B	950^{+2183}_{-650}	216.4 ± 4.9	N1	177^{+93}_{-55}	57.7 ± 2.0
N	278^{+76}_{-68}	71.3 ± 0.7	B	1630^{+3027}_{-1060}	211.0 ± 2.0
-	-	-	N2	349^{+129}_{-111}	44.6 ± 0.7
Global	311^{+76}_{-66}	-	Global	325^{+122}_{-103}	-
J1442-0209, f_{esc}(UV) = 11.97, Strong LCE					
B	738^{+1898}_{-507}	167.8 ± 2.2	B1	601^{+1398}_{-382}	113.9 ± 3.6
N	188^{+90}_{-61}	63.5 ± 0.5	B2	-	236.4 ± 8.1
-	-	-	N	234^{+131}_{-90}	61.9 ± 0.6
Global	185^{+99}_{-59}	-	Global	210^{+142}_{-77}	-
J1154+2443, f_{esc}(UV) = 62.47, Strong LCE					
B	-	151.1 ± 3.7	B1	-	109.0 ± 6.2
N	855^{+565}_{-354}	53.5 ± 0.5	N	706^{+478}_{-319}	51.2 ± 0.7
-	-	-	B2	-	248.4 ± 25.0
Global	984^{+1957}_{-663}	-	Global	1074^{+2763}_{-763}	-

[a] Component of the model.

[b] Electron density (cm^{-3}) calculated with *pyneb* using the ratio of [SII]$\lambda\lambda$6717, 6731Å (see text for details).

[c] Intrinsic velocity ($km\ s^{-1}$) dispersion of Hα (see text for details).

simulation to make a temperature distribution for each galaxy, and then calculate the median density of the obtained distribution. The n_e median values with $1-\sigma$ uncertainties for all the kinematics components are found in Table 4.3 and Table 4.4, for the *Izotov* sample and the *LzLCS* sample, respectively.

Once again, we emphasize that for some galaxies not all the kinematics components are found in [SII]$\lambda\lambda$6717, 6731Å (generally the broader component), or sometimes they are too faint to be compared, arising unphysical values. Therefore, for the individual components, we consider only the estimations that give a reasonable astrophysical sense, while global estimations can be comparable. Thus, we encourage

Table 4.4: Same as Table 4.3, but for the *LzLCS* sample.

Comp.[a]	ne([SII])[b]	$\sigma_{\mathrm{int,H}\alpha}$[c]	Comp.[a]	ne([SII])[b]	$\sigma_{\mathrm{int,H}\alpha}$[c]
J081409, $f_{\mathrm{esc}}(\mathrm{UV}) < 0.75$, Non-LCE					
B	209^{+156}_{-80}	96.0 ± 1.8	B	451^{+868}_{-271}	136.2 ± 4.0
N	292^{+234}_{-131}	56.8 ± 1.4	N1	351^{+160}_{-127}	71.0 ± 0.8
-	-	-	N2	-	15.5 ± 2.4
Global	199^{+120}_{-70}	-	Global	205^{+126}_{-73}	-
J003601, $f_{\mathrm{esc}}(\mathrm{UV}) < 2.91$, Non-LCE					
B	1129^{+3034}_{-831}	99.6 ± 2.4	N1	966^{+2734}_{-668}	52.7 ± 2.2
N	586^{+400}_{-262}	37.3 ± 0.7	B	1188^{+3355}_{-856}	152.2 ± 5.1
-	-	-	N2	939^{+1702}_{-604}	27.3 ± 2.3
Global	742^{+992}_{-438}	-	Global	911^{+2129}_{-613}	-
J004743, $f_{\mathrm{esc}}(\mathrm{UV}) = 1.32$, Weak LCE					
B	176^{+108}_{-58}	140.5 ± 0.9	B1	889^{+2074}_{-600}	233.4 ± 19.5
N	367^{+311}_{-182}	48.0 ± 0.4	B2	445^{+882}_{-263}	121.3 ± 2.8
-	-	-	N	422^{+435}_{-226}	45.7 ± 0.5
Global	175^{+98}_{-54}	-	Global	354^{+436}_{-190}	-
J131037, $f_{\mathrm{esc}}(\mathrm{UV}) = 1.63$, Weak LCE					
N	292^{+200}_{-128}	47.4 ± 0.9	B1	541^{+922}_{-331}	178.0 ± 5.1
B	170^{+67}_{-46}	124.0 ± 1.0	N	349^{+263}_{-162}	44.7 ± 0.8
-	-	-	B2	188^{+110}_{-61}	104.7 ± 1.8
Global	185^{+65}_{-52}	-	Global	219^{+116}_{-80}	-
J095838, $f_{\mathrm{esc}}(\mathrm{UV}) = 1.88$, Weak LCE					
N	255^{+291}_{-117}	43.5 ± 0.3	N1	981^{+2642}_{-703}	14.1 ± 2.6
B	2716^{+3897}_{-1555}	102.3 ± 2.0	N2	537^{+1169}_{-349}	45.6 ± 0.4
-	-	-	B	2393^{+3730}_{-1443}	110.2 ± 2.1
Global	456^{+433}_{-242}	-	Global	509^{+729}_{-300}	-
J011309, $f_{\mathrm{esc}}(\mathrm{UV}) = 2.20$, Weak LCE					
B	192^{+120}_{-66}	93.9 ± 1.0	N1	422^{+457}_{-226}	73.3 ± 1.2
N	218^{+192}_{-88}	41.0 ± 0.7	B	584^{+1447}_{-376}	157.4 ± 6.2
-	-	-	N2	387^{+667}_{-222}	34.6 ± 0.9
Global	158^{+86}_{-42}	-	Global	245^{+241}_{-109}	-
J091113, $f_{\mathrm{esc}}(\mathrm{UV}) = 2.32$, Weak LCE					
B	124^{+29}_{-16}	121.2 ± 0.8	B1	119^{+26}_{-15}	104.0 ± 1.8
N	-	34.0 ± 1.2	B2	4530^{+4430}_{-2250}	239.5 ± 14.4
-	-	-	N	10797^{+2283}_{-3152}	36.5 ± 1.1
Global	205^{+56}_{-47}	-	Global	311^{+116}_{-101}	-
J012217, $f_{\mathrm{esc}}(\mathrm{UV}) = 3.76$, Weak LCE					
N	203^{+160}_{-76}	53.6 ± 0.4	N1	281^{+268}_{-133}	37.5 ± 1.9
B	1663^{+3395}_{-1112}	163.0 ± 2.8	B	1606^{+2697}_{-1000}	153.8 ± 2.2
-	-	-	N2	304^{+420}_{-157}	30.2 ± 1.6
Global	422^{+396}_{-226}	-	Global	370^{+328}_{-190}	-

[a] Component of the model.

[b] Electron density (cm^{-3}) calculated with *pyneb* using the ratio of [SII].

[c] Intrinsic velocity ($km\ s^{-1}$) dispersion of Hα (see text for details).

to take this analysis carefully, and consider the broad components electron densities values as upper-limits due to large uncertainties.

Remarkable is the case of J091113, where [SII]$\lambda\lambda$6717, 6731Å shows different profiles in comparison to the others emission-lines of the optical spectra, causing difficulties in the fitting. Here, almost no contribution of the narrower component is found, so we only consider the global measurement. Additionally, because of the red-shift of some of these objects, the [SII]$\lambda\lambda$6717, 6731Å sometimes falls into the rest-frame of telluric absorption lines, introducing uncertainties in the measured fluxes. So, caution must be taken in this detailed analysis.

The **global** contribution of the [SII]$\lambda\lambda$6717, 6731Å emission-lines shows a wide range of electron densities from $n_e > 190\ cm^{-3}$ to $n_e < 1070\ cm^{-3}$ without notorious differences between the *LCE* category. For G2 and G3 models, the determined values are well consistent within errors, which demonstrate coherence in our fitting procedure. The electron number densities of the *Izotov* sample galaxies are in good agreement with those derived by Guseva et al. (2020) using the same data, but distinct approaches of determination. We note contrasting values for J1154, but the derivation of n_e[SII] in that work was taken from n_e[OII]. Other derivations of n_e[SII] using SDSS spectra (Izotov et al., 2016b, 2018a,b) are also consistent with our global estimations.

Similar to the findings made by Hogarth et al. (2020), when we compare the individual components is noticeable that narrower ones tend to follow the global electron densities, independently of the model (G2 or G3), suggesting that these components trace a similar gas of the interstellar medium. On the other hand, the broader components greatly exceeds the global values, tracing a turbulent and and denser gas inside these galaxies. Later we will discuss a scenario where strong stellar feedback, with the contribution of supernovae events may shred this clumpier gas, enhancing the turbulence and eroding the interstellar medium.

4.4. Non-parametric analysis

The use of interpencentile range measurements allows us to compare our multi-components kinematic models with a non-parametric kinematic description by using the [OIII]λ5007Å emission-line, which provides us with information about the profile width ($FWZI$), and quantification of the asymmetry (A and K values). Here we incorporate seven galaxies observed with *ISIS* (one from *Izotov* sample and six from

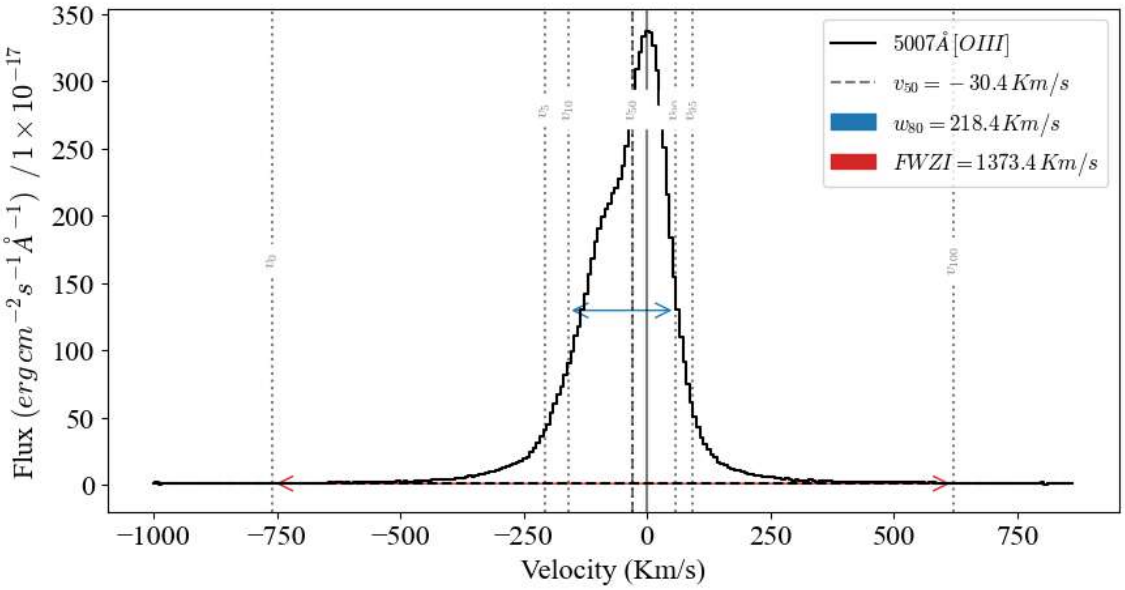

Figure 4.7: Inter-percentile analysis of the *SLCE* J0925, using the [OIII]λ5007Å emission-line. Each percentile is represented as a v_i gray dotted-line with i indicating the percentile. The full width zero intensity ($FWZI$) and the w_{80} ($v_{90} - v_{10}$) are shown as a red and blue arrow, respectively.

LzLCS sample), to have a better understanding of the involved characteristics of the emission-lines profiles from *NLCE* and *LCE*. The results are summarized in Table 4.5 and Table 4.6, while illustrative figures of the analysis for each galaxy are found in the Appendix A.

The w_{80} (i.e the line width that cover 80 % of the emission-line flux), exhibit velocities from $\sim 140 - 320\ km\ s^{-1}$. The complexity of the [OIII]λ5007Å emission-lines profiles of both, *Non-LCE* and *LCE*, produce no specific trend in compliance with this parameter. In contrast, the $FWZI$ (i.e the extension of the emission-line profile until crosses the continuum level) expands in a wide range of velocities from $\sim 580{-}1380\ km\ s^{-1}$. These values are in good agreement with those found in Hogarth et al. (2020); Bosch et al. (2019); Amorín et al. (2012b). The mentioned works suggest that high $FWZI$ velocities, which characterize the broad emission of the extended low brightness wings, are evidence of starburst-driven outflows that cause large expansion velocities. Further, we found that *NLCE* have lower $FWZI$ velocities than *WLCE*, and *SLCE*, as revealed in Figure 4.8. In addition, $FWZI$ medians for each category also show this difference, with values of $FWZI_{\rm median,NLCE} = 746.2\ km\ s^{-1}$, $FWZI_{\rm median,WLCE} = 875.1\ km\ s^{-1}$, and $FWZI_{\rm median,NLCE} = 1211.4\ km\ s^{-1}$. This indicates that stellar feedback not only may play a key role in the escape of ionizing radiation, but the strength of the driven turbulence could determine the escape of

Table 4.5: Results of the Non-parametric analysis performed on the [OIII]λ5007Å emission-line profile for the *Izotov* sample. The upper part of the table shows the galaxies observed with *X-Shooter* spectrograph, while the lower part of the table shows the galaxies observed with *ISIS* spectro-imager.

Galaxy ID	Label [a]	FWZI [b]	w80 [c]	A [d]	K [e]
J0901	Weak LCE	1244.3	186.4	-0.061	1.537
J0925	Strong LCE	1373.4	218.4	-0.192	1.352
J1011	Strong LCE	1314.6	205.6	-0.027	1.155
J1154	Strong LCE	885.6	168.1	-0.062	1.195
J1442	Strong LCE	1256.6	218.9	-0.095	1.415
J1152	Strong LCE	1166.2	307.5	-0.020	1.828

[a] Category of the galaxy according $f_{\rm esc}^{LyC}(UV)$ and significance.
[b] Full width at zero intensity ($km\ s^{-1}$).
[c] w80 ($km\ s^{-1}$).
[d] The asymmetry parameter. For a Gaussian profile $|A| = 0$.
[e] The shape parameter. For a Gaussian profile $K = 1$.

Table 4.6: Same as Table 4.5 but with *LzLCS* sampe.

Galaxy ID	Label [a]	FWZI [b]	w80 [c]	A [d]	K [e]
J003601	Non-LCE	746.2	154.9	-0.003	1.648
J004743	Weak LCE	982.0	241.7	-0.129	2.037
J011309	Weak LCE	742.6	185.0	-0.069	1.444
J012217	Weak LCE	947.2	174.5	0.028	1.394
J081409	Non-LCE	751.4	196.8	-0.045	1.281
J091113	Weak LCE	1147.8	279.9	-0.174	1.522
J095838	Weak LCE	763.6	155.7	0.081	1.327
J131037	Weak LCE	886.7	270.8	0.030	1.603
J091703	Strong LCE	987.4	320.6	-0.109	2.251
J105331	Weak LCE	813.2	265.3	-0.038	1.278
J113304	Weak LCE	636.7	139.0	0.025	1.694
J124835	Weak LCE	742.4	156.9	-0.010	1.750
J144010	Weak LCE	875.1	227.9	-0.045	1.973
J154050	Non-LCE	579.3	262.0	-0.041	1.855

[a] Category of the galaxy according $f_{\rm esc}^{LyC}(UV)$ and significance.
[b] Full width at zero intensity ($km\ s^{-1}$).
[c] w80 ($km\ s^{-1}$).
[d] The asymmetry parameter. For a Gaussian profile $|A| = 0$.
[e] The shape parameter. For a Gaussian profile $K = 1$.

ionizing radiation into the IGM.

In the lower row of Figure 4.8 we show the histograms of the shape parameter K, and the asymmetry parameter A, which are related to the kurtosis and the skewness of a Gaussian profile ($K = 1$ and $A = 0$). All the galaxies, without exception, have a shape parameter $K > 1$, thus indicating strong emission-line wings that revealed

a non-Gaussian nature. According to our data, the *NLCE* show more symmetric emission-lines ($|A| < 0.045$) when compared to the *LCE*. Additionally, 16/20 of the galaxies have an asymmetry parameter $A < 0$, related to the blue-shifted asymmetry of the emission-lines profiles. These results can be interpreted as signatures of symmetric unresolved outflows where we only see the gas that is approaching us, while the receding part may be obscured by gas and dust hosted by the galaxies, or also could be non-isotropic outflows with more complex geometry.

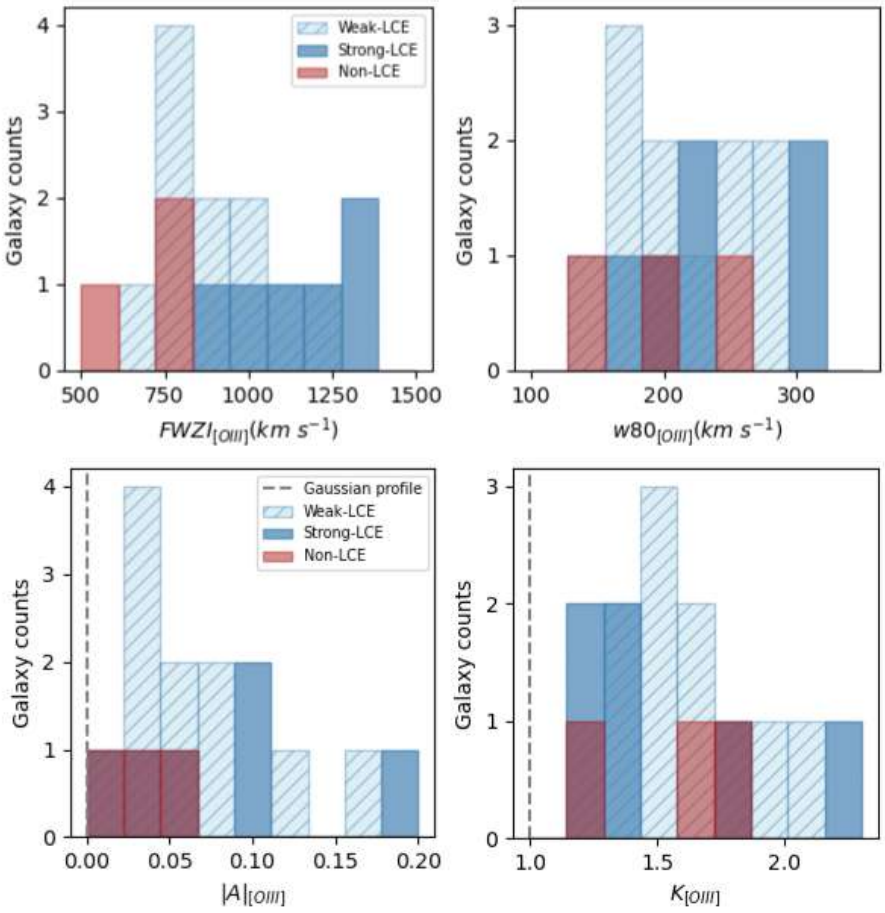

Figure 4.8: Histograms of Non-parametric values, including all the galaxies (*X-Shooter* and *ISIS*). The upper row shows the full width zero intensity ($FWZI$) and the w_{80}, related to the emission-line width. The lower row show the asymmetry parameter $|A|$ and the shape parameter K, also including the characteristic values for a clean Gaussian profile $|A| = 0$ and $K = 1$. The red bars represent *NLCE*, the blue bars represent *SLCE*, and the light blue-hatch bar represent *WLCE*. From this figure we can conclude that all galaxies show strong wings ($K > 1$), *LCE* show wider [OIII]λ5007Å emission-lines than *NLCE* (greater $FWZI$), and the *NLCE* have more symmetric emission-lines ($|A| < 0.07$).

Chapter 5

Discussions

Determine the kinematic characteristics of *LCEs* is fundamental to understand the processes which allow Lyman continuum photons to escape. Here, we propose interpretations about the kinematic status of the ionized gas inside the galaxies of our sample, using all the recompiled evidence in the previous chapters.

The separation of optical emission-lines in multiple kinematic components exhibits the complex nebular structure of the galaxies we study, showing a great variety of physical properties. Some *LCEs* galaxies need at least two well-separated ($\Delta vr \sim 60\ km\ s^{-1}$) narrow components ($\sigma_{int} < 70\ km\ s^{-1}$) to correctly fit the emissions, while the others *LCEs* can be modeled with one narrow component, and one or two broader components ($\sigma_{int} \sim 100\ km\ s^{-1}$). The latter are preferentially blue-shifted from the systemic velocity and try to model the great bump asymmetries in the global profiles ($> 40\,\%$ of the total flux), and the low surface brightness wings, respectively. On the other hand, the *NLCE* exhibit narrower and symmetrical emission-lines, with components close to the global velocity profile. However, is remarkable that all the galaxies, without exception, have a faint broad component that tries to reproduce the wings at least in the brighter emission-lines (i.e Hα, Hβ, [O III]). These kinematic features are not rare to us, and have already seen in other GPs (e.g Amorín et al., 2012b; Bosch et al., 2019; Hogarth et al., 2020).

Young star cluster complexes are typically found inside SFG at low and high redshifts (e.g Kennicutt, 1984; Jones et al., 2010; Vanzella et al., 2022), and they produce similar physical properties as those observed in the optical spectra of our sample. The diversity of kinematic components at different velocities suggests that the starburst are developed in numerous massive star-forming knots that can be associated with spatially unresolved star-forming regions displayed in the *HST COS/NUV*

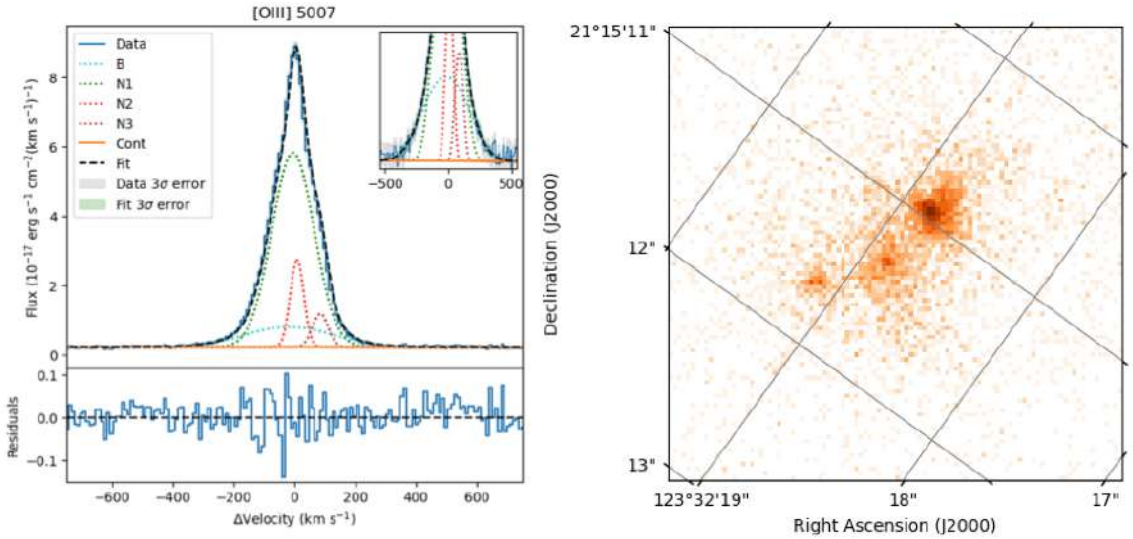

Figure 5.1: The fit of J081409 (*NLCE)*) [OIII]λ5007Å emission-line profile with four Gaussian components, and its morphology in NUV. The right panel shows the *NUV/COS* image of the galaxy in logarithmic scale, which trace young stellar populations. In the left panel, the blue line represents the observed spectra, and the dotted black line indicates the multi-Gaussian model. The local continuum fitting is shown as a solid orange line. Each fitted Gaussian component is shown as a dotted color line. B is light-blue, N1 is green, N2 is red, and N3 is brown. From the analysis in this section, we could relate the knots of star-forming regions with the narrow components, while the broad component may be related with a low surface brightness envelope of turbulent gas. We emphasize that the *COS/NUV* data trace young massive stars, but not the gas itself, so this analysis should be take carefully.

data. These images trace young stellar populations on spatial scales of the order of giant HII complexes, such as 30 Doradus or Mrk 71 (e.g Kennicutt, 1984; Micheva et al., 2017). For our objects, the *COS/NUV* images (Figure 4.3 and Figure 4.4) reveal two kinds of morphology: Six of them show a single central clump, while the other seven galaxies show at least one or two smaller substructures that are spatially separated from the main (brighter) clump. With this, we can try to relate the number of resolved clumps with the main narrow components as they contribute the greater amount of flux in the emission-line profiles.

We found that seven of the thirteen galaxies reveal a number of detected clumps/knots that matches the number of narrow components ($\sigma_{int} < 70\ km\ s^{-1}$) from the multi-Gaussian analysis performed. Following Amorín et al. (2012b) we interpret these main narrow components as the ionized gas gravitational bounded to the star-forming clumps. On the other hand, the other six galaxies (J0901, J1011, J1442, J081409, J003601, J131037) have a number of knots that mismatch from the predominant narrow components found in our kinematic analysis. Interestingly, J1011 is the only

galaxy that displays a higher number of narrow kinematic components than the number of knots revealed in the *HST COS/NUV* image. While at least two well-separated ($vr \sim 80\ km\ s^{-1}$) narrow components are necessary to describe the emission-line profiles of this object, the *COS/NUV* image does not show merger characteristics nor any indication of additional star-forming regions other than the single central knot. Similar is the case of J003601, but here the components are pretty close to the global velocity profile. In both cases, probably we are seeing the line-of-sight superposition of HII regions, as proposed in Amorín et al. (2012b). The other five galaxies (J0901, J1442, J081409, J131037), have a higher quantity of knots than narrow components, implying the presence of unresolved kinematic components. In these cases, by adding another kinematic component, the statistical measurements only improve for the brighter lines (Hα, [O III]) of J081409. Here, another narrow component emerge and can be associated with one of the star-forming regions, as shown in Figure 5.1. The velocity dispersion of the components of this model are $\sigma_{int,B} = 147.0 \pm 3.8$, $\sigma_{int,N1} = 70.3 \pm 0.7$, $\sigma_{int,N2} = 14.3 \pm 1.1$, $\sigma_{int,N3} = 26.1 \pm 2.4$, respectively. s We encourage to take this analysis carefully because the spacial structure of the ionized gas may be different to those presented in the *HST COS/NUV* images, which as said before, trace the young stellar populations, not the modeled gas.

5.1. Multi-component approach: The L-sigma relation

In our work, there is evidence that narrower components reflect the behavior of the main star-forming regions of these galaxies. When we compare the kinematic characteristics, the narrower Gaussian of the models always appears close to the peak of the emission-line, thus following the global velocity profile. Furthermore, they contribute at least half of the global flux in the emissions, and in some cases up to 80 % of the total flux. Also, the electron number densities of these components are in good agreement with the global values, while broader components have notorious differences in terms of physical properties. Hence, the narrow components may trace the main star-forming regions (clumps) that produce the gas excitation.

To prove the previous statements, we explore the well-known correlation between the emission-line luminosity and the ionized gas velocity dispersion ($L(H\beta) - \sigma_{int}$ Terlevich & Melnick, 1981). This relation traces virial motions through the gravita-

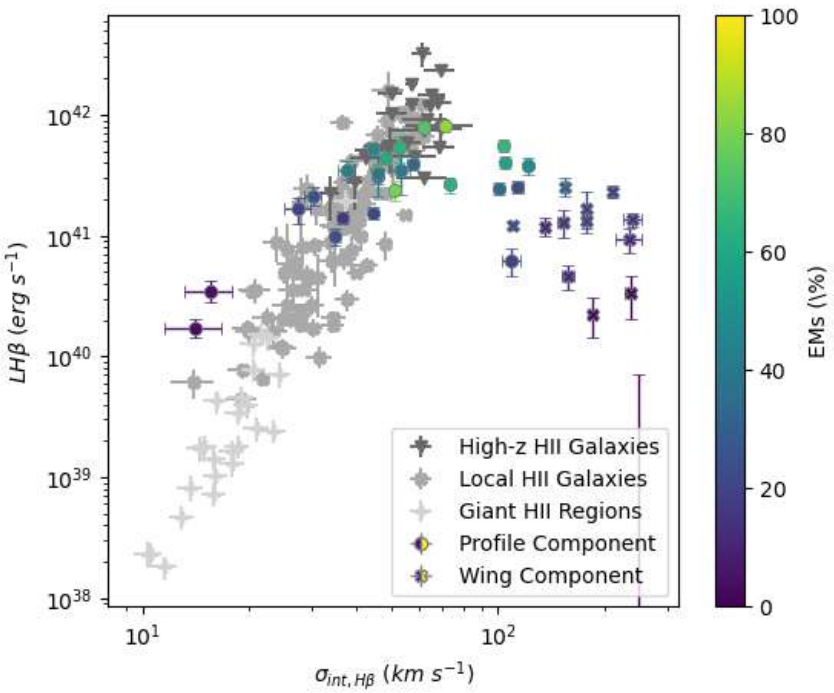

Figure 5.2: The well known $L(H\beta) - \sigma_{int}$; Terlevich & Melnick (1981), which traces virial motions in starburst. We show the location of all the individual components that compose the Hβ emission-line of the galaxies in both *LzLCS* and *Izotov* samples. The color of the individual components depends on the percentage of luminosity that contributes relative to the total luminosity of the emission-line (emission measurement). The broader components, which functionally fit the wings of the emissions are represented as crosses, while the other components are represented as circles. For comparison, we add the great sample of Terlevich et al. (2015) composed by 156 combined sources, which includes 25 high-z HII galaxies, 107 local HII galaxies, and 24 giant extragalactic HII regions, covering a final redshift range of $0 < z < 2.3$. Clearly, almost all the narrow components trace the global tendency, while the broader components have higher dispersion velocities that cannot be explained only with virial motions.

tional potential of a star-forming galaxy or giants star-forming regions. If the mass of the starburst increases, the ionizing radiation and the gas turbulence, which can be dominated by the gravitational potential of the star and gas, also increase (Krumholz & Burkhart, 2016). Thus, probing the location of multiple kinematic components of our models in the $L(H\beta) - \sigma_{int}$ relation (from here and after L-sigma relation) can be useful to test whether the virial motions are enough to explain the observed intrinsic velocity dispersion. We note that caution must be taken in this analysis since the L-sigma relation is generally used with integrate high-resolution spectra, and we are analysing individual kinematic components of our Gaussian decomposition. Therefore, we calculate the components luminosities by applying the following extinction correction to the emission-line fluxes using the *pyneb* library,

$$F_0(\lambda) = 10^{-\tau_\lambda} \cdot F_{obs}(\lambda) = 10^{(1+c(H\beta))\cdot f(\lambda)} \cdot F_{obs}(\lambda) \tag{5.1}$$

Here, $F_0(\lambda)$ is the final corrected emission-line flux, $F_{obs}(\lambda)$ is the observed flux and τ_λ is the optical depth which depends on the wavelength. Then, $c(H\beta)$ is the reddening constant, and $f(\lambda)$ is the extinction law that defines the amount of extinction as a function of the wavelength. The only parameter that we need to calculate in this expression is the reddening constant $c(H\beta)$, which can be determined by comparing the observed flux ratios between two bright hydrogen recombination lines and the predicted theoretical values (Balmer decrement),

$$\frac{I_0(\lambda)}{I_0(H\beta)} = \frac{F_{obs}(\lambda)}{F_{obs}(H\beta)} \cdot 10^{c(H\beta)\cdot[f(\lambda)-f(H\beta)]} \tag{5.2}$$

For this task, we use the theoretical expected value of the $I_0(H\alpha)/I_0(H\beta)$ ratio of 2.86 (Case B recombination, $n_e = 100\ cm^{-3}$ and $T_e = 10000\ K$; Osterbrock & Ferland (2006)). Subsequently, we obtain the global $c(H\beta)$ for each galaxy according to the observed $F_{obs}(H\alpha)/F_{obs}(H\beta)$ ratio. Despite each kinematic component may have different behavior in terms of the extinction coefficient, $c(H\beta)$, we decide to use the global $c(H\beta)$ value to avoid uncertainties when broad emissions are too faint. The corrected fluxes are determined using Equation 5.1 and assuming the (Cardelli et al., 1989) extinction law, and they are properly convert to luminosities using the expression,

$$L(H\beta) = 4 \cdot \pi \cdot D_l^2(z) \cdot F(H\beta) \tag{5.3}$$

where D_l is the luminosity distance, which is calculated with the python *astropy* package using the redshift z, and assuming a standard cosmology (see Section 1).

Finally, in order to compare the location of the individual kinematic components with other objects, we made use of the great sample of 156 sources assembled by Terlevich et al. (2015), which includes 25 high-redshift star-forming galaxies, 107 local star-forming galaxies, and 24 giant extragalactic star-forming regions, encompassing a redshift range of $0 < z < 2.33$. The extinction-corrected fluxes of the sample were transformed to luminosity using the same procedure mentioned above to be consistent. Consequently, the result of the L-sigma relation for our multi-component model fitting is shown in the Figure 5.2, also including the emission measure (percentage of the total emission) as a color gradient.

We find that narrow components fitted to our galaxies follow the L-sigma relation

of HII galaxies very well. They have $H\beta$ luminosities and velocity dispersions ($\sim$ 40 $km\ s^{-1}$) which are in agreement with those of local HII galaxies, and high-z HII galaxies (Terlevich et al., 2015), thus indicating that no additional energy input is needed to describe its virial motions.

There are six of the thirteen galaxies (all *LCEs*) that have a broad component ($\sigma_{int} \sim 100 - 120\ km\ s^{-1}$) that contribute between 20-70 percent of the global emission flux and try to model great asymmetries of the global profile. In five of these galaxies, the component is blue-shifted at least by $\Delta v_r\ -20\ km\ s^{-1}$ with respect to the global velocity profile. From the L-sigma relation, we can clearly see that their intrinsic velocity dispersion is higher than expected when compared to objects with similar luminosity, this allows us to conclude that their gravitational potential (viral motions) cannot explain the observed turbulence, so an additional broadening mechanism is required to contribute to the turbulence of the gas. In the same line, the broader components ($\sigma_{int} \sim 100 - 270\ km\ s^{-1}$), which fit the wings in all the galaxies of our sample, are even more displaced inside the L-sigma relation.

5.2. The origin of the broad components

Giant starburst regions and starburst galaxies often show broad components in nebular emission lines with velocities of several $km\ s^{-1}$. The combination of narrow and broad kinematic components has been detected in massive star-forming galaxies at high-redshift $z \sim 2$ (e.g Vanzella et al., 2022; Davies et al., 2019), in BCD (e.g Cairós & González-Pérez, 2017; Firpo et al., 2011; Izotov et al., 2007), local star-forming galaxies (e.g Westmoquette et al., 2009a), and also in giant extragalactic regions (e.g Melnick et al., 2021; Firpo et al., 2010).

Multiple broadening mechanism has been proposed as sources of turbulence to explain the origin of this broader component, which do not reflect viral motions: I) AGNs, II) stellar winds of massive stars, III) expansion of SNe remnants, IV) SNe-driven superbubble blow-up, and V) turbulent mixing layers.

The accretion of gas onto an intermediate-mass black hole could be responsible for broad emission-lines. In a large spectroscopic study of nearby BCD, Izotov et al. (2007) showed that broad emission can be fully explained by stellar photoionization, with no significant evidence of non-thermal emission produced by AGN activity. Similarly, the objects in our sample shows emission-line ratios that can be fully explained with excitation via stellar photoionization as illustrated in the diagnostic

diagrams. Also, the presence of the broader component in almost all the forbidden emission-lines is another hint that opposes the AGN as the main driver of turbulence. However, spatially resolved radio continuum and/or deep x-ray observations would be necessary to rule out any possible non-thermal source.

Alternatively, the interaction between hot starburst-driven winds and colder gas clouds can also enhance turbulent motions by producing a turbulent mixing layer (TML) on the surface of dense gas knots, which can be seen as broad components in emission-lines. Theoretical predictions shown to agree well with observations of the super star clusters enviroment of local star-forming galaxies such as M82 (Westmoquette et al., 2009b) and NGC 2363 (Binette et al., 2009). Accordingly, physical conditions of the nebulae, such as the ionization parameter (log U), affects the predictions of the TML models, changing the width of the observed components and their appearance in forbidden emission-lines, such as [N II] and [S II]. Integral field spectroscopy of a LyC emitting candidate (Bosch et al., 2019) show that two broad components reflect highly turbulent gas, which is moving likely decoupled from more ordered motions, consistent with some level of rotation, that are traced by the narrower component. The authors found a mid (broad) component that contributes with a great percentage of the total flux line and shows similar radial velocity patterns as the narrower one. However, when they compare the velocity dispersion map of this mid component, it clearly follows the dispersion map of the broader one, which functionally fits the low surface brightness extended wings of the emission-line profiles. These results suggest that the mid (broad) component originates from an external layer of gas that follows the overall rotational movement and interacts directly with the outflow (TML). Similarly, Hogarth et al. (2020) also attribute the mid (broad) component with TML as an alternative explanation to that of multiple unresolved HII regions as the broadening source. In this context, five of the six broad components in our models, that do not fit the wings of the emission-lines (see Figure 5.2), have negative velocity shifts (radial velocities), suggesting to be gas that is approaching us, and four of that six broad components are closer ($< 20\ km\ s^{-1}$) to the radial velocity of the narrower component, tracing a similar gas kinematic as in the case of Bosch et al. (2019). Hence, we hypothesize that TML could be the mechanism that produces the enhancement of turbulence in these components. However, this hypothesis is difficult to evaluate with only integrated long-slit spectra, and a spatially resolved analysis should be required to evaluate this in deeper detail.

Recent star formation activity and its associated stellar feedback driven by the

evolution of massive stars and supernovae (SNe) can increase the gas turbulence by injecting mechanical and radiative energy (Izotov et al., 2007). At lower spatial scales, Melnick et al. (2021) found that the wind produced by the cluster in 30 Doradus powers most of the turbulence, with a small contribution from the gravitational potential of stars and gas. More recently, Komarova et al. (2021) have demonstrated that radiation-power winds can also be responsible of originating such broad emission before the onset of SNe, and can be modeled with a power-law. Still, our evidence suggest that the radiation-driven feedback is not the main driven source of turbulence in the galaxies of our sample as in case of Mrk71 and the GP J1219+1526 (Komarova et al., 2021). The broad components in our models are slower ($FWZI < 6000\ km\ s^{-1}$) than the observed in the mentioned work, and contribute a greater percentage of the global emission-line fluxes. Of course, radiation may contribute a significant part to the observed turbulence, but it seems is not the principal source.

The kinematic analysis and the physical characteristics of the galaxies in our sample, such as its compactness and high specific star formation rate, indicate that stellar feedback and SNe may contribute the greatest part of the observed gas dispersion of the broader component (the one that fit the wings) observed in both forbidden and permitted lines. Indeed, this broad emission is blue-shifted in 10 out of 13 galaxies, suggesting an unresolved outflow, and enhancing the asymmetry of the global profiles. Furthermore, if strong stellar winds were the only source for this emission we would expect Hαemission-line luminosities of the order of $\sim 10^{37} - 10^{39}\ erg\ s^{-1}$ (Izotov et al., 2007). However, we found larger values for these components ($\sim 10^{41}\ erg\ s^{-1}$), which are in the range of emissions likely produced by SNe feedback. Assuming the last, shocks produced by young SNe remnants may contribute significantly to the turbulence of the ionized gas. According to Ho et al. (2014), these shock contributions can be seen as broad components with higher ratios of [N II],[S II],[O I] vs Hαin the diagnostic diagrams and higher values of electron density, which coincide with the properties of the component that we find (Figure 4.5, Table 4.3 ,Table 4.4). Hence, the contribution of strong stellar feedback and shocks of SNe remnants are likely the mechanisms that input energy in the turbulent ionized gas of these star-forming galaxies and is evidenced in the large velocity dispersion of some components, the large emission-line profile asymmetries, the large velocities of $\sim 1000 km\ s^{-1}$ as those measured from our non-parametric results (FWZI), and all the physical properties that we determine. However, a more extreme contribution of multiple SNe as the superbubble phenomenon appear unlikely as the mechanism to explain for the broad

emission, because the expansions velocities produced by these mechanism are generally higher than those found in our work, in the order of many thousands of $km\ s^{-1}$ (Roy et al., 1992).

These support a scenario where the narrow emission comes from high ionization gas in the inner parts of the massive star-forming regions, while the broader emission may come from clumpy and dense interstellar material that is being shredded by powerful outflows driven by the strong massive star winds and/or energetic outflows from supernovae events. According to this, we suggest that the broad component may trace low-ionization low-filling factor turbulent channels, through where Lyman continuum photons can escape (Ramambason et al., 2020). In the next section, we present how the escape fraction of ionizing radiation correlates with the intrinsic velocity dispersion and the width of the emission-line profiles.

5.3. Ionized gas kinematics and the escape of LyC radiation

Given the characteristics of *LCEs* is expected that stellar feedback plays a key role in the leakage of ionizing radiation. Hydrodynamical simulations of galaxy evolution have demonstrated this, showing that Lyman continuum photons escape through turbulence-generated low column density channels that are evacuated efficiently by radiative feedback before the onset of SNe (Kakiichi & Gronke, 2021), or after SNe events that inject turbulence and mechanical energy in the interstellar medium (e.g. Kimm et al. (2019); Trebitsch et al. (2017); Ma et al. (2016)). Observationally, it have been proved that the outflow kinematics of *LCEs* traced by UV absorption lines may not be extreme and different from other star-forming galaxies (Chisholm et al., 2017). Already mentioned studies (Komarova et al. (2021), Hogarth et al. (2020), Bosch et al. (2019),Amorín et al. (2012b)) show that *LCEs* candidates have clear imprints of highly turbulent ionized gas and outflows in form of broad emissions in both permitted and forbidden emission-lines. Still, a detailed analysis of the ionized kinematics and the physical properties of confirmed *LCEs* and a comparison with those of non-LCEs, has not been performed yet. Thus, looking for differences in the turbulent nature of the interstellar medium and the presence of strong outflows in *LCEs* and *NLCE* is crucial to understanding how the process of feedback affects the leakage of Lyman continuum photons and their implications in the early evolution

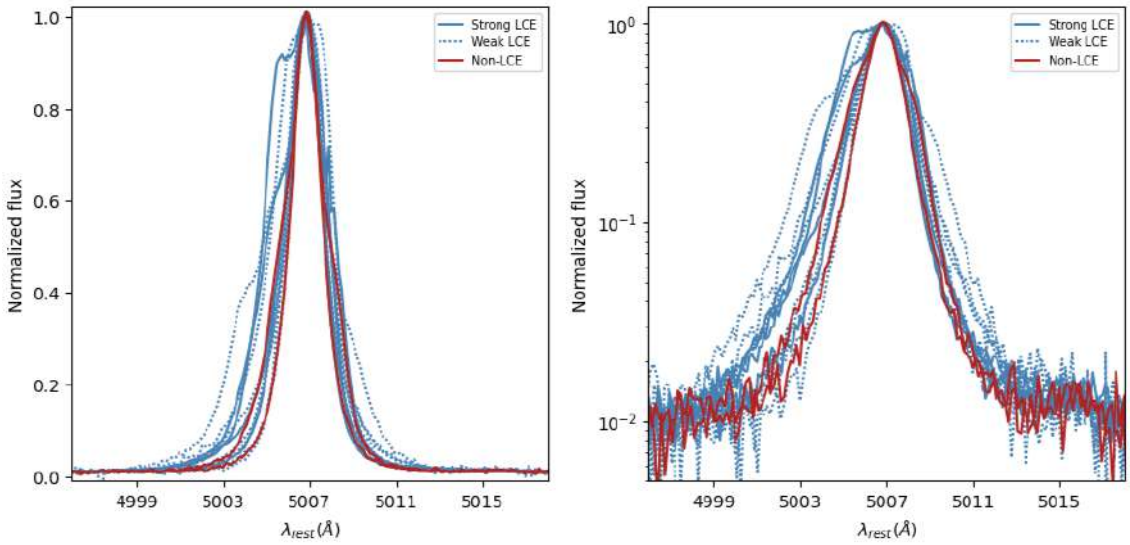

Figure 5.3: The normalized [OIII]λ5007Å emission-line profiles of the *Izotov*, and the *LzLCS* galaxies that we previously studied, whose spectra were obtained with *X-Shooter* instrument. The left figure is in linear scale, while the right figure is in logarithmic scale to see the bottom-line details. Here we subtract the local continuum, normalized to the maximum, and then added a pedestal to avoid uncertainties in the logarithmic visualization. The colors represent the different categories discussed in Section 3, where we use the escape fraction determined by the UV continuum fitting. The red solid line indicates the *NLCE* (2 galaxies), the light blue dashed line is the *WLCE* (6 galaxies), and the blue solid line represents the *SLCE* (5 galaxies). In both panels is clear that *NLCE* show narrower global profiles than *WLCE*, and *SLCE*.

of the universe.

Our study finds clear kinematic differences between *NLCE*, and both *WLCE* and *SLCE*. The multi-component Gaussian decomposition shows a broad component fitting the low-surface brightness extended wings in all the objects, which is broader at *SLCE*. Furthermore, the non-parametric inter-percentile analysis of the [OIII]λ5007Å emission-line also gives us valuable information about the dynamical status of these starburst galaxies. Similar to the mentioned result, the maximum velocity of the line profiles (FWZI) is larger in *LCEs*, reaching values $> 1000\ km\ s^{-1}$. Also, we find that *NLCE* have more symmetric profiles ($A \sim 0$) than the *LCEs*, which have significant asymmetries to the blue-side of the emission-lines ($A < 0$). All these hints and the derived physical properties of the kinematic components point to the interpretation that outflows are likely driven by stellar feedback, where massive star winds and radiation in the first few Myr after the onset of the recent starburst and the mechanical energy from SNe at slightly older ages ($\gtrsim 4$ Myr) have the collective effect of eroding the local interstellar medium and facilitate the escape of ionizing radiation. Motiva-

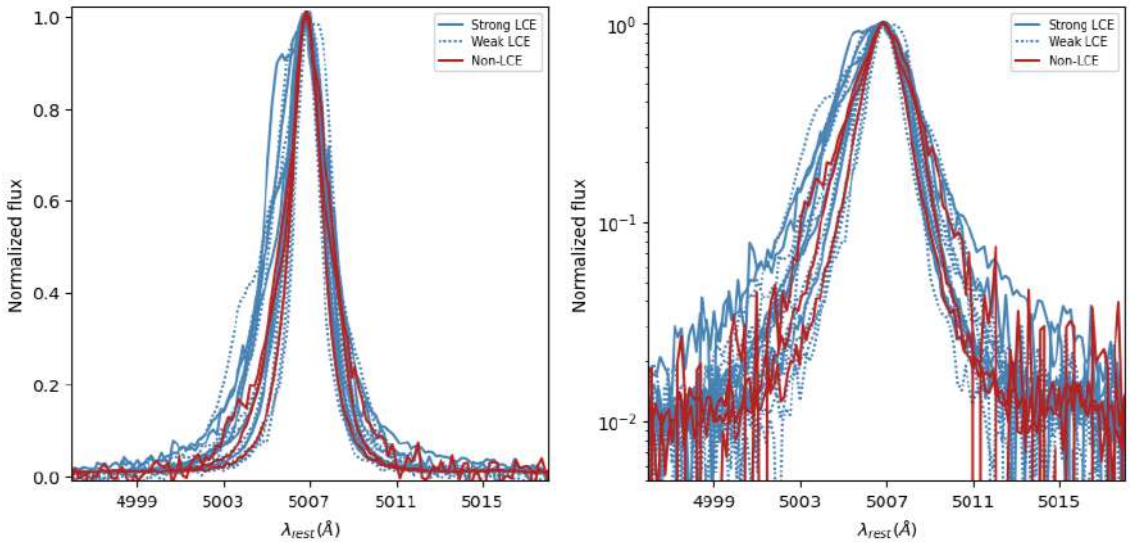

Figure 5.4: Same as Figure 5.3, but including seven more galaxies obtained with the *ISIS* spectro-imager. The total sample includes 3 *NLCE*, 11 *WLCE*, and 6 *SLCE*.

ted by this premise, we use the homogenized set of physical properties and redshifts presented in Flury et al. (2022b) to investigate for the first time how the ionized gas kinematics is related to the escape of Lyman continuum photons and some of the most important physical properties of *NLCE* and confirmed *LCEs* galaxies in order to strengthen our hypothesis, and if it is possible, give another indirect indication of Lyman continuum leakage to use at low and high redshifts.

Figure 5.3 shows the normalized [OIII]λ5007Å emission-line profile (at rest wavelength) of all the galaxies observed with the *X-Shooter* instrument, illustrating clear differences between galaxies in each *LCEs* category.

The categories were defined by considering the escape fraction of the UV continuum fitting (see Section 2.2). Thus, the line profiles of *NLCE*, *WLCE*, and *SLCE* are represented as a red solid line, a blue dotted line, and a blue solid line, respectively. The left panel shows the normalized emission line intensity in linear scale, while the right panel shows them in logarithmic scale in order to highlight the shape of the emission line wings. Similarly, in Figure 5.4 we show all the galaxies in our sample, includying the seven galaxies observed with *ISIS* (one from *Izotov* sample and six from *LzLCS* sample). These galaxies will be considered from now on in the analysis. Clearly, in both figures the *NLCEs* show narrower profiles than both *WLCEs* and *SLCEs*. Further, almost all the galaxies have blue-shifted asymmetries, but the *LCEs* have the most extended and complex emission-lines. This results suggest a possible

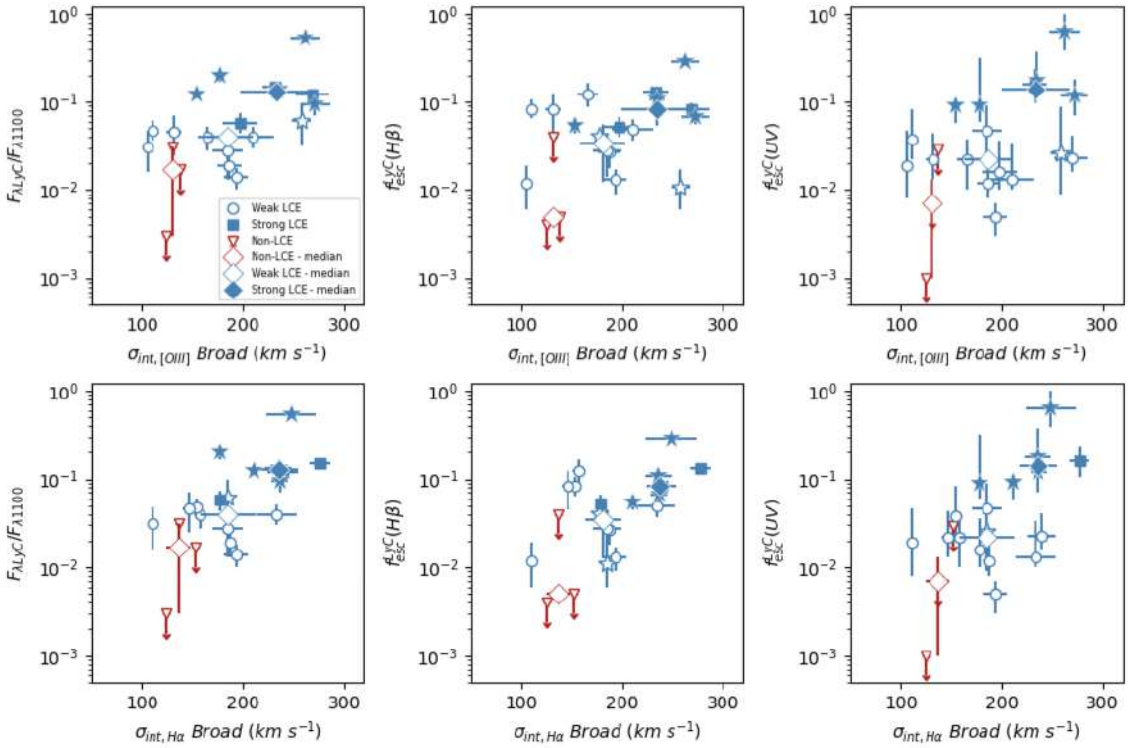

Figure 5.5: Behavior of the intrinsic velocity dispersion of the broader component in our multi-Gaussian models for Hα and [OIII]λ5007Å, respect to the three metrics of Lyman continuum leakage. The *NLCE* are represented as red open triangles, the *WLCE* as blue open circles, and the *SLCE* as blue filled squares. The objects of the *Izotov* sample are shown as stars, and correspond to the highest escape fractions in this work. Also, we include the medians values for each category as diamonds to better visualize if there is any trend. Broad emission show a good correlation with the escape of ionizing radiation.

relation between the level of leakage and the shape of the [OIII]λ5007Å emission-line profile.

We probe this in Figure 5.5, where we present the most important result of our investigation: a clear correlation between the intrinsic velocity dispersion of the broader component of [OIII]λ5007Å (upper panel) or Hα (bottom panel), and the LyC escape fraction (f_{esc}^{LyC}). The latter is represented using the three metrics presented by Flury et al. (2022a). In both panels, we show the *NLCEs* as red open triangles, the *WLCEs* as a blue open circles, and the *SLCEs* as filled squares. The *Izotov* objects are represented as stars, which represent the majority of strong leakers in our study. We also include the median values for each category to probe the global tendency. In this correlation the strongest leakers show a median velocity dispersion of $\sigma_{int,broad} > 220\ km\ s^{-1}$ and the non-leakers show in all cases $\sigma_{int,broad} < 150\ km\ s^{-1}$. This provide new observational evidence supporting predictions of models and si-

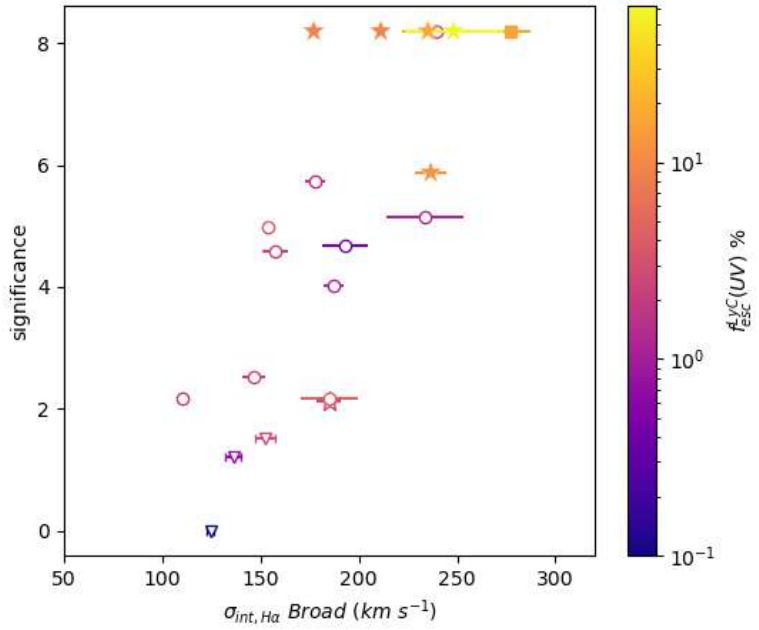

Figure 5.6: The correlation between the significance and the intrinsic velocity dispersion of the broader component in Hα.The significance is defined as the range of confidence (in σ) that the detection of Lyman continuum photons do not arises by chance from background fluctuations. In the figure, the *NLCE* are shown as open triangles, the *WLCE* are open circles, and the the *SLCE* are filled squares. The objects of the *Izotov* sample are represented as stars. Finally, the colors exhibit the escape fraction of ionizing radiation determined by UV continuum fitting. There is a tight correlation between the detection of Lyman continuum photons, and the broadening of the component that fits the emission-line wings, which we relate to outflows driven by stellar feedback.

mulations (e.g Trebitsch et al., 2017; Kakiichi & Gronke, 2021), which exhibit that ongoing starburst and their related mechanical and radiative feedback produce gas turbulence and outflows that play a key role in clearing channels throughout which ionizing radiation escape to the intergalactic medium. We note that the intrinsic velocity dispersion of the broad component of the recombination line Hα introduce less scatter in the relation than that of [OIII]λ5007Å. While the number of galaxies is small and not uniform for each category and the scatter is relatively large, the relations in Figure 5.5 appear solid against the emission line and the metric considered for the LyC escape fraction.

5.4. Non-parametric indicators and the escape of LyC radiation

The non-parametric analysis allow us to compare the objects that leaks ionizing radiation and those who do not, in terms of the the width and the shape of its brighter optical emission-line. Here we found a clear relation between the width of the [OIII]λ5007Å emission-line at the continuum level (FWZI) and the escape fraction of the ionizing photons, which gets weaker with the escape fraction determined by Hβ. This trend is expected from the histogram (see Figure 4.8) where *NLCE* have narrower widths than *LCEs*, and also from the correlation of the intrinsic velocity dispersion of the broader component that trace the extension of the wings of the emission-lines. The FWZI is independent of any model and is related to the maximum expansion velocity for an accelerated gas. The values we measure for the [O III] emission-lines are in agreement to the terminal velocities associated with the following circumstellar gas (stellar winds) of massive young massive star such as WR, LBV and OB (Izotov et al., 2007). Thus, strengthen the evidence of stellar-feedback as the turbulence main driver.

Differently, the $w80$ ($|v_{90} - v_{10}|$) parameter show complex behavior with f_{esc}^{LyC}, with a larger scatter (Figure 5.7) in comparison with the FWZI. We associate the lack of trend with the fact that both *NLCEs* and *LCEs* have low-flux extended wings ($K > 1$) that are not considered in the 10th and 90th percentiles. Thus, the w80 is similarly distributed around to the peak (global velocity profile) for both categories. In contrast, if we consider the the extension of all the wings (i.e FWZI) we find clear differences as shown before.

There is a clear trend of the *NLCEs* to be more symmetric ($A \sim 0$) than the *LCEs*. In fact, the *SLCEs* show the largest asymmetries and the broader components of the sample (Figure 5.7). Finally, we find that all the galaxies in our sample have non-Gaussian wings according to the K parameter (i.e. $K > 1$), independently of their escape fractions. This result may reflect the fact that these wings are shaped by the level of turbulence present in the environs of any young starburst, and they are not sufficient to distinguish if the galaxies are optically thin or thick to the LyC photons.

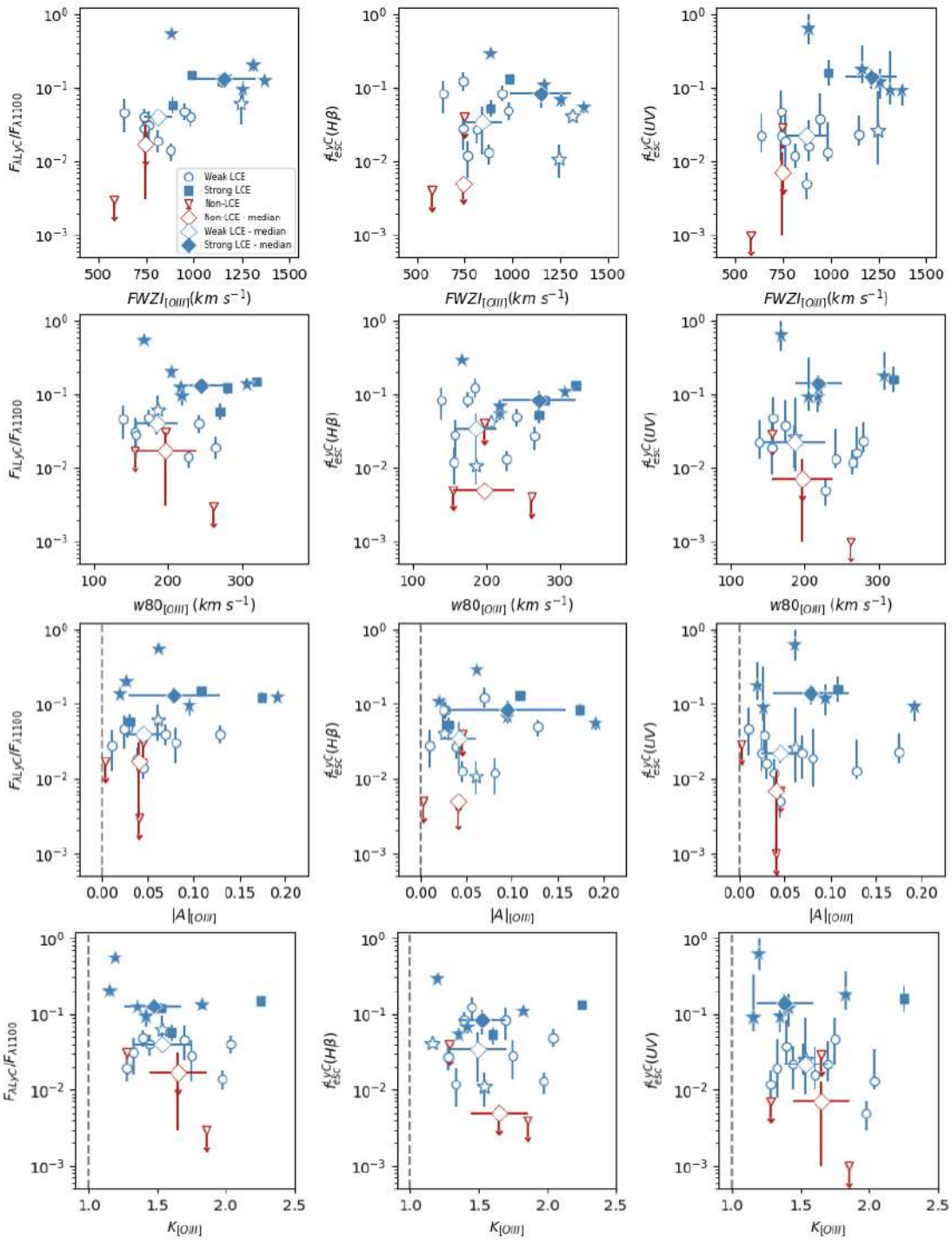

Figure 5.7: Same as Figure 5.5 but considering the results of the inter-percentile analysis of the [OIII]λ5007Å emission-line. The rows show the relation of the metrics of LyC and the full width zero intensity (FWZI), the w80, the asymmetry parameter (A), and the shape parameter (K), respectively. Also, for A and K is shown the typical values for Gaussian profiles as a gray dashed line.

5.5. Ionized gas kinematics and physical properties of the galaxies

Many efforts have been accomplished to characterize LCEs and find observable properties to determine the escape of Lyman continuum radiation indirectly. Existing trends suggest that a combination of concentrated star formation and line-of-sight effects play pivotal roles in the detection of ionizing photons. Mechanical and radiative feedback from compact young star cluster complexes in galaxies with high SFR densities (ΣSFR; star formation per unit of area) can shape the interstellar medium and clear paths along Lyman continuum can escape (Heckman et al., 2011). Similarly, a low neutral gas density, which is opaque to this radiation, also favor the process of leakage. The latter phenomena can be traced with the emission-line ratio $[OIII]\lambda5007$Å$/[OII]\lambda3727$Å (O_{32}; Izotov et al., 2018b), where high values indicate that the ISM is predominantly ionized like in density-bounded regions (Jaskot & Oey, 2013). Similarly, the Lyα emission is closely related to LyC and give a unique opportunity to study the leakage of ionizing photons, because at relative low amounts of HI (low column density) both radiations are suppressed, and recombination lines are reprocessed Lyman continuum in hydrogen atoms. Indeed, Lyα is bright and easy to observed in low-metallicity starburst galaxies, often with double-peaked emission due to the blue and red-shifted components relative to the systemic velocity. While the blue-shifted component is fainter than the red-shifted peak, their peak separation is proportional to the hydrogen column density (Verhamme et al., 2015). Izotov et al. (2018b) found a clear anti-correlation between the peak separation and f_{esc}^{LyC}, and later confirmed in Izotov et al. (2021), showing that small peak separations ($v_{sep} < 450\ km\ s^{-1}$) are a good indirect indication of LyC leakage. On global scales, the Lyα EW (EW Lyα) and the escape fraction of Lyα ($f_{esc}^{Ly\alpha}$) also correlate with f_{esc}^{LyC} (Saldana-Lopez et al., 2022; Gazagnes et al., 2020; Steidel et al., 2018). Nevertheless, all these correlations between global physical properties and Lyman continuum leakage show large scatter (Flury et al., 2022b). Perhaps more importantly, the fact that quantitites related to Lyα are the best predictors of LyC escape makes difficult any search and quantification of reionization galaxies at $z > 6$, where the opacity of the IGM makes extremely challenging the detection of Lyα emission.

Recently, Flury et al. (2022b) confirmed the statistical significance of the above trends using the largest sample of 89 galaxies at $z < 0.4$ from the LzLCS, and

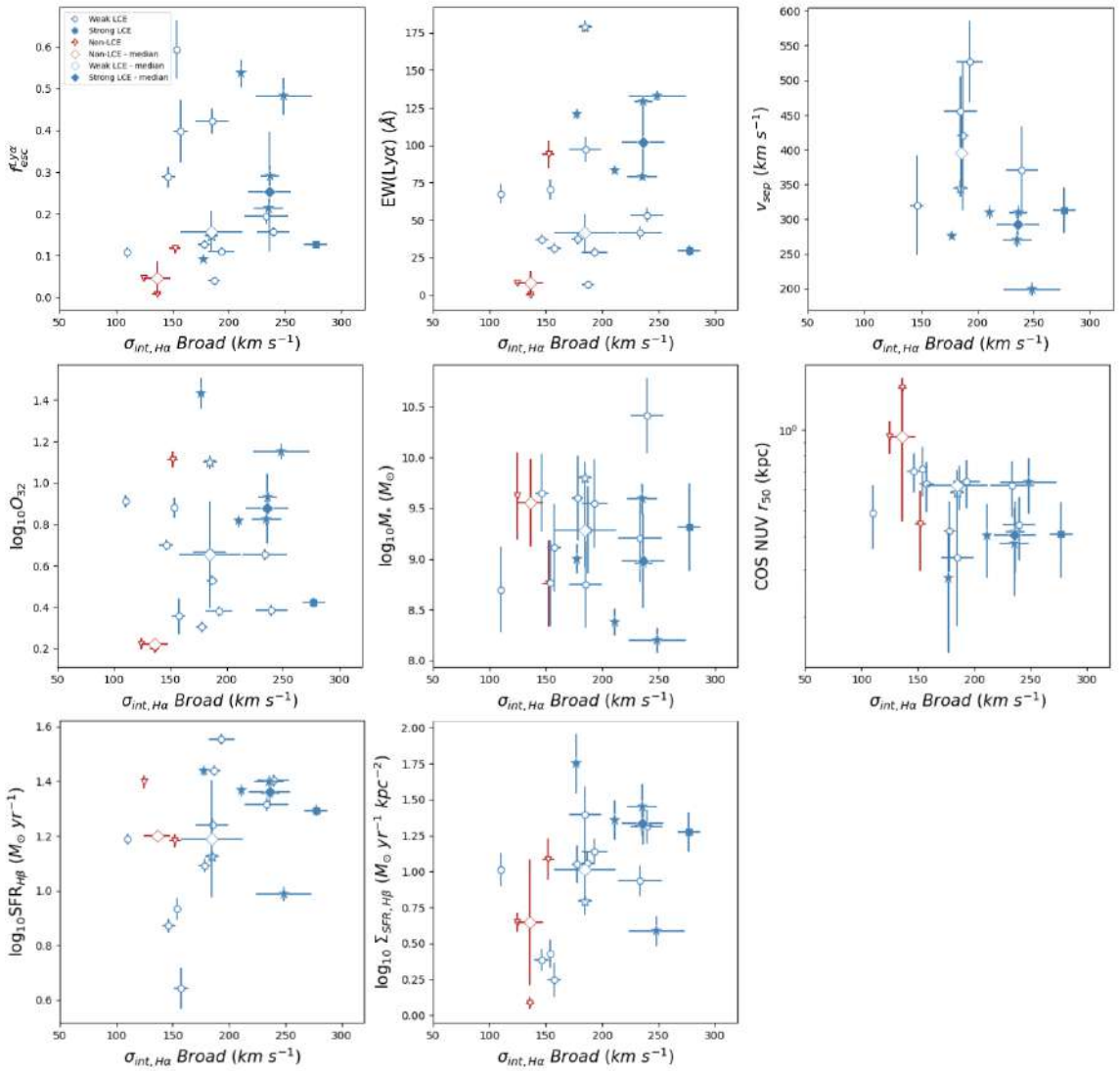

Figure 5.8: Relations of the intrinsic velocity dispersion of the broader component in Hα emission-line model and important physical properties of the galaxies such as the escape fraction of Lyα ($f_{esc}^{Ly\alpha}$), the equivalent width of Lyα (EW LYα), the peak separation of LYα (v_{sep}), the O_{32} ratio ($\log_{10}O_{32}$), the stellar mass ($\log_{10}M_*$), the NUV half light radius (COS NUV r_{50}), the star forming rate measured from Hβ ($\log_{10}SFR_{h\beta}$), and the star forming density ($\log_{10}\Sigma SFR_{h\beta}$). The symbols represent the same than in Figure 5.7.

demonstrated that objects with larger escape fractions are predominantly the ones showing more compact morphology and higher star formation per unit area (low COS NUV r_{50}, high ΣSFR). These objects typically show a highly ionized ISM (i.e. higher O_{32} ratio), and more transparent line-of-sight (i.e. higher EW Lyα, higher $f_{esc}^{Ly\alpha}$, and lower $v_{sep} < 250\ km\ s^{-1}$). Using the properties derived by the *Low-z Lyman Continuum Survey* in Flury et al. (2022a,b), we investigate the relation

between the ionized gas kinematics and other relevant global physical properties of the galaxies in our sample.

Figure 5.8 shows the relation of the intrinsic velocity dispersion of the broader component in our Gaussian models for the Hα emission-line profile and the following physical properties: stellar mass ($\log_{10}M_*$), SFR and SFR per unit area (Σ_{SFR}) derived from the extinction-corrected Hβ luminosity ($\log_{10}$ SFR$_H\beta$), ionization parameter (traced by the O_{32} ratio), NUV half-light radius (r_{50}), and the Lyα EW, $f_{\rm esc}$ and peak separation ($v_{\rm peak}$). As expected, the properties regarding the Lyα emission show trends with the ionized gas kinematic, as they correlate with the escape fraction of ionizing radiation. While large scatter remains in these relations, we do not find *NLCEs* with high escape of Lyα radiation, which indicates that line-of-sight effects have a great impact in both emissions (LyC and Lyα) to escape. From all the other properties we highlight the relation between the star formation surface density (Σ_{SFR}) and the velocity dispersion of the broad emission, which evidence that the compactness of the star formation development is related to grade of turbulence observed in the ionized gas. More details about the correlations are shown in the following section.

5.6. Statistics and implication of the correlations

To be consistent with other works of the *Low-z Lyman Continuum Survey* collaboration (e.g Marques-Chaves et al. (2022); Xu et al. (2022) ;Saldana-Lopez et al. (2022); Flury et al. (2022b); and quantify if there is any trend, we compute the Kendall-τ rank correlation coefficient following the Akritas & Siebert (1996) prescription for censored data to account for the upper limits on f_{esc}^{LyC} of the *NLCE* which were calculated considering the 1σ upper limit on the Lyman continuum flux density for all the metrics. This quantification give us two parameters, τ which provides information about the strength of the correlation, and p, which is the probability that the measured τ is consistent with the null hypothesis that there are no correlation between the variables. Hence, for a sample of 20 objects (*X-Shooter* and *ISIS* galaxies) we consider that there is a significant correlation with 2σ confidence if $p < 2.275 \times 10^{-2}$, and $|\tau| \geq 0.261$, while a weak correlation with 1σ confidence correspond to values of $p < 1.587 \times 10^{-1}$, and $|\tau| \geq 0.162$.

The values of the coefficients for the intrinsic velocity dispersion of the broader component are reported in the Table 5.1, and show a strong correlation ($p <$

Table 5.1: Kendall-τ coefficients for the three metrics of Lyman continuum leakage ($F_{\lambda LyC}/F_{1100}$, $f_{esc}^{LyC}(H\beta)$ and $f_{esc}^{LyC}(UV)$) respect to the intrinsic velocity dispersion of the broader component in our models (for Hα and [OIII]λ5007Å), and the coefficient values from the inter-percentile analysis performed to the [OIII]λ5007Å emission-line (FWZI, w80, the asymmetry parameter (A), and the shape parameter (K)). We consider a significant correlation if $p < 2.275 \times 10^{-2}$, and $|\tau| \geq 0.261$, while a weak correlation correspond to values of $p < 1.587 \times 10^{-1}$, and $|\tau| \geq 0.162$.

	$F_{\lambda LyC}/F_{1100}$		$f_{esc}^{LyC}(H\beta)$		$f_{esc}^{LyC}(UV)$	
	τ	p	τ	p	τ	p
$\sigma_{int,H\alpha-\text{Broad}}$	$0.458^{+0.121}_{-0.121}$	4.763×10^{-3}	$0.426^{+0.121}_{-0.127}$	8.589×10^{-3}	$0.432^{+0.121}_{-0.122}$	7.804×10^{-3}
$\sigma_{int,[\text{OIII}]-\text{Broad}}$	$0.363^{+0.093}_{-0.098}$	2.518×10^{-2}	$0.247^{+0.128}_{-0.136}$	1.273×10^{-1}	$0.316^{+0.104}_{-0.121}$	5.158×10^{-2}
$\text{FWZI}_{[\text{OIII}]}$	$0.500^{+0.094}_{-0.073}$	2.055×10^{-3}	$0.195^{+0.128}_{-0.112}$	2.300×10^{-1}	$0.368^{+0.076}_{-0.080}$	2.314×10^{-2}
$\text{w80}_{[\text{OIII}]}$	$0.195^{+0.154}_{-0.135}$	2.300×10^{-1}	$0.174^{+0.152}_{-0.153}$	2.843×10^{-1}	$0.063^{+0.121}_{-0.127}$	6.970×10^{-1}
$\lvert A\rvert_{[\text{OIII}]}$	$0.226^{+0.130}_{-0.132}$	1.630×10^{-1}	$0.132^{+0.120}_{-0.136}$	4.173×10^{-1}	$0.042^{+0.106}_{-0.111}$	7.952×10^{-1}
$\text{K}_{[\text{OIII}]}$	$-0.153^{+0.174}_{-0.167}$	3.468×10^{-1}	$-0.005^{+0.148}_{-0.139}$	9.741×10^{-1}	$-0.084^{+0.169}_{-0.152}$	6.037×10^{-1}

8.589×10^{-3} and $|\tau| > 0.432$) between the broader components in Hα and the three metrics of measurement for Lyman continuum leakage, which is in agreement with the Figure 5.5. On the other hand, the broader components of the [OIII]λ5007Å show weaker correlations reflected in good values of $|\tau| \geq 0.261$, but with a lower range of confidence between 2σ and 1σ ($2.275 \times 10^{-2} < p < 1.587 \times 10^{-1}$). Also, because the category of *LCEs* depends on the probability that the Lyman continuum emission do not come from background fluctuations (significance), we investigate its relation with the intrinsic velocity dispersion of the broad component Hα in the Figure 5.6 for the Hα emission-line, while the Kendall-τ coefficients for both principal emission (including [OIII]λ5007Å) are in the Table 5.2. This parameter have the strongest correlation with the intrinsic velocity dispersion of the broader emission component ($p < 1.907 \times 10^{-4}$ and $|\tau| > 0.606$), indicating that the detection of ionizing radiation have a great dependence on the identification of extended wings in emission-line profiles. Moreover, the galaxies that have greater confidence of detection in Lyman continuum photons (significance > 6) show the highest values of escape fractions.

From the non-parametric analysis, the greatest correlation we find is between the width of the [OIII]λ5007Å emission-line at the continuum level (FWZI) and the escape fraction of the ionizing radiation (Figure 5.7, Table 5.1) with 2σ of confidence. Clearly, *NLCEs* have narrower widths than *LCEs*, which is in agreement with the correlation of the intrinsic velocity dispersion of the broader component. On the other hand, there is no clear correlation between $w80$ and the escape fraction of LyC. In this case, the τ and p values do not satisfy any requirement with any of the

Table 5.2: Kendall-τ coefficients for intrinsic velocity dispersion of the broader component in our models (for Hα and [OIII]λ5007Å), and some of the most important physical properties of the galaxies (for details see Section 2.2.2). We consider a significant correlation if $p < 2.275 \times 10^{-2}$, and $|\tau| \geq 0.261$, while a weak correlation correspond to values of $p < 1.587 \times 10^{-1}$, and $|\tau| \geq 0.162$.

	$\sigma_{int,\mathrm{H}\alpha-\mathrm{Broad}}$		$\sigma_{int,[\mathrm{OIII}]-\mathrm{Broad}}$	
	τ	p	τ	p
significance	$0.605^{+0.083}_{-0.077}$	1.907×10^{-4}	$0.437^{+0.121}_{-0.108}$	7.084×10^{-3}
$f_{esc}^{Ly\alpha}$	$0.263^{+0.129}_{-0.121}$	1.048×10^{-1}	$0.189^{+0.160}_{-0.143}$	2.428×10^{-1}
EW($Ly\alpha$)	$0.200^{+0.123}_{-0.141}$	2.176×10^{-1}	$0.274^{+0.098}_{-0.114}$	9.158×10^{-2}
v_{sep} [a]	$-0.167^{+0.167}_{-0.163}$	4.507×10^{-1}	$-0.136^{+0.143}_{-0.143}$	5.371×10^{-1}
$\log_{10}O_{32}$	$0.095^{+0.130}_{-0.153}$	5.592×10^{-1}	$0.084^{+0.130}_{-0.147}$	6.037×10^{-1}
$\log_{10}M_*$	$-0.011^{+0.154}_{-0.154}$	9.483×10^{-1}	$0.189^{+0.168}_{-0.145}$	2.428×10^{-1}
COS NUV r_{50}	$-0.289^{+0.123}_{-0.123}$	7.435×10^{-2}	$-0.279^{+0.129}_{-0.121}$	8.551×10^{-2}
$\log_{10}\mathrm{SFR}_{H\beta}$	$0.211^{+0.112}_{-0.109}$	1.944×10^{-1}	$0.158^{+0.104}_{-0.114}$	3.304×10^{-1}
$\log_{10}\ \Sigma_{\mathrm{SFR},H\beta}$	$0.316^{+0.121}_{-0.126}$	5.158×10^{-2}	$0.242^{+0.103}_{-0.140}$	1.356×10^{-1}

[a] There are only 12 galaxies with v_{sep} measurement. The ideal τ and p values depends on number of data points.

metrics of ionizing radiation leakage.

The asymmetry parameter (A) show great scatter (Figure 5.7), but still a weak correlation with the escape fraction. While the τ and p are barely satisfied for the $F_{\lambda LyC}/F_{\lambda 1100}$ metric, there is a notorious tendency of the *NLCEs* to be more symmetric ($A \sim 0$) than the *SLCEs*. Finally, we do not find correlation between the shape parameter (K) and escape fractions, which is in accordance that all the galaxies in our sample have non-Gaussian wings (i.e. $K > 1$).

Regarding the correlations between the physical properties of the galaxies and the ionized gas kinematics our statistical analysis based on the Kendall-τ coefficients (Table 5.2) show three physical properties that do not have significant correlation with neither the Hα nor the [OIII]λ5007Å broader component emission.

One of these properties is the stellar mass, which is highly scattered and does not correlate with escape fraction (Izotov et al., 2021). According to the median values, galaxies with larger O_{32} ratio tend to have broader lines, but the relation exhibits a large scatter.

There is only one *SLCE* that has a relatively low O_{32} compared to the others *SLCE*. Yet, Izotov et al. (2021) established that this property has a weak dependence on f_{esc}^{LyC}. Finally, the SFR-related quantities also show large scatter, with a less evident dependence on *LCEs* category. Only if we consider the star formation rate density, that is the SFR normalized by the area encircled by the UV emitting region (i.e. area where massive stars are being formed) we obtain a correlation (between

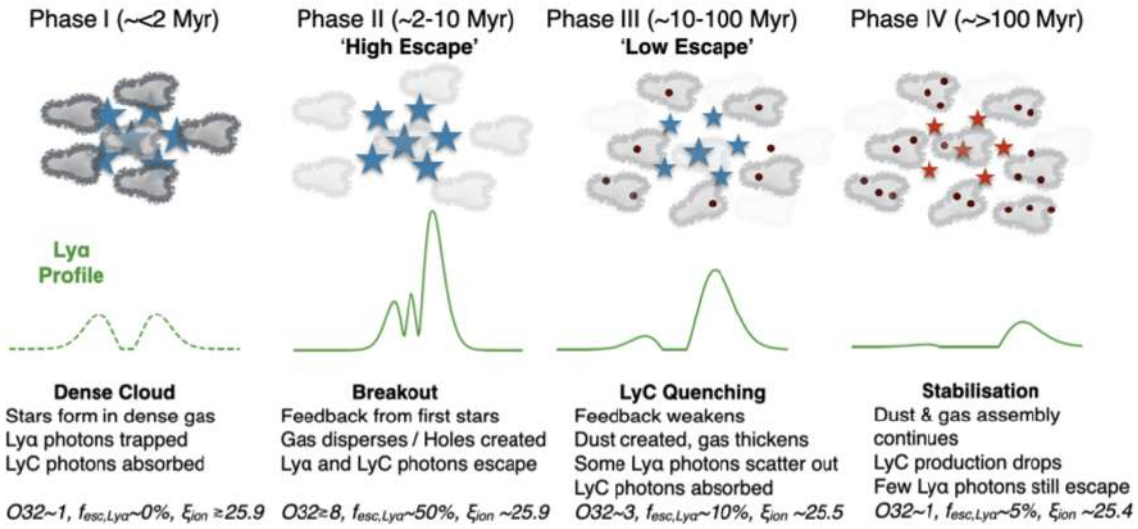

Figure 5.9: Schematic of the LyC duty cycle. Young stellar populations are represented as blue stars with sizes scaled by stellar mass, and old stars are in red. Neutral clouds are shown as gray clouds with color varying with the density, and dust is shown as dark brown points. The cycle is divided in four phases and show the expected emergent Lyα profile in green respectively. In phase I, massive stars are born embedded in dense clouds, and despite the hard ionizing radiation that emanate this cannot escape. In phase II, the feedback from the massive stars disrupt the birth clouds allowing the ionizing radiation to escape. In phase III young stars are still present and producing ionizing radiation, however, the most massive ones already exploded as SNe, and the dust/HI begin to opaque the ISM, reducing the escape of LyC photons. In phase IV there are older stellar populations and a dusty, high column HI ISM. The figure is from Naidu et al. (2022).

1σ and 2σ of confidence) with the velocity dispersion of the broader component in both Hα and [OIII]λ5007Å. Here, nearly all the *SLCE* are above $\Sigma SFR_{H\beta} \sim 10\ M_{\odot}\ yr^{-1}\ kpc^{-2}$. The above results suggest that high star formation rate is not sufficient to generate the required turbulence and outflow velocity that characterize the escape of ionizing photons. Instead, the compactness of such star formation makes a greater impact, i.e. the gravitational potential of the regions where young massive star complexes are evolving (Heckman et al., 2011). Another evidence of the latter is the anti-correlation between the galaxy's half radius from the *COS/NUV* images, which mostly trace younger stellar populations within galaxies, and the intrinsic velocity dispersion of the broader component. Here, the *SLCEs*, which have the broader components, also have the smallest radius when compared to the *NLCEs*.

The tendency of the *SLCEs* for having low r_{50} and high $\Sigma SFR_{H\beta}$ suggests that large concentrations of relatively massive star forming regions are required to provide the necessary feedback to disrupt the ISM and enable the channels from which the ionizing radiation escapes. Moreover, the correlations between the three Lyα properties ($f_{esc}^{Ly\alpha}$, EW Lyα, and v_{sep}) and the broad emissions from both Hα and

[OIII]λ5007Å demonstrate that outflows and turbulence clear neutral gas from line-of-sight paths. As in Flury et al. (2022b), *SLCEs* have the highest escape fractions and equivalent widths in Lyα, and the smaller peak separation ($v_{sep} < 320\ km\ s^{-1}$).

Our findings are in agreement with the unified scheme proposed by Naidu et al. (2022) (see Figure 5.9). This physical picture emerges by analyzing the characteristics of two stacks (*LCEs* and *NLCEs*) of LAEs at $z \sim 2$, with escape fractions inferred from Lyα profiles (v_{sep} and central fluxes). In the scheme, they distinguish four phases to describe the state of high-redshift SFG: In Phase I ($\lesssim$ 2 Myr), massive star cluster complexes form vigorous starbursts in dense regions which absorb LyC radiation. In Phase II ($\sim 2 - 10$ Myr) massive stars disrupt the ISM producing clean channels via feedback, while young massive stars are still forming and emitting ionizing radiation with high efficiency. This phase describes the state of galaxies with high escape fractions in the order of those galaxies in the *Izotov* sample. In Phase III ($\sim 10 - 100$ Myr) the feedback weakens since the most massive stars are gone and dust is created, which makes the ISM opaque to both LyC and Lyα radiation. Some of the *WLCEs* in our sample may be in the early stages of this phase. Finally, in Phase IV ($\gtrsim$ 100 Myr) old stellar populations are surrounded by a dusty ISM with high columns of HI. Notoriously, the high escape fraction stack (galaxies in Phase II) is described by properties that can be traced with parameters that correlate with the ionizing gas kinematic i.e low column densities and high ionization state of the ISM.

Chapter 6

Conclusions and future directions

As part of the *Low-z Lyman Continuum Survey* collaboration, we study the ionized gas kinematics of a sample of green pea galaxies composed by non-emitters and emitters of ionizing radiation. We find significant observational evidence that ionized gas kinematics have a profound impact on the escape of LyC photons. Our results strongly suggest that low metallicity starbursts with broader wings and more asymmetric emission-lines in integrated spectra are expected to show LyC leakage and their escape fractions scale with their emission line widths at the low surface brightness wings, i.e. their outflow velocities. These *SLCEs* are naturally more compact, and their star-forming regions appear mostly concentrated in single and relatively massive unresolved complexes of a few hundred pc in size.

Thus, our results add a new observational constraint to models and simulations predicting strong stellar feedback from massive stars radiation and winds, along with energetic SNe explosions, as the drivers of shaping the local ISM and allow a fraction of the massively produced Lyα and LyC photons to escape into the IGM. Hence, the ionized gas kinematics might be a useful diagnostic tool to identify Lyman continuum leakers candidates at high redshifts ($z \gtrsim 2$) with new state-of-the-art instrumentation such as NIRSpec on board of the *James Webb Space Telescope*, which can reach high spectral resolutions ($R \sim 2700, 47\ km\ s^{-1}$) of optical rest-frame emission-line profiles, thus allowing to distinguish between multiple kinematics components.

This study demonstrate that high resolution long-slit spectra provides crucial astrophysical information about the galaxies. However, integral field spectroscopy would be necessary to spatially resolve this objects and understand better the astrophysical mechanisms that accelerate the ionized gas, allowing the escape of ionizing radiation.

Finally, as part of this project, we are deriving the main outflows properties of the galaxies from the Hα and the [OIII]λ5007Å multi-component models, i.e the outflow velocity, the mass-loading factor and the mass outflow rate. Determine these quantities is relevant in order to understand how outflows favor the escape of ionizing radiation, and also to constrain models of stellar feedback.

Bibliography

Akaike, H. 1974, IEEE Transactions on Automatic Control, 19, 716

Akritas, M. G. & Siebert, J. 1996, MNRAS, 278, 919.

Amorín, R., Pérez-Montero, E., Vílchez, J. M., et al. 2012, ApJ, 749, 185

Amorín, R., Vílchez, J. M., Hägele, G. F., et al. 2012, ApJL, 754, L22

Amorín, R. O., Pérez-Montero, E., & Vílchez, J. M. 2010, ApJL, 715, L128

Andrae, R., Schulze-Hartung, T., & Melchior, P. 2010, arXiv:1012.3754

Astropy Collaboration, Robitaille, T. P., Tollerud, E. J., et al. 2013, A&A, 558, A33

Baldwin, J. A., Phillips, M. M., & Terlevich, R. 1981, PASP, 93, 5

Becker, G. D., D'Aloisio, A., Christenson, H. M., et al. 2021, MNRAS, 508, 1853.

Becker, G. D., Bolton, J. S., Madau, P., et al. 2015, MNRAS, 447, 3402.

Binette, L., Drissen, L., Ubeda, L., et al. 2009, A&A, 500, 817.

Bosch, G., Hägele, G. F., Amorín, R., et al. 2019, MNRAS, 489, 1787

Bouwens, R. J., Illingworth, G. D., Oesch, P. A., et al. 2015, ApJ, 811, 140

Bouwens, R. J., Smit, R., Labbé, I., et al. 2016, ApJ, 831, 176. doi:10.3847/0004-637X/831/2/176

Bouwens, R. J., Illingworth, G. D., Ellis, R. S., et al. 2022, arXiv:2205.11526

Calzetti, D. 2001, PASP, 113, 1449.

Cairós, L. M., & González-Pérez, J. N. 2017, A&A, 600, A125

Cardamone, C., Schawinski, K., Sarzi, M., et al. 2009, MNRAS, 399, 1191

Cardelli, J. A., Clayton, G. C., & Mathis, J. S. 1989, ApJ, 345, 245.

Chisholm, J., Orlitová, I., Schaerer, D., et al. 2017, A&A, 605, A67

Davies, R. L., Förster Schreiber, N. M., Übler, H., et al. 2019, ApJ, 873, 122

Dayal, P., Volonteri, M., Choudhury, T. R., et al. 2020, MNRAS, 495, 3065.

de Barros, S., Vanzella, E., Amorín, R., et al. 2016, A&A, 585, A51

Dopita, M. A. & Sutherland, R. S. 2003, Astrophysics of the diffuse universe, Berlin, New York: Springer, 2003. Astronomy and astrophysics library, ISBN 3540433627

Fan, X., Strauss, M. A., Becker, R. H., et al. 2006, AJ, 132, 117.

Fernández, V., Amorín, R., Pérez-Montero, E., et al. 2022, MNRAS, 511, 2515. doi:10.1093/mnras/stab3150

Finkelstein, S. L., Hill, G. J., Gebhardt, K., et al. 2011, ApJ, 729, 140.

Finkelstein, S. L. 2016, PASA, 33, e037.

Finkelstein, S. L., D'Aloisio, A., Paardekooper, J.-P., et al. 2019, ApJ, 879, 36.

Firpo, V., Bosch, G., Hägele, G. F., et al. 2010, MNRAS, 406, 1094

Firpo, V., Bosch, G., Hägele, G. F., et al. 2011, MNRAS, 414, 3288

Fitzpatrick, E. L. 1999, PASP, 111, 63.

Flury S. R., Jaskot A. E., Ferguson H. C., Worseck G., Makan K., Chisholm J., Saldana-Lopez A., et al. 2022, ApJS, 260, 1.

Flury, S. R., Jaskot, A. E., Ferguson, H. C., et al. 2022, ApJ, 930, 126

Freudling, W., Romaniello, M., Bramich, D. M., et al. 2013, A&A, 559, A96

Gazagnes, S., Chisholm, J., Schaerer, D., et al. 2020, A&A, 639, A85.

Giallongo, E., Grazian, A., Fiore, F., et al. 2015, A&A, 578, A83.

Green, A. W., Glazebrook, K., McGregor, P. J., et al. 2010, Nature, 467, 684

Green, G. M., Schlafly, E. F., Finkbeiner, D., et al. 2018, MNRAS, 478, 651.

Gunn, J. E. & Peterson, B. A. 1965, ApJ, 142, 1633.

Guseva, N. G., Izotov, Y. I., Schaerer, D., et al. 2020, MNRAS, 497, 4293.

Heckman, T. M., Borthakur, S., Overzier, R., et al. 2011, ApJ, 730, 5

Henry, A., Scarlata, C., Martin, C. L., et al. 2015, ApJ, 809, 19

Ho, I.-T., Kewley, L. J., Dopita, M. A., et al. 2014, MNRAS, 444, 3894

Hägele, G. F., Díaz, Á. I., Cardaci, M. V., et al. 2007, MNRAS, 378, 163

Hägele, G. F., Firpo, V., Bosch, G., et al. 2012, MNRAS, 422, 3475

Hogarth, L., Amorín, R., Vílchez, J. M., et al. 2020, MNRAS, 494, 3541.

Inoue, A. K., Shimizu, I., Iwata, I., et al. 2014, MNRAS, 442, 1805.

Izotov, Y. I., Schaerer, D., Thuan, T. X., et al. 2016, MNRAS, 461, 3683

Izotov, Y. I., Orlitová, I., Schaerer, D., et al. 2016, Nature, 529, 178

Izotov, Y. I., Schaerer, D., Worseck, G., et al. 2018, MNRAS, 474, 4514

Izotov, Y. I., Worseck, G., Schaerer, D., et al. 2018, MNRAS, 478, 4851

Izotov, Y. I., Thuan, T. X., & Guseva, N. G. 2007, ApJ, 671, 1297

Izotov, Y. I., Guseva, N. G., & Thuan, T. X. 2011, ApJ, 728, 161

Izotov, Y. I., Worseck, G., Schaerer, D., et al. 2021, MNRAS, 503, 1734.

Jaskot, A. E., & Oey, M. S. 2013, ApJ, 766, 91

Jaskot, A. E., Dowd, T., Oey, M. S., et al. 2019, ApJ, 885, 96.

Ji, Z., Giavalisco, M., Vanzella, E., et al. 2020, ApJ, 888, 109

Jones, T. A., Swinbank, A. M., Ellis, R. S., et al. 2010, MNRAS, 404, 1247.

Kakiichi, K. & Gronke, M. 2021, ApJ, 908, 30. doi:10.3847/1538-4357/abc2d9

Kauffmann, G., Heckman, T. M., Tremonti, C., et al. 2003, MNRAS, 346, 1055

Kennicutt, R. C. 1984, ApJ, 287, 116.

Kennicutt, R. C., & Evans, N. J. 2012, ARA&A, 50, 531

Kewley, L. J., Dopita, M. A., Sutherland, R. S., et al. 2001, ApJ, 556, 121

Kewley, L. J., Groves, B., Kauffmann, G., et al. 2006, MNRAS, 372, 961

Khostovan, A. A., Sobral, D., Mobasher, B., et al. 2016, MNRAS, 463, 2363

Kimm, T., Blaizot, J., Garel, T., et al. 2019, MNRAS, 486, 2215

Kim, K. J., Malhotra, S., Rhoads, J. E., et al. 2021, ApJ, 914, 2. doi:10.3847/1538-4357/abf833

Komarova, L., Oey, M. S., Krumholz, M. R., et al. 2021, ApJL, 920, L46.

Kroupa, P. 2001, MNRAS, 322, 231.

Krumholz, M. R., & Burkhart, B. 2016, MNRAS, 458, 1671

Leitherer, C., Ortiz Otálvaro, P. A., Bresolin, F., et al. 2010, ApJS, 189, 309

Lintott, C. J., Schawinski, K., Slosar, A., et al. 2008, MNRAS, 389, 1179.

Liu, G., Zakamska, N. L., Greene, J. E., et al. 2013, MNRAS, 436, 2576.

Luridiana, V., Morisset, C., & Shaw, R. A. 2015, A&A, 573, A42.

Lusso, E., Worseck, G., Hennawi, J. F., et al. 2015, MNRAS, 449, 4204.

Ma, X., Hopkins, P. F., Kasen, D., et al. 2016, MNRAS, 459, 3614

Ma, X., Quataert, E., Wetzel, A., et al. 2020, arXiv:2003.05945

Madau, P. & Haardt, F. 2015, ApJL, 813, L8.

Madau, P. & Dickinson, M. 2014, ARA&A, 52, 415.

Marques-Chaves, R., Schaerer, D., Amorín, R. O., et al. 2022, A&A, 663, L1.

Matthee, J., Sobral, D., Gronke, M., et al. 2018, A&A, 619, A136. doi:10.1051/0004-6361/201833528

Matsuoka, Y., Strauss, M. A., Kashikawa, N., et al. 2018, ApJ, 869, 150.

Melnick, J., Tenorio-Tagle, G., & Terlevich, R. 1999, MNRAS, 302, 677.

Melnick, J., Tenorio-Tagle, G., & Telles, E. 2021, A&A, 649, A175.

Micheva, G., Oey, M. S., Jaskot, A. E., et al. 2017, ApJ, 845, 165

Naidu R. P., Tacchella S., Mason C. A., Bose S., Oesch P. A., Conroy C., 2020, ApJ, 892, 109.

Naidu, R. P., Matthee, J., Oesch, P. A., et al. 2022, MNRAS, 510, 4582.

Nakajima, K., & Ouchi, M. 2014, MNRAS, 442, 900

Nakajima, K., Ellis, R. S., Robertson, B. E., et al. 2020, ApJ, 889, 161.

Newville, M., Stensitzki, T., Allen, D. B., et al. 2014, Zenodo

Ocvirk, P., Gillet, N., Shapiro, P. R., et al. 2016, MNRAS, 463, 1462

Orlitová, I., Verhamme, A., Henry, A., et al. 2018, A&A, 616, A60

Osterbrock, D. E., & Ferland, G. J. 2006, Astrophysics of gaseous nebulae and active galactic nuclei

Ouchi, M., Ono, Y., & Shibuya, T. 2020, ARA&A, 58, 617.

Planck Collaboration, Aghanim, N., Akrami, Y., et al. 2020, A&A, 641, A6.

Ramambason, L., Schaerer, D., Stasińska, G., et al. 2020, A&A, 644, A21.

Reddy, N. A., Steidel, C. C., Pettini, M., et al. 2016, ApJ, 828, 107.

Robertson, B. E., Furlanetto, S. R., Schneider, E., et al. 2013, ApJ, 768, 71.

Robertson, B. E., Ellis, R. S., Furlanetto, S. R., et al. 2015, ApJL, 802, L19

Robertson, B. E. 2021, arXiv:2110.13160

Roy, J.-R., Aube, M., McCall, M. L., et al. 1992, ApJ, 386, 498

Rosdahl, J., Blaizot, J., Katz, H., et al. 2022, MNRAS, 515, 2386.

Saldana-Lopez, A., Schaerer, D., Chisholm, J., et al. 2022, A&A, 663, A59.

Saxena, A., Pentericci, L., Ellis, R. S., et al. 2022, MNRAS, 511, 120.

Schaerer, D., Izotov, Y. I., Verhamme, A., et al. 2016, A&A, 591, L8

Shen, X., Hopkins, P. F., Faucher-Giguère, C.-A., et al. 2020, MNRAS, 495, 3252.

Stark, D. P., Ellis, R. S., & Ouchi, M. 2011, ApJL, 728, L2. doi:10.1088/2041-8205/728/1/L2

Steidel, C. C., Bogosavljević, M., Shapley, A. E., et al. 2018, ApJ, 869, 123

Tenorio-Tagle, G., Wünsch, R., Silich, S., et al. 2010, ApJ, 708, 1621

Terlevich, R., & Melnick, J. 1981, MNRAS, 195, 839

Terlevich, R., Terlevich, E., Melnick, J., et al. 2015, MNRAS, 451, 3001

Trebitsch, M., Blaizot, J., Rosdahl, J., et al. 2017, MNRAS, 470, 224.

Vanzella, E., de Barros, S., Vasei, K., et al. 2016, ApJ, 825, 41

Vanzella, E., Castellano, M., Bergamini, P., et al. 2022, A&A, 659, A2

Veilleux, S., & Osterbrock, D. E. 1987, ApJS, 63, 295

Verhamme, A., Orlitová, I., Schaerer, D., et al. 2017, A&A, 597, A13

Verhamme, A., Orlitová, I., Schaerer, D., et al. 2015, A&A, 578, A7

Fernández, V., Amorín, R., Pérez-Montero, E., et al. 2022, MNRAS, 511, 2515.

Wang, B., Heckman, T. M., Leitherer, C., et al. 2019, ApJ, 885, 57.

Wang, B., Heckman, T. M., Amorín, R., et al. 2021, ApJ, 916, 3.

Wei, J.-J., Wu, X.-F., & Melia, F. 2016, MNRAS, 463, 1144.

Westmoquette, M. S., Smith, L. J., Gallagher, J. S., et al. 2009, ApJ, 696, 192.

Westmoquette, M. S., Gallagher, J. S., Smith, L. J., et al. 2009, ApJ, 706, 1571.

Whittle, M. 1985, MNRAS, 213, 1.

Wyithe, J. S. B. & Loeb, A. 2013, MNRAS, 428, 2741.

Yang, H., Malhotra, S., Gronke, M., et al. 2017, ApJ, 844, 171

Yang, J., Wang, F., Fan, X., et al. 2020, ApJ, 904, 26.

Xu, X., Henry, A., Heckman, T., et al. 2022, ApJ, 933, 202.

Yoo, T., Kimm, T., & Rosdahl, J. 2020, MNRAS, 499, 5175.

Zackrisson, E., Inoue, A. K., & Jensen, H. 2013, ApJ, 777, 39.

Appendix A

Ionized gas kinematics, components properties, and non-parametric analysis: *The Izotov sample*

J0901+2119

Table A.1: Fit statistics of principal emission-line profiles in J0921+2119

λ_0 [a]	Ion	Model [b]	χ^2 [c]	χ^2_ν [d]	AIC [e]	BIC [f]	P(Gα) [g]
$6563 + 6548, 6584$	Hα + [NII]	G2	32534.1	55.9	2381.9	2416.9	0.0
		G3	20508.5	35.5	2117.6	2170.2	100.0
5007	[OIII]	G2	26101.9	71.7	1586.8	1610.3	0.0
		G3	12215.5	33.8	1311.9	1347.1	100.0
4861	Hβ	G2	16898.6	53.1	1273.3	1280.9	0.1
		G3	15992.8	50.5	1257.7	1269.0	99.9
$6717, 6731$	[SII]	G2	26138.3	52.7	1986.3	2003.1	1.3
		G3	25483.6	51.6	1977.6	2002.9	98.7

[a] Rest wavelength in Å.
[b] G2: Two gaussian components model, G3: Three gaussian components model.
[c] Chi square (see text for details).
[d] Reduced chi square (see text for details).
[e] Akaike Information Criteria (see text for details).
[f] Bayesian Information Criteria (see text for details).
[g] Likelihood percentage of model Gα to be correct respect the other (see text for details).

Table A.2: Results of the two Gaussian components model (G2) fitting of J0901+2119

λ_0 [a]	Ion	Comp. [b]	Δv_r [c]	σ_{int} [d]	Flux [e]	EM_f [f]	GlobalFlux [g]
6563	Hα	B	-19.2 ± 1.2	131.4 ± 1.5	115.1 ± 2.9	29.0	397.2 ± 4.4
		N	-2.0 ± 0.4	51.2 ± 0.4	282.1 ± 3.2	71.0	
5007	[OIII]	B	-21.0 ± 1.3	125.6 ± 1.6	228.6 ± 6.8	28.5	800.9 ± 9.9
		N	1.1 ± 0.4	49.7 ± 0.5	572.3 ± 7.2	71.5	
4861	Hβ	B	-19.2 ± 1.2	131.4 ± 1.5	30.3 ± 1.2	27.5	110.3 ± 1.8
		N	-2.0 ± 0.4	51.2 ± 0.4	80.0 ± 1.4	72.5	
4959	[OIII]	B	-21.0 ± 1.3	125.6 ± 1.6	73.9 ± 1.5	27.4	269.7 ± 2.4
		N	1.1 ± 0.4	49.7 ± 0.5	195.9 ± 1.8	72.6	
6300	[OI]	B	-19.2 ± 1.2	131.7 ± 1.5	0.0 ± 0.0	0.0	3.5 ± 0.3
		N	-2.0 ± 0.4	52.1 ± 0.4	3.5 ± 0.3	100.0	
6548	[NII]	B	-19.2 ± 1.2	131.7 ± 1.5	2.1 ± 0.1	41.6	5.1 ± 0.2
		N	-2.0 ± 0.4	52.0 ± 0.4	3.0 ± 0.1	58.4	
6584	[NII]	B	-19.2 ± 1.2	131.7 ± 1.5	6.4 ± 0.4	41.6	15.4 ± 0.6
		N	-2.0 ± 0.4	52.0 ± 0.4	9.0 ± 0.4	58.4	
6717	[SII]	B	-19.2 ± 1.2	131.7 ± 1.5	0.8 ± 0.4	7.8	10.0 ± 0.5
		N	-2.0 ± 0.4	52.1 ± 0.4	9.2 ± 0.4	92.2	
6731	[SII]	B	-19.2 ± 1.2	131.7 ± 1.5	3.0 ± 0.4	31.1	9.7 ± 0.6
		N	-2.0 ± 0.4	52.1 ± 0.4	6.7 ± 0.4	68.9	

[a] Rest wavelength in Å.

[b] Component of the model.

[c] Velocity shift between the central peak of the emission-line and the center of the component (see text for details).

[d] Intrinsic velocity dispersion (see text for details).

[e] Flux of the component (10^{-17} erg s^{-1} cm^{-2}).

[f] Percentage of relative to global flux of the emission-line.

[g] Global flux of the emission-line (10^{-17} erg s^{-1} cm^{-2}).

Table A.3: Results of the three Gaussian components model (G3) fitting of J0901+2119

λ_0 [a]	Ion	Comp. [b]	Δv_r [c]	σ_{int} [d]	Flux [e]	EM_f [f]	GlobalFlux [g]
6563	Hα	B1	-25.1 ± 1.6	100.5 ± 2.5	117.9 ± 5.3	29.5	399.5 ± 8.3
		N	0.2 ± 0.4	48.3 ± 0.5	249.0 ± 4.9	62.3	
		B2	13.0 ± 5.9	184.8 ± 6.1	32.6 ± 4.1	8.1	
5007	[OIII]	B1	-22.1 ± 1.0	105.5 ± 1.5	260.9 ± 7.3	32.3	807.0 ± 11.1
		N	2.8 ± 0.3	49.2 ± 0.4	515.1 ± 8.0	63.8	
		B2	35.8 ± 8.4	258.1 ± 9.7	31.0 ± 2.6	3.8	
4861	Hβ	B1	-25.1 ± 1.6	100.5 ± 2.5	38.7 ± 2.0	35.2	109.9 ± 2.8
		N	0.2 ± 0.4	48.3 ± 0.5	67.8 ± 1.6	61.6	
		B2	13.0 ± 5.9	184.8 ± 6.1	3.5 ± 1.2	3.2	
4959	[OIII]	B1	-22.1 ± 1.0	105.5 ± 1.5	88.6 ± 2.1	32.8	270.3 ± 3.0
		N	2.8 ± 0.3	49.2 ± 0.4	175.4 ± 2.0	64.9	
		B2	35.8 ± 8.4	258.1 ± 9.7	6.4 ± 0.9	2.3	
6300	[OI]	B1	-25.1 ± 1.6	100.9 ± 2.5	0.2 ± 0.5	5.7	3.5 ± 0.6
		N	0.2 ± 0.4	49.2 ± 0.5	3.3 ± 0.3	94.3	
		B2	13.0 ± 5.9	185.0 ± 6.1	0.0 ± 0.0	0.0	
6548	[NII]	B1	-25.1 ± 1.6	100.9 ± 2.5	0.0 ± 0.2	0.0	5.4 ± 0.3
		N	0.2 ± 0.4	49.2 ± 0.5	3.2 ± 0.1	59.6	
		B2	13.0 ± 5.9	185.0 ± 6.1	2.2 ± 0.2	40.4	
6584	[NII]	B1	-25.1 ± 1.6	100.9 ± 2.5	0.0 ± 0.7	0.0	16.3 ± 1.0
		N	0.2 ± 0.4	49.2 ± 0.5	9.7 ± 0.4	59.6	
		B2	13.0 ± 5.9	185.0 ± 6.1	6.6 ± 0.6	40.4	
6717	[SII]	B1	-25.1 ± 1.6	100.9 ± 2.5	1.8 ± 0.6	17.4	10.1 ± 0.9
		N	0.2 ± 0.4	49.3 ± 0.5	8.4 ± 0.5	82.6	
		B2	13.0 ± 5.9	185.0 ± 6.1	0.0 ± 0.5	0.0	
6731	[SII]	B1	-25.1 ± 1.6	100.9 ± 2.5	3.1 ± 0.8	32.3	9.7 ± 1.1
		N	0.2 ± 0.4	49.3 ± 0.5	5.8 ± 0.5	60.1	
		B2	13.0 ± 5.9	185.0 ± 6.1	0.7 ± 0.6	7.6	

[a] Rest wavelength in Å.

[b] Component of the model.

[c] Velocity shift between the central peak of the emission-line and the center of the component (see text for details).

[d] Intrinsic velocity dispersion (see text for details).

[e] Flux of the component (10^{-17} erg s^{-1} cm^{-2}).

[f] Percentage of relative to global flux of the emission-line.

[g] Global flux of the emission-line (10^{-17} erg s^{-1} cm^{-2}).

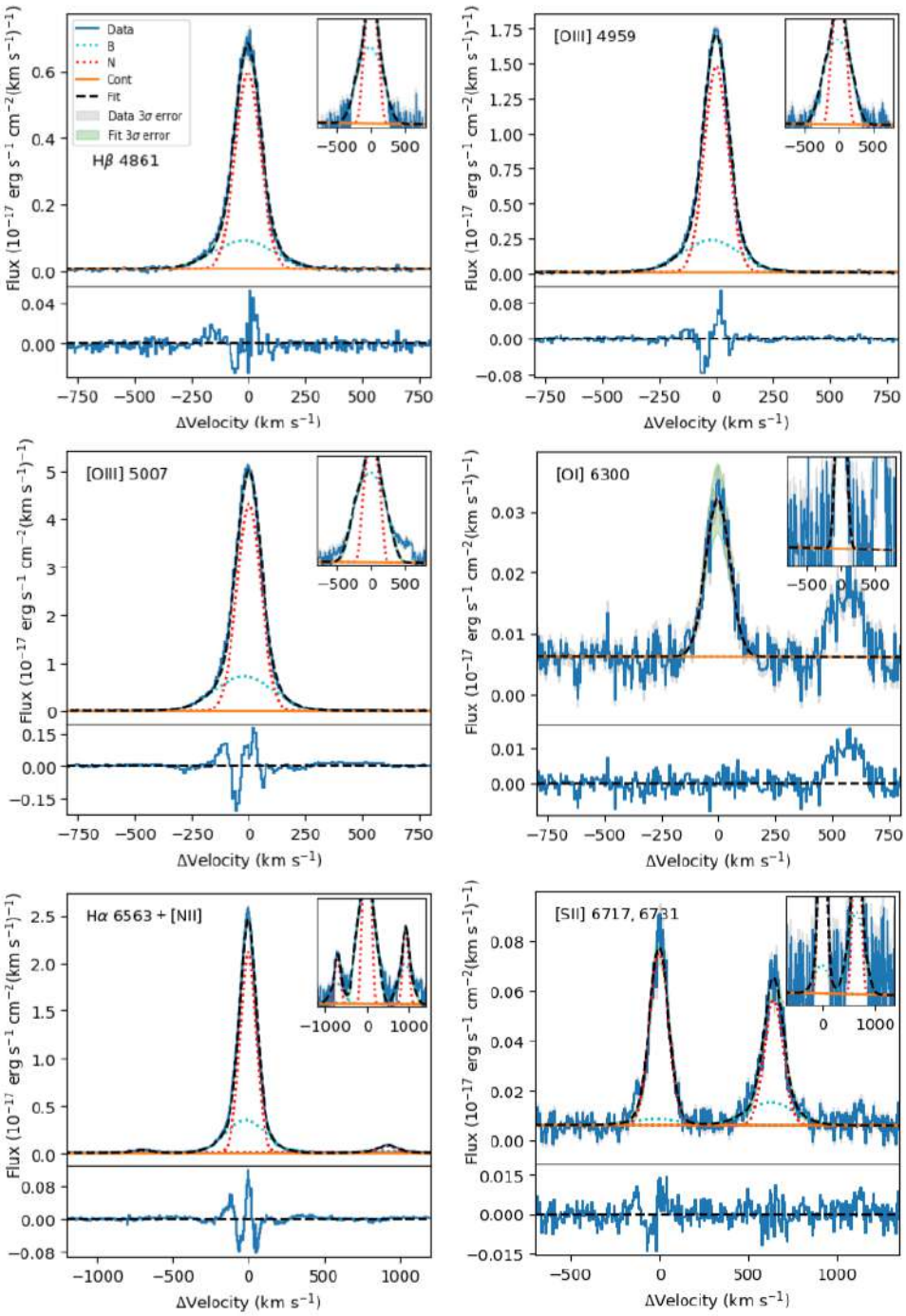

Figure A.1: The fit of faint and bright emission-line profiles of J0901+2119 with two gaussian component models (G2). The blue line represents the original data and the dashed black line the overall model that includes a broad component (B) shown as a cyan dotted line, and a narrow component (N) represented with a red dotted line. The local continuum fitting (Cont) is shown as a solid orange line. We also show the 3σ error spectrum in gray and the 3σ error of the fitted model. A zoomed-in box is shown in the upper-right corner, with $y - axis$ in logarithmic scale. Details of the kinematics and fluxes by component are in Table A.2, while fit statistics are in A.1.

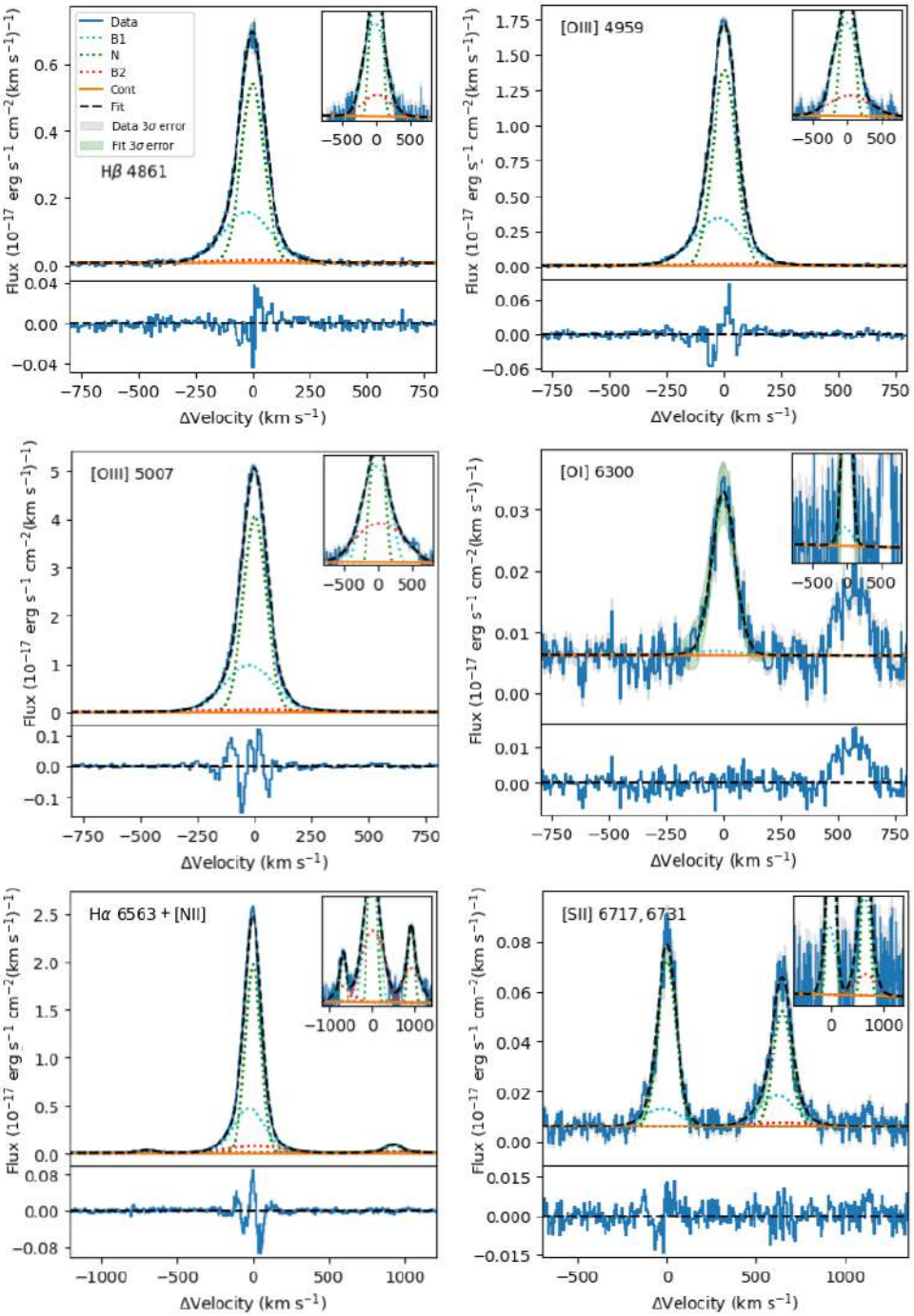

Figure A.2: The fit of faint and bright emission-line profiles of J0901+2119 with three gaussian component models (G3). The blue line represents the original data and the dashed black line the overall model that includes two broad component (B1-B2) shown as a cyan and a red dotted line respectively, and a narrow component (N) represented with a green dotted line. The local continuum fitting (Cont) is shown as a solid orange line. We also show the 3σ error spectrum in gray and the 3σ error of the fitted model. A zoomed-in box is shown in the upper-right corner, with $y-axis$ in logarithmic scale. Details of the kinematics and fluxes by component are in Table A.3, while fit statistics are in A.1.

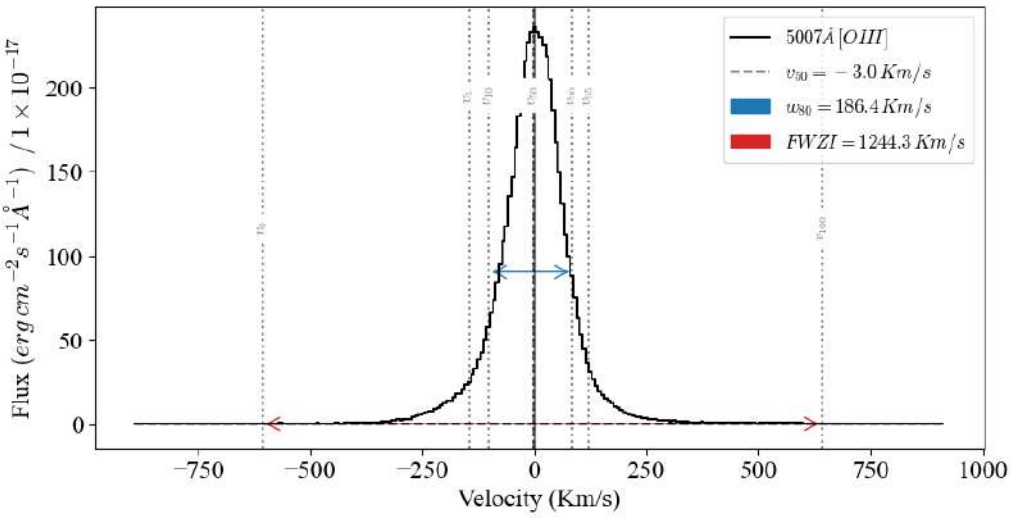

Figure A.3: Inter-percentile analysis of the *WLCE* J0901+2119, using the [OIII]λ5007Å emission-line. Each percentile is represented as a v_i gray dotted-line with i indicating the percentile. The full width zero intensity ($FWZI$) and the w_{80} ($v_{90} - v_{10}$) are shown as a red and blue arrow, respectively.

J0925+1403

Table A.4: Fit statistics of principal emission-lines in J0925+1403

λ_0 [a]	Ion	Model [b]	χ^2 [c]	χ^2_ν [d]	AIC [e]	BIC [f]	P(Gα) [g]
$6563 + 6548, 6584$	Hα + [NII]	G2	58214.6	109.4	2543.4	2577.7	0.0
		G3	11286.9	21.4	1665.5	1717.0	100.0
5007	[OIII]	G2	54372.4	184.9	1572.0	1594.2	0.0
		G3	12285.3	42.2	1131.7	1165.1	100.0
4861	Hβ	G2	9793.2	38.0	947.5	954.6	0.0
		G3	3001.2	11.7	642.0	652.7	100.0
$6717, 6731$	[SII]	G2	9075.3	16.6	1549.9	1567.1	0.0
		G3	8301.2	15.3	1504.8	1530.7	100.0

[a] Rest wavelength in Å.
[b] G2: Two gaussian components model, G3: Three gaussian components model.
[c] Chi square (see text for details).
[d] Reduced chi square (see text for details).
[e] Akaike Information Criteria (see text for details).
[f] Bayesian Information Criteria (see text for details).
[g] Likelihood percentage of model Gα to be correct respect the other (see text for details).

Table A.5: Results of the two Gaussian components model (G2) fitting of J0925+1403

λ_0 [a]	Ion	Comp. [b]	Δv_r [c]	σ_{int} [d]	Flux [e]	EM_f [f]	GlobalFlux [g]
6563	Hα	B	-93.2 ± 4.4	216.4 ± 4.9	160.9 ± 6.1	22.3	720.1 ± 9.4
		N	-46.3 ± 0.7	71.3 ± 0.7	559.3 ± 7.1	77.7	
5007	[OIII]	B	-66.1 ± 1.4	92.5 ± 1.0	919.2 ± 22.3	72.0	1276.0 ± 30.3
		N	-8.6 ± 1.3	32.8 ± 1.5	356.8 ± 20.5	28.0	
4861	Hβ	B	-93.2 ± 4.4	216.4 ± 4.9	39.2 ± 2.0	18.6	210.4 ± 3.1
		N	-46.3 ± 0.7	71.3 ± 0.7	171.2 ± 2.4	81.4	
4959	[OIII]	B	-66.1 ± 1.4	92.5 ± 1.0	308.8 ± 3.8	72.0	429.0 ± 4.8
		N	-8.6 ± 1.3	32.8 ± 1.5	120.1 ± 3.0	28.0	
6300	[OI]	B	-93.2 ± 4.4	216.6 ± 4.9	0.3 ± 0.5	3.8	7.9 ± 0.6
		N	-46.3 ± 0.7	71.9 ± 0.7	7.6 ± 0.4	96.2	
6548	[NII]	B	-93.2 ± 4.4	216.6 ± 4.9	4.8 ± 0.5	42.4	11.3 ± 0.6
		N	-46.3 ± 0.7	71.9 ± 0.7	6.5 ± 0.4	57.6	
6584	[NII]	B	-93.2 ± 4.4	216.6 ± 4.9	14.3 ± 1.5	42.4	33.8 ± 1.9
		N	-46.3 ± 0.7	71.9 ± 0.7	19.4 ± 1.1	57.6	
6717	[SII]	B	-93.2 ± 4.4	216.6 ± 4.9	1.8 ± 0.6	7.7	23.5 ± 0.8
		N	-46.3 ± 0.7	72.0 ± 0.7	21.7 ± 0.5	92.3	
6731	[SII]	B	-93.2 ± 4.4	216.6 ± 4.9	1.8 ± 0.6	9.4	19.5 ± 0.8
		N	-46.3 ± 0.7	72.0 ± 0.7	17.7 ± 0.5	90.6	

[a] Rest wavelength in Å.

[b] Component of the model.

[c] Velocity shift between the central peak of the emission-line and the center of the component (see text for details).

[d] Intrinsic velocity dispersion (see text for details).

[e] Flux of the component (10^{-17} erg s^{-1} cm^{-2}).

[f] Percentage of relative to global flux of the emission-line.

[g] Global flux of the emission-line (10^{-17} erg s^{-1} cm^{-2}).

Table A.6: Results of the three Gaussian components model (G3) fitting of J0925+1403

λ_0 [a]	Ion	Comp. [b]	Δv_r [c]	σ_{int} [d]	Flux [e]	EM_f [f]	GlobalFlux [g]
6563	Hα	N1	-107.0 ± 4.2	57.7 ± 2.0	230.3 ± 15.8	31.4	734.0 ± 22.3
		B	-72.2 ± 1.6	211.0 ± 2.0	175.7± 2.7	23.9	
		N2	-9.8 ± 1.5	44.6 ± 0.7	327.9 ± 15.5	44.7	
5007	[OIII]	N1	-95.1 ± 5.2	58.1 ± 2.7	458.9 ± 38.6	35.2	1302.8 ± 53.9
		B	-69.8 ± 1.8	154.0 ± 2.5	306.1 ± 11.2	23.5	
		N2	-3.8 ± 1.5	38.5 ± 0.9	537.8 ± 36.0	41.3	
4861	Hβ	N1	-107.0 ± 4.2	57.7 ± 2.0	72.4 ± 1.1	33.8	214.3 ± 1.910
		B	-72.2 ± 1.6	211.0 ± 2.0	43.4 ± 1.1	20.2	
		N2	-9.8 ± 1.5	44.6 ± 0.7	98.5 ± 1.1	46.0	
4959	[OIII]	N1	-95.1 ± 5.2	58.1 ± 2.7	154.1 ± 1.8	35.2	437.5 ± 3.0
		B	-69.8 ± 1.8	154.0 ± 2.5	99.0 ± 1.8	22.6	
		N2	-3.8 ± 1.5	38.5 ± 0.9	184.5 ± 1.6	42.2	
6300	[OI]	N1	-107.0 ± 4.2	58.5 ± 2.0	3.2 ± 0.3	40.5	7.9 ± 0.7
		B	-72.2 ± 1.6	211.2 ± 2.0	0.5 ± 0.5	6.3	
		N2	-9.8 ± 1.5	45.6 ± 0.7	4.2 ± 0.3	53.2	
6548	[NII]	N1	-107.0 ± 4.2	58.5 ± 2.0	2.5 ± 0.2	22.1	11.3 ± 0.4
		B	-72.2 ± 1.6	211.2 ± 2.0	5.2 ± 0.2	46.0	
		N2	-9.8 ± 1.5	45.6 ± 0.7	3.7 ± 0.2	32.7	
6584	[NII]	N1	-107.0 ± 4.2	58.5 ± 2.0	7.4 ± 0.7	22.1	34.0 ± 1.1
		B	-72.2 ± 1.6	211.2 ± 2.0	15.5 ± 0.7	46.0	
		N2	-9.8 ± 1.5	45.6 ± 0.7	11.1 ± 0.6	32.7	
6717	[SII]	N1	-107.0 ± 4.2	58.5 ± 2.0	11.0 ± 0.4	46.8	23.5 ± 0.8
		B	-72.2 ± 1.6	211.2 ± 2.0	1.6 ± 0.6	6.8	
		N2	-9.8 ± 1.5	45.6 ± 0.7	10.9 ± 0.4	46.4	
6731	[SII]	N1	-107.0 ± 4.2	58.5 ± 2.0	8.2 ± 0.4	41.8	19.6 ± 0.8
		B	-72.2 ± 1.6	211.2 ± 2.0	2.2 ± 0.6	11.2	
		N2	-9.8 ± 1.5	45.6 ± 0.7	9.2 ± 0.4	47.0	

[a] Rest wavelength in Å.

[b] Component of the model.

[c] Velocity shift between the central peak of the emission-line and the center of the component (see text for details).

[d] Intrinsic velocity dispersion (see text for details).

[e] Flux of the component (10^{-17} erg s^{-1} cm^{-2}).

[f] Percentage of relative to global flux of the emission-line.

[g] Global flux of the emission-line (10^{-17} erg s^{-1} cm^{-2}).

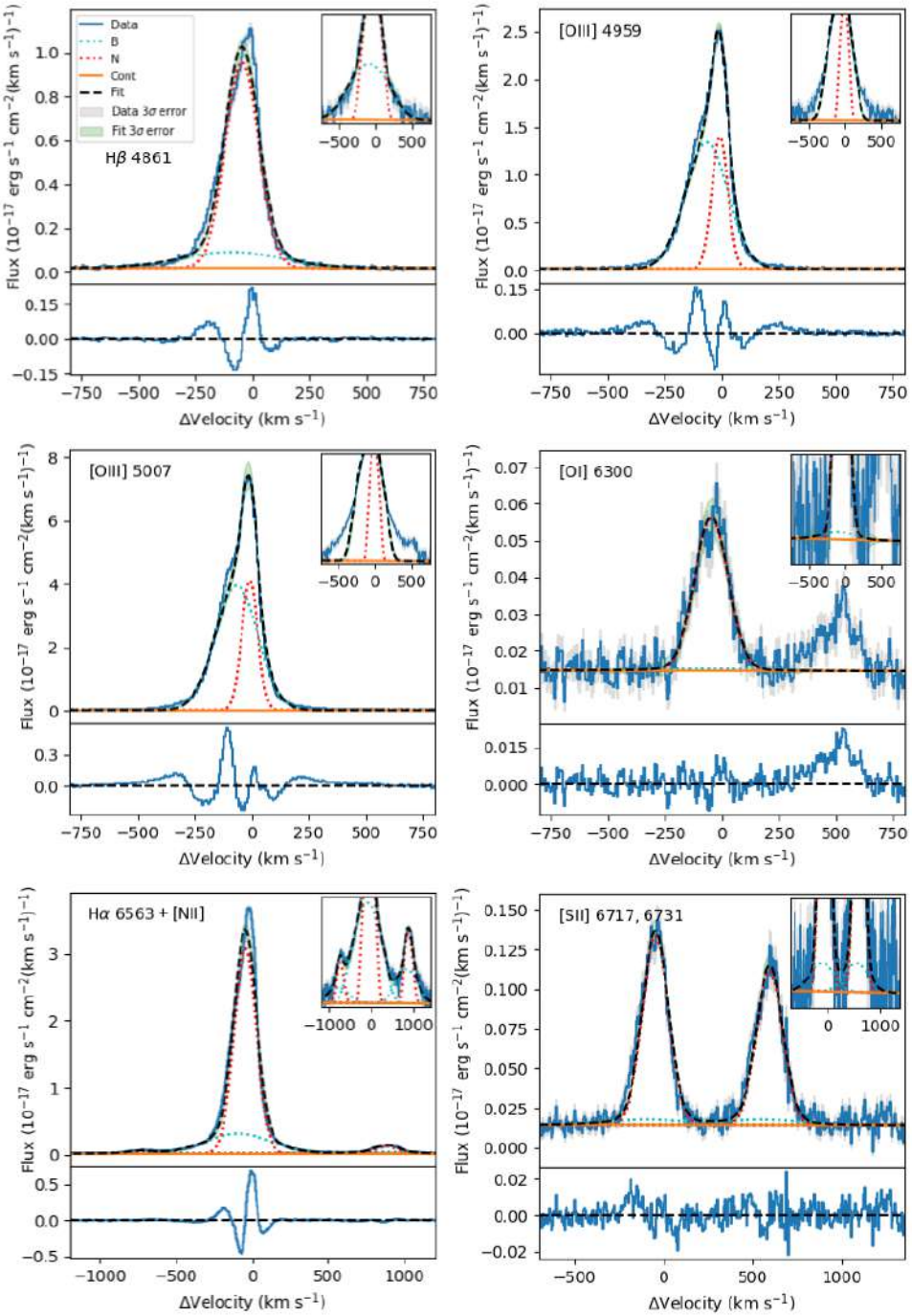

Figure A.4: The fit of faint and bright emission-line profiles of J0925+1403 with two gaussian component models (G2). The blue line represents the original data and the dashed black line the overall model that includes a broad component (B) shown as a cyan dotted line, and a narrow components (N) represented with a red dotted line respectively. The local continuum fitting (Cont) is shown as a solid orange line. We also show the 3σ error spectrum in gray and the 3σ error of the fitted model. A zoomed-in box is shown in the upper-right corner, with $y-axis$ in logarithmic scale. Details of the kinematics and fluxes by component are in Table A.5 , while fit statistics are in A.4.

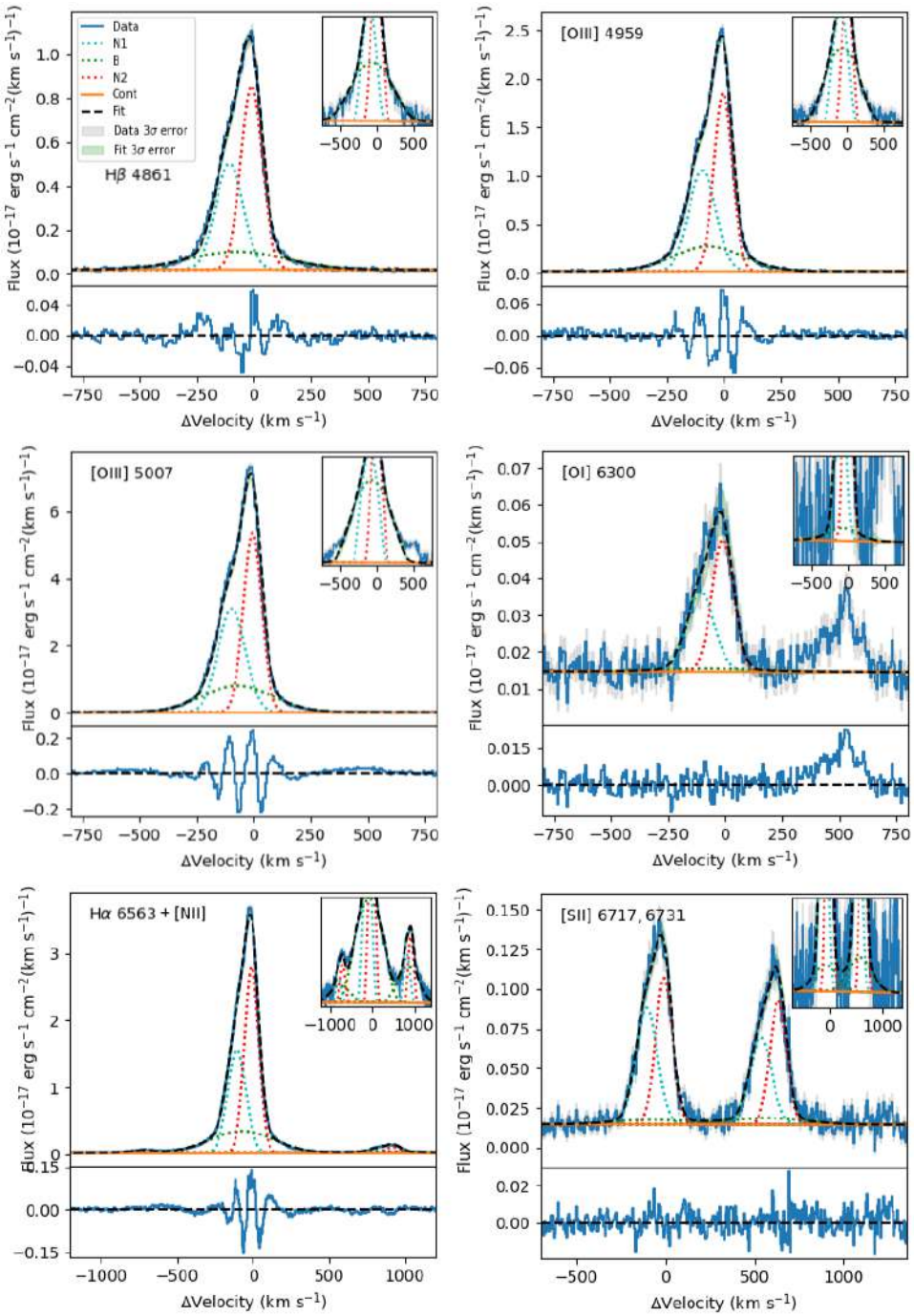

Figure A.5: The fit of faint and bright emission-line profiles of J0925+1403 with three gaussian component models (G3). The blue line represents the original data and the dashed black line the overall model that includes a broad component (B) shown as a green dotted line, and two narrow components (N1-N2) represented with a cyan and red dotted line respectively. The local continuum fitting (Cont) is shown as a solid orange line. We also show the 3σ error spectrum in gray and the 3σ error of the fitted model. A zoomed-in box is shown in the upper-right corner, with $y - axis$ in logarithmic scale. Details of the kinematics and fluxes by component are in Table A.6 , while fit statistics are in A.4.

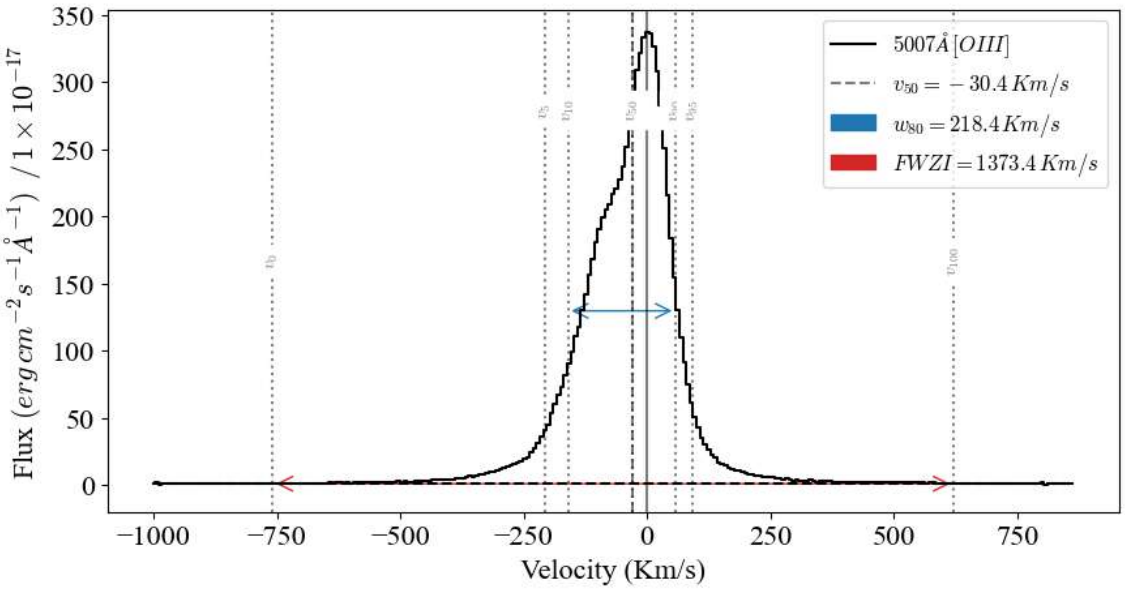

Figure A.6: Inter-percentile analysis of the *SLCE* J0925+1403, using the [OIII]λ5007Å emission-line. Each percentile is represented as a v_i gray dotted-line with i indicating the percentile. The full width zero intensity ($FWZI$) and the w_{80} ($v_{90} - v_{10}$) are shown as a red and blue arrow, respectively.

J1011+1947

Table A.7: Fit statistics of principal emission-lines in J1011+1947

λ_0 [a]	Ion	Model [b]	χ^2 [c]	χ^2_ν [d]	AIC [e]	BIC [f]	P(Gα) [g]
$6563 - 6548, 6584$	Hα + [NII]	G2	33308.8	56.3	2426.00	2461.2	0.0
		G3	25817.1	46.3	2197.5	2249.7	100.0
5007	[OIII]	G2	26870.1	94.6	1325.4	1347.4	0.0
		G3	21687.5	77.2	1269.2	1302.3	100.0
4861	Hβ	G2	15176.4	42.4	1350.9	1358.7	0.0
		G3	13131.2	36.8	1300.8	1312.5	100.0
$6717, 6731$	[SII]	G2	22460.7	48.2	1825.4	1842.0	34.3
		G3	22208.3	47.9	1824.1	1849.0	65.7

[a] Rest wavelength in Å.
[b] G2: Two gaussian components model, G3: Three gaussian components model.
[c] Chi square (see text for details).
[d] Reduced chi square (see text for details).
[e] Akaike Information Criteria (see text for details).
[f] Bayesian Information Criteria (see text for details).
[g] Likelihood percentage of model Gα to be correct respect the other (see text for details).

Table A.8: Results of the two Gaussian components model (G2) fitting of J1011+1947

λ_0 [a]	Ion	Comp. [b]	Δv_r [c]	σ_{int} [d]	Flux [e]	EM_f [f]	GlobalFlux [g]
6563	Hα	B	-34.2 ± 3.2	202.1 ± 4.2	70.9 ± 2.6	16.4	433.3 ± 4.0
		N	-28.4 ± 0.4	67.7 ± 0.5	362.4 ± 3.1	83.6	
5007	[OIII]	B	-5.7 ± 6.7	243.1 ± 8.6	101.5 ± 5.6	9.1	1116.7 ± 10.0
		N	-24.8 ± 0.5	72.2 ± 0.5	1015.3 ± 8.3	90.9	
4861	Hβ	B	-34.2 ± 3.2	202.1 ± 4.2	18.4 ± 1.1	14.6	126.6 ± 1.8
		N	-28.4 ± 0.4	67.7 ± 0.5	108.2 ± 1.4	85.4	
4959	[OIII]	B	-5.7 ± 6.7	243.1 ± 8.6	29.2 ± 1.4	8.1	362.6 ± 2.9
		N	-24.8 ± 0.5	72.2 ± 0.5	333.4 ± 2.5	91.9	
6300	[OI]	B	-34.2 ± 3.2	202.3 ± 4.2	0.1 ± 0.4	5.4	2.2 ± 0.5
		N	-28.4 ± 0.4	68.3 ± 0.5	2.0 ± 0.3	94.6	
6548	[NII]	B	-34.2 ± 3.2	202.3 ± 4.2	2.3 ± 0.2	78.2	3.0 ± 0.3
		N	-28.4 ± 0.4	68.3 ± 0.5	0.6 ± 0.1	21.8	
6584	[NII]	B	-34.2 ± 3.2	202.3 ± 4.2	7.0 ± 0.6	78.2	8.9 ± 0.8
		N	-28.4 ± 0.4	68.3 ± 0.5	1.9 ± 0.4	21.8	
6717	[SII]	B	-34.2 ± 3.2	202.3 ± 4.2	0.0 ± 0.2	0.0	4.0 ± 0.3
		N	-28.4 ± 0.4	68.4 ± 0.5	4.0 ± 0.2	100.0	
6731	[SII]	B	-34.2 ± 3.2	202.3 ± 4.2	0.0 ± 0.4	0.2	4.1 ± 0.5
		N	-28.4 ± 0.4	68.4 ± 0.5	4.1 ± 0.3	99.8	

[a] Rest wavelength in Å.

[b] Component of the model.

[c] Velocity shift between the central peak of the emission-line and the center of the component (see text for details).

[d] Intrinsic velocity dispersion (see text for details).

[e] Flux of the component (10^{-17} erg s^{-1} cm^{-2}).

[f] Percentage of relative to global flux of the emission-line.

[g] Global flux of the emission-line (10^{-17} erg s^{-1} cm^{-2}).

Table A.9: Results of the three Gaussian components model (G3) fitting of J1011+1947

λ_0 [a]	Ion	Comp. [b]	Δv_r [c]	σ_{int} [d]	Flux [e]	EM_f [f]	GlobalFlux [g]
6563	Hα	N1	-66.1 ± 8.9	53.3 ± 3.2	182.5 ± 33.2	42.1	433.7 ± 46.8
		B	-29.4 ± 2.3	177.3 ± 2.9	91.9 ± 2.9	21.2	
		N2	13.3 ± 6.0	45.9 ± 2.0	159.3 ± 32.9	36.7	
5007	[OIII]	N1	-63.8 ± 8.2	54.7 ± 3.1	517.0 ± 81.0	46.3	1116.8 ± 114.5
		B	-18.5 ± 3.4	177.5 ± 4.4	177.1 ± 8.7	15.9	
		N2	22.2 ± 6.1	46.9 ± 2.2	422.6 ± 80.5	37.8	
4861	Hβ	N1	-66.1 ± 8.9	53.3 ± 3.2	51.9 ± 1.2	40.8	127.0 ± 1.9
		B	-29.4 ± 2.3	177.2 ± 2.9	25.2 ± 1.1	19.8	
		N2	13.3 ± 6.0	45.9 ± 2.0	49.9 ± 1.1	39.3	
4959	[OIII]	N1	-63.8 ± 8.2	54.7 ± 3.1	175.2 ± 1.9	48.2	363.7 ± 2.9
		B	-18.5 ± 3.4	177.5 ± 4.4	55.0 ± 1.5	15.1	
		N2	22.2 ± 6.1	46.9 ± 2.2	133.6 ± 1.7	36.7	
6300	[OI]	N1	-66.1 ± 8.9	54.1 ± 3.3	1.1 ± 0.2	52.3	2.2 ± 0.6
		B	-29.4 ± 2.3	177.5 ± 2.9	0.2 ± 0.4	11.2	
		N2	13.3 ± 6.0	46.9 ± 2.0	0.8 ± 0.2	36.5	
6548	[NII]	N1	-66.1 ± 8.9	54.1 ± 3.3	0.0 ± 0.1	0.5	3.0 ± 0.2
		B	-29.4 ± 2.3	177.5 ± 2.9	2.6 ± 0.2	85.2	
		N2	13.3 ± 6.0	46.9 ± 2.0	0.4 ± 0.1	14.3	
6584	[NII]	N1	-66.1 ± 8.9	54.1 ± 3.3	0.1 ± 0.3	0.5	9.1 ± 0.7
		B	-29.4 ± 2.3	177.5 ± 2.9	7.8 ± 0.6	85.2	
		N2	13.3 ± 6.0	46.9 ± 2.0	1.3 ± 0.3	14.3	
6717	[SII]	N1	-66.1 ± 8.9	54.2 ± 3.3	2.4 ± 0.2	59.5	4.0 ± 0.3
		B	-29.4 ± 2.3	177.5 ± 2.9	0.0 ± 0.1	0.0	
		N2	13.3 ± 6.0	46.9 ± 2.0	1.6 ± 0.2	40.5	
6731	[SII]	N1	-66.1 ± 8.9	54.2 ± 3.3	2.0 ± 0.2	48.3	4.2 ± 0.5
		B	-29.4 ± 2.3	177.5 ± 2.9	0.2 ± 0.4	4.9	
		N2	13.3 ± 6.0	46.9 ± 2.0	2.0 ± 0.2	46.8	

[a] Rest wavelength in Å.

[b] Component of the model.

[c] Velocity shift between the central peak of the emission-line and the center of the component (see text for details).

[d] Intrinsic velocity dispersion (see text for details).

[e] Flux of the component (10^{-17} erg s^{-1} cm^{-2}).

[f] Percentage of relative to global flux of the emission-line.

[g] Global flux of the emission-line (10^{-17} erg s^{-1} cm^{-2}).

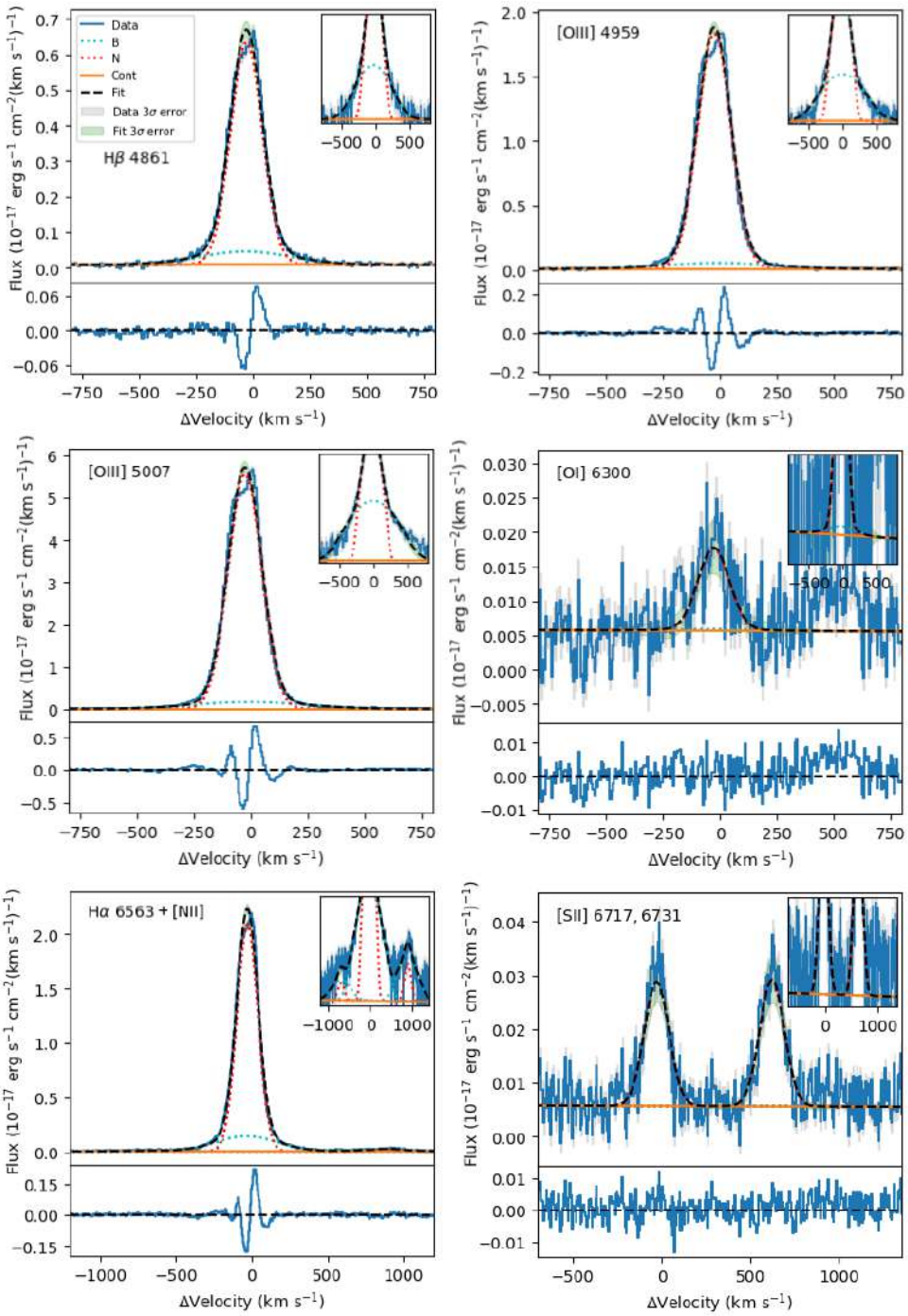

Figure A.7: The fit of faint and bright emission-line profiles of J1011+1947 with two gaussian component models (G2). The blue line represents the original data and the dashed black line the overall model that includes a broad component (B) shown as a cyan dotted line, and a narrow components (N) represented with a red dotted line respectively. The local continuum fitting (Cont) is shown as a solid orange line. We also show the 3σ error spectrum in gray and the 3σ error of the fitted model. A zoomed-in box is shown in the upper-right corner, with $y-axis$ in logarithmic scale. Details of the kinematics and fluxes by component are in Table A.8 , while fit statistics are in A.7.

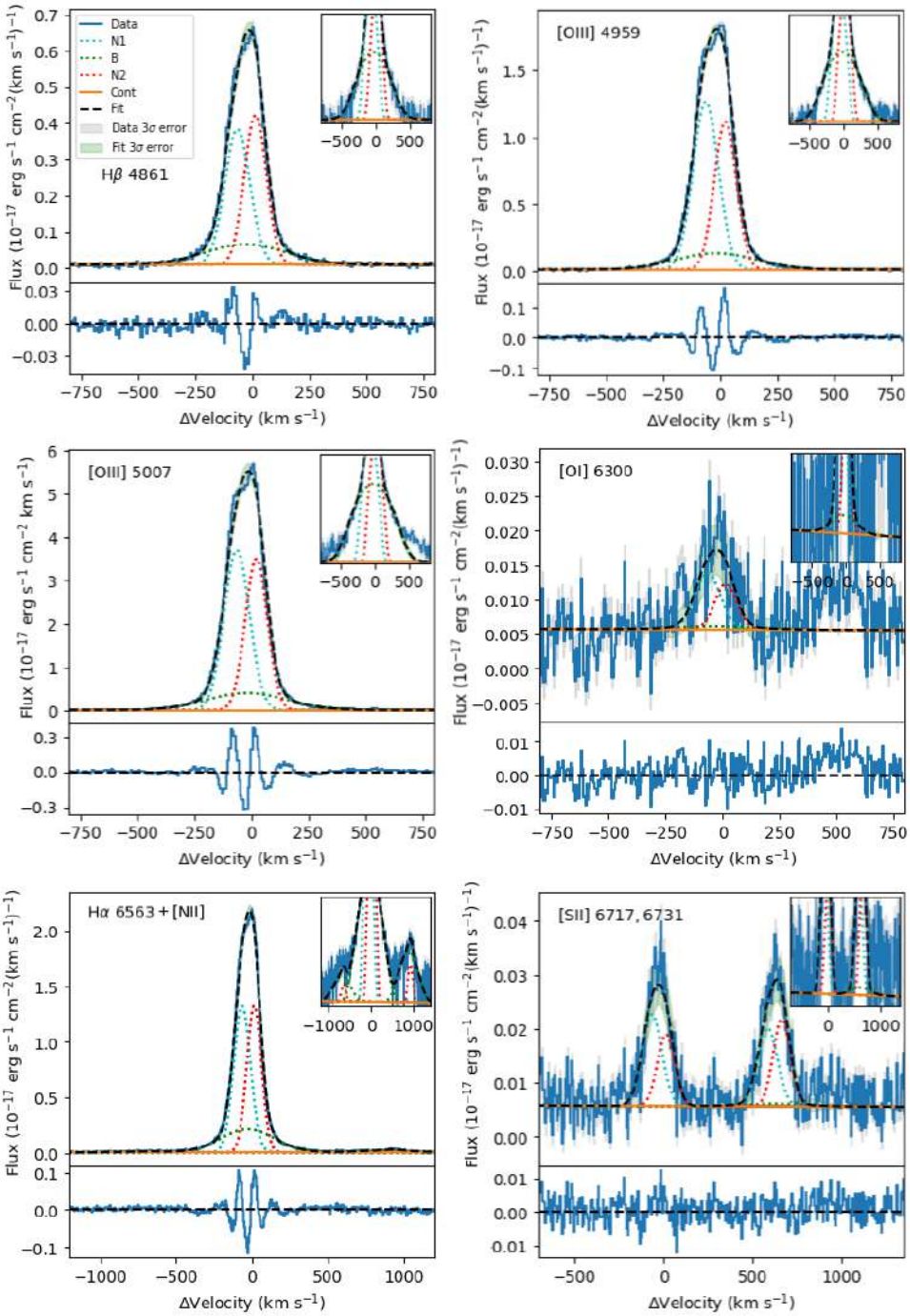

Figure A.8: The fit of faint and bright emission-line profiles of J1011+1947 with three gaussian component models (G3). The blue line represents the original data and the dashed black line the overall model that includes a broad component (B) shown as a green dotted line, and two narrow components (N1-N2) represented with a cyan and red dotted line respectively. The local continuum fitting (Cont) is shown as a solid orange line. We also show the 3σ error spectrum in gray and the 3σ error of the fitted model. A zoomed-in box is shown in the upper-right corner, with $y-axis$ in logarithmic scale. Details of the kinematics and fluxes by component are in Table A.9 , while fit statistics are in A.7.

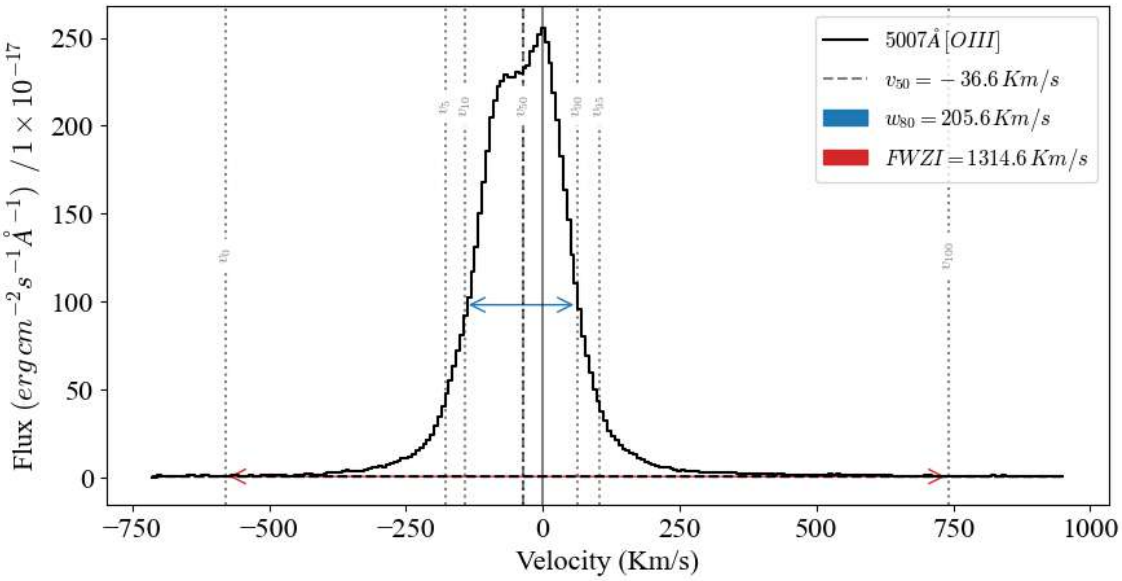

Figure A.9: Inter-percentile analysis of the *SLCE* J1011+1947, using the [OIII]λ5007Å emission-line. Each percentile is represented as a v_i gray dotted-line with i indicating the percentile. The full width zero intensity ($FWZI$) and the w_{80} ($v_{90} - v_{10}$) are shown as a red and blue arrow, respectively.

J1154+2443

Table A.10: Fit statistics of principal emission-lines in J1154+2443

λ_0 [a]	Ion	Model [b]	χ^2 [c]	χ^2_ν [d]	AIC [e]	BIC [f]	P(Gα) [g]
$6563 - 6548, 6584$	Hα + [NII]	G2	5727.1	9.7	1369.6	1404.8	0.0
		G3	5277.5	9.0	1326.6	1374.9	100.0
5007	[OIII]	G2	6125.7	18.9	976.0	998.8	0.0
		G3	4395.3	13.7	872.4	906.6	100.0
4861	Hβ	G2	4475.4	9.7	1056.9	1065.2	27.9
		G3	4438.2	9.6	1055.0	1067.5	72.1
$6717, 6731$	[SII]	G2	4418.8	8.9	1097.5	1114.4	88.1
		G3	4418.8	8.9	1101.5	1126.8	11.9

[a] Rest wavelength in Å.
[b] G2: Two gaussian components model, G3: Three gaussian components model.
[c] Chi square (see text for details).
[d] Reduced chi square (see text for details).
[e] Akaike Information Criteria (see text for details).
[f] Bayesian Information Criteria (see text for details).
[g] Likelihood percentage of model Gα to be correct respect the other (see text for details).

Table A.11: Results of the two Gaussian components model (G2) fitting of J1154+2443

λ_0 [a]	Ion	Comp. [b]	Δv_r [c]	σ_{int} [d]	Flux [e]	EM_f [f]	GlobalFlux [g]
6563	Hα	B	-16.8 ± 2.7	151.1 ± 3.7	23.8 ± 1.1	16.1	147.9 ± 1.7
		N	2.7 ± 0.4	53.5 ± 0.5	124.1 ± 1.3	83.9	
5007	[OIII]	B	-21.7 ± 3.4	144.2 ± 4.3	42.0 ± 2.5	15.1	278.3 ± 3.9
		N	5.6 ± 0.5	54.9 ± 0.5	236.2 ± 3.0	84.9	
4861	Hβ	B	-16.8 ± 2.7	151.1 ± 3.7	5.9 ± 0.8	12.3	47.7 ± 1.5
		N	2.7 ± 0.4	53.5 ± 0.5	41.8 ± 1.2	87.7	
4959	[OIII]	B	-21.7 ± 3.4	144.2 ± 4.3	13.3 ± 0.6	14.3	92.8 ± 1.1
		N	5.6 ± 0.5	54.9 ± 0.5	79.5 ± 0.9	85.7	
6300	[OI]	B	-16.8 ± 2.7	151.4 ± 3.7	0.2 ± 0.3	23.2	1.1 ± 0.3
		N	2.7 ± 0.4	54.3 ± 0.5	0.8 ± 0.2	76.8	
6548	[NII]	B	-16.8 ± 2.7	151.4 ± 3.7	0.4 ± 0.1	48.4	0.9 ± 0.1
		N	2.7 ± 0.4	54.3 ± 0.5	0.5 ± 0.1	51.6	
6584	[NII]	B	-16.8 ± 2.7	151.4 ± 3.7	1.3 ± 0.2	48.4	2.8 ± 0.3
		N	2.7 ± 0.4	54.3 ± 0.5	1.4 ± 0.2	51.6	
6717	[SII]	B	-16.8 ± 2.7	151.4 ± 3.7	0.0 ± 0.1	0.0	2.3 ± 0.4
		N	2.7 ± 0.4	54.3 ± 0.5	2.3 ± 0.2	100.0	
6731	[SII]	B	-16.8 ± 2.7	151.4 ± 3.7	0.0 ± 0.4	0.0	2.3 ± 0.7
		N	2.7 ± 0.4	54.3 ± 0.5	2.3 ± 0.2	100.0	

[a] Rest wavelength in Å.

[b] Component of the model.

[c] Velocity shift between the central peak of the emission-line and the center of the component (see text for details).

[d] Intrinsic velocity dispersion (see text for details).

[e] Flux of the component (10^{-17} erg s^{-1} cm^{-2}).

[f] Percentage of relative to global flux of the emission-line.

[g] Global flux of the emission-line (10^{-17} erg s^{-1} cm^{-2}).

Table A.12: Results of the three Gaussian components model (G3) fitting of J1154+2443

λ_0 [a]	Ion	Comp. [b]	Δv_r [c]	σ_{int} [d]	Flux [e]	EM_f [f]	GlobalFlux [g]
6563	Hα	B1	-17.1 ± 3.2	109.0 ± 6.2	27.3 ± 2.5	18.4	148.6 ± 4.1
		N	3.9 ± 0.5	51.2 ± 0.7	114.5 ± 2.8	77.0	
		B2	14.2 ± 15.7	248.4 ± 25.0	6.8 ± 1.5	4.6	
5007	[OIII]	B1	-22.9 ± 4.2	89.8 ± 3.5	61.7 ± 7.8	22.0	280.7 ± 11.2
		N	9.4 ± 0.7	51.7 ± 0.9	204.0 ± 8.0	72.7	
		B2	24.6 ± 11.8	261.9 ± 14.8	15.0 ± 1.4	5.3	
4959	[OIII]	B1	-22.9 ± 4.2	89.8 ± 3.5	21.3 ± 1.0	22.8	93.4 ± 1.5
		N	9.4 ± 0.7	51.7 ± 0.9	68.3 ± 1.1	73.1	
		B2	24.6 ± 11.8	261.9 ± 14.8	3.8 ± 0.5	4.1	
4861	Hβ	B1	-17.1 ± 3.2	109.0 ± 6.2	9.8 ± 1.6	20.6	47.4 ± 2.4
		N	3.9 ± 0.5	51.2 ± 0.7	37.6 ± 1.4	79.4	
		B2	14.2 ± 15.7	248.3 ± 25.0	0.0 ± 1.1	0.0	
6300	[OI]	B1	-17.1 ± 3.2	109.4 ± 6.2	0.5 ± 0.4	43.7	1.1 ± 0.7
		N	3.9 ± 0.5	52.0 ± 0.7	0.6 ± 0.2	56.3	
		B2	14.2 ± 15.7	248.5 ± 25.0	0.0 ± 0.5	0.0	
6548	[NII]	B1	-17.1 ± 3.2	109.4 ± 6.2	0.4 ± 0.1	51.2	0.8 ± 0.1
		N	3.9 ± 0.5	52.0 ± 0.7	0.4 ± 0.1	48.8	
		B2	14.2 ± 15.7	248.5 ± 25.0	0.0 ± 0.0	0.0	
6584	[NII]	B1	-17.1 ± 3.2	109.4 ± 6.2	1.3 ± 0.2	51.2	2.5 ± 0.3
		N	3.9 ± 0.5	52.0 ± 0.7	1.2 ± 0.2	48.8	
		B2	14.2 ± 15.7	248.5 ± 25.0	0.0 ± 0.0	0.0	
6717	[SII]	B1	-17.1 ± 3.2	109.4 ± 6.2	0.0 ± 0.3	0.0	2.3 ± 0.5
		N	3.9 ± 0.5	52.1 ± 0.7	2.3 ± 0.2	100.0	
		B2	14.2 ± 15.7	248.5 ± 25.0	0.0 ± 0.1	0.0	
6731	[SII]	B1	-17.1 ± 3.2	109.4 ± 6.2	0.0 ± 0.3	0.0	2.2 ± 1.4
		N	3.9 ± 0.5	52.1 ± 0.7	2.2 ± 0.2	100.0	
		B2	14.2 ± 15.7	248.5 ± 25.0	0.0 ± 0.1	0.0	

[a] Rest wavelength in Å.

[b] Component of the model.

[c] Velocity shift between the central peak of the emission-line and the center of the component (see text for details).

[d] Intrinsic velocity dispersion (see text for details).

[e] Flux of the component (10^{-17} erg s^{-1} cm^{-2}).

[f] Percentage of relative to global flux of the emission-line.

[g] Global flux of the emission-line (10^{-17} erg s^{-1} cm^{-2}).

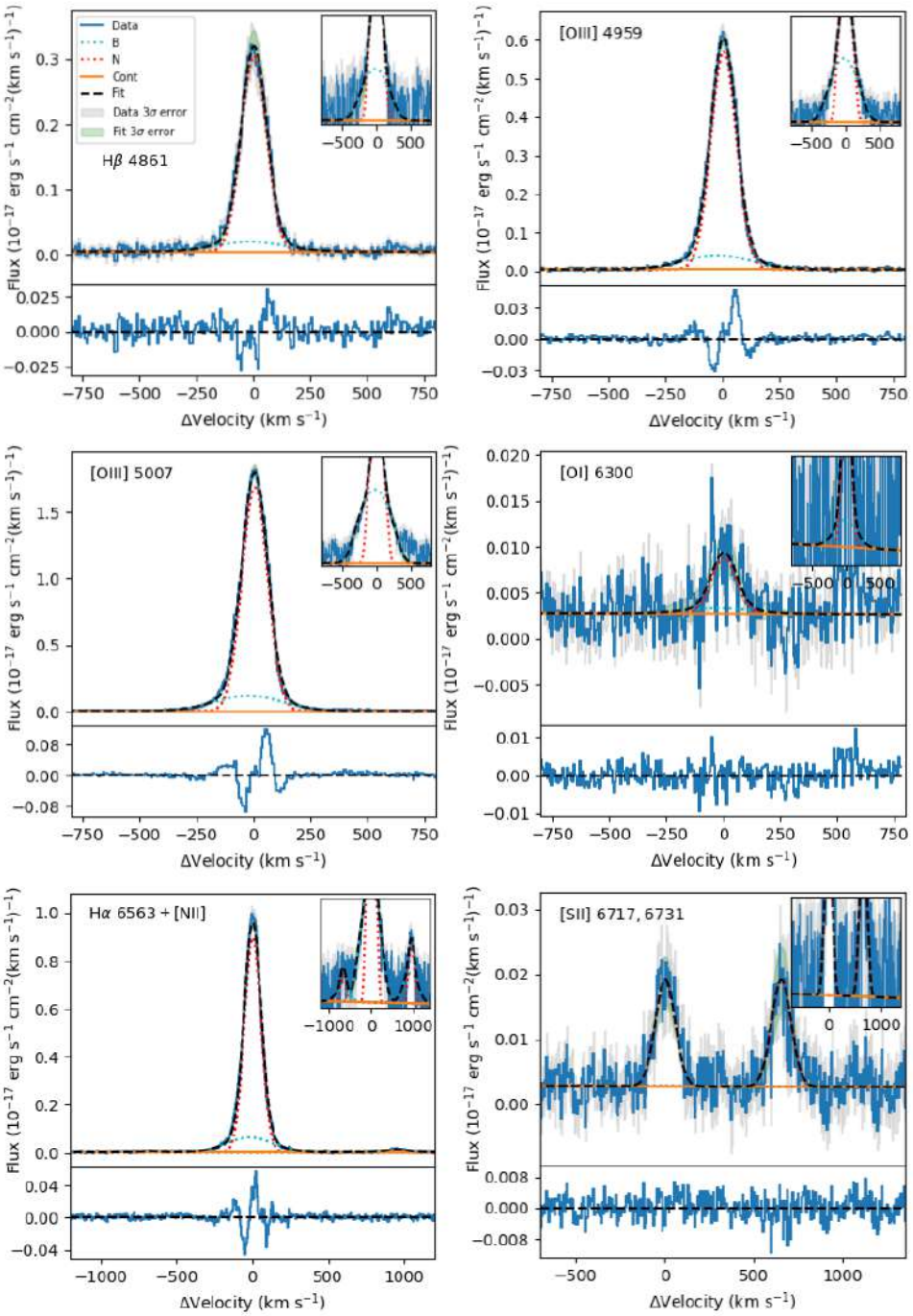

Figure A.10: The fit of faint and bright emission-line profiles of J1154+2443 with two gaussian component models (G2). The blue line represents the original data and the dashed black line the overall model that includes a broad component (B) shown as a cyan dotted line, and a narrow components (N) represented with a red dotted line respectively. The local continuum fitting (Cont) is shown as a solid orange line. We also show the 3σ error spectrum in gray and the 3σ error of the fitted model. A zoomed-in box is shown in the upper-right corner, with $y-axis$ in logarithmic scale. Details of the kinematics and fluxes by component are in Table A.11 , while fit statistics are in A.10.

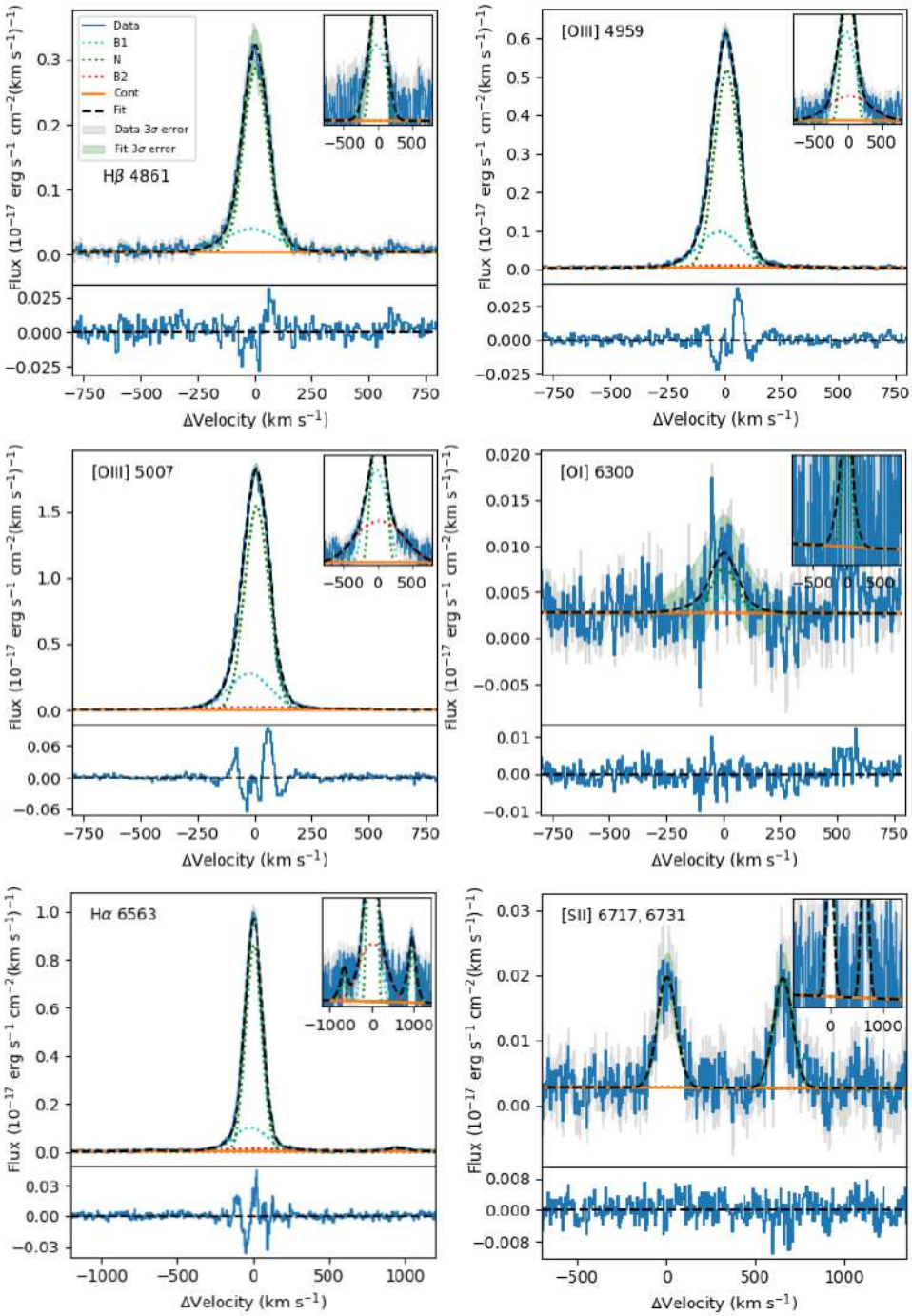

Figure A.11: The fit of faint and bright emission-line profiles of J1154+2443 with three gaussian component models (G3). The blue line represents the original data and the dashed black line the overall model that includes two broad components (B1-B2) shown as a cyan and a red dotted line respectively, and a narrow component (N) represented with a green dotted line. The local continuum fitting (Cont) is shown as a solid orange line. We also show the 3σ error spectrum in gray and the 3σ error of the fitted model. A zoomed-in box is shown in the upper-right corner, with $y-axis$ in logarithmic scale. Details of the kinematics and fluxes by component are in Table A.12 , while fit statistics are in A.10.

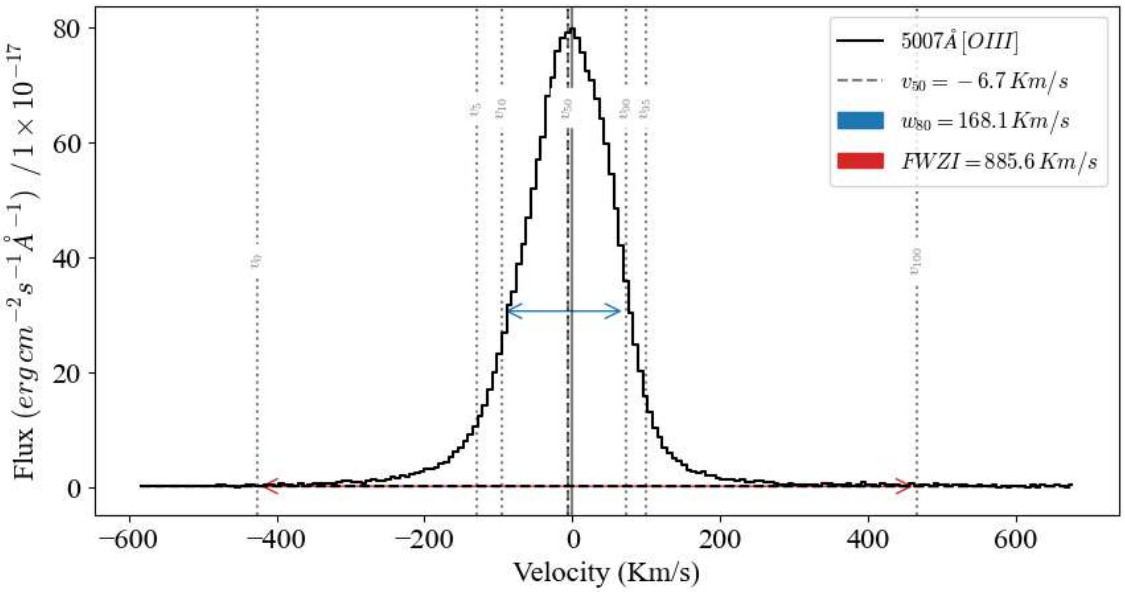

Figure A.12: Inter-percentile analysis of the *SLCE* J1154+2443, using the [OIII]λ5007Å emission-line. Each percentile is represented as a v_i gray dotted-line with i indicating the percentile. The full width zero intensity ($FWZI$) and the w_{80} ($v_{90} - v_{10}$) are shown as a red and blue arrow, respectively.

J1442-0209

Table A.13: Fit statistics of principal emission-lines in J1442-0209

λ_0 [a]	Ion	Model [b]	χ^2 [c]	χ^2_ν [d]	AIC [e]	BIC [f]	P(Gα) [g]
$6563 - 6548, 6584$	Hα + [NII]	G2	19115.1	30.7	2165.9	2201.5	0.0
		G3	12652.5	19.8	1951.6	2000.9	100.0
5007	[OIII]	G2	19592.2	52.4	1510.2	1533.9	0.0
		G3	12511.6	33.7	1345.8	1381.3	100.0
4861	Hβ	G2	16037.0	48.9	1285.6	1293.2	0.0
		G3	14991.9	45.9	1265.3	1276.7	100.0
$6717, 6731$	[SII]	G2	9239.0	20.4	1392.0	1416.8	0.0
		G3	8982.0	19.9	1375.1	1399.8	100.0

[a] Rest wavelength in Å.
[b] G2: Two gaussian components model, G3: Three gaussian components model.
[c] Chi square (see text for details).
[d] Reduced chi square (see text for details).
[e] Akaike Information Criteria (see text for details).
[f] Bayesian Information Criteria (see text for details).
[g] Likelihood percentage of model Gα to be correct respect the other (see text for details).

Table A.14: Results of the two Gaussian components model (G2) fitting of J1442-0209

λ_0 [a]	Ion	Comp. [b]	Δv_r [c]	σ_{int} [d]	Flux [e]	EM_f [f]	GlobalFlux [g]
6563	Hα	B	-51.2 ± 2.0	167.8 ± 2.2	164.0 ± 4.2	24.6	666.7 ± 6.4
		N	-3.4 ± 0.4	63.5 ± 0.5	502.7 ± 4.8	75.4	
5007	[OIII]	B	-59.7 ± 2.4	160.3 ± 2.3	296.6 ± 8.8	23.3	1274.5 ± 13.6
		N	-2.3 ± 0.5	62.2 ± 0.5	978.0 ± 10.4	76.7	
4959	[OIII]	B	-59.7 ± 2.4	160.3 ± 2.3	95.5 ± 2.7	22.7	420.2 ± 4.2
		N	-2.3 ± 0.5	62.2 ± 0.5	324.7 ± 3.3	77.3	
4861	Hβ	B	-51.2 ± 2.0	167.8 ± 2.2	39.4 ± 2.1	20.8	189.1 ± 3.2
		N	-3.4 ± 0.4	63.5 ± 0.5	149.7 ± 2.3	79.2	
6300	[OI]	B	-51.2 ± 2.0	168.1 ± 2.2	0.0 ± 0.3	0.0	5.9 ± 0.5
		N	-3.4 ± 0.4	64.2 ± 0.5	5.9 ± 0.3	100.0	
6548	[NII]	B	-51.2 ± 2.0	168.1 ± 2.2	2.8 ± 0.2	43.9	6.4 ± 0.3
		N	-3.4 ± 0.4	64.2 ± 0.5	3.6 ± 0.2	56.1	
6584	[NII]	B	-51.2 ± 2.0	168.1 ± 2.2	8.4 ± 0.7	43.9	19.2 ± 0.9
		N	-3.4 ± 0.4	64.2 ± 0.5	10.8 ± 0.6	56.1	
6717	[SII]	B	-51.2 ± 2.0	168.1 ± 2.2	2.1 ± 0.6	10.5	20.1 ± 0.8
		N	-3.4 ± 0.4	64.3 ± 0.5	18.0 ± 0.6	89.5	
6731	[SII]	B	-51.2 ± 2.0	168.1 ± 2.2	1.4 ± 0.5	8.9	15.1 ± 0.7
		N	-3.4 ± 0.4	64.3 ± 0.5	13.8 ± 0.5	91.1	

[a] Rest wavelength in Å.

[b] Component of the model.

[c] Velocity shift between the central peak of the emission-line and the center of the component (see text for details).

[d] Intrinsic velocity dispersion (see text for details).

[e] Flux of the component (10^{-17} erg s^{-1} cm^{-2}).

[f] Percentage of relative to global flux of the emission-line.

[g] Global flux of the emission-line (10^{-17} erg s^{-1} cm^{-2}).

Table A.15: Results of the three Gaussian components model (G3) fitting of J1442-0209

λ_0 [a]	Ion	Comp. [b]	Δv_r [c]	σ_{int} [d]	Flux [e]	EM_f [f]	GlobalFlux [g]
6563	Hα	B1	-65.3 ± 6.0	113.9 ± 3.6	131.6 ± 11.9	19.6	670.1 ± 16.2
		B2	-14.0 ± 6.1	236.4 ± 8.1	68.4 ± 6.2	10.2	
		N	0.9 ± 0.5	61.9 ± 0.6	470.1 ± 9.2	70.2	
5007	[OIII]	B1	-70.9 ± 4.9	127.7 ± 3.5	249.0 ± 16.7	19.4	1283.5 ± 23.2
		B2	-2.9 ± 11.9	272.3 ± 13.7	77.1 ± 9.6	6.0	
		N	0.2 ± 0.5	61.7 ± 0.5	957.4 ± 12.9	74.6	
4959	[OIII]	B1	-70.9 ± 4.9	127.7 ± 3.5	87.9 ± 3.4	20.9	420.3 ± 5.3
		B2	-2.9 ± 11.9	272.3 ± 13.7	16.7 ± 2.4	4.0	
		N	0.2 ± 0.5	61.7 ± 0.5	315.6 ± 3.3	75.1	
4861	Hβ	B1	-65.3 ± 6.0	113.9 ± 3.6	44.1 ± 2.8	23.5	187.7 ± 4.3
		B2	-14.0 ± 6.1	236.4 ± 8.1	5.8 ± 2.2	3.1	
		N	0.9 ± 0.5	61.9 ± 0.6	137.8 ± 2.4	73.4	
6300	[OI]	B1	-65.3 ± 6.0	114.3 ± 3.6	0.5 ± 0.5	8.0	6.0 ± 1.8
		B2	-14.0 ± 6.1	236.6 ± 8.1	0.0 ± 1.7	0.0	
		N	0.9 ± 0.5	62.6 ± 0.6	5.6 ± 0.4	92.0	
6548	[NII]	B1	-65.3 ± 6.0	114.3 ± 3.6	0.0 ± 0.0	0.0	6.7 ± 0.2
		B2	-14.0 ± 6.1	236.6 ± 8.1	2.7 ± 0.2	41.1	
		N	0.9 ± 0.5	62.6 ± 0.6	3.9 ± 0.1	58.9	
6584	[NII]	B1	-65.3 ± 6.0	114.3 ± 3.6	0.0 ± 0.0	0.0	20.0 ± 0.7
		B2	-14.0 ± 6.1	236.6 ± 8.1	8.2 ± 0.6	41.1	
		N	0.9 ± 0.5	62.6 ± 0.6	11.8 ± 0.4	58.9	
6717	[SII]	B1	-65.3 ± 6.0	114.3 ± 3.6	3.6 ± 0.9	17.8	20.2 ± 1.2
		B2	-14.0 ± 6.1	236.6 ± 8.1	0.0 ± 0.0	0.0	
		N	0.9 ± 0.5	62.6 ± 0.6	16.6 ± 0.8	82.2	
6731	[SII]	B1	-65.3 ± 6.0	114.3 ± 3.6	2.2 ± 0.6	14.2	15.1 ± 0.9
		B2	-14.0 ± 6.1	236.6 ± 8.1	0.0 ± 0.0	0.0	
		N	0.9 ± 0.5	62.6 ± 0.6	13.0 ± 0.6	85.8	

[a] Rest wavelength in Å.

[b] Component of the model.

[c] Velocity shift between the central peak of the emission-line and the center of the component (see text for details).

[d] Intrinsic velocity dispersion (see text for details).

[e] Flux of the component (10^{-17} erg s^{-1} cm^{-2}).

[f] Percentage of relative to global flux of the emission-line.

[g] Global flux of the emission-line (10^{-17} erg s^{-1} cm^{-2}).

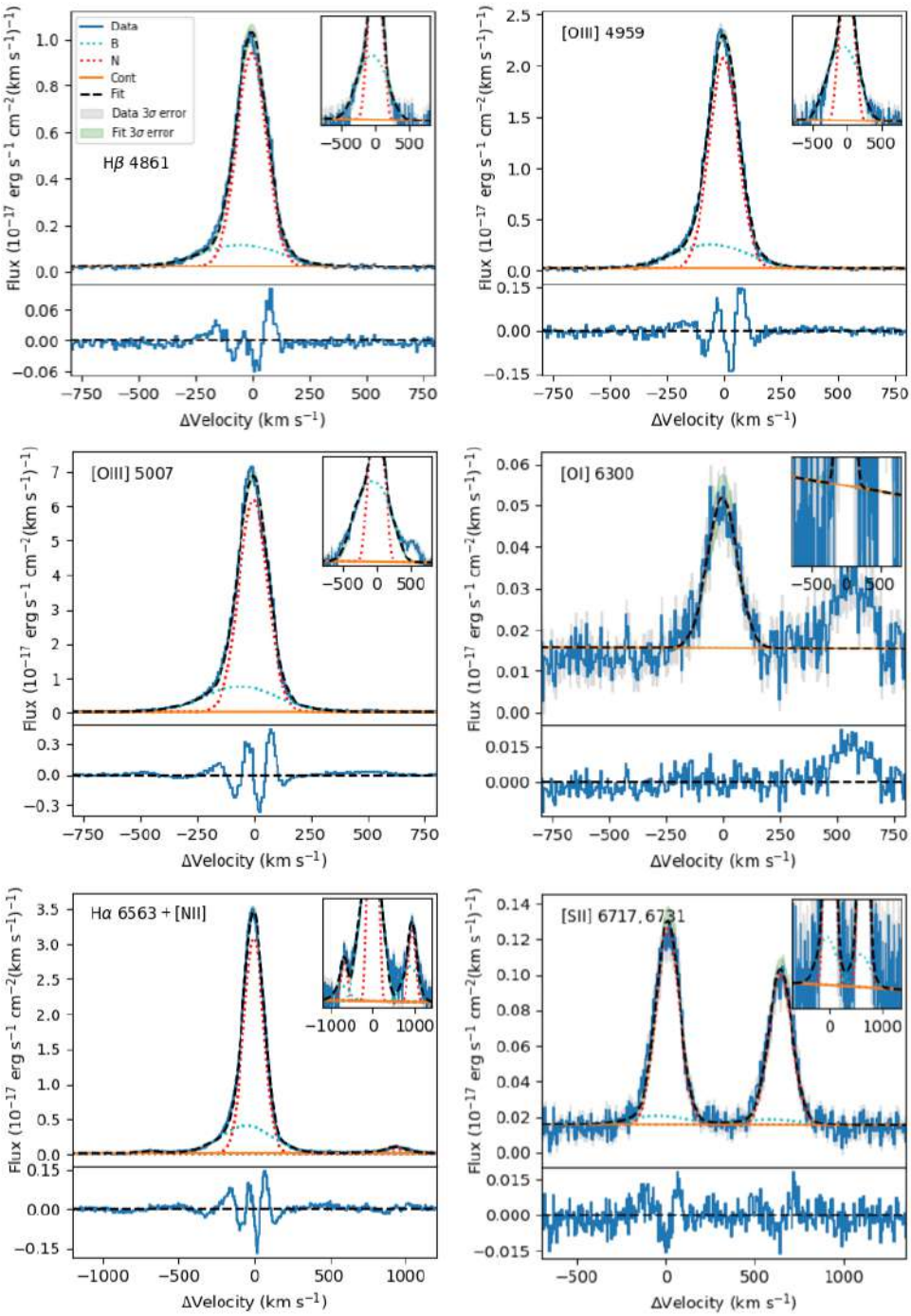

Figure A.13: The fit of faint and bright emission-line profiles of J1442-0209 with two gaussian component models (G2). The blue line represents the original data and the dashed black line the overall model that includes a broad component (B) shown as a cyan dotted line, and a narrow components (N) represented with a red dotted line respectively. The local continuum fitting (Cont) is shown as a solid orange line. We also show the 3σ error spectrum in gray and the 3σ error of the fitted model. A zoomed-in box is shown in the upper-right corner, with $y - axis$ in logarithmic scale. Details of the kinematics and fluxes by component are in Table A.14 , while fit statistics are in A.13.

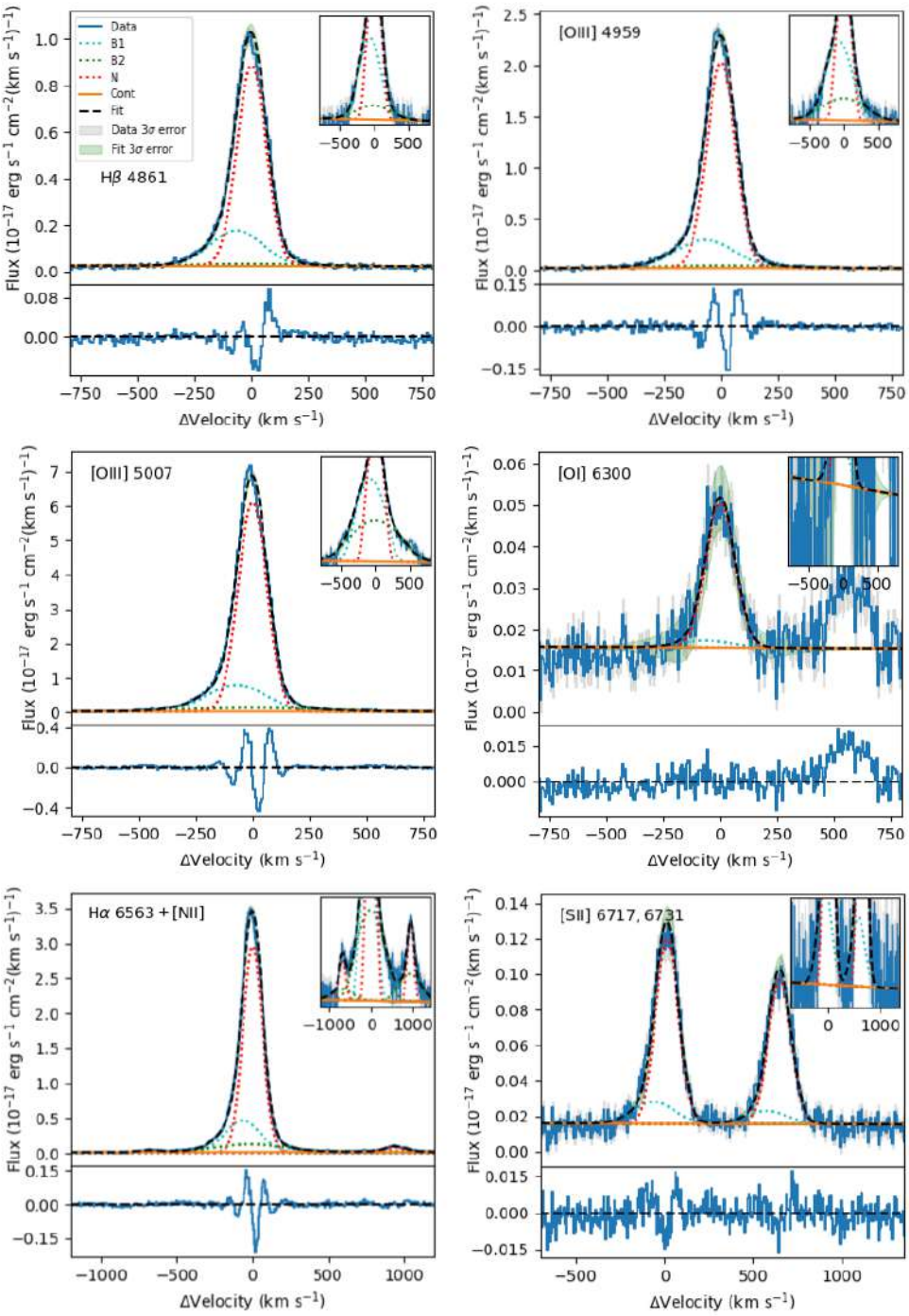

Figure A.14: The fit of faint and bright emission-line profiles of J1442-0209 with three gaussian component models (G3). The blue line represents the original data and the dashed black line the overall model that includes two broad components (B1-B2) shown as a cyan and a red dotted line respectively, and a narrow component (N) represented with a green dotted line. The local continuum fitting (Cont) is shown as a solid orange line. We also show the 3σ error spectrum in gray and the 3σ error of the fitted model. A zoomed-in box is shown in the upper-right corner, with $y - axis$ in logarithmic scale. Details of the kinematics and fluxes by component are in Table A.15 , while fit statistics are in A.13.

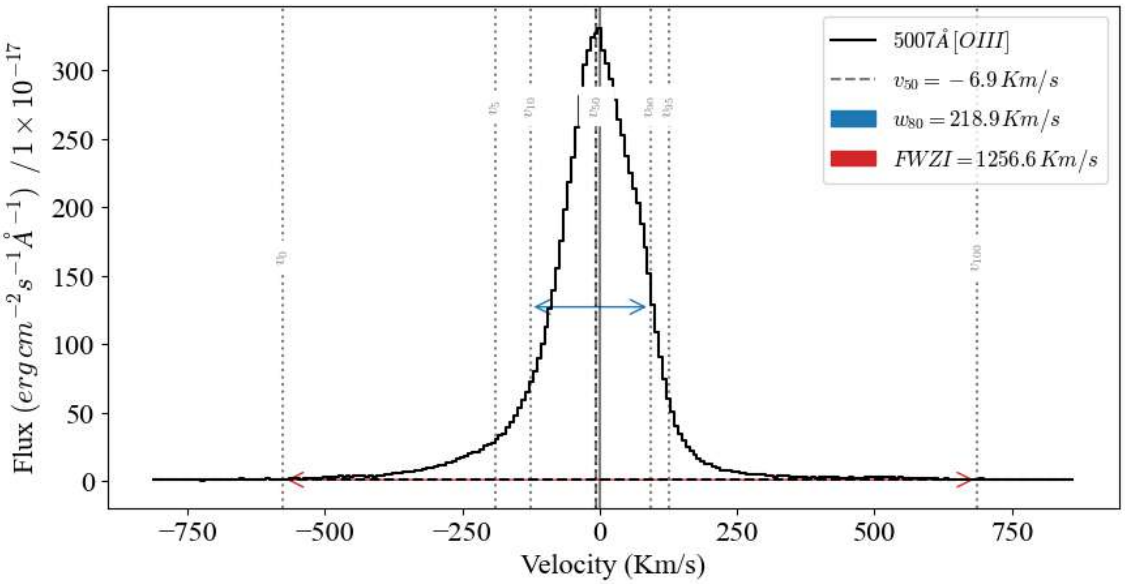

Figure A.15: Inter-percentile analysis of the *SLCE* J1442-0209, using the [OIII]λ5007Å emission-line. Each percentile is represented as a v_i gray dotted-line with i indicating the percentile. The full width zero intensity ($FWZI$) and the w_{80} ($v_{90} - v_{10}$) are shown as a red and blue arrow, respectively.

Appendix B

Ionized gas kinematics, components properties, and non-parametric analysis: *The Low-z Lyman Continuum Survey sample*

J003601+003307

Table B.1: Fit statistics of principal emission-lines in J003601+003307

λ_0 [a]	Ion	Model [b]	χ^2 [c]	χ^2_ν [d]	AIC [e]	BIC [f]	P(Gα) [g]
$6563 + 6548, 6584$	Hα + [NII]	G2	2955.1	8.2	784.8	816.1	0.0
		G3	1474.3	4.1	536.3	583.3	100.0
5007	[OIII]	G2	1587.0	8.2	426.3	446.1	0.0
		G3	762.8	4.00	285.7	315.4	100.0
4861	Hβ	G2	669.8	3.2	247.6	254.3	0.0
		G3	568.0	2.7	215.0	225.0	100.0
$6717, 6731$	[SII]	G2	640.7	2.1	233.1	248.0	41.3
		G3	631.1	2.1	232.4	254.8	58.7

[a] Rest wavelength in Å.
[b] G2: Two gaussian components model, G3: Three gaussian components model.
[c] Chi square (see text for details).
[d] Reduced chi square (see text for details).
[e] Akaike Information Criteria (see text for details).
[f] Bayesian Information Criteria (see text for details).
[g] Likelihood percentage of model Gα to be correct respect the other (see text for details).

Table B.2: Results of the two Gaussian components model (G2) fitting of J003601+003307

λ_0 [a]	Ion	Comp. [b]	Δv_r [c]	σ_{int} [d]	Flux [e]	EM_f [f]	GlobalFlux [g]
6563	Hα	B	-0.1 ± 1.4	99.6 ± 2.4	174.4 ± 6.7	42.6	409.4 ± 9.6
		N	-1.9 ± 0.4	37.3 ± 0.7	235.1 ± 6.8	57.4	
5007	[OIII]	B	-3.6 ± 0.9	92.4 ± 1.5	308.1 ± 9.2	39.8	773.5 ± 13.3
		N	-1.1 ± 0.3	37.5 ± 0.5	465.4 ± 9.5	60.2	
4959	[OIII]	B	-3.6 ± 0.9	92.4 ± 1.5	102.0 ± 2.2	39.6	257.6 ± 2.8
		N	-1.1 ± 0.3	37.5 ± 0.5	155.6 ± 1.8	60.4	
4861	Hβ	B	-0.1 ± 1.4	99.6 ± 2.4	46.5 ± 1.5	36.6	127.1 ± 2.0
		N	-1.9 ± 0.4	37.3 ± 0.7	80.6 ± 1.3	63.4	
6300	[OI]	B	-0.1 ± 1.4	100.0 ± 2.4	0.9 ± 0.8	41.7	2.1 ± 1.0
		N	-1.9 ± 0.4	38.5 ± 0.7	1.2 ± 0.7	58.3	
6548	[NII]	B	-0.1 ± 1.4	100.0 ± 2.4	2.9 ± 0.5	63.8	4.6 ± 0.6
		N	-1.9 ± 0.4	38.4 ± 0.7	1.7 ± 0.3	36.2	
6584	[NII]	B	-0.1 ± 1.4	100.0 ± 2.4	8.8 ± 1.5	63.8	13.8 ± 1.8
		N	-1.9 ± 0.4	38.4 ± 0.7	5.0 ± 1.0	36.2	
6717	[SII]	B	-0.1 ± 1.4	100.0 ± 2.4	0.5 ± 0.7	8.7	5.5 ± 0.8
		N	-1.9 ± 0.4	38.5 ± 0.7	5.1 ± 0.4	91.3	
6731	[SII]	B	-0.1 ± 1.4	100.0 ± 2.4	0.5 ± 0.7	9.2	5.2 ± 0.8
		N	-1.9 ± 0.4	38.5 ± 0.7	4.7 ± 0.4	90.8	

[a] Rest wavelength in Å.
[b] Component of the model.
[c] Velocity shift between the central peak of the emission-line and the center of the component (see text for details).
[d] Intrinsic velocity dispersion (see text for details).
[e] Flux of the component (10^{-17} erg s^{-1} cm^{-2}).
[f] Percentage of relative to global flux of the emission-line.
[g] Global flux of the emission-line (10^{-17} erg s^{-1} cm^{-2}).

Table B.3: Results of the three Gaussian components model (G3) fitting of J003601+003307

λ_0[a]	Ion	Comp.[b]	Δv_r[c]	σ_{int}[d]	Flux[e]	EM_f[f]	GlobalFlux[g]
6563	Hα	N1	-2.6 ± 0.7	52.7 ± 2.2	228.3 ± 18.1	54.3	420.5 ± 27.9
		B	6.6 ± 2.6	152.2 ± 5.1	104.6 ± 4.9	24.9	
		N2	-1.0 ± 0.8	27.3 ± 2.3	87.6 ± 20.6	20.8	
5007	[OIII]	N1	-3.1 ± 0.5	59.6 ± 1.8	409.3 ± 15.0	52.4	780.5 ± 27.2
		B	-1.5 ± 2.4	137.3 ± 5.6	121.4 ± 10.7	15.6	
		N2	-0.2 ± 0.4	29.6 ± 0.9	249.8 ± 20.0	32.0	
4959	[OIII]	N1	-3.1 ± 0.5	59.6 ± 1.8	132.3 ± 3.8	50.8	260.5 ± 5.1
		B	-1.5 ± 2.4	137.3 ± 5.6	42.8 ± 2.6	16.4	
		N2	-0.2 ± 0.4	29.6 ± 0.9	85.4 ± 2.3	32.8	
4861	Hβ	N1	-2.6 ± 0.7	52.7 ± 2.2	82.5 ± 2.4	64.6	127.7 ± 3.4
		B	6.6 ± 2.6	152.2 ± 5.1	19.9 ± 1.6	15.6	
		N2	-1.0 ± 0.8	27.3 ± 2.3	25.3 ± 1.8	19.8	
6300	[OI]	N1	-2.6 ± 0.7	53.5 ± 2.2	1.0 ± 1.4	47.6	2.1 ± 2.0
		B	6.6 ± 2.6	152.5 ± 5.1	0.4 ± 1.0	18.4	
		N2	-1.0 ± 0.8	28.8 ± 2.3	0.7 ± 1.0	34.0	
6548	[NII]	N1	-2.6 ± 0.7	53.4 ± 2.2	0.4 ± 0.6	7.6	5.4 ± 0.9
		B	6.6 ± 2.6	152.5 ± 5.1	3.6 ± 0.5	66.4	
		N2	-1.0 ± 0.8	28.8 ± 2.3	1.4 ± 0.4	26.1	
6584	[NII]	N1	-2.6 ± 0.7	53.4 ± 2.2	1.2 ± 1.9	7.6	16.2 ± 2.7
		B	6.6 ± 2.6	152.5 ± 5.1	10.7 ± 1.4	66.4	
		N2	-1.0 ± 0.8	28.8 ± 2.3	4.2 ± 1.2	26.1	
6717	[SII]	N1	-2.6 ± 0.7	53.5 ± 2.2	2.5 ± 1.1	44.2	5.6 ± 1.5
		B	6.6 ± 2.6	152.5 ± 5.1	0.3 ± 0.9	5.1	
		N2	-1.0 ± 0.8	28.8 ± 2.3	2.8 ± 0.6	50.7	
6731	[SII]	N1	-2.6 ± 0.7	53.5 ± 2.2	1.9 ± 1.0	35.7	5.3 ± 1.4
		B	6.6 ± 2.6	152.5 ± 5.1	0.5 ± 0.8	10.2	
		N2	-1.0 ± 0.8	28.8 ± 2.3	2.8 ± 0.6	54.1	

[a] Rest wavelength in Å.

[b] Component of the model.

[c] Velocity shift between the central peak of the emission-line and the center of the component (see text for details).

[d] Intrinsic velocity dispersion (see text for details).

[e] Flux of the component (10^{-17} erg s^{-1} cm^{-2}).

[f] Percentage of relative to global flux of the emission-line.

[g] Global flux of the emission-line (10^{-17} erg s^{-1} cm^{-2}).

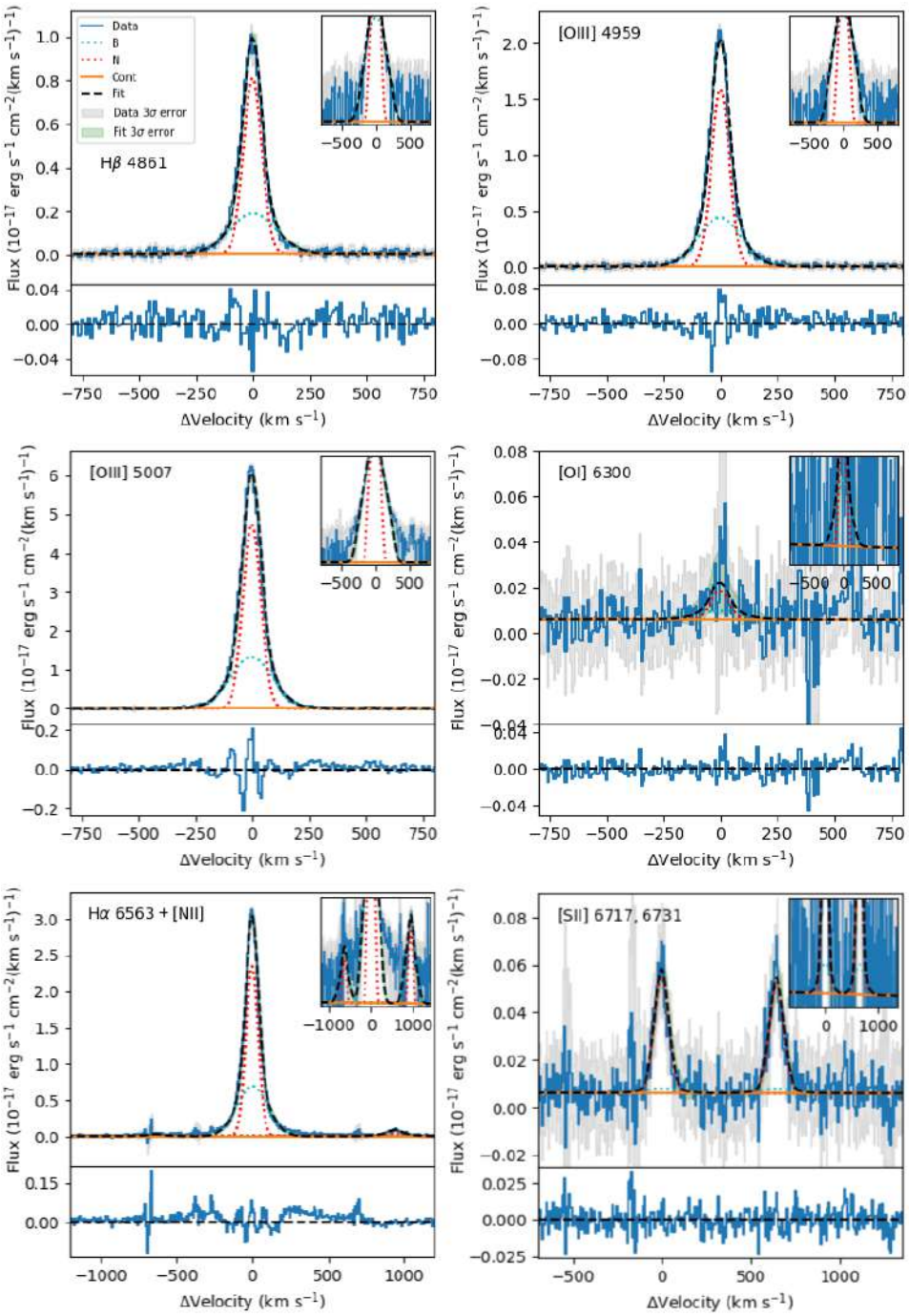

Figure B.1: The fit of faint and bright emission-line profiles of J003601+003307 with two gaussian component models (G2). The blue line represents the original data and the dashed black line the overall model that includes a broad component (B) shown as a cyan dotted line, and a narrow components (N) represented with a red dotted line respectively. The local continuum fitting (Cont) is shown as a solid orange line. We also show the 3σ error spectrum in gray and the 3σ error of the fitted model. A zoomed-in box is shown in the upper-right corner, with $y-axis$ in logarithmic scale. Details of the kinematics and fluxes by component are in Table B.2 , while fit statistics are in B.1.

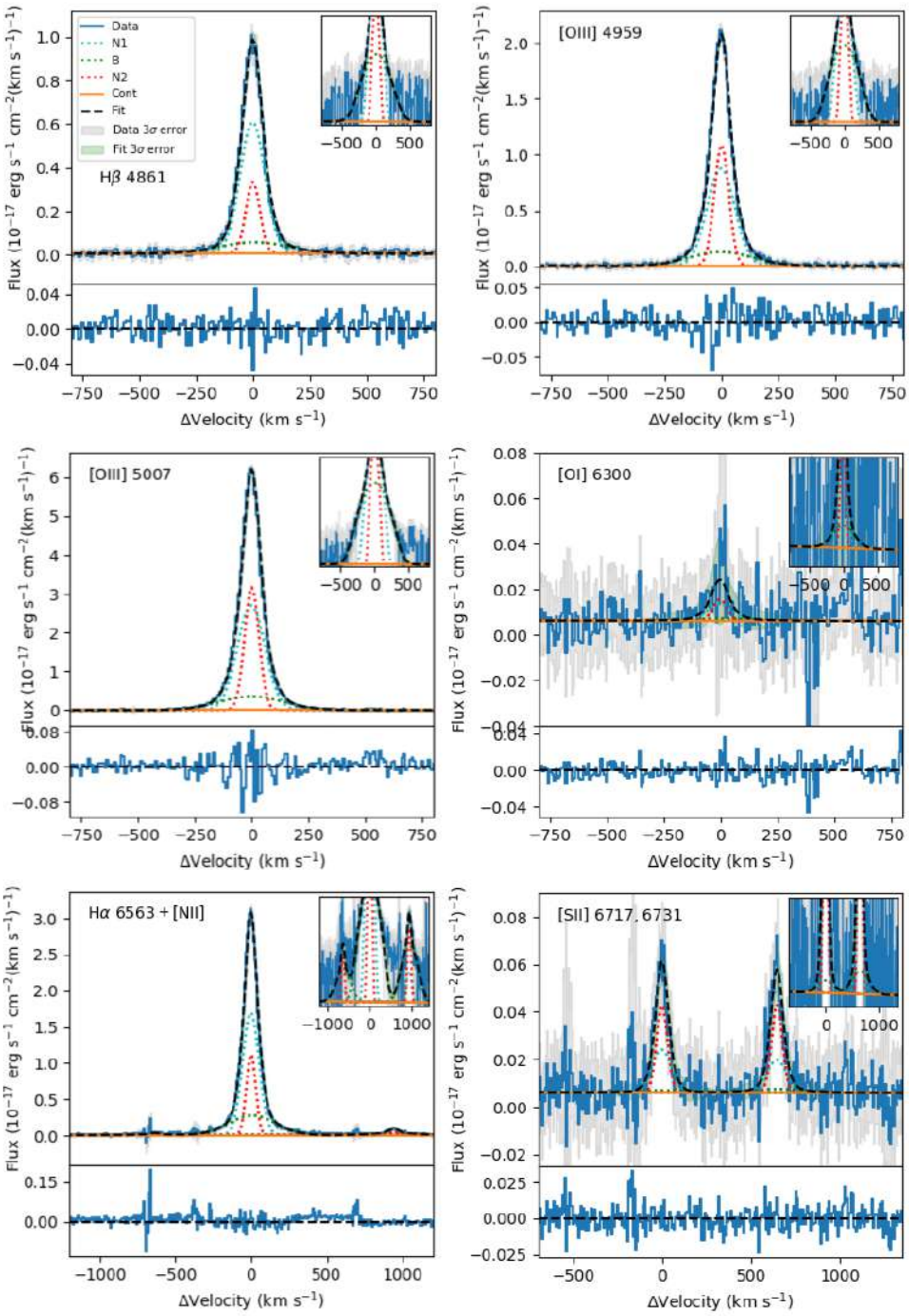

Figure B.2: The fit of faint and bright emission-line profiles of J003601+003307 with three gaussian component models (G3). The blue line represents the original data and the dashed black line the overall model that includes a broad component (B) shown as a green dotted line , and two narrow components (N1-N2) represented with a cyan and a red dotted line. The local continuum fitting (Cont) is shown as a solid orange line. We also show the 3σ error spectrum in gray and the 3σ error of the fitted model. A zoomed-in box is shown in the upper-right corner, with $y-axis$ in logarithmic scale. Details of the kinematics and fluxes by component are in Table B.3 , while fit statistics are in B.1.

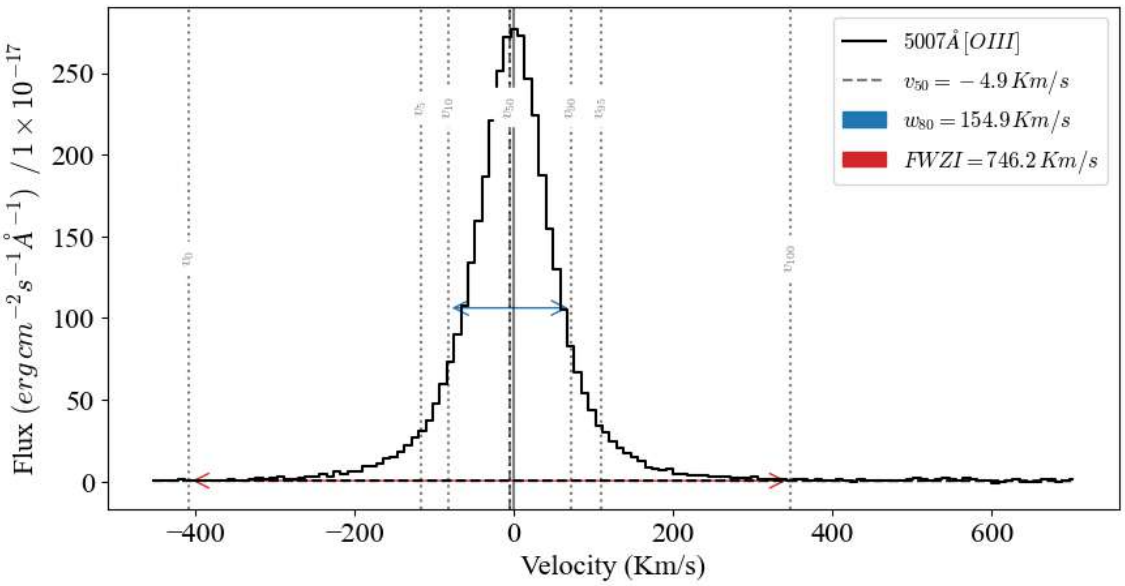

Figure B.3: Inter-percentile analysis of the *NLCE* J003601+003307, using the [OIII]λ5007Å emission-line. Each percentile is represented as a v_i gray dotted-line with i indicating the percentile. The full width zero intensity ($FWZI$) and the w_{80} ($v_{90} - v_{10}$) are shown as a red and blue arrow, respectively.

J004743+015440

Table B.4: Fit statistics of principal emission-lines in J004743+015440

λ_0 [a]	Ion	Model [b]	χ^2 [c]	χ^2_ν [d]	AIC [e]	BIC [f]	P(Gα) [g]
$6563 + 6548, 6584$	Hα + [NII]	G2	2812.1	3.8	1003.9	1040.8	0.0
		G3	2310.0	3.2	866.4	921.7	100.0
5007	[OIII]	G2	3272.1	10.8	742.6	765.0	0.0
		G3	2697.0	9.0	688.6	722.3	100.0
4861	Hβ	G2	1654.8	5.2	531.1	538.6	16.1
		G3	1628.0	5.1	527.8	539.2	83.9
$6717, 6731$	[SII]	G2	1229.7	3.9	438.8	453.9	18.2
		G3	1203.3	3.8	435.8	458.4	81.8

[a] Rest wavelength in Å.
[b] G2: Two gaussian components model, G3: Three gaussian components model.
[c] Chi square (see text for details).
[d] Reduced chi square (see text for details).
[e] Akaike Information Criteria (see text for details).
[f] Bayesian Information Criteria (see text for details).
[g] Likelihood percentage of model Gα to be correct respect the other (see text for details).

Table B.5: Results of the two Gaussian components model (G2) fitting of J004743+015440

λ_0 [a]	Ion	Comp. [b]	Δv_r [c]	σ_{int} [d]	Flux [e]	EM_f [f]	GlobalFlux [g]
6563	Hα	B	-32.9 ± 0.8	140.5 ± 0.9	285.6 ± 2.6	56.1	508.7 ± 3.8
		N	1.3 ± 0.3	48.0 ± 0.4	223.1 ± 2.8	43.9	
5007	[OIII]	B	-25.6 ± 0.9	134.1 ± 1.1	471.3 ± 5.3	50.5	932.5 ± 7.6
		N	3.1 ± 0.3	44.8 ± 0.4	461.2 ± 5.4	49.5	
4959	[OIII]	B	-25.6 ± 0.9	134.1 ± 1.1	163.4 ± 2.0	51.9	314.9 ± 2.5
		N	3.1 ± 0.3	44.8 ± 0.4	151.5 ± 1.4	48.1	
4861	Hβ	B	-32.9 ± 0.8	140.5 ± 0.9	97.1 ± 2.0	55.6	174.7 ± 2.4
		N	1.3 ± 0.3	48.0 ± 0.4	77.6 ± 1.3	44.4	
6300	[OI]	B	-32.9 ± 0.8	140.8 ± 0.9	5.3 ± 0.7	75.1	7.0 ± 0.8
		N	1.3 ± 0.3	48.9 ± 0.4	1.7 ± 0.4	24.9	
6548	[NII]	B	-32.9 ± 0.8	140.8 ± 0.9	7.6 ± 0.3	80.1	9.5 ± 0.4
		N	1.3 ± 0.3	48.9 ± 0.4	1.9 ± 0.2	19.9	
6584	[NII]	B	-32.9 ± 0.8	140.8 ± 0.9	22.8 ± 1.0	80.1	28.4 ± 1.2
		N	1.3 ± 0.3	48.9 ± 0.4	5.7 ± 0.6	19.9	
6717	[SII]	B	-32.9 ± 0.8	140.8 ± 0.9	19.1 ± 0.9	73.7	25.9 ± 1.1
		N	1.3 ± 0.3	48.9 ± 0.4	6.8 ± 0.6	26.3	
6731	[SII]	B	-32.9 ± 0.8	140.8 ± 0.9	13.4 ± 0.9	70.5	19.0 ± 0.0
		N	1.3 ± 0.3	48.9 ± 0.4	5.6 ± 0.5	29.5	

[a] Rest wavelength in Å.
[b] Component of the model.
[c] Velocity shift between the central peak of the emission-line and the center of the component (see text for details).
[d] Intrinsic velocity dispersion (see text for details).
[e] Flux of the component (10^{-17} erg s^{-1} cm^{-2}).
[f] Percentage of relative to global flux of the emission-line.
[g] Global flux of the emission-line (10^{-17} erg s^{-1} cm^{-2}).

Table B.6: Results of the three Gaussian components model (G3) fitting of J004743+015440

λ_0 [a]	Ion	Comp. [b]	Δv_r [c]	σ_{int} [d]	Flux [e]	EM_f [f]	GlobalFlux [g]
6563	Hα	B1	-43.2 ± 8.1	233.4 ± 19.5	62.1 ± 12.8	12.1	513.0 ± 17.8
		B2	-28.9 ± 1.3	121.3 ± 2.8	249.6 ± 11.7	48.7	
		N	2.1 ± 0.4	45.7 ± 0.5	201.3 ± 3.9	39.2	
5007	[OIII]	B1	-60.1 ± 14.1	210.2 ± 20.5	102.1 ± 31.0	10.9	939.9 ± 42.0
		B2	-18.7 ± 1.8	116.5 ± 4.0	412.2 ± 27.0	43.9	
		N	3.3 ± 0.3	43.2 ± 0.5	425.7 ± 8.4	45.3	
4959	[OIII]	B1	-60.1 ± 14.1	210.2 ± 20.5	34.2 ± 3.9	10.8	317.0 ± 5.9
		B2	-18.7 ± 1.8	116.5 ± 4.0	143.5 ± 4.1	45.3	
		N	3.3 ± 0.3	43.2 ± 0.5	139.3 ± 1.6	43.9	
4861	Hβ	B1	-43.2 ± 8.1	233.4 ± 19.5	20.7 ± 3.6	11.7	176.5 ± 5.4
		B2	-28.9 ± 1.3	121.3 ± 2.8	85.6 ± 3.7	48.5	
		N	2.1 ± 0.4	45.7 ± 0.5	70.2 ± 1.4	39.8	
6300	[OI]	B1	-43.2 ± 8.1	233.6 ± 19.5	1.0 ± 1.7	13.9	7.1 ± 2.4
		B2	-28.9 ± 1.3	121.7 ± 2.8	4.7 ± 1.6	66.2	
		N	2.1 ± 0.4	46.6 ± 0.5	1.4 ± 0.5	19.8	
6548	[NII]	B1	-43.2 ± 8.1	233.6 ± 19.5	3.5 ± 1.0	35.3	10.0 ± 1.4
		B2	-28.9 ± 1.3	121.7 ± 2.8	4.6 ± 0.9	45.7	
		N	2.1 ± 0.4	46.6 ± 0.5	1.9 ± 0.2	19.0	
6584	[NII]	B1	-43.2 ± 8.1	233.6 ± 19.5	10.6 ± 3.0	35.3	29.9 ± 4.1
		B2	-28.9 ± 1.3	121.7 ± 2.8	13.7 ± 2.8	45.7	
		N	2.1 ± 0.4	46.6 ± 0.5	5.7 ± 0.6	19.0	
6717	[SII]	B1	-43.2 ± 8.1	233.6 ± 19.5	7.0 ± 2.0	26.3	26.7 ± 2.8
		B2	-28.9 ± 1.3	121.7 ± 2.8	13.1 ± 1.9	49.1	
		N	2.1 ± 0.4	46.7 ± 0.5	6.6 ± 0.7	24.5	
6731	[SII]	B1	-43.2 ± 8.1	233.6 ± 19.5	6.5 ± 2.2	32.5	19.9 ± 0.0
		B2	-28.9 ± 1.3	121.7 ± 2.8	7.8 ± 1.9	39.2	
		N	2.1 ± 0.4	46.7 ± 0.5	5.6 ± 0.6	28.3	

[a] Rest wavelength in Å.

[b] Component of the model.

[c] Velocity shift between the central peak of the emission-line and the center of the component (see text for details).

[d] Intrinsic velocity dispersion (see text for details).

[e] Flux of the component (10^{-17} erg s^{-1} cm^{-2}).

[f] Percentage of relative to global flux of the emission-line.

[g] Global flux of the emission-line (10^{-17} erg s^{-1} cm^{-2}).

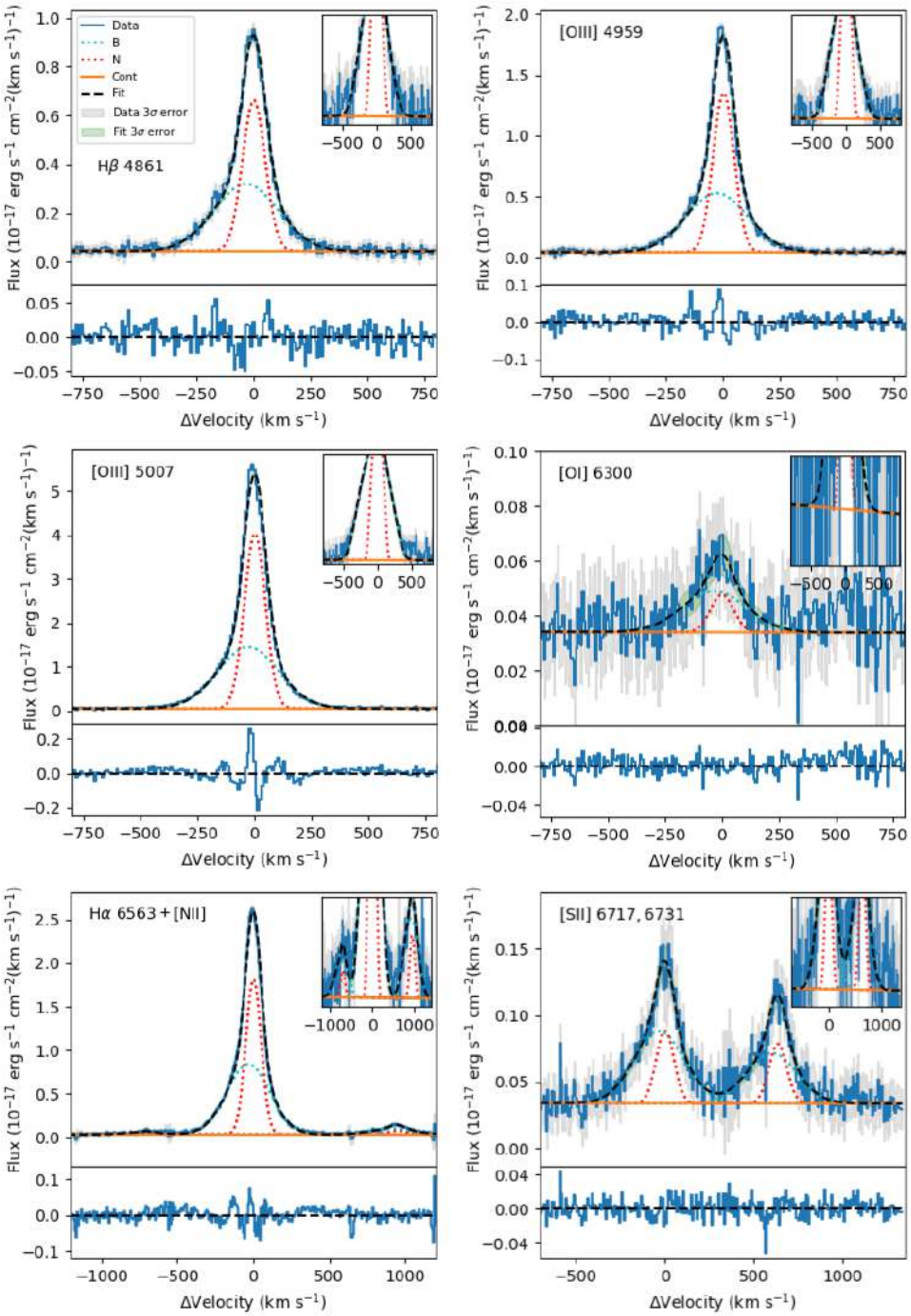

Figure B.4: The fit of faint and bright emission-line profiles of J004743+015440 with two gaussian component models (G2). The blue line represents the original data and the dashed black line the overall model that includes a broad component (B) shown as a cyan dotted line, and a narrow components (N) represented with a red dotted line respectively. The local continuum fitting (Cont) is shown as a solid orange line. We also show the 3σ error spectrum in gray and the 3σ error of the fitted model. A zoomed-in box is shown in the upper-right corner, with $y-axis$ in logarithmic scale. Details of the kinematics and fluxes by component are in Table B.5 , while fit statistics are in B.4.

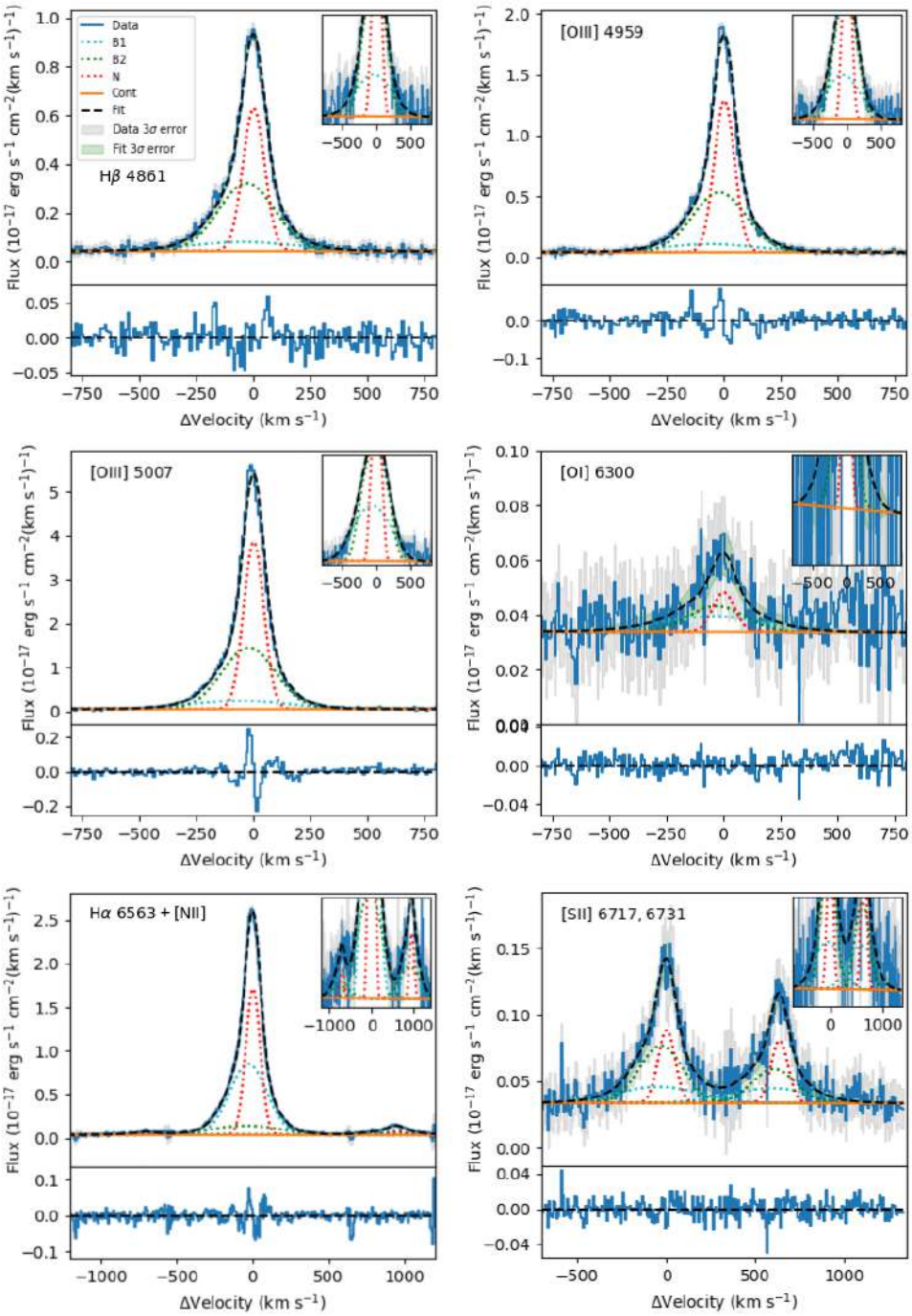

Figure B.5: The fit of faint and bright emission-line profiles of J004743+015440 with three gaussian component models (G3). The blue line represents the original data and the dashed black line the overall model that includes two broad components (B1-B2) shown as a cyan and a green dotted line respectively, and a narrow components (N) represented with a red dotted line. The local continuum fitting (Cont) is shown as a solid orange line. We also show the 3σ error spectrum in gray and the 3σ error of the fitted model. A zoomed-in box is shown in the upper-right corner, with $y-axis$ in logarithmic scale. Details of the kinematics and fluxes by component are in Table B.6 , while fit statistics are in B.4.

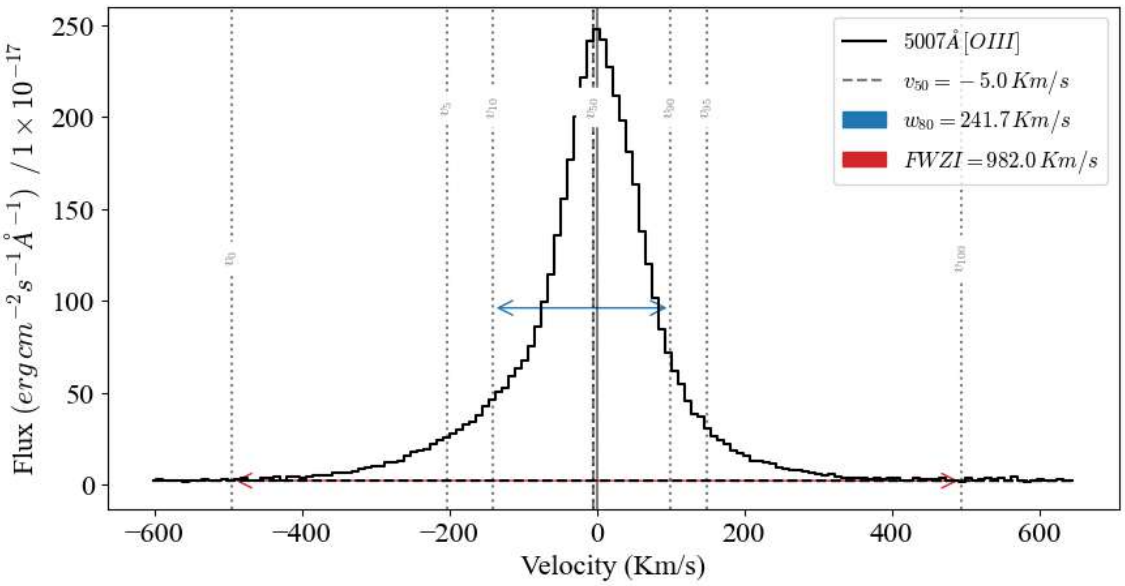

Figure B.6: Inter-percentile analysis of the *WLCE* J004743+015440, using the [OIII]λ5007Å emission-line. Each percentile is represented as a v_i gray dotted-line with i indicating the percentile. The full width zero intensity ($FWZI$) and the w_{80} ($v_{90} - v_{10}$) are shown as a red and blue arrow, respectively.

J011309+000223

Table B.7: Fit statistics of principal emission-lines in J011309+000223

λ_0 [a]	Ion	Model [b]	χ^2 [c]	χ^2_ν [d]	AIC [e]	BIC [f]	P(Gα) [g]
$6563 + 6548, 6584$	Hα + [NII]	G2	2585.3	6.0	795.2	827.9	0.0
		G3	1215.0	2.8	470.9	520.0	100.0
5007	[OIII]	G2	2608.6	11.2	584.6	605.5	0.0
		G3	1351.4	5.9	432.8	464.1	100.0
4861	Hβ	G2	772.4	3.0	287.1	294.2	5.2
		G3	749.7	2.9	281.3	292.0	94.8
$6717, 6731$	[SII]	G2	929.4	2.4	347.3	363.1	10.4
		G3	909.5	2.4	343.0	366.7	89.6

[a] Rest wavelength in Å.
[b] G2: Two gaussian components model, G3: Three gaussian components model.
[c] Chi square (see text for details).
[d] Reduced chi square (see text for details).
[e] Akaike Information Criteria (see text for details).
[f] Bayesian Information Criteria (see text for details).
[g] Likelihood percentage of model Gα to be correct respect the other (see text for details).

Table B.8: Results of the two Gaussian components model (G2) fitting of J011309+000223

λ_0 [a]	Ion	Comp. [b]	Δv_r [c]	σ_{int} [d]	Flux [e]	EM_f [f]	GlobalFlux [g]
6563	Hα	B	-6.4 ± 0.7	93.9 ± 1.0	208.1 ± 4.3	62.3	333.9 ± 6.1
		N	9.4 ± 0.4	41.0 ± 0.7	125.8 ± 4.4	37.7	
5007	[OIII]	B	-5.5 ± 1.0	87.8 ± 1.3	315.3 ± 9.6	58.7	537.2 ± 13.7
		N	12.6 ± 0.5	39.8 ± 0.9	221.9 ± 9.8	41.3	
4959	[OIII]	B	-5.5 ± 1.0	87.8 ± 0.0	103.3 ± 1.7	58.0	178.1 ± 2.2
		N	12.6 ± 0.5	39.8 ± 0.0	74.9 ± 1.3	42.0	
4861	Hβ	B	-6.4 ± 0.7	93.9 ± 1.0	65.3 ± 1.7	58.5	111.6 ± 2.1
		N	9.4 ± 0.4	41.0 ± 0.7	46.3 ± 1.2	41.5	
6300	[OI]	B	-6.4 ± 0.7	94.4 ± 1.0	2.2 ± 0.7	42.4	5.2 ± 0.9
		N	9.4 ± 0.4	42.1 ± 0.7	3.0 ± 0.5	57.6	
6548	[NII]	B	-6.4 ± 0.7	94.4 ± 1.0	3.7 ± 0.4	70.4	5.3 ± 0.4
		N	9.4 ± 0.4	42.1 ± 0.7	1.6 ± 0.2	29.6	
6584	[NII]	B	-6.4 ± 0.7	94.4 ± 1.0	11.1 ± 1.1	70.4	15.8 ± 1.3
		N	9.4 ± 0.4	42.1 ± 0.7	4.7 ± 0.7	29.6	
6717	[SII]	B	-6.4 ± 0.7	94.4 ± 1.0	16.2 ± 0.9	69.4	23.3 ± 1.1
		N	9.4 ± 0.4	42.1 ± 0.7	7.1 ± 0.6	30.6	
6731	[SII]	B	-6.4 ± 0.7	94.4 ± 1.0	11.7 ± 0.8	71.9	16.3 ± 0.9
		N	9.4 ± 0.4	42.1 ± 0.7	4.6 ± 0.5	28.1	

[a] Rest wavelength in Å.

[b] Component of the model.

[c] Velocity shift between the central peak of the emission-line and the center of the component (see text for details).

[d] Intrinsic velocity dispersion (see text for details).

[e] Flux of the component (10^{-17} erg s^{-1} cm^{-2}).

[f] Percentage of relative to global flux of the emission-line.

[g] Global flux of the emission-line (10^{-17} erg s^{-1} cm^{-2}).

Table B.9: Results of the three Gaussian components model (G3) fitting of J011309+000223

λ_0 [a]	Ion	Comp. [b]	Δv_r [c]	σ_{int} [d]	Flux [e]	EM_f [f]	GlobalFlux [g]
6563	Hα	N1	-5.8 ± 0.7	73.3 ± 1.2	203.9 ± 5.2	60.1	339.1 ± 8.4
		B	6.6 ± 3.3	157.4 ± 6.2	58.1 ± 5.0	17.1	
		N2	14.7 ± 0.6	34.6 ± 0.9	77.1 ± 4.3	22.7	
5007	[OIII]	N1	-3.5 ± 1.0	70.8 ± 1.6	320.4 ± 10.7	58.5	547.3 ± 17.5
		B	-2.0 ± 5.3	165.7 ± 10.3	74.7 ± 8.5	13.6	
		N2	16.5 ± 0.7	35.4 ± 1.0	152.2 ± 10.9	27.8	
4959	[OIII]	N1	-3.5 ± 1.0	70.8 ± 1.6	102.3 ± 2.4	56.2	182.1 ± 3.4
		B	-2.0 ± 5.3	165.7 ± 10.3	26.9 ± 2.0	14.8	
		N2	16.5 ± 0.7	35.4 ± 1.0	52.9 ± 1.4	29.1	
4861	Hβ	N1	-5.8 ± 0.7	73.3 ± 1.2	72.5 ± 2.6	64.8	112.0 ± 3.7
		B	6.6 ± 3.3	157.4 ± 6.2	12.5 ± 2.3	11.2	
		N2	14.7 ± 0.6	34.6 ± 0.9	26.9 ± 1.3	24.1	
6300	[OI]	N1	-5.8 ± 0.7	73.9 ± 1.2	3.4 ± 0.7	65.1	5.2 ± 1.4
		B	6.6 ± 3.3	157.7 ± 6.2	0.0 ± 1.2	0.0	
		N2	14.7 ± 0.6	35.9 ± 0.9	1.8 ± 0.5	34.9	
6548	[NII]	N1	-5.8 ± 0.7	73.9 ± 1.2	2.1 ± 0.4	36.7	5.6 ± 0.5
		B	6.6 ± 3.3	157.7 ± 6.2	2.2 ± 0.3	39.8	
		N2	14.7 ± 0.6	35.9 ± 0.9	1.3 ± 0.2	23.5	
6584	[NII]	N1	-5.8 ± 0.7	73.9 ± 1.2	6.2 ± 1.3	36.7	16.8 ± 1.7
		B	6.6 ± 3.3	157.7 ± 6.2	6.7 ± 1.0	39.8	
		N2	14.7 ± 0.6	35.9 ± 0.9	4.0 ± 0.6	23.5	
6717	[SII]	N1	-5.8 ± 0.7	74.0 ± 1.2	12.7 ± 1.3	52.5	24.2 ± 2.2
		B	6.6 ± 3.3	157.7 ± 6.2	6.7 ± 1.5	27.6	
		N2	14.7 ± 0.6	35.9 ± 0.9	4.8 ± 0.5	19.9	
6731	[SII]	N1	-5.8 ± 0.7	74.0 ± 1.2	10.7 ± 1.4	64.7	16.6 ± 1.9
		B	6.6 ± 3.3	157.7 ± 6.2	3.4 ± 1.1	20.4	
		N2	14.7 ± 0.6	35.9 ± 0.9	2.5 ± 0.6	14.8	

[a] Rest wavelength in Å.

[b] Component of the model.

[c] Velocity shift between the central peak of the emission-line and the center of the component (see text for details).

[d] Intrinsic velocity dispersion (see text for details).

[e] Flux of the component (10^{-17} erg s^{-1} cm^{-2}).

[f] Percentage of relative to global flux of the emission-line.

[g] Global flux of the emission-line (10^{-17} erg s^{-1} cm^{-2}).

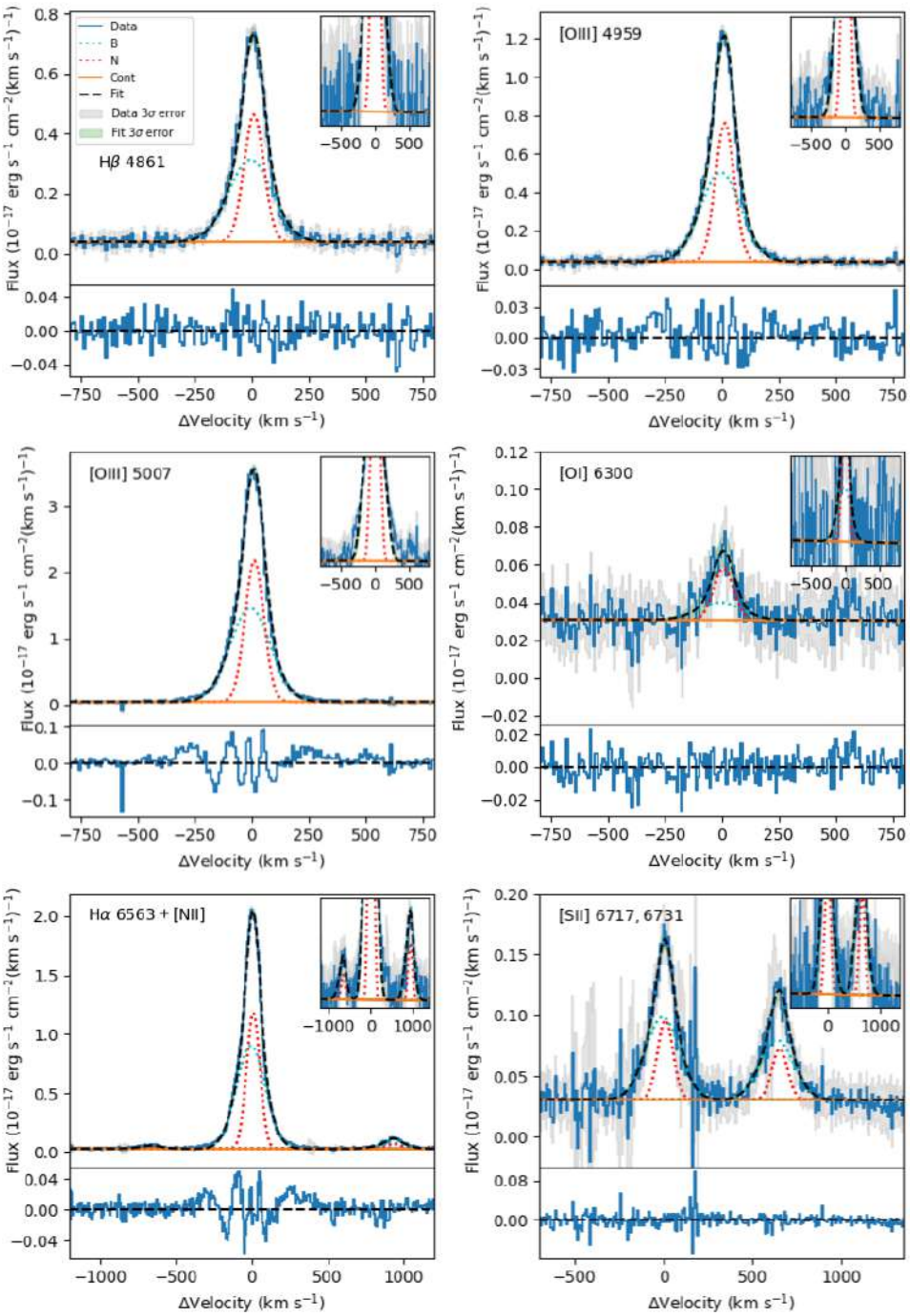

Figure B.7: The fit of faint and bright emission-line profiles of J011309+000223 with two gaussian component models (G2). The blue line represents the original data and the dashed black line the overall model that includes a broad component (B) shown as a cyan dotted line, and a narrow components (N) represented with a red dotted line respectively. The local continuum fitting (Cont) is shown as a solid orange line. We also show the 3σ error spectrum in gray and the 3σ error of the fitted model. A zoomed-in box is shown in the upper-right corner, with $y-axis$ in logarithmic scale. Details of the kinematics and fluxes by component are in Table B.8 , while fit statistics are in B.7.

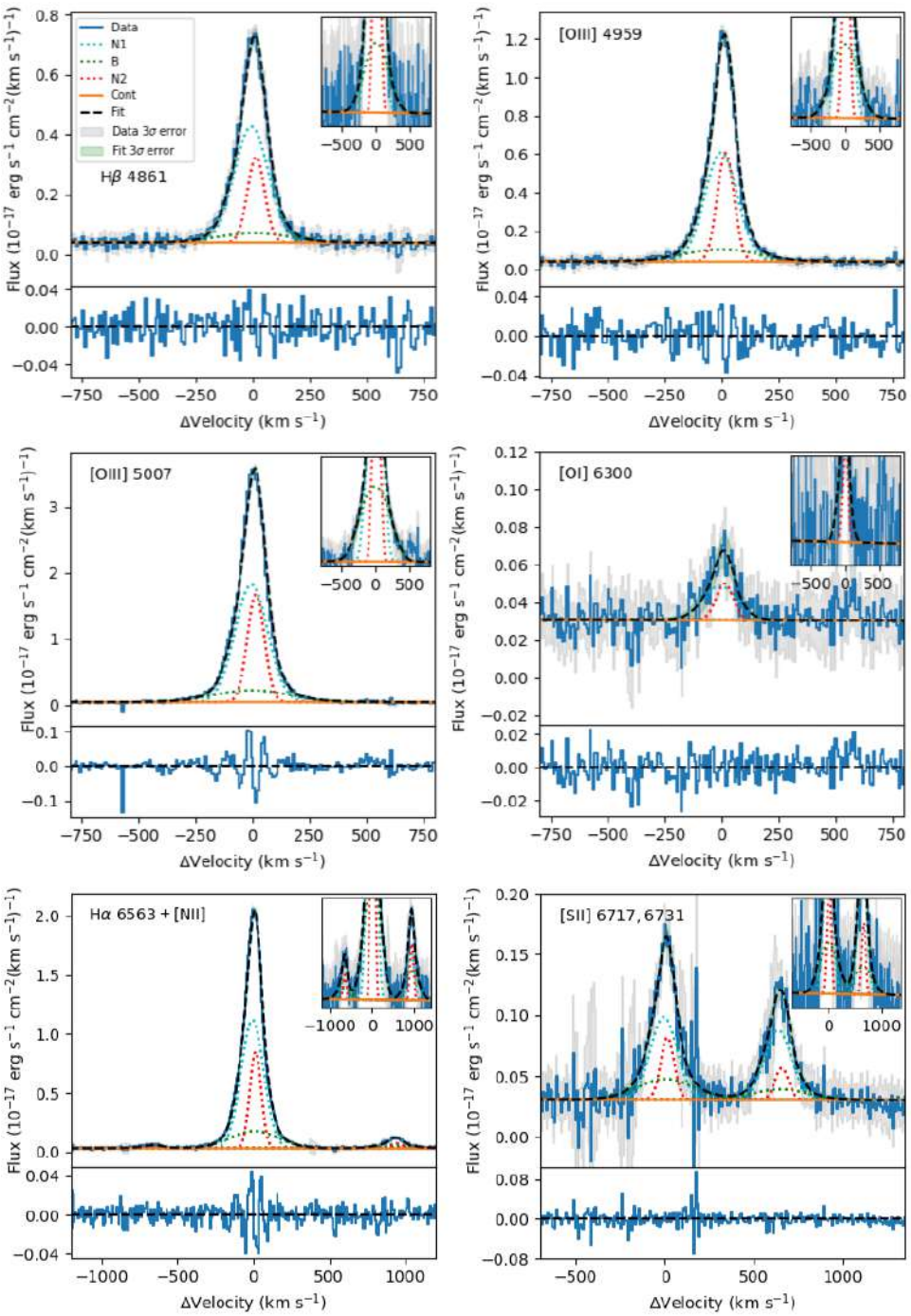

Figure B.8: The fit of faint and bright emission-line profiles of J011309+000223 with three gaussian component models (G3). The blue line represents the original data and the dashed black line the overall model that includes a broad component (B) shown as a green dotted line, and two narrow components (N1-N2) represented with a cyan and red dotted line respectively. The local continuum fitting (Cont) is shown as a solid orange line. We also show the 3σ error spectrum in gray and the 3σ error of the fitted model. A zoomed-in box is shown in the upper-right corner, with $y-axis$ in logarithmic scale. Details of the kinematics and fluxes by component are in Table B.9 , while fit statistics are in B.7.

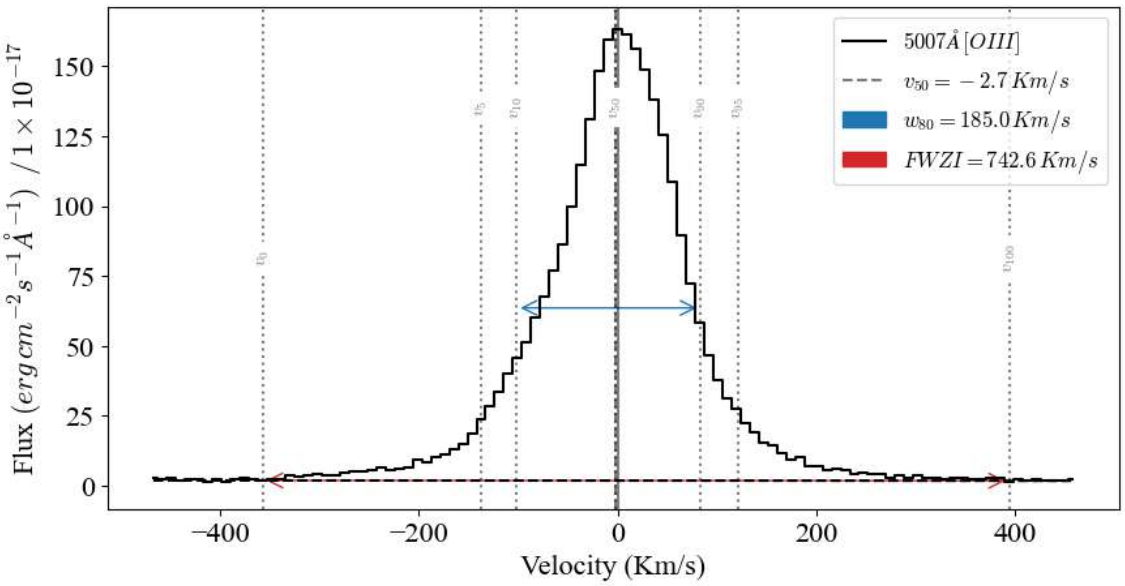

Figure B.9: Inter-percentile analysis of the *WLCE* J011309+000223, using the [OIII]λ5007Å emission-line. Each percentile is represented as a v_i gray dotted-line with i indicating the percentile. The full width zero intensity ($FWZI$) and the w_{80} ($v_{90} - v_{10}$) are shown as a red and blue arrow, respectively.

J012217+052044

Table B.10: Fit statistics of principal emission-lines in J012217+052044

λ_0 [a]	Ion	Model [b]	χ^2 [c]	χ^2_ν [d]	AIC [e]	BIC [f]	P(Gα) [g]
$6563 + 6548, 6584$	Hα + [NII]	G2	3648.2	8.6	935.4	967.9	100.0
		G3	3752.3	9.0	955.5	1004.3	0.0
5007	[OIII]	G2	4083.0	13.9	795.2	817.5	0.0
		G3	2286.3	7.9	627.3	660.6	100.0
4861	Hβ	G2	1094.9	4.4	373.2	380.3	0.0
		G3	944.5	3.8	338.3	348.9	100
$6717, 6731$	[SII]	G2	716.0	2.3	265.7	280.8	90.8
		G3	717.3	2.3	270.3	292.9	9.2

[a] Rest wavelength in Å.
[b] G2: Two gaussian components model, G3: Three gaussian components model.
[c] Chi square (see text for details).
[d] Reduced chi square (see text for details).
[e] Akaike Information Criteria (see text for details).
[f] Bayesian Information Criteria (see text for details).
[g] Likelihood percentage of model Gα to be correct respect the other (see text for details).

Table B.11: Results of the two Gaussian components model (G2) fitting of J012217+052044

λ_0 [a]	Ion	Comp. [b]	Δv_r [c]	σ_{int} [d]	Flux [e]	EM_f [f]	GlobalFlux [g]
6563	Hα	N	6.6 ± 0.3	53.6 ± 0.4	290.0 ± 3.2	67.0	432.9 ± 4.5
		B	9.7 ± 1.9	163.0 ± 2.8	142.9 ± 3.1	33.0	
5007	[OIII]	N	8.3 ± 0.3	50.9 ± 0.4	583.1 ± 7.6	75.7	770.4 ± 10.6
		B	20.5 ± 2.4	137.2 ± 3.7	187.3 ± 7.4	24.3	
4959	[OIII]	N	8.3 ± 0.3	50.9 ± 0.4	193.6 ± 1.3	75.2	257.5 ± 2.2
		B	20.5 ± 2.4	137.2 ± 3.7	63.9 ± 1.7	24.8	
4861	Hβ	N	6.6 ± 0.3	53.6 ± 0.4	105.9 ± 1.2	76.6	138.3 ± 2.1
		B	9.7 ± 1.9	163.0 ± 2.8	32.4 ± 1.8	23.4	
6300	[OI]	N	6.6 ± 0.3	54.4 ± 0.4	3.8 ± 0.4	73.1	5.2 ± 0.8
		B	9.7 ± 1.9	163.2 ± 2.8	1.4 ± 0.7	26.9	
6548	[NII]	N	6.6 ± 0.3	54.4 ± 0.4	2.0 ± 0.3	25.1	8.1 ± 0.5
		B	9.7 ± 1.9	163.2 ± 2.8	6.0 ± 0.4	74.9	
6584	[NII]	N	6.6 ± 0.3	54.4 ± 0.4	6.1 ± 0.8	25.1	24.2 ± 1.5
		B	9.7 ± 1.9	163.2 ± 2.8	18.1 ± 1.3	74.9	
6717	[SII]	N	6.6 ± 0.3	54.4 ± 0.4	8.5 ± 0.5	80.9	10.6 ± 0.9
		B	9.7 ± 1.9	163.2 ± 2.8	2.0 ± 0.8	19.1	
6731	[SII]	N	6.6 ± 0.3	54.4 ± 0.4	5.9 ± 0.5	67.6	8.8 ± 1.0
		B	9.7 ± 1.9	163.2 ± 2.8	2.8 ± 0.9	32.4	

[a] Rest wavelength in Å.

[b] Component of the model.

[c] Velocity shift between the central peak of the emission-line and the center of the component (see text for details).

[d] Intrinsic velocity dispersion (see text for details).

[e] Flux of the component (10^{-17} erg s^{-1} cm^{-2}).

[f] Percentage of relative to global flux of the emission-line.

[g] Global flux of the emission-line (10^{-17} erg s^{-1} cm^{-2}).

Table B.12: Results of the three Gaussian components model (G3) fitting of J012217+052044

λ_0 [a]	Ion	Comp. [b]	Δv_r [c]	σ_{int} [d]	Flux [e]	EM_f [f]	GlobalFlux [g]
6563	Hα	N1	-16.5 ± 3.5	37.5 ± 1.9	171.4 ± 15.1	39.9	430.0 ± 21.5
		B	12.2 ± 1.6	153.8 ± 2.2	166.7 ± 2.9	38.8	
		N2	50.1 ± 3.5	30.2 ± 1.6	92.0 ± 15.0	21.4	
5007	[OIII]	N1	-14.9 ± 2.1	34.4 ± 1.1	302.1 ± 17.9	39.4	765.9 ± 25.8
		B	16.8 ± 1.1	110.3 ± 1.5	288.7 ± 6.0	37.7	
		N2	46.6 ± 2.1	28.0 ± 1.0	175.1 ± 17.6	22.9	
4959	[OIII]	N1	-14.9 ± 2.1	34.4 ± 1.1	101.4 ± 0.9	39.6	256.4 ± 1.9
		B	16.8 ± 1.1	110.3 ± 1.5	98.8 ± 1.5	38.5	
		N2	46.6 ± 2.1	28.0 ± 1.0	56.2 ± 0.8	21.9	
4861	Hβ	N1	-16.5 ± 3.5	37.5 ± 1.9	59.7 ± 0.8	42.8	139.4 ± 1.9
		B	12.2 ± 1.6	153.8 ± 2.2	43.4 ± 1.6	31.1	
		N2	50.1 ± 3.5	30.2 ± 1.6	36.3 ± 0.7	26.0	
6300	[OI]	N1	-16.5 ± 3.5	38.6 ± 2.0	2.3 ± 0.3	43.0	5.3 ± 0.8
		B	12.2 ± 1.6	154.1 ± 2.2	1.9 ± 0.7	36.3	
		N2	50.1 ± 3.5	31.5 ± 1.7	1.1 ± 0.3	20.7	
6548	[NII]	N1	-16.5 ± 3.5	38.6 ± 2.0	1.3 ± 0.2	16.6	8.0 ± 0.5
		B	12.2 ± 1.6	154.1 ± 2.2	6.3 ± 0.4	78.4	
		N2	50.1 ± 3.5	31.5 ± 1.7	0.4 ± 0.2	5.0	
6584	[NII]	N1	-16.5 ± 3.5	38.6 ± 2.0	4.0 ± 0.7	16.6	24.1 ± 1.6
		B	12.2 ± 1.6	154.1 ± 2.2	18.9 ± 1.3	78.4	
		N2	50.1 ± 3.5	31.5 ± 1.7	1.2 ± 0.6	5.0	
6717	[SII]	N1	-16.5 ± 3.5	38.6 ± 2.0	4.7 ± 0.3	44.6	10.7 ± 0.8
		B	12.2 ± 1.6	154.1 ± 2.2	2.9 ± 0.7	26.8	
		N2	50.1 ± 3.5	31.5 ± 1.7	3.0 ± 0.3	28.6	
6731	[SII]	N1	-16.5 ± 3.5	38.6 ± 2.0	3.5 ± 0.4	39.6	8.8 ± 0.9
		B	12.2 ± 1.6	154.1 ± 2.2	3.6 ± 0.8	40.4	
		N2	50.1 ± 3.5	31.5 ± 1.7	1.8 ± 0.3	20.0	

[a] Rest wavelength in Å.

[b] Component of the model.

[c] Velocity shift between the central peak of the emission-line and the center of the component (see text for details).

[d] Intrinsic velocity dispersion (see text for details).

[e] Flux of the component (10^{-17} erg s^{-1} cm^{-2}).

[f] Percentage of relative to global flux of the emission-line.

[g] Global flux of the emission-line (10^{-17} erg s^{-1} cm^{-2}).

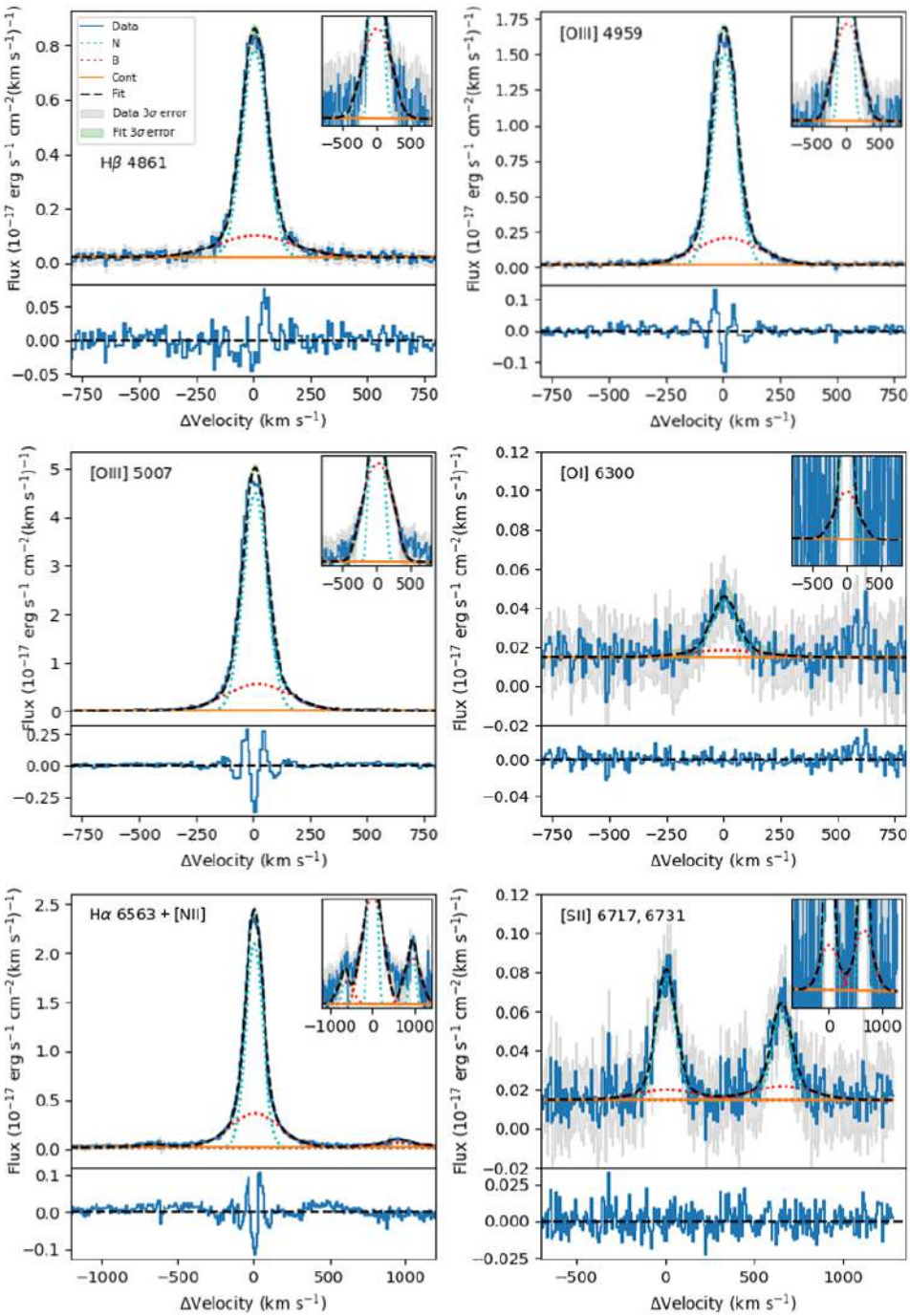

Figure B.10: The fit of faint and bright emission-line profiles of J012217+052044 with two gaussian component models (G2). The blue line represents the original data and the dashed black line the overall model that includes a broad component (B) shown as a red dotted line, and a narrow components (N) represented with a cyan dotted line respectively. The local continuum fitting (Cont) is shown as a solid orange line. We also show the 3σ error spectrum in gray and the 3σ error of the fitted model. A zoomed-in box is shown in the upper-right corner, with $y - axis$ in logarithmic scale. Details of the kinematics and fluxes by component are in Table B.11 , while fit statistics are in B.10.

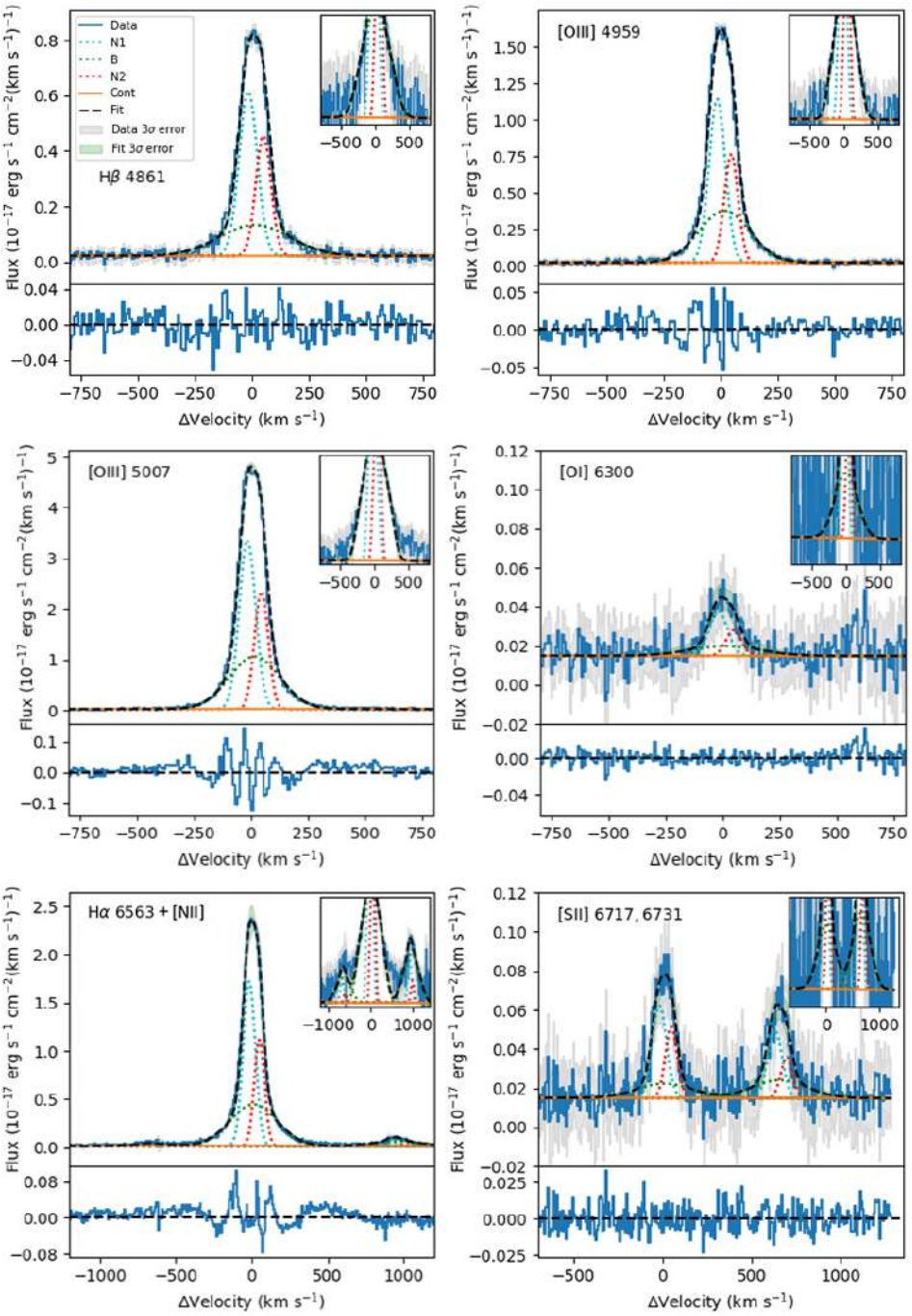

Figure B.11: The fit of faint and bright emission-line profiles of J012217+052044 with three gaussian component models (G3). The blue line represents the original data and the dashed black line the overall model that includes a broad component (B) shown as a green dotted line, and two narrow components (N1-N2) represented with a cyan and red dotted line respectively. The local continuum fitting (Cont) is shown as a solid orange line. We also show the 3σ error spectrum in gray and the 3σ error of the fitted model. A zoomed-in box is shown in the upper-right corner, with $y-axis$ in logarithmic scale. Details of the kinematics and fluxes by component are in Table B.12 , while fit statistics are in B.10.

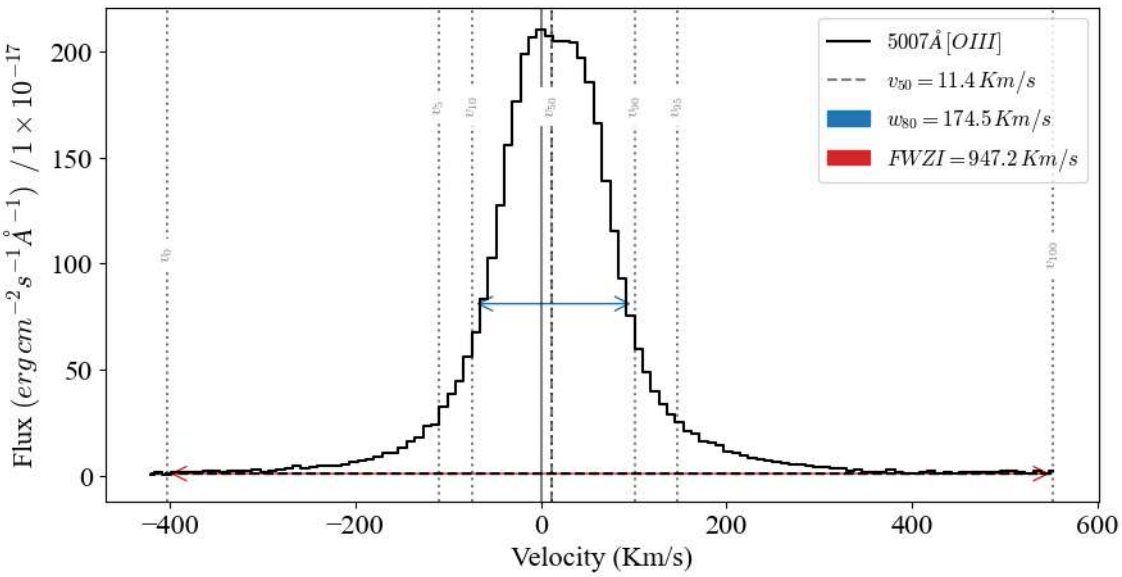

Figure B.12: Inter-percentile analysis of the *WLCE* J012217+052044, using the [OIII]λ5007Å emission-line. Each percentile is represented as a v_i gray dotted-line with i indicating the percentile. The full width zero intensity ($FWZI$) and the w_{80} ($v_{90} - v_{10}$) are shown as a red and blue arrow, respectively.

J081409+211459

Table B.13: Fit statistics of principal emission-lines in J081409+211459

λ_0 [a]	Ion	Model [b]	χ^2 [c]	χ^2_ν [d]	AIC [e]	BIC [f]	P(Gα) [g]
$6563 + 6548, 6584$	Hα + [NII]	G2	6108.8	13.5	1205.7	1238.7	0.0
		G3	3376.0	7.5	940.9	990.5	100.0
5007	[OIII]	G2	5283.4	15.8	944.8	967.7	0.0
		G3	2141.2	6.5	643.7	678.1	100.0
4861	Hβ	G2	1354.0	4.3	465.6	473.1	0.0
		G3	1236.9	3.9	438.7	450.0	100.0
$6717, 6731$	[SII]	G2	4415.9	12.2	918.0	933.6	0.0
		G3	4152.4	11.6	899.5	922.9	100.0

[a] Rest wavelength in Å.
[b] G2: Two gaussian components model, G3: Three gaussian components model.
[c] Chi square (see text for details).
[d] Reduced chi square (see text for details).
[e] Akaike Information Criteria (see text for details).
[f] Bayesian Information Criteria (see text for details).
[g] Likelihood percentage of model Gα to be correct respect the other (see text for details).

Table B.14: Results of the two Gaussian components model (G2) fitting of J081409+211459

λ_0 [a]	Ion	Comp. [b]	Δv_r [c]	σ_{int} [d]	Flux [e]	EM_f [f]	GlobalFlux [g]
6563	Hα	B	-10.2 ± 1.2	96.0 ± 1.8	687.7 ± 46.2	54.0	1272.9 ± 65.7
		N	6.5 ± 0.8	56.8 ± 1.4	585.2 ± 46.7	46.0	
5007	[OIII]	B	-9.0 ± 1.8	94.8 ± 2.6	728.7 ± 58.7	52.6	1384.5 ± 83.5
		N	7.9 ± 0.9	52.3 ± 1.7	655.8 ± 59.4	47.4	
4959	[OIII]	B	-9.0 ± 1.8	94.8 ± 2.6	245.9 ± 6.1	53.0	463.8 ± 7.9
		N	7.9 ± 0.9	52.3 ± 1.7	217.9 ± 5.0	47.0	
4861	Hβ	B	-10.2 ± 1.2	96.0 ± 1.8	203.8 ± 7.5	52.2	390.3 ± 9.7
		N	6.5 ± 0.8	56.8 ± 1.4	186.4 ± 6.2	47.8	
6300	[OI]	B	-10.2 ± 1.2	96.6 ± 1.8	10.5 ± 2.2	41.1	25.5 ± 2.8
		N	6.5 ± 0.8	57.7 ± 1.4	15.0 ± 1.7	58.9	
6548	[NII]	B	-10.2 ± 1.2	96.6 ± 1.8	26.0 ± 2.2	55.6	46.8 ± 3.0
		N	6.5 ± 0.8	57.7 ± 1.4	20.8 ± 2.0	44.4	
6584	[NII]	B	-10.2 ± 1.2	96.6 ± 1.8	78.1 ± 6.5	55.6	140.5 ± 8.9
		N	6.5 ± 0.8	57.7 ± 1.4	62.4 ± 6.1	44.4	
6717	[SII]	B	-10.2 ± 1.2	96.6 ± 1.8	65.9 ± 4.0	59.6	110.5 ± 5.2
		N	6.5 ± 0.8	57.7 ± 1.4	44.6 ± 3.3	40.4	
6731	[SII]	B	-10.2 ± 1.2	96.6 ± 1.8	47.6 ± 3.9	57.5	82.9 ± 5.0
		N	6.5 ± 0.8	57.7 ± 1.4	35.3 ± 3.1	42.5	

[a] Rest wavelength in Å.
[b] Component of the model.
[c] Velocity shift between the central peak of the emission-line and the center of the component (see text for details).
[d] Intrinsic velocity dispersion (see text for details).
[e] Flux of the component (10^{-17} erg s^{-1} cm^{-2}).
[f] Percentage of relative to global flux of the emission-line.
[g] Global flux of the emission-line (10^{-17} erg s^{-1} cm^{-2}).

Table B.15: Results of the three Gaussian components model (G3) fitting of J081409+211459

λ_0 [a]	Ion	Comp. [b]	Δv_r [c]	σ_{int} [d]	Flux [e]	EM_f [f]	GlobalFlux [g]
6563	Hα	B	-31.4 ± 3.6	136.2 ± 4.0	220.1 ± 19.4	17.1	1283.6 ± 26.9
		N1	2.0 ± 0.4	71.0 ± 0.8	1013.9 ± 17.6	79.0	
		N2	3.2 ± 1.1	15.5 ± 2.4	49.6 ± 5.9	3.9	
5007	[OIII]	B	-40.5 ± 7.2	130.6 ± 5.6	210.4 ± 28.0	15.1	1395.4 ± 38.8
		N1	4.0 ± 0.5	69.3 ± 0.9	1103.1 ± 26.2	79.1	
		N2	5.7 ± 0.7	12.5 ± 1.2	81.9 ± 5.7	5.9	
4959	[OIII]	B	-40.5 ± 7.2	130.6 ± 5.6	77.7 ± 4.5	16.6	469.0 ± 6.7
		N1	4.0 ± 0.5	69.3 ± 0.9	363.2 ± 4.6	77.4	
		N2	5.7 ± 0.7	12.5 ± 1.2	28.2 ± 1.7	6.0	
4861	Hβ	B	-31.4 ± 3.6	136.2 ± 4.0	48.4 ± 6.8	12.4	389.6 ± 9.9
		N1	2.0 ± 0.4	71.0 ± 0.8	327.0 ± 6.8	83.9	
		N2	3.2 ± 1.1	15.5 ± 2.4	14.2 ± 2.4	3.6	
6300	[OI]	B	-31.4 ± 3.6	136.6 ± 4.0	3.4 ± 2.4	12.9	26.1 ± 3.3
		N1	2.0 ± 0.4	71.7 ± 0.8	21.7 ± 2.1	83.1	
		N2	3.2 ± 1.1	18.5 ± 1.3	1.1 ± 0.6	4.1	
6548	[NII]	B	-31.4 ± 3.6	136.6 ± 4.0	9.0 ± 1.2	19.0	47.4 ± 1.7
		N1	2.0 ± 0.4	71.7 ± 0.8	36.9 ± 1.2	77.9	
		N2	3.2 ± 1.1	18.5 ± 1.3	1.4 ± 0.4	3.0	
6584	[NII]	B	-31.4 ± 3.6	136.6 ± 4.0	27.1 ± 3.7	19.0	142.2 ± 5.3
		N1	2.0 ± 0.4	71.7 ± 0.8	110.8 ± 3.6	77.9	
		N2	3.2 ± 1.1	18.5 ± 1.3	4.3 ± 1.1	3.0	
6717	[SII]	B	-31.4 ± 3.6	136.6 ± 4.0	24.0 ± 3.7	21.5	111.5 ± 5.3
		N1	2.0 ± 0.4	71.7 ± 0.8	81.4 ± 3.6	73.0	
		N2	3.2 ± 1.1	18.6 ± 1.3	6.1 ± 1.3	5.5	
6731	[SII]	B	-31.4 ± 3.6	136.6 ± 4.0	15.3 ± 3.7	18.2	84.1 ± 5.2
		N1	2.0 ± 0.4	71.7 ± 0.8	68.8 ± 3.6	81.8	
		N2	3.2 ± 1.1	18.6 ± 1.3	0.0 ± 0.1	0.0	

[a] Rest wavelength in Å.

[b] Component of the model.

[c] Velocity shift between the central peak of the emission-line and the center of the component (see text for details).

[d] Intrinsic velocity dispersion (see text for details).

[e] Flux of the component (10^{-17} erg s^{-1} cm^{-2}).

[f] Percentage of relative to global flux of the emission-line.

[g] Global flux of the emission-line (10^{-17} erg s^{-1} cm^{-2}).

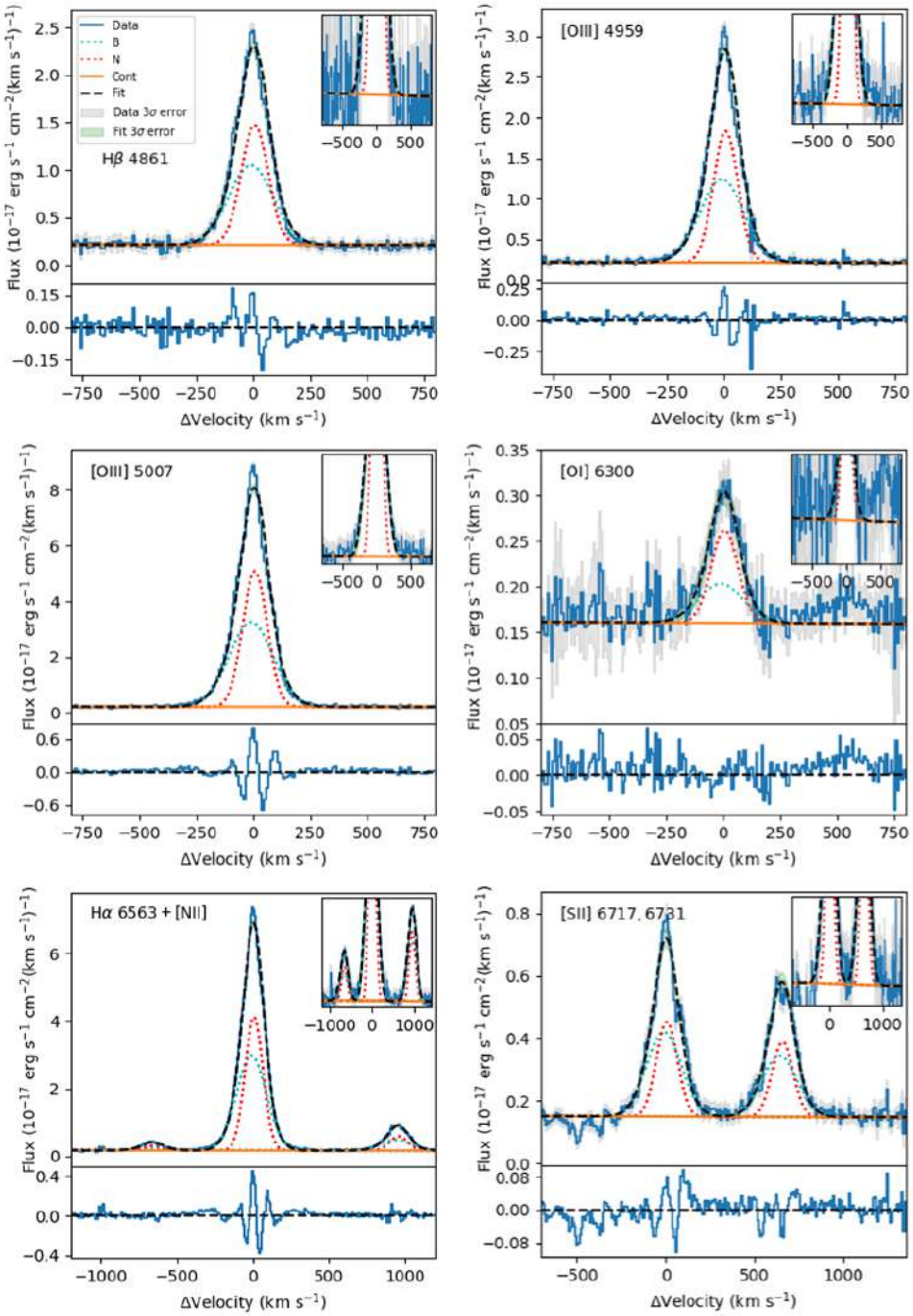

Figure B.13: The fit of faint and bright emission-line profiles of J081409+211459 with two gaussian component models (G2). The blue line represents the original data and the dashed black line the overall model that includes a broad component (B) shown as a cyan dotted line, and a narrow components (N) represented with a red dotted line respectively. The local continuum fitting (Cont) is shown as a solid orange line. We also show the 3σ error spectrum in gray and the 3σ error of the fitted model. A zoomed-in box is shown in the upper-right corner, with $y - axis$ in logarithmic scale. Details of the kinematics and fluxes by component are in Table B.14 , while fit statistics are in B.13.

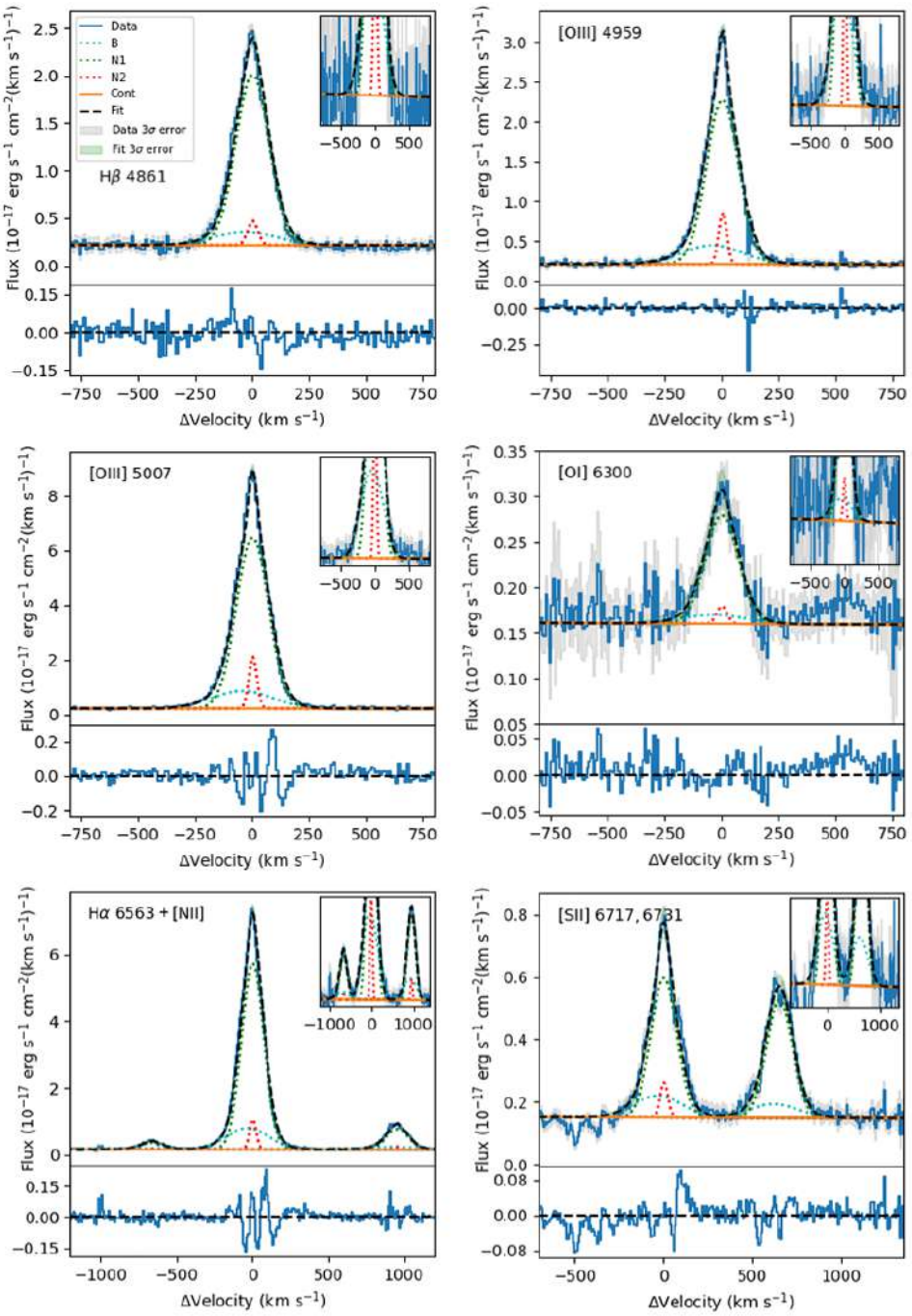

Figure B.14: The fit of faint and bright emission-line profiles of J081409+211459 with three gaussian component models (G3). The blue line represents the original data and the dashed black line the overall model that includes a broad component (B) shown as a cyan dotted line, and two narrow components (N1-N2) represented with a green and red dotted line respectively. The local continuum fitting (Cont) is shown as a solid orange line. We also show the 3σ error spectrum in gray and the 3σ error of the fitted model. A zoomed-in box is shown in the upper-right corner, with $y-axis$ in logarithmic scale. Details of the kinematics and fluxes by component are in Table B.15 , while fit statistics are in B.13.

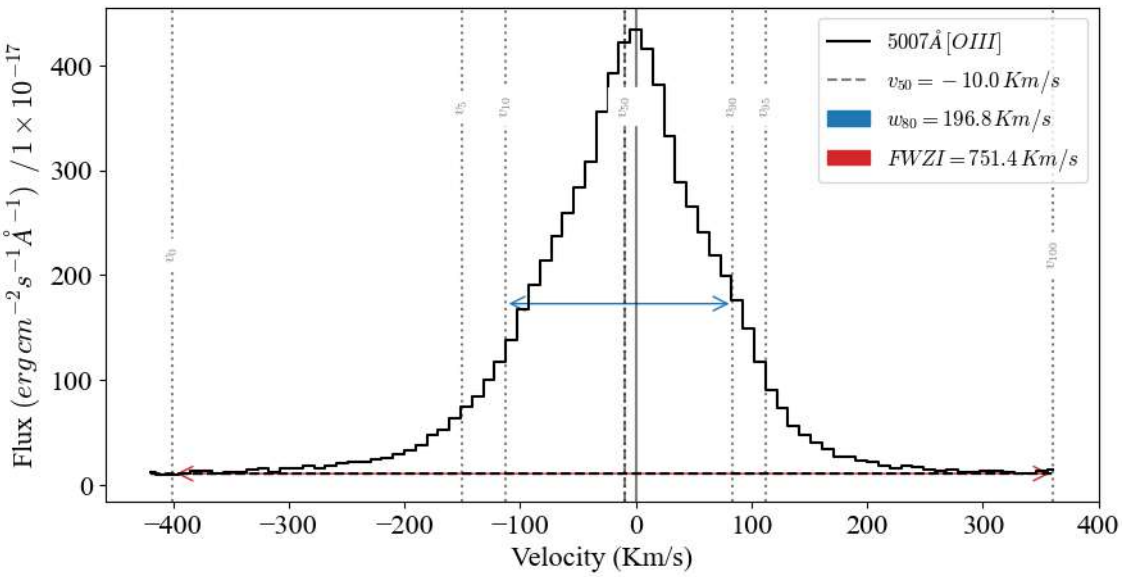

Figure B.15: Inter-percentile analysis of the *NLCE* J081409+211459, using the [OIII]λ5007Å emission-line. Each percentile is represented as a v_i gray dotted-line with i indicating the percentile. The full width zero intensity ($FWZI$) and the w_{80} ($v_{90} - v_{10}$) are shown as a red and blue arrow, respectively.

J091113+183108

Table B.16: Fit statistics of principal emission-lines in J091113+183108

λ_0 [a]	Ion	Model [b]	χ^2 [c]	χ^2_ν [d]	AIC [e]	BIC [f]	P(Gα) [g]
$6563 + 6548, 6584$	Hα + [NII]	G2	9224.8	17.3	1548.6	1582.9	0.0
		G3	5425.4	10.3	1269.9	1321.4	100.0
5007	[OIII]	G2	3788.2	13.8	741.4	763.2	0.0
		G3	1742.8	6.4	530.0	562.7	100.0
4861	Hβ	G2	982.8	2.9	364.9	372.5	0.0
		G3	854.3	2.5	319.3	330.8	100.0
$6717, 6731$	[SII]	G2	1041.6	3.1	388.7	404.0	0.0
		G3	888.4	2.7	338.6	361.5	100.0

[a] Rest wavelength in Å.
[b] G2: Two gaussian components model, G3: Three gaussian components model.
[c] Chi square (see text for details).
[d] Reduced chi square (see text for details).
[e] Akaike Information Criteria (see text for details).
[f] Bayesian Information Criteria (see text for details).
[g] Likelihood percentage of model Gα to be correct respect the other (see text for details).

Table B.17: Results of the two Gaussian components model (G2) fitting of J091113+183108

λ_0 [a]	Ion	Comp. [b]	Δv_r [c]	σ_{int} [d]	Flux [e]	EM_f [f]	GlobalFlux [g]
6563	Hα	B	-64.4 ± 1.2	121.2 ± 0.8	781.6 ± 9.2	80.5	970.9 ± 11.8
		N	6.3 ± 0.9	34.0 ± 1.2	189.3 ± 7.4	19.5	
5007	[OIII]	B	-61.2 ± 0.9	114.4 ± 0.7	926.1 ± 8.1	80.9	1145.2 ± 10.5
		N	9.0 ± 0.7	29.7 ± 0.9	219.1 ± 6.7	19.1	
4959	[OIII]	B	-61.2 ± 0.9	114.4 ± 0.7	313.4 ± 2.3	81.1	386.2 ± 2.7
		N	9.0 ± 0.7	29.7 ± 0.9	72.8 ± 1.3	18.9	
4861	Hβ	B	-64.4 ± 1.2	121.2 ± 0.8	273.9 ± 2.4	84.8	323.1 ± 2.8
		N	6.3 ± 0.9	34.0 ± 1.2	49.2 ± 1.4	15.2	
6300	[OI]	B	-64.4 ± 1.2	121.6 ± 0.8	16.1 ± 0.9	95.5	16.9 ± 1.0
		N	6.3 ± 0.9	35.4 ± 1.3	0.8 ± 0.5	4.5	
6548	[NII]	B	-64.4 ± 1.2	121.6 ± 0.8	35.2 ± 0.9	79.9	44.1 ± 1.1
		N	6.3 ± 0.9	35.4 ± 1.3	8.8 ± 0.7	20.1	
6584	[NII]	B	-64.4 ± 1.2	121.6 ± 0.8	105.7 ± 2.8	79.9	132.3 ± 3.5
		N	6.3 ± 0.9	35.4 ± 1.3	26.5 ± 2.1	20.1	
6717	[SII]	B	-64.4 ± 1.2	121.6 ± 0.8	70.2 ± 1.1	100.0	70.2 ± 1.1
		N	6.3 ± 0.9	35.5 ± 0.0	0.0 ± 0.5	0.0	
6731	[SII]	B	-64.4 ± 1.2	121.6 ± 0.8	51.5 ± 1.1	93.2	55.3 ± 1.3
		N	6.3 ± 0.9	35.5 ± 0.0	3.8 ± 0.6	6.8	

[a] Rest wavelength in Å.
[b] Component of the model.
[c] Velocity shift between the central peak of the emission-line and the center of the component (see text for details).
[d] Intrinsic velocity dispersion (see text for details).
[e] Flux of the component (10^{-17} erg s^{-1} cm^{-2}).
[f] Percentage of relative to global flux of the emission-line.
[g] Global flux of the emission-line (10^{-17} erg s^{-1} cm^{-2}).

Table B.18: Results of the three Gaussian components model (G3) fitting of J091113+183108

λ_0 [a]	Ion	Comp. [b]	Δv_r [c]	σ_{int} [d]	Flux [e]	EM_f [f]	GlobalFlux [g]
6563	Hα	B1	-72.2 ± 2.0	104.0 ± 1.8	618.7 ± 23.5	62.3	993.0 ± 30.4
		B2	-42.3 ± 7.2	239.5 ± 14.4	164.1 ± 17.0	16.5	
		N	10.7 ± 0.8	36.5 ± 1.1	210.3 ± 9.1	21.2	
5007	[OIII]	B1	-61.9 ± 0.9	105.1 ± 1.0	823.8 ± 14.0	70.0	1177.3 ± 19.0
		B2	-49.7 ± 9.2	269.1 ± 16.6	135.7 ± 11.8	11.5	
		N	10.6 ± 0.5	29.6 ± 0.6	217.8 ± 5.1	18.5	
4959	[OIII]	B1	-61.9 ± 0.9	105.1 ± 1.0	282.7 ± 2.9	71.5	395.5 ± 4.4
		B2	-49.7 ± 9.2	269.1 ± 16.6	41.0 ± 3.1	10.4	
		N	10.6 ± 0.5	29.6 ± 0.6	71.8 ± 1.3	18.2	
4861	Hβ	B1	-72.2 ± 2.0	104.0 ± 1.8	219.7 ± 3.0	66.8	328.9 ± 4.8
		B2	-42.3 ± 7.2	239.5 ± 14.4	53.5 ± 3.5	16.3	
		N	10.7 ± 0.8	36.5 ± 1.1	55.7 ± 1.3	16.9	
6300	[OI]	B1	-72.2 ± 2.0	104.4 ± 1.8	11.8 ± 1.2	65.7	18.0 ± 2.1
		B2	-42.3 ± 7.2	239.7 ± 14.4	5.1 ± 1.7	28.5	
		N	10.7 ± 0.8	37.8 ± 1.1	1.0 ± 0.5	5.8	
6548	[NII]	B1	-72.2 ± 2.0	104.4 ± 1.8	27.2 ± 1.5	61.8	44.0 ± 2.4
		B2	-42.3 ± 7.2	239.7 ± 14.4	7.3 ± 1.7	16.5	
		N	10.7 ± 0.8	37.8 ± 1.1	9.5 ± 0.6	21.7	
6584	[NII]	B1	-72.2 ± 2.0	104.4 ± 1.8	81.5 ± 4.4	61.8	131.9 ± 6.9
		B2	-42.3 ± 7.2	239.7 ± 14.4	21.8 ± 5.0	16.5	
		N	10.7 ± 0.8	37.8 ± 1.1	28.6 ± 1.8	21.7	
6717	[SII]	B1	-72.2 ± 2.0	104.5 ± 1.8	61.3 ± 1.3	89.9	68.1 ± 2.2
		B2	-42.3 ± 7.2	239.7 ± 14.4	5.9 ± 1.7	8.6	
		N	10.7 ± 0.8	37.9 ± 1.1	1.0 ± 0.5	1.5	
6731	[SII]	B1	-72.2 ± 2.0	104.5 ± 1.8	39.9 ± 1.5	70.4	56.7 ± 2.4
		B2	-42.3 ± 7.2	239.7 ± 14.4	11.6 ± 1.8	20.4	
		N	10.7 ± 0.8	37.9 ± 1.1	5.2 ± 0.5	9.2	

[a] Rest wavelength in Å.

[b] Component of the model.

[c] Velocity shift between the central peak of the emission-line and the center of the component (see text for details).

[d] Intrinsic velocity dispersion (see text for details).

[e] Flux of the component (10^{-17} erg s^{-1} cm^{-2}).

[f] Percentage of relative to global flux of the emission-line.

[g] Global flux of the emission-line (10^{-17} erg s^{-1} cm^{-2}).

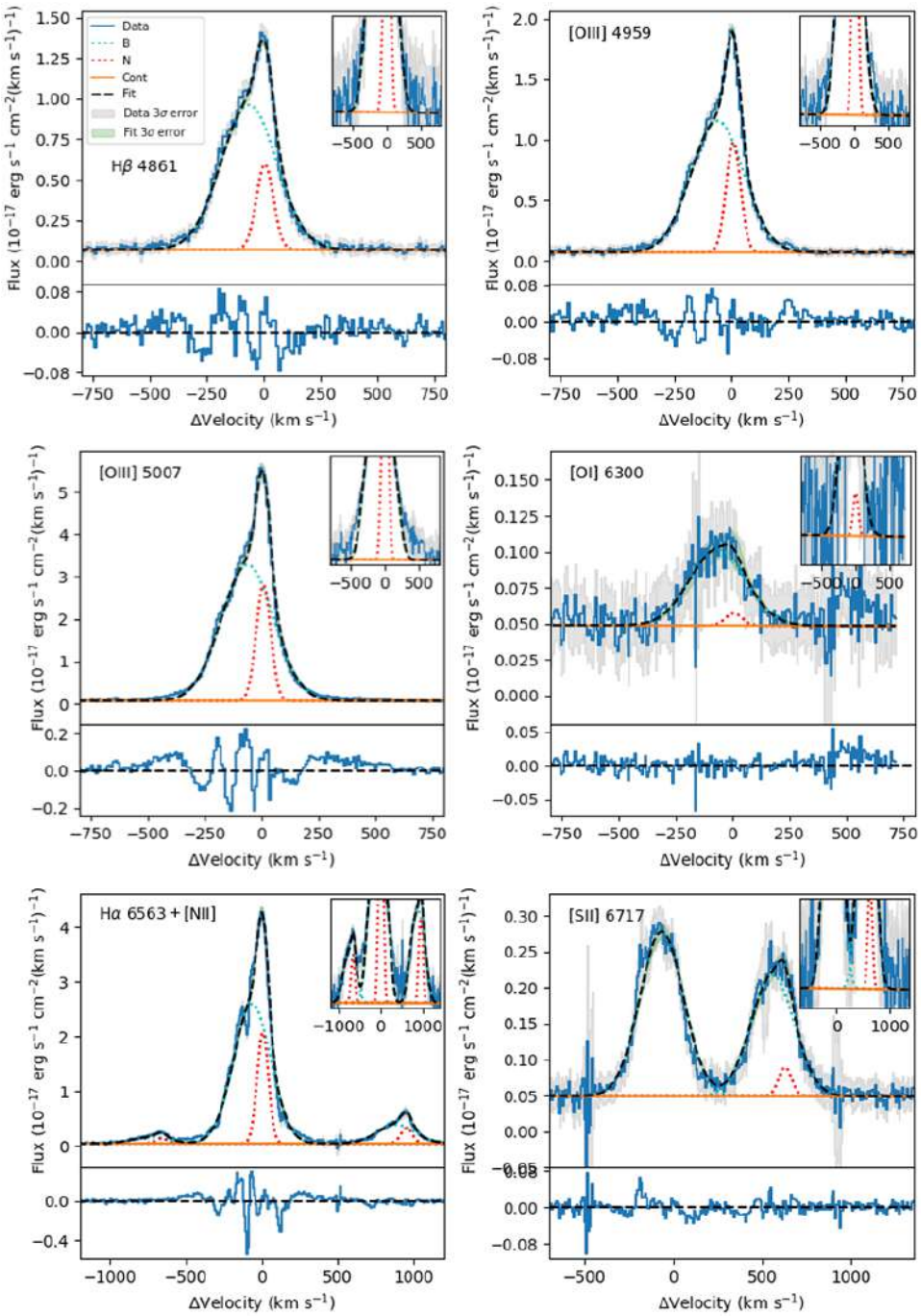

Figure B.16: The fit of faint and bright emission-line profiles of J091113+183108 with two gaussian component models (G2). The blue line represents the original data and the dashed black line the overall model that includes a broad component (B) shown as a cyan dotted line, and a narrow components (N) represented with a red dotted line respectively. The local continuum fitting (Cont) is shown as a solid orange line. We also show the 3σ error spectrum in gray and the 3σ error of the fitted model. A zoomed-in box is shown in the upper-right corner, with $y-axis$ in logarithmic scale. Details of the kinematics and fluxes by component are in Table B.17 , while fit statistics are in B.16.

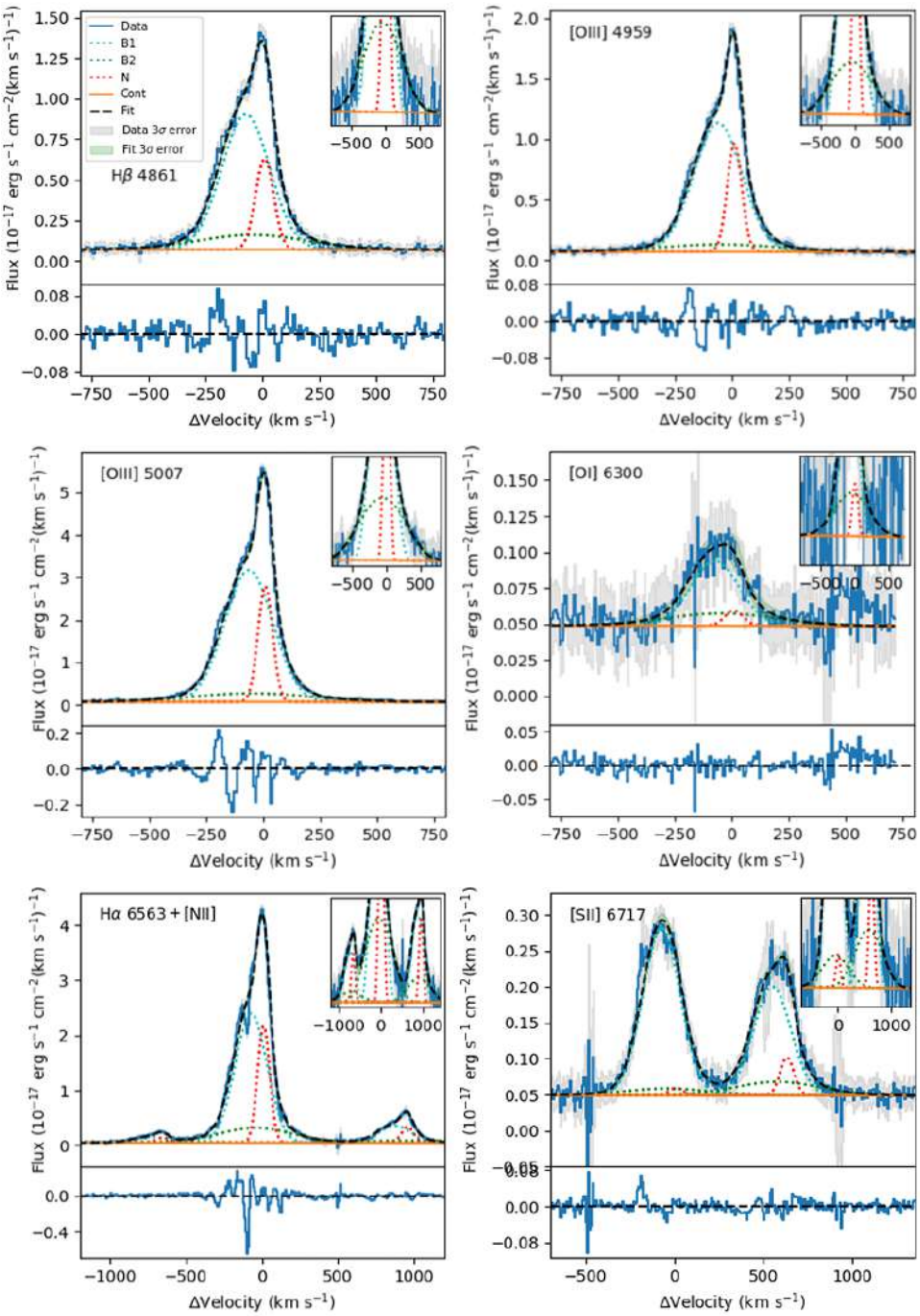

Figure B.17: The fit of faint and bright emission-line profiles of J091113+183108 with three gaussian component models (G3). The blue line represents the original data and the dashed black line the overall model that includes a broad component (B) shown as a cyan dotted line, and two narrow components (N1-N2) represented with a green and red dotted line respectively. The local continuum fitting (Cont) is shown as a solid orange line. We also show the 3σ error spectrum in gray and the 3σ error of the fitted model. A zoomed-in box is shown in the upper-right corner, with $y-axis$ in logarithmic scale. Details of the kinematics and fluxes by component are in Table B.18 , while fit statistics are in B.16.

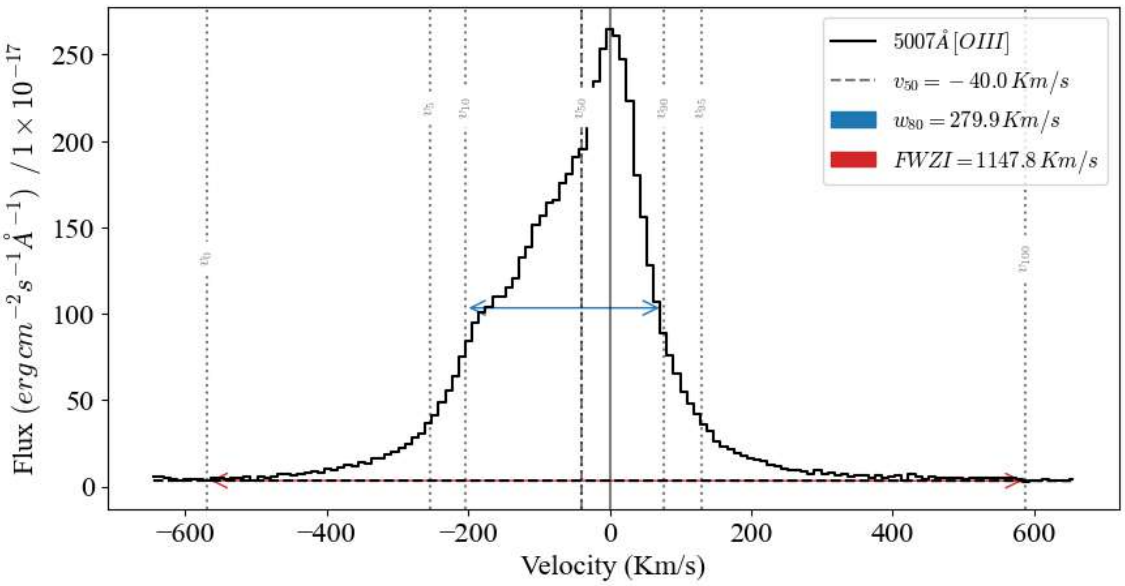

Figure B.18: Inter-percentile analysis of the *WLCE* J091113+183108, using the [OIII]λ5007Å emission-line. Each percentile is represented as a v_i gray dotted-line with i indicating the percentile. The full width zero intensity ($FWZI$) and the w_{80} ($v_{90} - v_{10}$) are shown as a red and blue arrow, respectively.

J095838+202508

Table B.19: Fit statistics of principal emission-lines in J095838+202508

λ_0 [a]	Ion	Model [b]	χ^2 [c]	χ^2_ν [d]	AIC [e]	BIC [f]	P(Gα) [g]
$6563 + 6548, 6584$	Hα + [NII]	G2	993.8	2.8	381.6	412.9	0.0
		G3	704.1	2.0	262.1	309.0	100.0
5007	[OIII]	G2	1613.1	3.7	583.6	608.1	0.0
		G3	1198.1	2.8	458.8	495.5	100.0
4861	Hβ	G2	641.6	1.9	220.0	227.6	0.0
		G3	608.7	1.8	204.0	215.5	100.0
$6717, 6731$	[SII]	G2	526.3	1.7	172.1	187.0	1.9
		G3	506.5	1.7	164.2	186.6	98.1

[a] Rest wavelength in Å.
[b] G2: Two gaussian components model, G3: Three gaussian components model.
[c] Chi square (see text for details).
[d] Reduced chi square (see text for details).
[e] Akaike Information Criteria (see text for details).
[f] Bayesian Information Criteria (see text for details).
[g] Likelihood percentage of model Gα to be correct respect the other (see text for details).

Table B.20: Results of the two Gaussian components model (G2) fitting of J095838+202508

λ_0 [a]	Ion	Comp. [b]	Δv_r [c]	σ_{int} [d]	Flux [e]	EM_f [f]	GlobalFlux [g]
6563	Hα	N	2.7 ± 0.2	43.5 ± 0.3	330.7 ± 4.6	72.5	455.8 ± 6.4
		B	22.2 ± 1.5	102.3 ± 2.0	125.2 ± 4.4	27.5	
5007	[OIII]	N	5.8 ± 0.2	45.3 ± 0.3	674.9 ± 7.8	74.4	907.1 ± 10.9
		B	31.8 ± 1.4	104.7 ± 1.7	232.2 ± 7.5	25.6	
4959	[OIII]	N	5.8 ± 0.2	45.3 ± 0.3	238.3 ± 1.7	76.3	312.1 ± 2.6
		B	31.8 ± 1.4	104.7 ± 1.7	73.8 ± 2.0	23.7	
4861	Hβ	N	2.7 ± 0.2	43.5 ± 0.3	112.1 ± 1.4	71.3	157.1 ± 2.4
		B	22.2 ± 1.5	102.3 ± 2.0	45.1 ± 1.9	28.7	
6300	[OI]	N	2.7 ± 0.2	44.6 ± 0.3	1.3 ± 0.5	45.4	2.9 ± 0.9
		B	22.2 ± 1.5	102.8 ± 2.0	1.6 ± 0.7	54.6	
6548	[NII]	N	2.7 ± 0.2	44.6 ± 0.3	2.4 ± 0.2	66.5	3.6 ± 0.4
		B	22.2 ± 1.5	102.8 ± 2.0	1.2 ± 0.3	33.5	
6584	[NII]	N	2.7 ± 0.2	44.6 ± 0.3	7.2 ± 0.6	66.5	10.8 ± 1.1
		B	22.2 ± 1.5	102.8 ± 2.0	3.6 ± 0.9	33.5	
6717	[SII]	N	2.7 ± 0.2	44.6 ± 0.3	10.5 ± 0.6	79.1	13.3 ± 1.1
		B	22.2 ± 1.5	102.8 ± 2.0	2.8 ± 0.9	20.9	
6731	[SII]	N	2.7 ± 0.2	44.6 ± 0.3	6.7 ± 1.0	59.7	11.3 ± 1.4
		B	22.2 ± 1.5	102.8 ± 2.0	4.5 ± 1.0	40.3	

[a] Rest wavelength in Å.
[b] Component of the model.
[c] Velocity shift between the central peak of the emission-line and the center of the component (see text for details).
[d] Intrinsic velocity dispersion (see text for details).
[e] Flux of the component (10^{-17} erg s^{-1} cm^{-2}).
[f] Percentage of relative to global flux of the emission-line.
[g] Global flux of the emission-line (10^{-17} erg s^{-1} cm^{-2}).

Table B.21: Results of the three Gaussian components model (G3) fitting of J095838+202508

λ_0 [a]	Ion	Comp. [b]	Δv_r [c]	σ_{int} [d]	Flux [e]	EM_f [f]	GlobalFlux [g]
6563	Hα	N1	-18.4 ± 1.5	14.1 ± 2.6	16.1 ± 2.7	3.5	456.9 ± 6.2
		N2	4.7 ± 0.3	45.6 ± 0.4	331.4 ± 4.1	72.5	
		B	22.3 ± 1.4	110.2 ± 2.1	109.3 ± 3.7	23.9	
5007	[OIII]	N1	-32.5 ± 1.2	7.7 ± 2.4	18.6 ± 2.5	2.1	908.1 ± 10.6
		N2	7.5 ± 0.3	45.2 ± 0.3	654.0 ± 7.7	72.0	
		B	28.9 ± 1.2	105.5 ± 1.6	235.4 ± 6.8	25.9	
4959	[OIII]	N1	-32.5 ± 1.2	7.7 ± 2.4	6.0 ± 0.8	1.9	312.2 ± 2.9
		N2	7.5 ± 0.3	45.2 ± 0.3	231.5 ± 1.9	74.1	
		B	28.9 ± 1.2	105.5 ± 1.6	74.8 ± 2.0	23.9	
4861	Hβ	N1	-18.4 ± 1.5	14.1 ± 2.6	5.6 ± 0.9	3.5	157.5 ± 2.8
		N2	4.7 ± 0.3	45.6 ± 0.4	112.7 ± 1.9	71.6	
		B	22.3 ± 1.4	110.2 ± 2.1	39.3 ± 1.9	24.9	
6300	[OI]	N1	-18.4 ± 1.5	17.0 ± 3.1	0.3 ± 0.3	10.0	3.0 ± 1.1
		N2	4.7 ± 0.3	46.6 ± 0.4	1.0 ± 0.7	31.7	
		B	22.3 ± 1.4	110.6 ± 2.1	1.8 ± 0.8	58.3	
6548	[NII]	N1	-18.4 ± 1.5	17.0 ± 3.1	0.1 ± 0.1	3.3	3.6 ± 0.4
		N2	4.7 ± 0.3	46.6 ± 0.4	2.4 ± 0.2	67.1	
		B	22.3 ± 1.4	110.6 ± 2.1	1.1 ± 0.3	29.6	
6584	[NII]	N1	-18.4 ± 1.5	17.0 ± 3.1	0.4 ± 0.3	3.3	10.8 ± 1.1
		N2	4.7 ± 0.3	46.6 ± 0.4	7.2 ± 0.7	67.1	
		B	22.3 ± 1.4	110.6 ± 2.1	3.2 ± 0.8	29.6	
6717	[SII]	N1	-18.4 ± 1.5	17.1 ± 3.1	1.5 ± 0.4	10.9	13.5 ± 1.4
		N2	4.7 ± 0.3	46.7 ± 0.4	8.9 ± 0.9	65.8	
		B	22.3 ± 1.4	110.6 ± 2.1	3.1 ± 1.0	23.3	
6731	[SII]	N1	-18.4 ± 1.5	17.1 ± 3.1	1.1 ± 0.7	10.1	11.1 ± 2.1
		N2	4.7 ± 0.3	46.7 ± 0.4	5.2 ± 1.6	47.4	
		B	22.3 ± 1.4	110.6 ± 2.1	4.7 ± 1.1	42.5	

[a] Rest wavelength in Å.

[b] Component of the model.

[c] Velocity shift between the central peak of the emission-line and the center of the component (see text for details).

[d] Intrinsic velocity dispersion (see text for details).

[e] Flux of the component (10^{-17} erg s^{-1} cm^{-2}).

[f] Percentage of relative to global flux of the emission-line.

[g] Global flux of the emission-line (10^{-17} erg s^{-1} cm^{-2}).

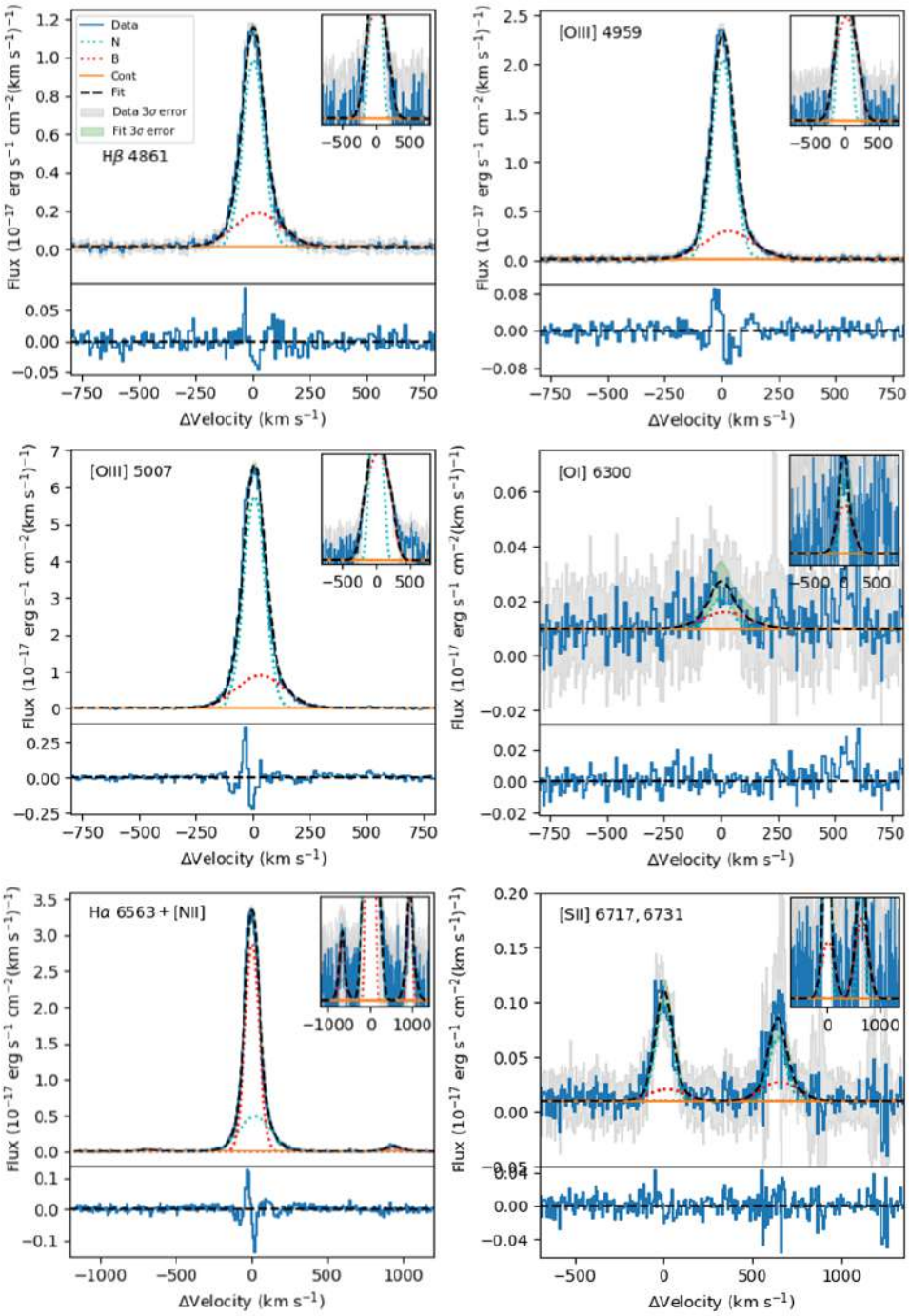

Figure B.19: The fit of faint and bright emission-line profiles of J095838+202508 with two gaussian component models (G2). The blue line represents the original data and the dashed black line the overall model that includes a broad component (B) shown as a red dotted line, and a narrow components (N) represented with a cyan dotted line respectively. The local continuum fitting (Cont) is shown as a solid orange line. We also show the 3σ error spectrum in gray and the 3σ error of the fitted model. A zoomed-in box is shown in the upper-right corner, with $y - axis$ in logarithmic scale. Details of the kinematics and fluxes by component are in Table B.20 , while fit statistics are in B.19.

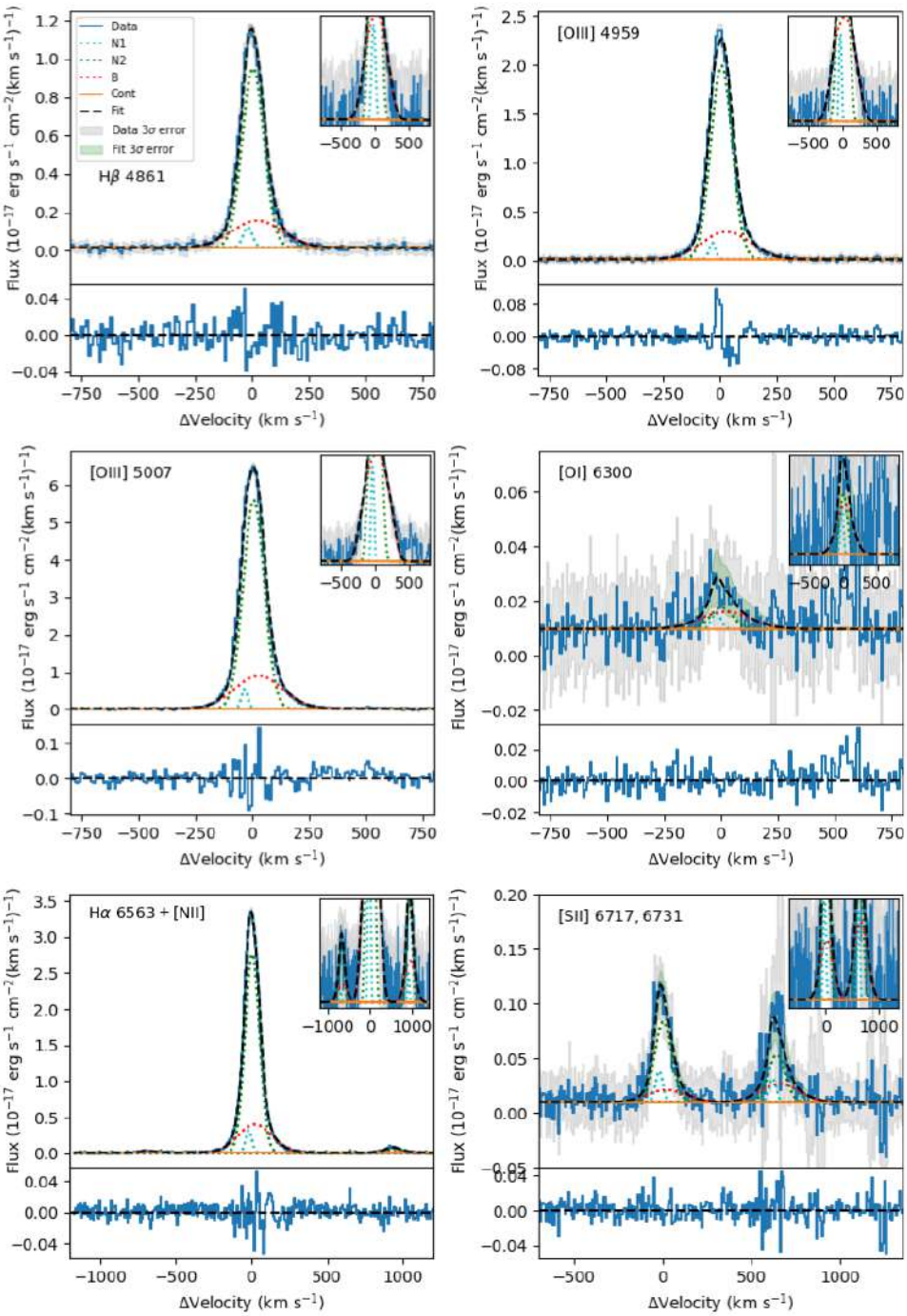

Figure B.20: The fit of faint and bright emission-line profiles of J095838+202508 with three gaussian component models (G3). The blue line represents the original data and the dashed black line the overall model that includes a broad component (B) shown as a red dotted line, and two narrow components (N1-N2) represented with a cyan and green dotted line respectively. The local continuum fitting (Cont) is shown as a solid orange line. We also show the 3σ error spectrum in gray and the 3σ error of the fitted model. A zoomed-in box is shown in the upper-right corner, with $y-axis$ in logarithmic scale. Details of the kinematics and fluxes by component are in Table B.21 , while fit statistics are in B.19.

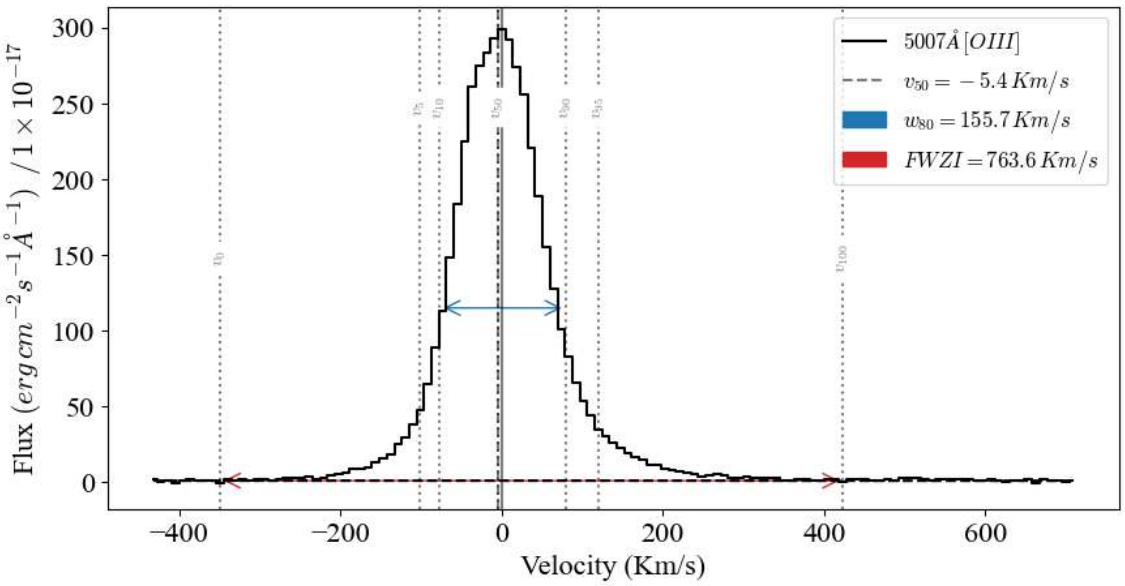

Figure B.21: Inter-percentile analysis of the *WLCE* J095838+202508, using the [OIII]λ5007Å emission-line. Each percentile is represented as a v_i gray dotted-line with i indicating the percentile. The full width zero intensity ($FWZI$) and the w_{80} ($v_{90} - v_{10}$) are shown as a red and blue arrow, respectively.

J131037+214817

Table B.22: Fit statistics of principal emission-lines in J131037+214817

λ_0 [a]	Ion	Model [b]	χ^2 [c]	χ^2_ν [d]	AIC [e]	BIC [f]	P(Gα) [g]
$6563 + 6548, 6584$	Hα + [NII]	G2	3174.7	7.2	895.2	928.0	0.0
		G3	1357.6	3.1	520.9	570.2	100.0
5007	[OIII]	G2	1335.0	6.5	400.4	420.5	0.0
		G3	954.0	4.8	335.9	366.0	100.0
4861	Hβ	G2	710.7	2.1	254.7	262.3	2.9
		G3	692.2	2.0	247.7	259.2	97.1
$6717, 6731$	[SII]	G2	679.5	1.9	236.7	252.2	1.6
		G3	656.7	1.9	228.4	252.2	98.4

[a] Rest wavelength in Å.
[b] G2: Two gaussian components model, G3: Three gaussian components model.
[c] Chi square (see text for details).
[d] Reduced chi square (see text for details).
[e] Akaike Information Criteria (see text for details).
[f] Bayesian Information Criteria (see text for details).
[g] Likelihood percentage of model Gα to be correct respect the other (see text for details).

Table B.23: Results of the two Gaussian components model (G2) fitting of J131037+214817

λ_0 [a]	Ion	Comp. [b]	Δv_r [c]	σ_{int} [d]	Flux [e]	EM_f [f]	GlobalFlux [g]
6563	Hα	N	-7.9 ± 0.5	47.4 ± 0.9	169.9 ± 5.6	28.7	592.9 ± 8.0
		B	4.6 ± 0.7	124.0 ± 1.0	423.0 ± 5.7	71.3	
5007	[OIII]	N	-2.3 ± 0.7	50.3 ± 1.2	229.7 ± 10.5	33.0	697.0 ± 14.7
		B	6.8 ± 1.0	123.9 ± 1.6	467.4 ± 10.3	67.0	
4959	[OIII]	N	-2.3 ± 0.7	50.3 ± 1.2	76.6 ± 1.3	33.1	231.6 ± 2.2
		B	6.8 ± 1.0	123.9 ± 1.6	155.0 ± 1.8	66.9	
4861	Hβ	N	-7.9 ± 0.5	47.4 ± 0.9	49.6 ± 1.1	26.8	185.0 ± 1.9
		B	4.6 ± 0.7	124.0 ± 1.0	135.4 ± 1.5	73.2	
6300	[OI]	N	-7.9 ± 0.5	48.4 ± 0.9	2.5 ± 0.4	19.9	12.4 ± 0.8
		B	4.6 ± 0.7	124.3 ± 1.0	9.9 ± 0.7	80.1	
6548	[NII]	N	-7.9 ± 0.5	48.4 ± 0.9	7.0 ± 0.4	26.4	26.7 ± 0.6
		B	4.6 ± 0.7	124.3 ± 1.0	19.6 ± 0.5	73.6	
6584	[NII]	N	-7.9 ± 0.5	48.4 ± 0.9	21.1 ± 1.2	26.4	80.1 ± 1.9
		B	4.6 ± 0.7	124.3 ± 1.0	58.9 ± 1.5	73.6	
6717	[SII]	N	-7.9 ± 0.5	48.4 ± 0.9	10.9 ± 0.6	23.7	46.0 ± 1.1
		B	4.6 ± 0.7	124.4 ± 1.0	35.1 ± 0.9	76.3	
6731	[SII]	N	-7.9 ± 0.5	48.4 ± 0.9	8.9 ± 0.7	25.0	35.7 ± 1.2
		B	4.6 ± 0.7	124.4 ± 1.0	26.8 ± 1.0	75.0	

[a] Rest wavelength in Å.

[b] Component of the model.

[c] Velocity shift between the central peak of the emission-line and the center of the component (see text for details).

[d] Intrinsic velocity dispersion (see text for details).

[e] Flux of the component (10^{-17} erg s^{-1} cm^{-2}).

[f] Percentage of relative to global flux of the emission-line.

[g] Global flux of the emission-line (10^{-17} erg s^{-1} cm^{-2}).

Table B.24: Results of the three Gaussian components model (G3) fitting of J131037+214817

λ_0 [a]	Ion	Comp. [b]	Δv_r [c]	σ_{int} [d]	Flux [e]	EM_f [f]	GlobalFlux [g]
6563	Hα	B1	-50.3 ± 9.3	178.0 ± 5.1	109.2 ± 12.7	18.3	597.6 ± 18.4
		N	-13.1 ± 0.5	44.7 ± 0.8	142.7 ± 5.4	23.9	
		B2	15.2 ± 1.4	104.7 ± 1.8	345.7 ± 12.2	57.8	
5007	[OIII]	B1	-45.9 ± 20.2	197.3 ± 17.4	93.7 ± 26.5	13.3	704.9 ± 38.4
		N	-4.9 ± 0.9	47.9 ± 1.4	195.1 ± 13.4	27.7	
		B2	12.6 ± 1.9	108.4 ± 3.6	416.1 ± 24.4	59.0	
4959	[OIII]	B1	-45.9 ± 20.2	197.3 ± 17.4	33.4 ± 2.5	14.2	234.6 ± 4.2
		N	-4.9 ± 0.9	47.9 ± 1.4	65.3 ± 1.4	27.8	
		B2	12.6 ± 1.9	108.4 ± 3.6	136.0 ± 3.1	57.9	
4861	Hβ	B1	-50.3 ± 9.3	178.0 ± 5.1	35.7 ± 2.1	19.1	186.6 ± 3.3
		N	-13.1 ± 0.5	44.7 ± 0.8	41.5 ± 1.1	22.2	
		B2	15.2 ± 1.4	104.7 ± 1.8	109.4 ± 2.3	58.6	
6300	[OI]	B1	-50.3 ± 9.3	178.2 ± 5.1	2.4 ± 1.0	19.4	12.4 ± 1.6
		N	-13.1 ± 0.5	45.8 ± 0.8	2.1 ± 0.5	16.8	
		B2	15.2 ± 1.4	105.2 ± 1.8	7.9 ± 1.1	63.8	
6548	[NII]	B1	-50.3 ± 9.3	178.2 ± 5.1	3.7 ± 0.7	13.8	26.5 ± 1.0
		N	-13.1 ± 0.5	45.7 ± 0.8	5.7 ± 0.3	21.4	
		B2	15.2 ± 1.4	105.2 ± 1.8	17.1 ± 0.7	64.8	
6584	[NII]	B1	-50.3 ± 9.3	178.2 ± 5.1	11.0 ± 2.0	13.8	79.4 ± 3.0
		N	-13.1 ± 0.5	45.7 ± 0.8	17.0 ± 1.0	21.4	
		B2	15.2 ± 1.4	105.2 ± 1.8	51.4 ± 2.0	64.8	
6717	[SII]	B1	-50.3 ± 9.3	178.2 ± 5.1	8.0 ± 1.1	17.4	46.0 ± 1.8
		N	-13.1 ± 0.5	45.8 ± 0.8	9.1 ± 0.6	19.8	
		B2	15.2 ± 1.4	105.2 ± 1.8	28.9 ± 1.3	62.8	
6731	[SII]	B1	-50.3 ± 9.3	178.2 ± 5.1	6.7 ± 1.6	18.8	35.8 ± 2.2
		N	-13.1 ± 0.5	45.8 ± 0.8	7.7 ± 0.7	21.4	
		B2	15.2 ± 1.4	105.2 ± 1.8	21.4 ± 1.4	59.8	

[a] Rest wavelength in Å.

[b] Component of the model.

[c] Velocity shift between the central peak of the emission-line and the center of the component (see text for details).

[d] Intrinsic velocity dispersion (see text for details).

[e] Flux of the component (10^{-17} erg s^{-1} cm^{-2}).

[f] Percentage of relative to global flux of the emission-line.

[g] Global flux of the emission-line (10^{-17} erg s^{-1} cm^{-2}).

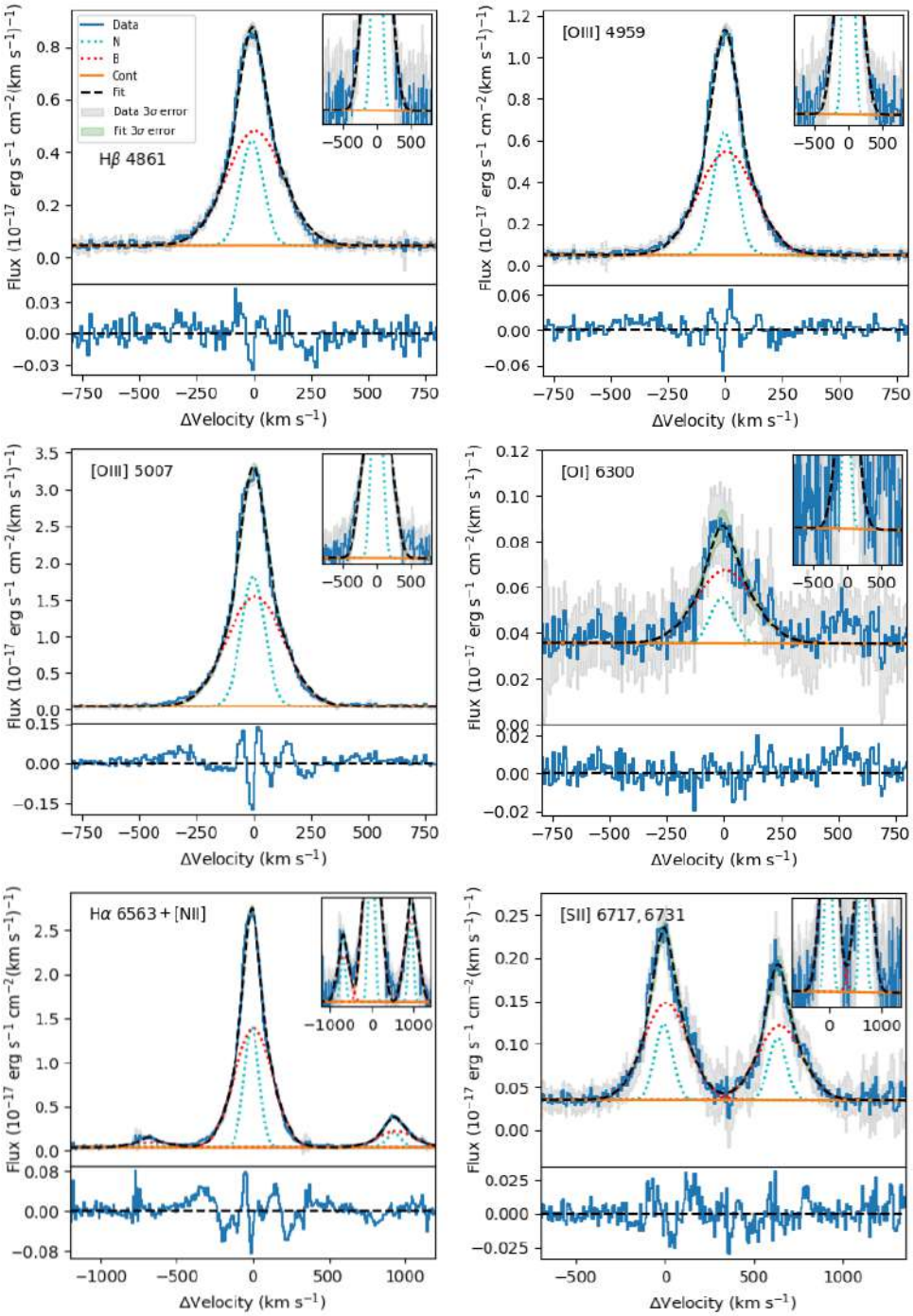

Figure B.22: The fit of faint and bright emission-line profiles of J131037+214817 with two gaussian component models (G2). The blue line represents the original data and the dashed black line the overall model that includes a broad component (B) shown as a red dotted line, and a narrow components (N) represented with a cyan dotted line respectively. The local continuum fitting (Cont) is shown as a solid orange line. We also show the 3σ error spectrum in gray and the 3σ error of the fitted model. A zoomed-in box is shown in the upper-right corner, with $y - axis$ in logarithmic scale. Details of the kinematics and fluxes by component are in Table B.23 , while fit statistics are in B.22.

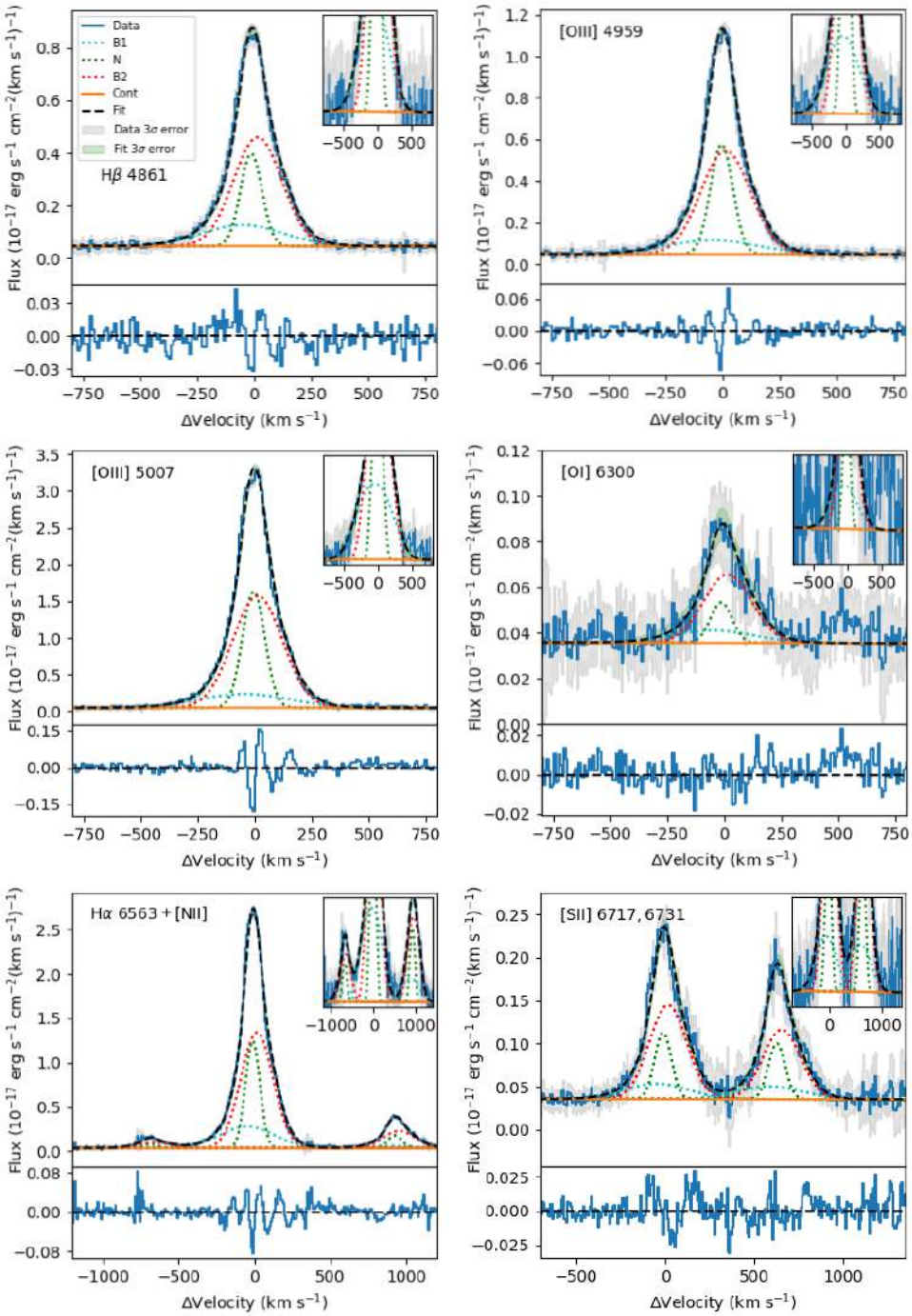

Figure B.23: The fit of faint and bright emission-line profiles of J131037+214817 with three gaussian component models (G3). The blue line represents the original data and the dashed black line the overall model that includes two broad components (B1-B2) shown as a cyan and a red dotted line respectively, and a narrow components (N) represented with a green dotted line. The local continuum fitting (Cont) is shown as a solid orange line. We also show the 3σ error spectrum in gray and the 3σ error of the fitted model. A zoomed-in box is shown in the upper-right corner, with $y-axis$ in logarithmic scale. Details of the kinematics and fluxes by component are in Table B.24 , while fit statistics are in B.22.

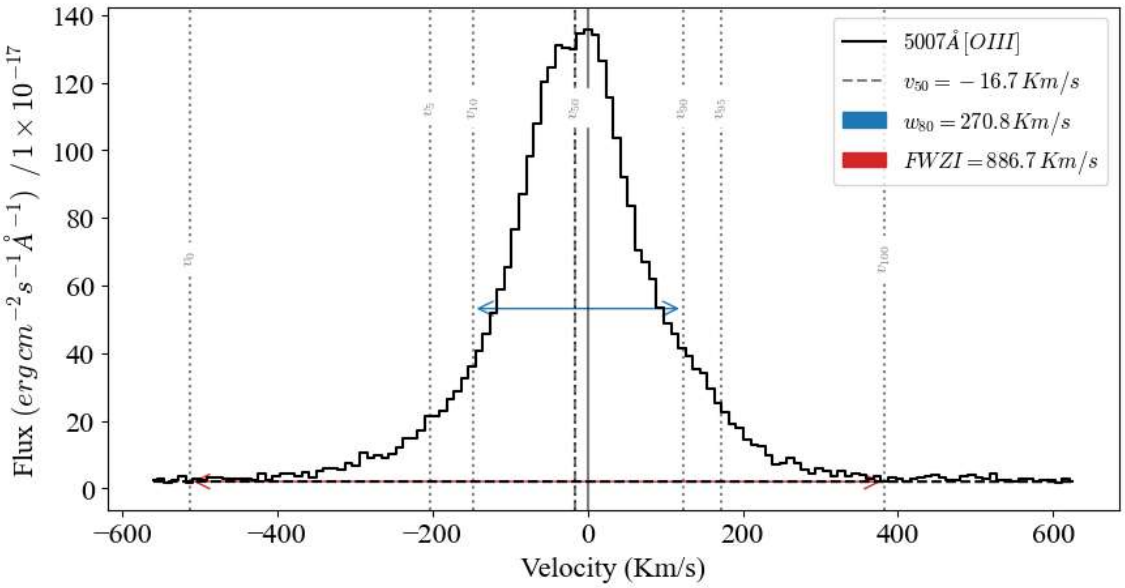

Figure B.24: Inter-percentile analysis of the *WLCE* J131037+214817, using the [OIII]λ5007Å emission-line. Each percentile is represented as a v_i gray dotted-line with i indicating the percentile. The full width zero intensity ($FWZI$) and the w_{80} ($v_{90} - v_{10}$) are shown as a red and blue arrow, respectively.